



**HELLENIC REPUBLIC  
UNIVERSITY OF IOANNINA  
SCHOOL OF ENGINEERING  
DEPARTMENT OF MATERIALS SCIENCE AND ENGINEERING**

**Enhanced light-matter interactions and optoelectronic devices based on graphene and other 2D materials**

**Dagkli Alkmini-Vasiliki**

**PhD Dissertation**

**Ioannina 2024**





**ΕΛΛΗΝΙΚΗ ΔΗΜΟΚΡΑΤΙΑ  
ΠΑΝΕΠΙΣΤΗΜΙΟ ΙΩΑΝΝΙΝΩΝ  
ΠΟΛΥΤΕΧΝΙΚΗ ΣΧΟΛΗ  
ΤΜΗΜΑ ΜΗΧΑΝΙΚΩΝ ΕΠΙΣΤΗΜΗΣ ΥΛΙΚΩΝ**

**Ενισχυμένες αλληλεπιδράσεις φωτός-ύλης και οπτοηλεκτρονικές διατάξεις βασισμένες  
στο γραφένιο και άλλα δισδιάστατα υλικά**

**Δαγκλή Αλκμήνη Βασιλική**

**Διδακτορική διατριβή**

**Ιωάννινα 2024**

*«Η έγκριση της διδακτορικής διατριβής από το Τμήμα Μηχανικών Επιστήμης Υλικών της Πολυτεχνικής Σχολής του Πανεπιστημίου Ιωαννίνων δεν υποδηλώνει αποδοχή των γνώμων του συγγραφέα Ν. 5343/32, άρθρο 202, παράγραφος 2».*

**Date of Application of Mrs. Dagkli Alkmini-Vasiliki:** 19-09-2016

**Date of Appointment of PhD Advisory Committee:** 05-10-2016

**Members of the three-member Advisory Committee:**

Thesis Supervisor

**Elefterios Lidorikis**, Professor in the Department of Materials Science and Engineering at the School of Engineering of the University of Ioannina

Members

**Dimitrios Papageorgiou**, Associate Professor in the Department of Materials Science and Engineering at the School of Engineering of the University of Ioannina

**Spyridon Kaziannis**, Assistant Professor in the Department of Physics at the School of Sciences of the University of Ioannina

**Date of dissertation topic assignment:** 05-10-2016

« Enhanced light-matter interactions and optoelectronic devices based on graphene»

**Date of dissertation topic modification:** 13-06-2023

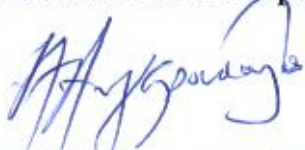
« Enhanced light-matter interactions and optoelectronic devices based on graphene and other 2D materials»

**DATE OF APPOINTMENT OF THE SEVEN-MEMBER EXAMINATION COMMITTEE:** 24-04-2024

1. **Elefterios Lidorikis**, Professor in the Department of Materials Science and Engineering at the School of Engineering of the University of Ioannina
2. **Dimitrios Papageorgiou**, Associate Professor in the Department of Materials Science and Engineering at the School of Engineering of the University of Ioannina
3. **Spyridon Kaziannis**, Assistant Professor in the Department of Physics at the School of Sciences of the University of Ioannina
4. **Michail Sigalas**, Professor in the Department of Materials Science at the School of Natural Sciences of the University of Patras
5. **Maria Kandyla**, Principal Researcher at the Institute of Theoretical Physics and Chemistry (ITPC) of the National Hellenic Research Foundation
6. **Christina Lekka**, Associate Professor in the Department of Materials Science and Engineering at the School of Engineering of the University of Ioannina
7. **Nikolaos Kalfagiannis**, Assistant Professor in the Department of Materials Science and Engineering at the School of Engineering of the University of Ioannina.

The PhD dissertation was approved with a grade of «Excellent» at 11-06-2024

**The chairman of the Department**



**Apostolos Avgeropoulos**  
Professor



**The Secretary of the Department**



**Maria Kontou**

Ημερομηνία αίτησης της κ. Δαγκλή Αλκμήνης-Βασιλικής: 19-09-2016  
Ημερομηνία ορισμού Τριμελούς Συμβουλευτικής επιτροπής: 05-10-2016

**Μέλη Τριμελούς Συμβουλευτικής επιτροπής:**

Επιβλέπων

**Ελευθέριος Λοιδωρικής**, Καθηγητής του Τμήματος Μηχανικών Επιστήμης Υλικών της Πολυτεχνικής Σχολής του Πανεπιστημίου Ιωαννίνων

Μέλη

**Δημήτριος Παπαγεωργίου**, Αναπληρωτής Καθηγητής του Τμήματος Μηχανικών Επιστήμης Υλικών της Πολυτεχνικής Σχολής του Πανεπιστημίου Ιωαννίνων

**Σπυρίδων Καζιάννης**, Επίκουρος Καθηγητής του Τμήματος Φυσικής της Σ.Θ.Ε. του Πανεπιστημίου Ιωαννίνων

**Ημερομηνία ορισμού θέματος:** 05-10-2016

«Ενισχυμένες αλληλεπιδράσεις φωτός-ύλης και οπτοηλεκτρονικές διατάξεις βασισμένες στο γραφένιο»

**Ημερομηνία τροποποίησης θέματος:** 13-06-2023

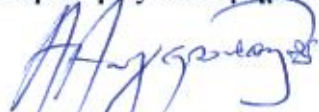
«Enhanced light-matter interactions and optoelectronic devices based on graphene and other 2D materials»

**ΔΙΟΡΙΣΜΟΣ ΕΠΤΑΜΕΛΟΥΣ ΕΞΕΤΑΣΤΙΚΗΣ ΕΠΙΤΡΟΠΗΣ:** 24-04-2024

1. **Ελευθέριος Λοιδωρικής**, Καθηγητής του Τμήματος Μηχανικών Επιστήμης Υλικών της Πολυτεχνικής Σχολής του Πανεπιστημίου Ιωαννίνων
2. **Δημήτριος Παπαγεωργίου**, Αναπληρωτής Καθηγητής του Τμήματος Μηχανικών Επιστήμης Υλικών της Πολυτεχνικής Σχολής του Πανεπιστημίου Ιωαννίνων
3. **Σπυρίδων Καζιάννης**, Επίκουρος Καθηγητής του Τμήματος Φυσικής της Σ.Θ.Ε. του Πανεπιστημίου Ιωαννίνων
4. **Μιχαήλ Σιγάλας**, Καθηγητής του Τμήματος Επιστήμης Υλικών της Σ.Θ.Ε. του Πανεπιστημίου Πατρών
5. **Μαρία Κάνδυλα**, Κύρια Ερευνήτρια του Ινστιτούτου Θεωρητικής Φυσικής και Χημείας (ΙΘΦΧ) του Εθνικού Ιδρύματος Ερευνών
6. **Χριστίνα Λέκκα**, Αναπληρώτρια Καθηγήτρια του Τμήματος Μηχανικών Επιστήμης Υλικών της Πολυτεχνικής Σχολής του Πανεπιστημίου Ιωαννίνων
7. **Νικόλαος Καλφαγιάννης**, Επίκουρος Καθηγητής του Τμήματος Μηχανικών Επιστήμης Υλικών της Πολυτεχνικής Σχολής του Πανεπιστημίου Ιωαννίνων.

Έγκριση Διδακτορικής Διατριβής με βαθμό «ΑΡΙΣΤΑ» στις 11-06-2024

Ο Πρόεδρος του Τμήματος



Απόστολος Αυγερόπουλος  
Καθηγητής



Η Γραμματέας του τμήματος



Μαρία Κόντου

*"Where the world ceases to be the scene of our personal hopes and wishes, where we face it as free beings admiring, asking, and observing, there we enter the realm of Art and Science. If what is seen and experienced is portrayed in the language of logic, we are engaged in science. If it is communicated through forms whose connections are not accessible to the conscious mind but are recognized intuitively as meaningful, then we are engaged in art. Common to both is the loving devotion to that which transcends personal concerns and volition."*

Albert Einstein, quoted in German magazine Dukas and Hoffmann, *the Human Side*, p.37 (1921)

# Abstract

Enhancing the process of converting light into electricity, and vice versa, within materials is a fundamental goal within the domain of optoelectronics. This crucial physical process underpins various technologies, including solar cells, light emitting diodes (LEDs), ultrafast optical communication systems etc. As conventional materials reach their performance limits, there is a growing demand for optoelectronic platforms, that offer novel properties in terms of efficiency, speed and wavelength range. The spotlight has recently shifted towards two-dimensional (2D) layered materials, such as single-layer graphene (SLG) and transition metal dichalcogenides (TMDs), as prime candidates in photonic and optoelectronic applications. These one-atom-thick materials have garnered significant attention, owing to their exceptional electrical and optical properties, which differ from their bulk counterparts. Since the ground-breaking isolation of graphene in 2004, the list of 2D materials has expanded, including a diverse array of crystals with complementary properties. Gathering these 2D building blocks into vertical heterostructures opens up the possibility for designing artificial atomic-layer materials. These resulting van der Waals heterostructures (vdWH), besides combining the properties of their constituent layers, serve as an interesting domain for exploring photophysical effects and implementing innovative light emitting diode schemes.

The goal of this thesis is to explore 2D material-light interactions and the optoelectronic behavior of devices based on graphene, other 2D materials and/or their heterostructures. Our aim is to comprehend the physical processes dictating Surface Enhanced Raman Scattering (SERS) in graphene, as well as the mechanisms governing light emission and manipulation, thereby facilitating the design of enhanced-performance plasmonic substrates, optical modulators, ultrafast pulse-shapers and LEDs, respectively. Utilizing computational methods and convenient analytical approaches, we explore various device configurations to showcase the potential and competitiveness of graphene and TMDs in optoelectronic devices.

For selective optical frequencies within the visible spectrum, we integrate graphene onto 3D plasmonic nanostructured silicon substrates. The conformation of SLG to metallic nanoparticle (NP)-decorated silicon nanopillars allows for the sampling of near-fields, from an increased number of NPs. Additionally, the synergistic effects of NP-Si nanopillars result in a non-local broadband SERS enhancement, reaching up to three orders of magnitude. Our theoretical results agree with corresponding experimental measurements. Exploring light manipulation with graphene in the near-infrared (NIR), we design a free-space optical modulator, operating in reflection mode, which combines graphene's electroabsorption tunability with dielectric Bragg nanocavity effects. By optimizing device's architecture, following practical considerations, we demonstrate the feasibility of achieving deep amplitude modulation (30 dB) at gigahertz (GHz) modulation frequencies, regardless of graphene quality. Moreover, this graphene-based device serves as a highly sensitive acousto-absorption modulator. In the same frequency range, we model graphene within

a dielectric Bragg nanocavity, when pumped by a single ultrafast pulse. The saturable absorption of graphene under high power induces pulse modulation in amplitude, duration and, even, shape, resulting in a more than one peak output pulse. Furthermore, this pulse-shaping device can be utilized as a highly sensitive diagnostic tool for identifying intrinsic graphene processes, manifested by its relaxation times. By employing specific TMD emitters, such as  $\text{WS}_2$  or  $\text{WSe}_2$ , within a graphene/hBN/TMD heterostructure, we design a nanoscale cavity-enhanced LED device for emission into free-space. This design leverages high quality factor (Q) nanocavity effects, to boost the external quantum efficiency (EQE) of LED. This enhancement results from a critical combination of high Purcell enhancement and low cavity losses. Similarly, in the context of an integrated device, designing an antenna-enhanced TMD-based LED on top of a dielectric single-mode silicon nitride (SiN) waveguide, we investigate the enhanced local fields, resulting from the presence of the plasmonic antenna. These fields overlap with SiN waveguide, effectively enhancing the final guided light. This enhancement arises from the critical interplay between plasmonically enhanced Purcell and notably high waveguide coupling efficiencies. Moreover, these innovative designs are not limited to a specific wavelength range. They can be extended across the entire visible-IR spectrum, by appropriately choosing the materials and scaling their dimensions. This versatility allows for the design and optimization of realistic optoelectronic devices.

In summary, this study significantly contributes to advancing our understanding of how graphene and other 2D materials, such as TMDs, interact with light. It achieves this by offering a comprehensive exploration of their optical-electronic properties and suggesting optimized designs for novel devices. The theoretical insights developed in this thesis establish a groundwork for further improvements in optoelectronic technology, based on graphene and TMDs.

# Περίληψη

Η βελτίωση της διαδικασίας μετατροπής του φωτός σε ηλεκτρισμό, όπως και το αντίστροφο, μέσω κατάλληλων υλικών, αποτελεί θεμελιώδη στόχο για τον τομέα της οπτοηλεκτρονικής. Αυτή η θεμελιώδης φυσική διαδικασία είναι κρίσιμη για διάφορες τεχνολογίες, συμπεριλαμβανομένων των ηλιακών κυττάρων (solar cells), των διόδων εκπομπής φωτός (LEDs), των συστημάτων υπεργρήγορης οπτικής επικοινωνίας (ultrafast communication systems) κλπ. Καθώς τα συμβατικά υλικά φτάνουν τα όρια απόδοσής τους, υπάρχει αυξανόμενη ζήτηση για οπτοηλεκτρονικές πλατφόρμες, που προσφέρουν νέες δυνατότητες όσον αφορά την απόδοση, την ταχύτητα και το εύρος των συχνοτήτων. Πρόσφατα, το ενδιαφέρον έχει μετακινηθεί σε δισδιάστατα (2D) στρώματα υλικών, όπως το μονοστρωματικό γραφένιο (SLG) και τα διχαλκογενίδια μετάλλων μετάβασης (TMDs), ως υποψήφια για φωτονικές και οπτοηλεκτρονικές εφαρμογές. Τα υλικά αυτά, πάχους ενός ατόμου, έχουν προσελκύσει το ενδιαφέρον, λόγω των εξαιρετικών ηλεκτρικών και οπτικών τους ιδιοτήτων, οι οποίες διαφέρουν από αυτές των πολυστρωματικών συγγενικών τους υλικών. Από την πρώτη καινοτόμα απομόνωση του γραφενίου το 2004, η λίστα των 2D υλικών έχει επεκταθεί σημαντικά, περιλαμβάνοντας πληθώρα κρυστάλλων με συμπληρωματικές ιδιότητες. Η συγκέντρωση αυτών των 2D υλικών, ως δομικά στοιχεία, σε κατακόρυφες ετεροδομές ανοίγει τον δρόμο για τον σχεδιασμό τεχνητών (artificial) υλικών ατομικού πάχους. Οι van der Waals ετεροδομές (vdWH) που δημιουργούνται, εκτός από το να συνδυάζουν τις ιδιότητες των στρωμάτων τους, ανοίγουν και ένα ενδιαφέρον πεδίο για τη μελέτη φωτοφυσικών φαινομένων και την υλοποίηση καινοτόμων διατάξεων διόδων εκπομπής φωτός.

Στόχος αυτής της διατριβής είναι η εξερεύνηση των αλληλεπιδράσεων των 2D υλικών με το φως, καθώς και της συμπεριφοράς τους σε οπτοηλεκτρονικές διατάξεις, που βασίζονται σε γραφένιο, άλλα 2D υλικά και/ή τις ετεροδομές τους. Σκοπός μας είναι να κατανοηθούν οι φυσικές διαδικασίες που καθορίζουν την επιφανειακή ενισχυμένη σκέδαση Raman (SERS) στο γραφένιο, καθώς και οι μηχανισμοί, που ελέγχουν τη εκπομπή και τον έλεγχο του φωτός, διευκολύνοντας έτσι τον σχεδιασμό υψηλής απόδοσης πλασματικών υποστρωμάτων, οπτικών διαμορφωτών, υπεργρήγορων διαμορφωτών παλμικού σχήματος και διόδων εκπομπής φωτός, αντιστοίχως. Χρησιμοποιώντας τις κατάλληλες υπολογιστικές μεθόδους και αναλυτικές προσεγγίσεις, εξετάζουμε ποικίλες διαμορφωμένες διατάξεις, για να αναδείξουμε τις δυνατότητες και την ανταγωνιστικότητα του γραφενίου και των TMDs όταν χρησιμοποιούνται σε οπτοηλεκτρονικές συσκευές.

Για επιλεγμένες οπτικές συχνότητες εντός του ορατού φάσματος, ενσωματώνουμε το γραφένιο σε τρισδιάστατα πλασματικά νανοδομημένα υποστρώματα πυριτίου. Η διαμόρφωση του SLG σε υβριδικές δομές μεταλλικών νανοσωματίδιων (NPs) επάνω σε νανοστήλες πυριτίου, επιτρέπει την ενίσχυση SERS εξαιτίας των κοντινών πεδίων από ένα αυξημένο αριθμό NPs. Επιπλέον, οι συνεργατικές επιδράσεις NP-νανοστηλών πυριτίου οδηγούν σε μη τοπική ευρυζωνική ενίσχυση SERS, που φτάνει μέχρι και τρεις τάξεις μεγέθους. Τα θεωρητικά μας αποτελέσματα συμφωνούν με αντίστοιχες πειραματικές μετρήσεις. Εξε-

τάζοντας τον έλεγχο του φωτός με γραφένιο στο εγγύς υπέρυθρο (NIR), σχεδιάζουμε έναν οπτικό διαμορφωτή για εκπομπή στον ελεύθερο χώρο, που εκμεταλλεύεται το μέγεθος της οπτικής αντανάκλασης και συνδυάζει την μετατοπίσιμη ηλεκτρο-απορρόφηση του γραφενίου με τα φαινόμενα που προκύπτουν μέσα σε μια διηλεκτρική Bragg νανοκοιλότητα. Βελτιώνοντας την αρχιτεκτονική της διάταξης, λαμβάνοντας υπόψη πρακτικές μεθόδους, αναδεικνύουμε την δυνατότητα επίτευξης υψηλού πλάτους διαμόρφωσης (30 dB) σε συχνότητες διαμόρφωσης της τάξης των gigahertz (GHz), ανεξαρτήτως της ποιότητας του γραφενίου. Επιπλέον, αυτή η διάταξη γραφενίου λειτουργεί και ως ένας υπερευαίσθητος ακουστο-απορροφητικός διαμορφωτής. Στον ίδιο εύρος συχνοτήτων, μοντελοποιούμε τη διάταξη γραφενίου μέσα σε διηλεκτρική Bragg νανοκοιλότητα, υπό την επίδραση ενός υπεργρήγορου (ultrafast) παλμού. Η κορέσιμη απορρόφηση του γραφενίου, υπό υψηλής έντασης παλμό, προκαλεί διαμόρφωση του πλάτους, της διάρκειας, καθώς και του σχήματος του παλμού, με αποτέλεσμα τη δημιουργία ενός εξερχόμενου παλμού με περισσότερες από μία κορυφές. Επιπλέον, αυτή η διάταξη διαμόρφωσης παλμού μπορεί να χρησιμοποιηθεί ως ένα υπερευαίσθητο διαγνωστικό εργαλείο για τον εντοπισμό των εγγενών διεργασιών του γραφενίου, που εκφράζονται μέσω των χρόνων χαλάρωσής του. Χρησιμοποιώντας συγκεκριμένους TMD εκπομπείς, όπως το  $WS_2$  ή το  $WSe_2$ , εντός μίας κάθετης ετεροδομής γραφενίου/hBN/TMD, σχεδιάζουμε μια ενισχυμένη διάταξη LED σε νανοκοιλότητα για εκπομπή φωτός στο ελεύθερο χώρο. Η διάταξη αυτή εκμεταλλεύεται το φαινόμενο του συντονισμού μέσα σε νανοκοιλότητα υψηλού παράγοντα ποιότητας (Q), για να ενισχύσει την εξωτερική κβαντική απόδοση (EQE) του LED. Η ενίσχυση αυτή προκύπτει από τον κατάλληλο συνδυασμό της ενίσχυσης Purcell με τις χαμηλές απώλειες της κοιλότητας. Επιπλέον, στο πλαίσιο μιας ολοκληρωμένης διάταξης, σχεδιάζοντας ενισχυμένης απόδοσης LED, βασισμένο σε TMDs, όταν έρχεται σε επαφή με νανοκεραία και τοποθετείται επάνω σε διηλεκτρικό μονοτροπικό κυματοδηγό νιτριδίου του πυριτίου (SiN WG), ερευνούμε τα ενισχυμένα τοπικά πεδία, που προκύπτουν από την παρουσία της πλασμαονικής κεραίας. Τα πεδία που δημιουργούνται επικαλύπτονται με τον κυματοδηγό, ενισχύοντας αποτελεσματικά το τελικό καθοδηγούμενο φως. Η ενίσχυση αυτή προκύπτει από τον κατάλληλο συνδυασμό της πλασμαονικώς ενισχυμένης απόδοσης Purcell και της αξιοσημείωτης απόδοσης σύζευξης μέσα στον κυματοδηγό (WG coupling). Επιπλέον, αυτές οι καινοτόμες διατάξεις δεν περιορίζονται σε συγκεκριμένο φασματικό εύρος συχνοτήτων. Μπορούν να επεκταθούν σε ολόκληρο το ορατό-υπέρυθρο φάσμα, επιλέγοντας τα κατάλληλα υλικά και προσδιορίζοντας την κλίμακα των διαστάσεων τους. Αυτή η ευελιξία επιτρέπει τον σχεδιασμό και τη βελτιστοποίηση ρεαλιστικών οπτοηλεκτρονικών διατάξεων.

Συνοπτικά, η μελέτη που ακολουθεί συνεισφέρει σημαντικά στην προώθηση της κατανόησης μας σχετικά με το πώς το γραφένιο και άλλα 2D υλικά, όπως τα TMDs, αλληλεπιδρούν με το φως. Αυτό επιτυγχάνεται μέσω μιας σφαιρικής εξερεύνησης των οπτικών-ηλεκτρονικών τους ιδιοτήτων και προτείνοντας βελτιστοποιημένες και καινοτόμες διατάξεις. Η θεωρητική μελέτη που αναπτύχθηκε σε αυτήν τη διατριβή θεμελιώνει τις βάσεις για περαιτέρω βελτιώσεις στην οπτοηλεκτρονική τεχνολογία που βασίζεται στο γραφένιο και τα TMDs.

# Acknowledgments

Within the following sentences, I would like to express my gratitude and appreciation for the people, who stood by me and supported, either academically or in other ways, my efforts to complete my Ph.D. studies. First and foremost, I would like to sincerely thank my supervisor, Prof. Elefterios Lidorikis, who stood by me as a true mentor throughout my doctoral studies and even earlier. His deep knowledge and impressive insight in the field of photonics and solid-state physics served as an inspiration for the study and deeper comprehension of all the physical mechanisms that were encountered during my research work. Through the interaction with Prof. Lidorikis, I learned how to approach and simplify the physical problems that may arise in a project. I was trained to model and simulate optical arrangements using computational programs, that can even approximate real experiments, while recognizing the beauty of programming and the use of simple analytical models, that can in some cases easily substitute for computational programs. Prof. Lidorikis helped me in writing academic publications, supervised my preparation of posters and oral presentations for meetings and conferences, while supporting my efforts by funding my research work in graphene photonics for several years. The completion of this Ph.D. thesis had several practical difficulties, but Prof. Lidorikis encouraged me during this challenging process. He motivated my collaboration with various young researchers, teaching me the invaluable human need for cooperation in achieving a high goal. Discussing with passionate young collaborators about our common concerns in solving computational physics problems, was an exciting experience. I feel very lucky to have collaborated with these people all these years and I hope that they will continue to research with passion and promote science with purity.

Furthermore, I would like to sincerely thank the other six members of my Ph.D. defense committee Prof. Dimitrios Papageorgiou, Prof. Spyridon Kaziannis, Prof. Michael Sigalas, Prof. Maria Kandyla, Prof. Christina Lekka and Prof. Nikolaos Kalfagiannis, who devoted their time to reviewing my thesis.

During my Ph.D. studies, I was funded by the European program Graphene Flagship, which was an important financial boost in allowing me to dedicate myself to research without distractions. This funding program gave me the opportunity to participate in various conferences and meetings and to meet experienced colleagues in the field. The additional collaborations with experimental researchers gave me a more comprehensive understanding of the connection between theory and experiment. One such collaboration, for example, was with the Ph.D. student Maria Kanidi from the National Research Foundation of Greece under the supervision of Prof. Maria Kandyla, which is detailed in Chapter 5 of the thesis. Within this context, I would like to also thank Alisson Cadore from Cambridge Graphene Centre for the collaboration we had during their experiments on TMD-based LEDs, described in Chapter 7. I warmly thank former graduate student Alma Chatzilaris and Ph.D. colleague Spyros Doukas for the creative discussion and efficient collaboration we had for many years, resulting in the production of many interesting results detailed

in Chapter 6, some of which have been published and others that will be published soon. Supervising the work of graduate student Alma Chatzilari and other student works like Polina's Palla, among others, opened up new avenues in understanding and describing physical phenomena in a simple and understandable way. Referring to my daily collaborators, fellow "travelers on the journey of knowledge" and friends, I deeply appreciate and want to thank Ioannis Vangelidis, for our endless afternoon discussions about physics, philosophy, and human relationships, and Dr Dimitris Bellas for his selfless support whenever I needed his valuable advices, regarding the physical and computational problems that arose, as well as the technical support, and his encouragement during difficult times. I would also like to thank all the members of Computational Material Science Laboratory, with whom we harmoniously coexisted for so many years. Specifically, I want to warmly thank fellow Ph.D. candidate and friend Maria Andrea for our pleasant discussions on both science and everyday life. Additionally, I would like to offer special thanks to the Ph.D. candidates Eleftheria Lampadariou, Konstantinos Kaklamanis, Konstantinos Kordos and Tasos Polymerakis for their kindness and support, contributing to the expansion of our collective knowledge in computational physics and programming.

Finally, I would like to extend my gratitude to those people, who were part of my out-of-university life and contributed to the completion of my Ph.D. studies. I will never forget the generous support of my friend, colleague, and partner in life Sokratis, who was always there in my good and bad times, offering me his philosophical and out-of-the-box advices and empathy. Many thanks to my friend and collaborator in another field that interests me, music, Vasilis, who emotionally supported me through melodies. I also want to thank Panagiotis, Nina, Lampros and so many other friends I met in Ioannina, who accompanied me in everyday life, as well as my old friends Stavroula, Lara, Pelia, Tonia, Sofia and Corina, who, although they lived miles away, gave meaning to my studies through their love. Finally, I couldn't forget to thank my extraordinary father Dimos, who inspired me from my young age to love physics, as well as the rest of my beloved family, my mother Elli and brother Michael, who are always by my side with love and tenderness and taught me to show respect to people and science. Now, that I have reached the end, I am sure that without them, I could not have completed this endeavor.

# Publications and conference participations

## Publications covered in this thesis

- Kanidi, M., Dagkli, A., Kelaidis, N., Palles, D., Aminalragia-Giamini, S., Marquez-Velasco, J., ... Kamitsos, E. I., *Surface-enhanced Raman spectroscopy of graphene integrated in plasmonic silicon platforms with three-dimensional nanotopography*, The Journal of Physical Chemistry C, 123(5), 3076-3087,(2019),  
<https://doi.org/10.1021/acs.jpcc.8b10356>
- S. Doukas, A. Chatzilari, A. Dagkli, A. Papagiannopoulos and E. Lidorikis, *Deep and fast free-space electro-absorption modulation in a mobility-independent graphene-loaded Bragg resonator*, Appl. Phys. Lett. 113, 011102 (2018),  
<https://doi.org/10.1063/1.5030699>
- A. R. Cadore, B. L. T. Rosa, I. Paradisanos, S. Mignuzzi, D. De Fazio, E. M. Alexeev, A. Dagkli, J. E. Muench, G. Kakavelakis, S. M. Shinde, D. Yoon, S. Tongay, K. Watanabe, T. Taniguchi, E. Lidorikis, I. Goykhman, G. Soavi, and A. C. Ferrari, *Monolayer WS<sub>2</sub> electro- and photo-luminescence enhancement by TFSI treatment*, 2D Materials (2024),  
<https://doi.org/10.1088/2053-1583/ad1a6a>
- A. Dagkli, S. Doukas, A. Chatzilari, A. C. Ferrari, and E. Lidorikis, *Extreme pulse shaping from saturable absorption in a critically-coupled graphene-loaded photonic crystal cavity*, Under submission
- A. Dagkli and E. Lidorikis, *Plasmonic ultrafast integrated TMD-based LED with Graphene*, In progress

## Conference participations

- A. Dagkli, E. Lidorikis, M. Kanidi, M. Kandyla, N. Kelaidis, D. Palles, S.A. Giamini, J. Marquez, A. Dimoulas, E.I. Kamitsos, *Modeling of surface enhanced Raman spectroscopy in monolayer graphene on top of plasmonic substrates*, Graphene Week 2017, 25-29 September 2017, Athens, Greece

- A. Dagkli and E. Lidorikis, *LEDs based on 2D material heterostructures*, Graphene Flagship Meeting (Core I (8.2.3) and Core II (8.3.4)), 18-20 December 2017, Aachen, Germany
- A. Dagkli, S. Doukas, A. Chatzilari, A. Papagiannopoulos, E. Lidorikis, *Deep and fast free-space electro-absorption modulation in a mobility-independent graphene-loaded Bragg resonator*, Graphene Week 2018, 10-14 September 2018, San Sebastian, Spain
- A. Dagkli, E. Lidorikis, M. Kanidi, M. Kandyla, A. Colli, N. Kelaidis, D. Palles, S.A. Giamini, J. Marquez, A. Dimoulas, E.I. Kamitsos, *Surface-enhanced Raman spectroscopy of graphene integrated in plasmonic silicon platforms with a three-dimensional nanotopography*, 15th International Conference on Nanoscience Nanotechnologies (NN18), 3-6 July 2018, Thessaloniki, Greece
- A. Dagkli, D. De Fazio, I. Goykhman, A.C. Ferrari, E. Lidorikis, *Light emitting diodes based on layered material heterostructures on cavities*, XXXIV Panhellenic Conference on Solid State Physics and Materials Science, 11-14 September 2019, Patras, Greece
- A. Dagkli, A. Chatzilari, S. Doukas, E. Lidorikis, *Electro-optic free-space ultrafast pulse-shaping in a graphene-loaded Bragg resonator*, XXXVI Panhellenic Conference on Solid State Physics and Materials Science, 26-28 September 2022, Heraklion, Greece

# Contents

<b>Abstract</b>	<b>ii</b>
<b>Acknowledgments</b>	<b>vi</b>
<b>Publications and conference participations</b>	<b>viii</b>
<b>1 Introduction</b>	<b>1</b>
1.1 Motivation	1
1.1.1 Graphene and other 2D materials	1
1.1.2 Optoelectronic applications	2
1.2 Scope of this thesis	3
1.3 Thesis layout	4
References	6
<b>2 Properties of 2D Materials and heterostructures</b>	<b>10</b>
2.1 Properties of Graphene	10
2.1.1 Electronic Structure of Graphene	10
2.1.2 Graphene doping via electrostatic gating	12
2.1.3 Optical Properties of Graphene - Optical conductivity	13
2.1.4 Dielectric function and Light Absorption in Graphene	15
2.1.5 Surface-Enhanced Raman Scattering in Graphene	18
2.1.6 Thermal Properties of Graphene - Photocarrier Dynamics	20
2.1.7 Graphene-based Optical Modulation	22
2.2 Properties of 2D TMDs	24
2.2.1 Electronic properties of TMDs	25
2.2.2 Optical Properties of TMDs: Light Absorption and Emission	26
2.3 Hexagonal boron nitride (hBN)	28
2.4 Van der Waals Heterostructures (vdWHs)	31
2.4.1 Electronic and Optical properties	32
2.4.2 Optoelectronic applications based on vdWHs	33
References	42
<b>3 Plasmonics, Photonics and Dipole Emission</b>	<b>57</b>
3.1 Plasmonic response of metals	57
3.1.1 Drude Model for metals	57
3.1.2 Surface Plasmon Polaritons at Planar Interfaces	58
3.1.3 Localized Surface Plasmons in metallic nanoparticles	61
3.2 Optical response of dielectrics	64
3.2.1 Lorentz oscillator	64

3.2.2	Distributed Bragg Reflector (DBR) - Optical Cavity	67
3.2.3	Optical Waveguides	71
3.3	Dipole Emission: Spontaneous decay rate and Optical Local Density of States (LDOS)	74
3.3.1	Electric Dipole in homogeneous medium	74
3.3.2	Electric Dipole in inhomogeneous medium: Spontaneous emission rate, LDOS and Purcell enhancement	76
	References	77
<b>4</b>	<b>Computational and analytical methods</b>	<b>83</b>
4.1	Transfer Matrix Method (TMM)	83
4.1.1	Interface Matrix	84
4.1.2	Propagation Matrix	85
4.1.3	Reflection, Transmission and Absorption coefficients	85
4.2	Finite Difference Time Domain(FDTD) Method	86
4.2.1	The Yee algorithm	86
4.2.2	EM Sources in FDTD	89
4.2.3	Boundary Conditions (BCs) in FDTD simulation	89
4.2.4	Benefits and limitations of FDTD Method	90
4.3	Finite Difference Eigenmode (FDE) Method	90
4.4	Runge-Kutta calculation method	91
	References	92
<b>5</b>	<b>SERS of Graphene on Plasmonic Silicon Substrates</b>	<b>94</b>
5.1	Introduction	95
5.2	SERS measurements of SLG on Si substrates	96
5.3	SERS on flat substrate	97
5.4	SERS on nanostructured Si substrate	99
5.5	SERS on Au-decorated nanostructured Si substrate	101
5.6	Comparisons-Numerical verification	103
5.7	Conclusions	105
	References	106
<b>6</b>	<b>Graphene-based Optical Modulation and Pulse-Shaping</b>	<b>111</b>
6.1	Introduction	113
6.2	Linear electro-absorption Modulation with Graphene	114
6.2.1	Device Layout	114
6.2.2	Modulation Depth and Frequencies	117
6.2.3	Acousto-optic Modulation and Sensing	118
6.3	Non-linear Ultrafast Pulse-Shaping with Graphene	119
6.3.1	Non-linear Pulse Excitation - Non equilibrium carriers	119
6.3.2	Wavelength Detuning	122
6.3.3	The impact of SLG Fermi level for non-linear excitation	124
6.3.4	The effect of SLG e-e relaxation time and Sensitivity	126
6.4	Conclusions	127
	References	127

<b>7</b>	<b>TMD-based LED with Graphene</b>	<b>134</b>
7.1	Introduction . . . . .	136
7.2	TMD-based LED performance metrics . . . . .	136
7.2.1	LED quantum efficiency and light coupling into a WG . . . . .	137
7.2.2	LED frequency response . . . . .	139
7.3	Experimental TMD-based LED . . . . .	140
7.4	TMD-based LED on typical SiO <sub>2</sub> /Si substrate . . . . .	142
7.5	TMD-based LED inside a photonic nanocavity . . . . .	143
7.6	Antenna-enhanced ultrafast TMD-based LED . . . . .	144
7.6.1	Antenna-enhanced TMD-based LED for free-space emission . . . . .	144
7.6.2	Antenna-enhanced TMD-based LED for integrated photonics . . . . .	146
7.7	Conclusions . . . . .	151
	References . . . . .	152
<b>8</b>	<b>Conclusions and Outlook</b>	<b>160</b>
8.1	Summary . . . . .	160
8.2	Outlook and future perspectives . . . . .	161
	References . . . . .	162
<b>A</b>	<b>SERS of Graphene on Plasmonic Silicon Substrates</b>	<b>168</b>
A.1	The role of SiO <sub>2</sub> layer . . . . .	168
A.2	Quenching effect of graphene on the optical properties of Au nanoparticles . . . . .	169
A.3	SERS of graphene on flat silicon with Au nanoparticles . . . . .	170
	References . . . . .	171
<b>B</b>	<b>Graphene-based Optical Modulation and Pulse-shaping</b>	<b>173</b>
B.1	Critical Coupling . . . . .	173
B.2	Electronic thermal cooling current . . . . .	175
	References . . . . .	176
<b>C</b>	<b>TMD-based LEDs with Graphene</b>	<b>179</b>
C.1	Bow-Tie antenna on WG: Geometrical optimization . . . . .	179
C.2	Reference LED device's EL efficiency . . . . .	180
C.3	Bow-Tie antenna: Material Parameters . . . . .	180
	References . . . . .	181
	<b>Short CV</b>	<b>182</b>

# Chapter 1

## Introduction

### 1.1 Motivation

#### 1.1.1 Graphene and other 2D materials

Recently, two-dimensional (2D) materials have proved as a promising platform for novel heterostructures, that overcome the limitations of conventional materials. These atomically thin materials, due to their promising optical, electrical and mechanical properties, have captured a lot of attention in multiple scientific fields, from optoelectronics to biomedical. The isolation of graphene in 2004 [1] and the following discovery of other 2D materials in 2005 [2], created a significant interest in these materials [3]. In their bulk form, they consist of atoms connected with strong in-plane covalent bonds, while individual layers are weakly bound to neighboring layers through van der Waals interactions. The weak interaction between layers facilitates the mechanical exfoliation of individual layers from the bulk materials. The simplicity of this isolation method (known as the "scotch-tape method") leads to the recent extensive research that reveals the unique properties of these materials. In case of graphene, these properties include, among others, high electronic mobility [4, 5], mechanical flexibility [6] and high thermal conductivity [7].

After years of studies focused exclusively on Single-Layer Graphene (SLG), the research spotlight moved to a broader array of 2D materials. Notably, hexagonal Boron Nitride (hBN) and Transition Metal Dichalcogenides (TMDs) captivate the interest for novel studies. These crystals exhibit a wide range of properties, that complement the intrinsic properties of gapless SLG. For instance, hBN stands out as a transparent insulator [8, 9], while TMDs, such as  $\text{WSe}_2$ , are semiconductors with bandgaps within the near-infrared (near-IR) to visible region (Figure 1.1). Furthermore, owing to the significant changes in their electronic band structures, 2D materials display different properties compared to their bulk equivalents. Notably, TMDs exhibit an indirect bandgap in their bulk form, while displaying a direct bandgap in the monolayer limit [10, 11]. There is a wide range of promising 2D materials including new additions, such as anisotropic semiconductors (black phosphorus) [12, 13], superconductors ( $\text{NbSe}_2$ ) [14], topological semi-metals ( $\text{WTe}_2$  or  $\text{MoTe}_2$ ) [15–17], ferromagnets ( $\text{CrL}_3$ ) [18] etc.

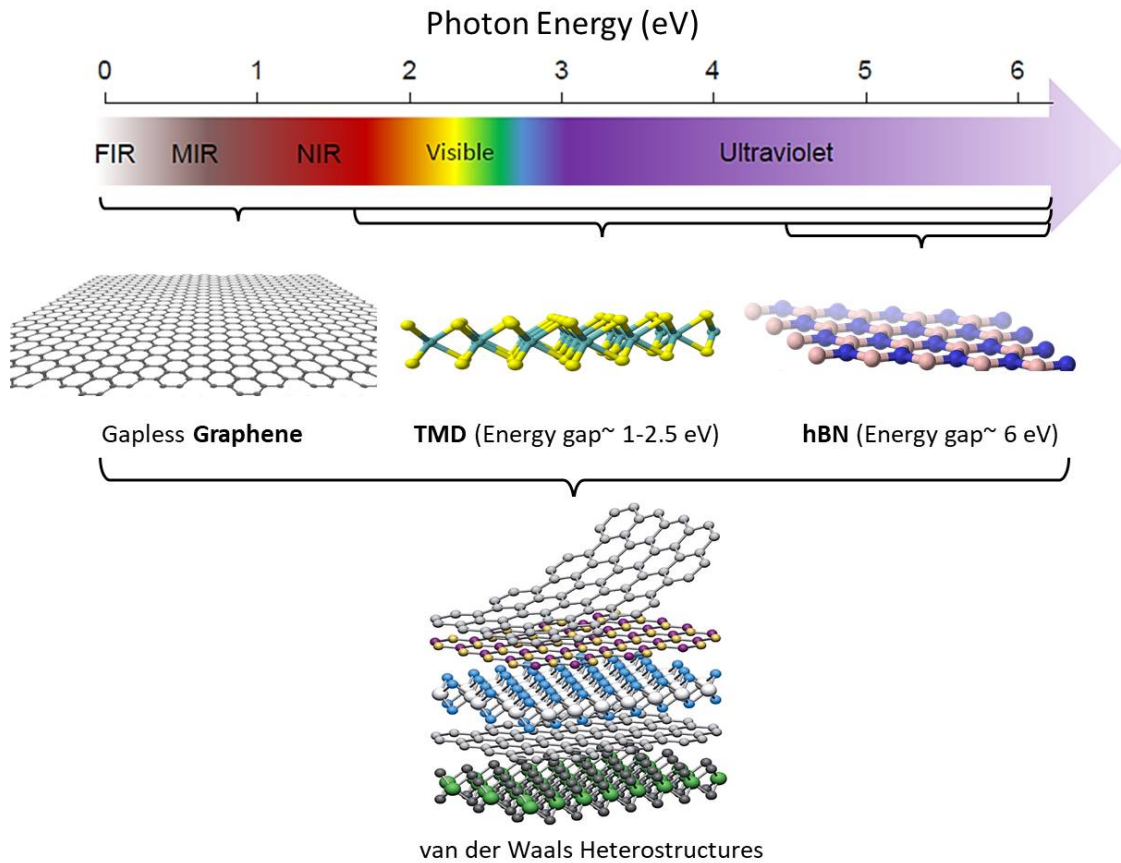


Figure 1.1: Schematics of the electromagnetic spectrum from ultraviolet to far-infrared, with distinct regions labelled as FIR (far-infrared), MIR (mid-infrared) and NIR (near-infrared). Below the photon energy spectrum, the atomic structures of graphene, TMD (e.g.  $\text{WSe}_2$ ) and hBN are depicted, along with their bandgap  $E_G$  and their respective absorption range (eV). At the bottom, a schematic of a vertical van der Waals Heterostructure (vdWH) is shown.

### 1.1.2 Optoelectronic applications

The field of optoelectronics [19] involves the investigation of electronic devices designed to detect and manipulate light. The efficiency of optoelectronic devices is inherently linked to the materials used in their fabrication. Currently, the materials mostly used in optoelectronics are GaN, GaAs and their alloys with In, Al, P, etc. However, these bulk inorganic materials face some noteworthy limitations, such as the limited spectral response, the need for special heteroepitaxy methods, their inadequacy for integration in flexible devices or on Si and SiN photonics [20, 21] (metal-oxide-semiconductor (CMOS) fabrication processes [22, 23]), etc. Therefore, it becomes evident that current material platforms are unable to manage with all the requirements for the development of next-generation optoelectronics.

On account of this, the growing potential of 2D materials, such as SLG and TMDs, along with their heterostructures, for photonic and optoelectronic applications, has become apparent [24–30]. A wide range of 2D material-based optoelectronic devices has been suc-

cessfully demonstrated, including optical modulators [31], photodetectors [32, 33], Light-Emitting Diodes (LEDs) [34], plasmonic devices [35], etc. The rise in research related to these devices, has been motivated by their prospects in terms of efficiency, speed, wavelength range and mechanical flexibility. Certainly, 2D materials (particularly SLG and TMDs) are efficient materials for several optoelectronic applications. Gapless graphene demonstrates a broadband optical response [36] (Figure 1.1), characterized by ultrafast dynamics [37]. This makes it promising for applications that demand ultrafast speed [38, 39]. On the other hand, TMD semiconductors exhibit strong light-exciton interactions [11, 40], presenting advantages in case of enhanced light emission applications [41]. The combination of these material properties within a van der Waals heterostructure is also a promising approach for multi-operational and high-performance optoelectronic devices.

## 1.2 Scope of this thesis

The aim of this thesis is to computationally and analytically investigate the enhanced 2D material-light interactions, as well as to explore the application of graphene and TMD-based heterostructures in optoelectronic devices. These devices include enhanced performance plasmonic substrates, nanoscale optical modulators, optical sensors, ultrafast pulse-shapers and 2D LEDs for both free-space and integrated emission, operating from visible to NIR frequency range.

To achieve this, we have to address the key issues related to 2D material-light interaction principles and the operation of these optoelectronic devices. Initially, we focus on the optical, electronic and thermal properties of graphene, along with other 2D materials, such as hBN, TMDs and their heterostructures. We, moreover, explore the fundamentals of plasmonics, photonics and dipole emission in order to support a thoughtful analysis of our numerical results. Furthermore, our aim is to simulate the photo-response of 2D materials within proposed optoelectronic device configurations, proving that they can overcome the limitations of conventional material devices, in terms of efficiency and speed. We describe the computational, analytical and post-analysis methods used throughout this thesis to calculate the optical performance of graphene- and TMD-based devices. Our study enables the representation of experimental optical devices, serving as a link between fundamental physics and practical device engineering.

Investigating enhanced graphene-light interactions, we integrate graphene onto 3D plasmonic nanostructured silicon substrates, in order to plasmonically enhance the broadband Surface Enhanced Raman Scattering (SERS) in graphene. Additionally, exploring light manipulation with graphene in the NIR, we design an efficient free-space optical modulator, which combines graphene's electro-absorption tunability with dielectric Bragg nanocavity effects, and can also be used as a sensitive acousto-absorption modulator. Modeling the same device under incident high power pulse, we exploit the tunable saturable absorption, ultra-fast carrier dynamics and slow cooling processes of graphene and manage to manipulate light in amplitude, duration and, even, shape, converting the device to an ultrafast pulse-shaper. This device can be easily used as a diagnostic tool for identifying the intrinsic physical processes in graphene, as well. Furthermore, we aim at cavity- and antenna- enhancing the external quantum efficiency (EQE) of a graphene/hBN/TMD heterostructure LED device for emission in free-space and into a single-mode SiN waveguide, respectively.

It is noteworthy that the methodologies developed and the final conclusions obtained from this thesis extend beyond the proposed devices, offering applicability to alternative

configurations, consisting of various combinations of 2D materials, that are not limited to a specific wavelength range. This versatility allows for the design and optimization of realistic optoelectronic devices.

### 1.3 Thesis layout

This thesis is organized as follows:

- Chapter 2 provides insight into the extraordinary optoelectronic properties of 2D materials, such as monolayer graphene, TMDs and hBN, and their heterostructures, focusing on the photocarrier dynamics. The basic concepts outlined in this chapter are used in the thesis to study graphene and TMD-based optoelectronic devices.
- Chapter 3 presents the fundamentals of light-matter interactions studied in the thesis. The plasmonic response of metals, i.e. SPPs at planar interfaces and LSPs in metallic NPs, and photonics, encompassing structures such as photonic crystals and dielectric waveguides, are comprehensively reviewed. Furthermore, this chapter provides an insightful exploration of dipole emission, describing the emission dynamics of 2D TMDs.
- In chapter 4 both computational and analytical methods, that are used throughout this thesis, are described. The analytical TM Method, along with the computational methods FDTD and FDE, determining the optical response of the studied devices, are thoroughly presented.
- Chapter 5 explores graphene-light interaction, when integrating it with 3D plasmonic nanostructured silicon substrates. Our computational results, complemented by experimental measurements, show that the conformation of SLG to metallic NP-decorated silicon nanopillars, enables graphene to sample near-fields from an increased number of NPs. In addition, due to NP-Si nanopillar synergistic effects, there is a non-local broad-band SERS enhancement, reaching up to three orders of magnitude. The study, presented in this chapter, is published in cooperation with respective experiments in Reference [42].
- Chapter 6 is divided into two distinct graphene applications. In the first application, the use of graphene for optical linear constant wave (CW) modulation is explored, while in the latter graphene is introduced as an effective material for achieving non-linear ultrafast pulse-shaping. Graphene is integrated with an asymmetric Fabry-Perot nanocavity, in order to be used, both in a free-space NIR electro-optic modulator and an ultrafast pulse-shaper. Focusing on optical modulation, our findings show that high performance and fast modulation can be achieved, independently of graphene quality. Furthermore, this device can be transformed into a highly sensitive acousto-absorption modulator. In the latter main exploration, graphene is revealed as a tunable saturable absorber, that can be a versatile tool for the modulation of pulse's amplitude, time duration and, even, shape, giving rise to more than one pulse peaks. Additionally, this pulse-shaper can be used as a sensitive diagnostic tool for the identification of intrinsic graphene processes. The optical modulation results, performed by Doukas et al., were published in Reference [43], while the publication related to ultrafast pulse-shaping with graphene is under submission.

- Chapter 7 constitutes a thorough examination of LEDs based on TMDs, driven by their potential for high efficiency and speed, extending up to the GHz range. Our focus encompasses both free-space and integrated photonic devices, highlighting their versatile applicability. Within this study, we explore a vertical LMH, comprising TMD, hBN, and graphene monolayers. Notably, our investigation reveals an interesting enhancement in  $\text{WS}_2$ -based LED emission, when affected by a photonic cavity, resulting in enhanced radiation for free-space applications. In addition, when an  $\text{WSe}_2$ -based LMH is positioned on top of a dielectric waveguide, antenna-coupling effects come into play, enhancing integrated LED emission. Our findings indicate that the combination of Purcell effects with light coupling (or free-space extraction of light), leads to a significant enhancement in waveguide (or external) efficiency, achieving a higher LED speed, as well. The part of our study, focusing on cavity-enhanced free-space TMD-based LEDs, has been published in Reference [44], while our ongoing computational work for antenna-enhanced integrated TMD-based LEDs is in progress for publication.
- Finally, in the Conclusion Chapter 8, a summary of the main achievements of this thesis is presented, along with a discussion on the potential of graphene and other 2D materials for future effective and ultrafast optoelectronic applications.

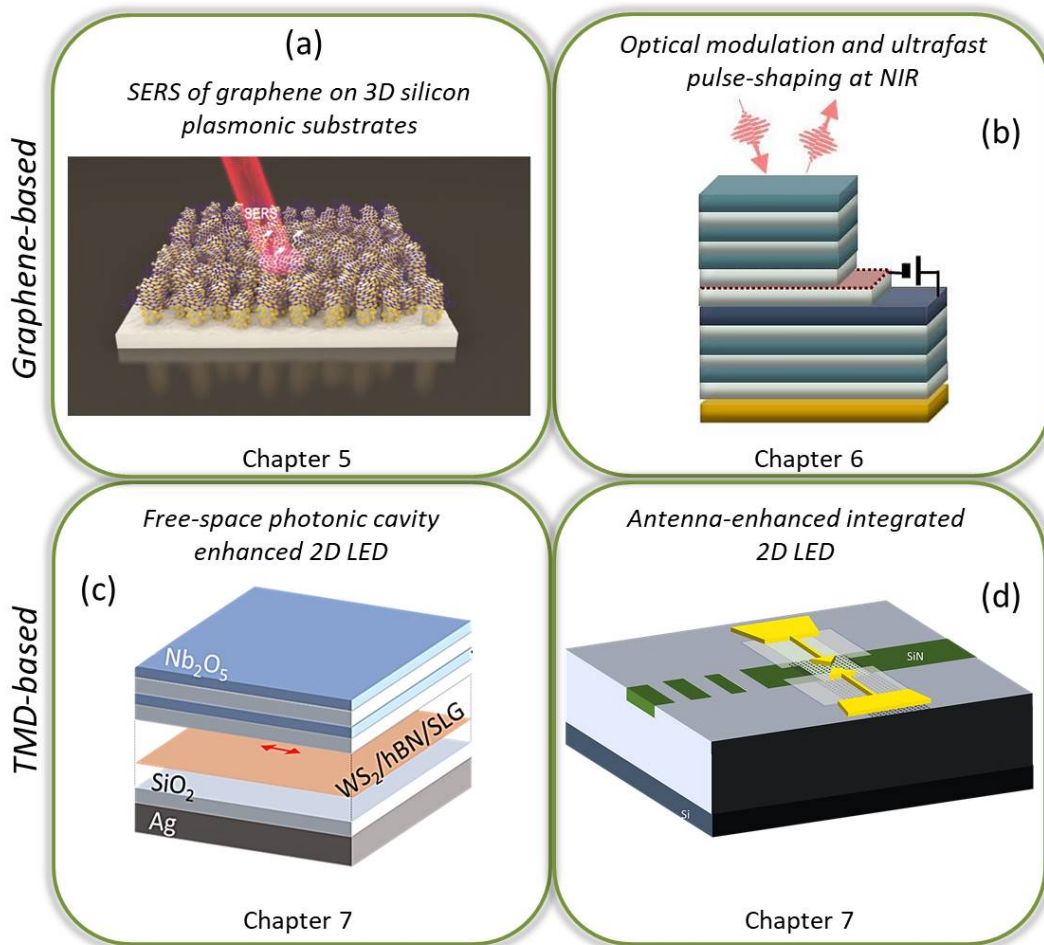


Figure 1.2: Schematics of the main 2D material systems studied in this thesis. The devices are arranged according to their photo-active material (graphene or TMD) and their application. The chapter in which each device is studied is indicated above.

## References

- [1] K. S. Novoselov, A. K. Geim, S. V. Morozov, D.-e. Jiang, Y. Zhang, S. V. Dubonos, I. V. Grigorieva, and A. A. Firsov, “Electric field effect in atomically thin carbon films,” *science*, vol. 306, no. 5696, pp. 666–669, 2004.
- [2] K. S. Novoselov, D. Jiang, F. Schedin, T. Booth, V. Khotkevich, S. Morozov, and A. K. Geim, “Two-dimensional atomic crystals,” *Proceedings of the National Academy of Sciences*, vol. 102, no. 30, pp. 10451–10453, 2005.
- [3] A. C. Ferrari, F. Bonaccorso, V. Fal’Ko, K. S. Novoselov, S. Roche, P. Bøggild, S. Borini, F. H. Koppens, V. Palermo, N. Pugno, *et al.*, “Science and technology roadmap for graphene, related two-dimensional crystals, and hybrid systems,” *Nanoscale*, vol. 7, no. 11, pp. 4598–4810, 2015.
- [4] K. I. Bolotin, K. Sikes, Z. Jiang, M. Klima, G. Fudenberg, J. Hone, P. Kim, and H. L. Stormer, “Ultrahigh electron mobility in suspended graphene,” *Solid state communications*, vol. 146, no. 9-10, pp. 351–355, 2008.
- [5] L. Wang, I. Meric, P. Huang, Q. Gao, Y. Gao, H. Tran, T. Taniguchi, K. Watanabe, L. Campos, D. Muller, *et al.*, “One-dimensional electrical contact to a two-dimensional material,” *Science*, vol. 342, no. 6158, pp. 614–617, 2013.
- [6] C. Lee, X. Wei, J. W. Kysar, and J. Hone, “Measurement of the elastic properties and intrinsic strength of monolayer graphene,” *science*, vol. 321, no. 5887, pp. 385–388, 2008.
- [7] A. A. Balandin, S. Ghosh, W. Bao, I. Calizo, D. Teweldebrhan, F. Miao, and C. N. Lau, “Superior thermal conductivity of single-layer graphene,” *Nano letters*, vol. 8, no. 3, pp. 902–907, 2008.
- [8] G. Cassabois, P. Valvin, and B. Gil, “Hexagonal boron nitride is an indirect bandgap semiconductor,” *Nature photonics*, vol. 10, no. 4, pp. 262–266, 2016.
- [9] G. Giovannetti, P. A. Khomyakov, G. Brocks, P. J. Kelly, and J. Van Den Brink, “Substrate-induced band gap in graphene on hexagonal boron nitride: Ab initio density functional calculations,” *Physical Review B*, vol. 76, no. 7, p. 073103, 2007.
- [10] Q. H. Wang, K. Kalantar-Zadeh, A. Kis, J. N. Coleman, and M. S. Strano, “Electronics and optoelectronics of two-dimensional transition metal dichalcogenides,” *Nature nanotechnology*, vol. 7, no. 11, pp. 699–712, 2012.
- [11] K. F. Mak, C. Lee, J. Hone, J. Shan, and T. F. Heinz, “Atomically thin mos 2: a new direct-gap semiconductor,” *Physical review letters*, vol. 105, no. 13, p. 136805, 2010.
- [12] A. Carvalho, M. Wang, X. Zhu, A. S. Rodin, H. Su, and A. H. Castro Neto, “Phosphorene: from theory to applications,” *Nature Reviews Materials*, vol. 1, no. 11, pp. 1–16, 2016.
- [13] L. Li, Y. Yu, G. J. Ye, Q. Ge, X. Ou, H. Wu, D. Feng, X. H. Chen, and Y. Zhang, “Black phosphorus field-effect transistors,” *Nature nanotechnology*, vol. 9, no. 5, pp. 372–377, 2014.

- [14] X. Xi, Z. Wang, W. Zhao, J.-H. Park, K. T. Law, H. Berger, L. Forró, J. Shan, and K. F. Mak, "Ising pairing in superconducting nbse 2 atomic layers," *Nature Physics*, vol. 12, no. 2, pp. 139–143, 2016.
- [15] Z. Fei, T. Palomaki, S. Wu, W. Zhao, X. Cai, B. Sun, P. Nguyen, J. Finney, X. Xu, and D. H. Cobden, "Edge conduction in monolayer wte2," *Nature Physics*, vol. 13, no. 7, pp. 677–682, 2017.
- [16] Y. Li, J. Zhang, D. Huang, H. Sun, F. Fan, J. Feng, Z. Wang, and C.-Z. Ning, "Room-temperature continuous-wave lasing from monolayer molybdenum ditelluride integrated with a silicon nanobeam cavity," *Nature nanotechnology*, vol. 12, no. 10, pp. 987–992, 2017.
- [17] Y.-Q. Bie, G. Grosso, M. Heuck, M. M. Furchi, Y. Cao, J. Zheng, D. Bunandar, E. Navarro-Moratalla, L. Zhou, D. K. Efetov, *et al.*, "A mote2-based light-emitting diode and photodetector for silicon photonic integrated circuits," *Nature nanotechnology*, vol. 12, no. 12, pp. 1124–1129, 2017.
- [18] B. Huang, G. Clark, E. Navarro-Moratalla, D. R. Klein, R. Cheng, K. L. Seyler, D. Zhong, E. Schmidgall, M. A. McGuire, D. H. Cobden, *et al.*, "Layer-dependent ferromagnetism in a van der waals crystal down to the monolayer limit," *Nature*, vol. 546, no. 7657, pp. 270–273, 2017.
- [19] J. Wilson and J. F. Hawkes, "Optoelectronics-an introduction," *Optoelectronics-An introduction (2nd edition)*, 1989.
- [20] G. T. Reed, "Silicon photonics: the state of the art," 2008.
- [21] D. Thomson, A. Zilkie, J. E. Bowers, T. Komljenovic, G. T. Reed, L. Vivien, D. Marris-Morini, E. Cassan, L. Virot, J.-M. Fédéli, *et al.*, "Roadmap on silicon photonics," *Journal of Optics*, vol. 18, no. 7, p. 073003, 2016.
- [22] I. A. Young, E. M. Mohammed, J. T. Liao, A. M. Kern, S. Palermo, B. A. Block, M. R. Reshotko, and P. L. Chang, "Optical technology for energy efficient i/o in high performance computing," *IEEE Communications Magazine*, vol. 48, no. 10, pp. 184–191, 2010.
- [23] N. Izhaky, M. T. Morse, S. Koehl, O. Cohen, D. Rubin, A. Barkai, G. Sarid, R. Cohen, and M. J. Paniccia, "Development of cmos-compatible integrated silicon photonics devices," *IEEE Journal of Selected Topics in Quantum Electronics*, vol. 12, no. 6, pp. 1688–1698, 2006.
- [24] F. Bonaccorso, Z. Sun, T. Hasan, and A. Ferrari, "Graphene photonics and optoelectronics," *Nature photonics*, vol. 4, no. 9, pp. 611–622, 2010.
- [25] Q. Bao and K. P. Loh, "Graphene photonics, plasmonics, and broadband optoelectronic devices," *ACS nano*, vol. 6, no. 5, pp. 3677–3694, 2012.
- [26] X. Duan, C. Wang, A. Pan, R. Yu, and X. Duan, "Two-dimensional transition metal dichalcogenides as atomically thin semiconductors: opportunities and challenges," *Chemical Society Reviews*, vol. 44, no. 24, pp. 8859–8876, 2015.

- [27] A. Bablich, S. Kataria, and M. C. Lemme, “Graphene and two-dimensional materials for optoelectronic applications,” *Electronics*, vol. 5, no. 1, p. 13, 2016.
- [28] Q. Wang, J. Lai, and D. Sun, “Review of photo response in semiconductor transition metal dichalcogenides based photosensitive devices,” *Optical Materials Express*, vol. 6, no. 7, pp. 2313–2327, 2016.
- [29] F. Xia, H. Wang, D. Xiao, M. Dubey, and A. Ramasubramaniam, “Two-dimensional material nanophotonics,” *Nature Photonics*, vol. 8, no. 12, pp. 899–907, 2014.
- [30] K. F. Mak and J. Shan, “Photonics and optoelectronics of 2d semiconductor transition metal dichalcogenides,” *Nature Photonics*, vol. 10, no. 4, pp. 216–226, 2016.
- [31] Z. Sun, A. Martinez, and F. Wang, “Optical modulators with 2d layered materials,” *Nature Photonics*, vol. 10, no. 4, pp. 227–238, 2016.
- [32] F. Koppens, T. Mueller, P. Avouris, A. Ferrari, M. Vitiello, and M. Polini, “Photodetectors based on graphene, other two-dimensional materials and hybrid systems,” *Nature nanotechnology*, vol. 9, no. 10, pp. 780–793, 2014.
- [33] Z. Lou, Z. Liang, and G. Shen, “Photodetectors based on two dimensional materials,” *Journal of Semiconductors*, vol. 37, no. 9, p. 091001, 2016.
- [34] F. Withers, O. Del Pozo-Zamudio, A. Mishchenko, A. Rooney, A. Gholinia, K. Watanabe, T. Taniguchi, S. J. Haigh, A. Geim, A. Tartakovskii, *et al.*, “Light-emitting diodes by band-structure engineering in van der waals heterostructures,” *Nature materials*, vol. 14, no. 3, pp. 301–306, 2015.
- [35] J. Chen, M. Badioli, P. Alonso-González, S. Thongrattanasiri, F. Huth, J. Osmond, M. Spasenović, A. Centeno, A. Pesquera, P. Godignon, *et al.*, “Optical nano-imaging of gate-tunable graphene plasmons,” *Nature*, vol. 487, no. 7405, pp. 77–81, 2012.
- [36] R. R. Nair, P. Blake, A. N. Grigorenko, K. S. Novoselov, T. J. Booth, T. Stauber, N. M. Peres, and A. K. Geim, “Fine structure constant defines visual transparency of graphene,” *science*, vol. 320, no. 5881, pp. 1308–1308, 2008.
- [37] N. M. Gabor, J. C. Song, Q. Ma, N. L. Nair, T. Taychatanapat, K. Watanabe, T. Taniguchi, L. S. Levitov, and P. Jarillo-Herrero, “Hot carrier–assisted intrinsic photoresponse in graphene,” *Science*, vol. 334, no. 6056, pp. 648–652, 2011.
- [38] T. Mueller, F. Xia, and P. Avouris, “Graphene photodetectors for high-speed optical communications,” *Nature photonics*, vol. 4, no. 5, pp. 297–301, 2010.
- [39] X. Gan, R.-J. Shiue, Y. Gao, I. Meric, T. F. Heinz, K. Shepard, J. Hone, S. Assefa, and D. Englund, “Chip-integrated ultrafast graphene photodetector with high responsivity,” *Nature photonics*, vol. 7, no. 11, pp. 883–887, 2013.
- [40] Y. Li, A. Chernikov, X. Zhang, A. Rigosi, H. M. Hill, A. M. Van Der Zande, D. A. Chenet, E.-M. Shih, J. Hone, and T. F. Heinz, “Measurement of the optical dielectric function of monolayer transition-metal dichalcogenides:  $\text{MoS}_2$ ,  $\text{MoSe}_2$ ,  $\text{WS}_2$ , and  $\text{WSe}_2$ ,” *Physical Review B*, vol. 90, no. 20, p. 205422, 2014.

- [41] L. Britnell, R. M. Ribeiro, A. Eckmann, R. Jalil, B. D. Belle, A. Mishchenko, Y.-J. Kim, R. V. Gorbachev, T. Georgiou, S. V. Morozov, *et al.*, “Strong light-matter interactions in heterostructures of atomically thin films,” *Science*, vol. 340, no. 6138, pp. 1311–1314, 2013.
- [42] M. Kanidi, A. Dagkli, N. Kelaidis, D. Palles, S. Aminalragia-Giamini, J. Marquez-Velasco, A. Colli, A. Dimoulas, E. Lidorikis, M. Kandyla, *et al.*, “Surface-enhanced raman spectroscopy of graphene integrated in plasmonic silicon platforms with three-dimensional nanotopography,” *The Journal of Physical Chemistry C*, vol. 123, no. 5, pp. 3076–3087, 2019.
- [43] S. Doukas, A. Chatzilari, A. Dagkli, A. Papagiannopoulos, and E. Lidorikis, “Deep and fast free-space electro-absorption modulation in a mobility-independent graphene-loaded bragg resonator,” *Applied Physics Letters*, vol. 113, no. 1, 2018.
- [44] A. Cadore, B. L. T. Rosa, I. Paradisanos, S. Mignuzzi, D. De Fazio, E. Alexeev, A. Dagkli, J. Muench, G. Kakavelakis, S. M. Schinde, *et al.*, “Monolayer ws<sub>2</sub> electro-and photo-luminescence enhancement by tfsi treatment,” *2D Materials*, 2024.

# Chapter 2

## Properties of 2D Materials and heterostructures

This chapter provides a comprehensive examination of 2D material properties, such as monolayer graphene (SLG), transition metal dichalcogenides (TMDs), hexagonal boron nitride (h-BN) and their heterostructures. It includes a thorough exploration of graphene's electronic, optical, and thermal properties, as well as an analysis of optoelectronic characteristics of TMDs and Van der Waals heterostructures in vertical and horizontal hetero-junction, respectively.

### 2.1 Properties of Graphene

#### 2.1.1 Electronic Structure of Graphene

Graphene is a monolayer of  $sp^2$ -hybridized carbon atoms organized in a two-dimensional hexagonal lattice, featuring a nearest-neighbor distance of 1.42 Å (see Figure 2.1). Each atom has an in-plane  $\sigma$  bond with its three closest neighbors, and the remaining valence electron contributes to a delocalized, out-of-plane  $\pi$ -bond. These bonding interactions result in the formation of the valence  $\pi$ -band and conduction  $\pi^*$ -bands, playing a pivotal role in the extraordinary electronic properties exhibited by graphene.

In 1947, Wallace demonstrated that the band structure of graphene could be obtained [1], by partitioning its honeycomb structure into two triangular sublattices (A and B in Figure 2.1(a)). Using the tight-binding approximation, the band structure of graphene could be accurately described. Graphene's band structure, illustrated in Figure 2.1(b), displays the relation between energy and momentum of electrons, exhibiting distinctive features at K and K' points of the Brillouin zone. These points, commonly known as Dirac points, signify the convergence of the conduction and valence bands, classifying graphene as a zero-band gap semi-metal.

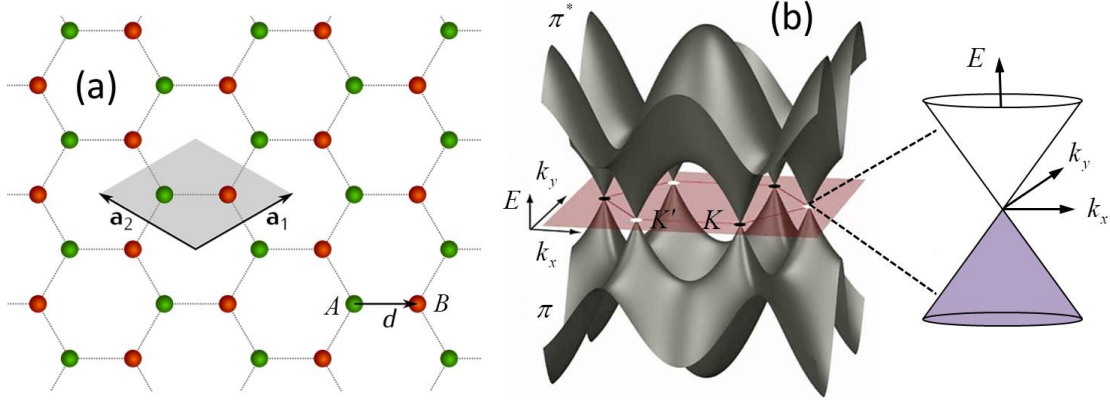


Figure 2.1: Structural and electronic properties of graphene. (a) The hexagonal lattice of graphene with the elementary cell (transparent grey area) containing two carbon atoms ( $a_1$  and  $a_2$  the lattice vectors), which belong to sublattices A (green) and B (red), respectively. Each atom in sublattice A has three nearest neighbours in sublattice B, and vice-versa. (b) The band structure of graphene. Energy dispersion for, both, the valence  $\pi$ -band and conduction  $\pi^*$ -band, calculated using the tight-binding approximation [2]. Brillouin zone and the high symmetry points K, K' are shown. The right inset is a scaling up close to one of the Dirac points, the Dirac cone with linear dispersion.

Near the Dirac points, valence and conduction bands form a conical structure (shown in the inset of Figure 2.1(b)), effectively characterized by the linear dispersion relation

$$E(\mathbf{k}) = \pm \hbar v_F |\mathbf{k}| \quad (2.1)$$

where  $\hbar$  is the reduced Planck constant,  $v_F \simeq c/300 \simeq 10^6 m/s$  is graphene's Fermi velocity and  $\mathbf{k}$  is the wave vector measured from the Dirac point. Remarkably, this corresponds to the spectrum of the Dirac-like Hamiltonian for massless Dirac fermions with a velocity  $v_F$  [3–5]. In the opposite side, charge carriers in bilayer graphene and conventional semiconductors are described by a non relativistic, parabolic dispersions.

This linear dispersion of graphene results to a density of states  $\nu(E)$  proportional to energy, which follows the expression

$$\nu(E) = \frac{g_s g_v}{2\pi (\hbar v_F)^2} |E| \quad (2.2)$$

where valley and spin degeneracies are  $g_v = 2$  and  $g_s = 2$ , respectively. The charge carrier density  $n(E)$  can be obtained by integrating  $\nu(E)$  up to E as

$$n(E) = \int_0^E \nu(E) dE = \frac{E^2}{\pi (\hbar v_F)^2} \quad (2.3)$$

The Fermi energy  $E_{F,SLG}$ , as a function of  $n(E)$ , can be obtained by integrating  $\nu(E)$  up to  $E_{F,SLG}$ . We get

$$E_{F,SLG} = \text{sgn}(n) \hbar v_F \sqrt{\pi |n|} \quad (2.4)$$

Therefore, the gapless nature of graphene's dispersion results in continuously tuning the carrier density, from electrons (positive  $n$ ) to holes (negative  $n$ ) or in the opposite way, by varying  $E_{F,SLG}$  (see Figure 2.2).

### 2.1.2 Graphene doping via electrostatic gating

A convenient way to modulate the charge carrier density in graphene, and other 2D materials as well, is by applying a voltage between graphene and a metallic gate, separated by an insulator. This electrostatic effect, known as field effect, is often used to induce charge density change  $\Delta n$  in SLG. As an example, the electrical conductance of graphene increases with the number of electrons and holes, showing a minimum, when Fermi energy is at the Dirac point, i.e. at the charge neutrality point.

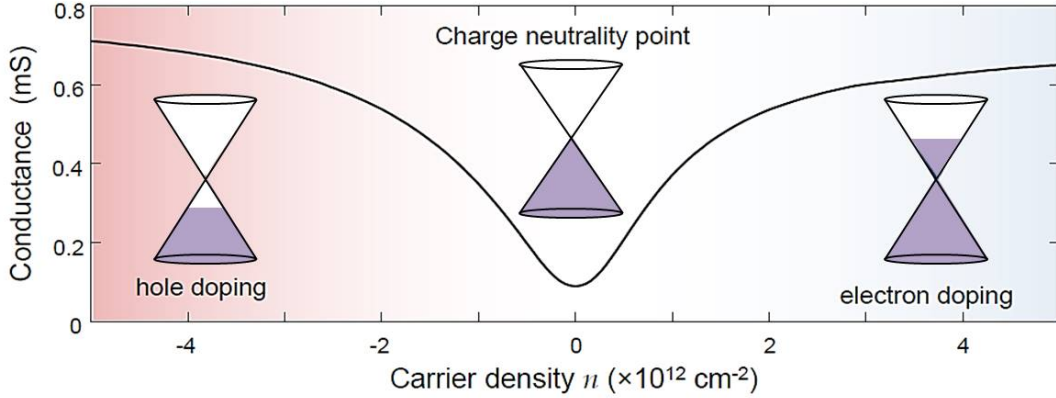


Figure 2.2: Graphene conductance as a function of the charge carrier density  $n$ . The insets correspond to Dirac cones with different doping levels (the blue region represents electron density).

From the above diagram of Figure 2.2 it is interesting to notice that conductance never totally diminishes, due to thermal effects and local variations in the Fermi level. For simple geometries,  $\Delta n$  can be analytically calculated by the capacitor model [6] as

$$\Delta n = \frac{C_G V_G}{q} = \frac{\epsilon_0 \epsilon_r V_G}{ed} \quad (2.5)$$

where  $C_G$  is the gate capacitance,  $V_G$  the voltage gate,  $\epsilon_0$  the vacuum permittivity,  $d$  the insulator thickness and  $e$  the electron charge. A conventional configuration for electrostatic doping of graphene [5], where  $\text{SiO}_2$  is used as a backgate dielectric on top of Si substrate is shown in the following Figure 2.3(a).

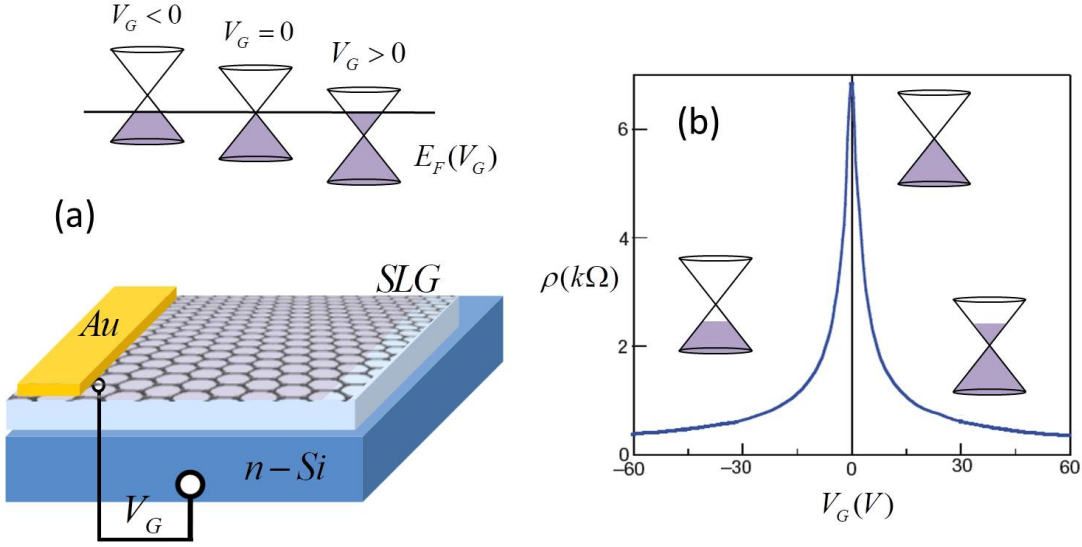


Figure 2.3: Schematics of graphene electrostatic doping. (a) A conventional configuration, with a  $\text{SiO}_2$  dielectric on top of a  $n$ -doped Si substrate is depicted. The top inset illustrates the change in charge density across SLG, in response to the applied gate voltage  $V_G$ , assuming the ideal case of pristine SLG, i.e.  $E_{F,SLG}=0$  at  $V_G=0$ . (b) Conical low-energy spectrum  $E(k)$ , indicating changes in the position of the Fermi energy  $E_{F,SLG}$  with changing gate voltage  $V_G$ . Positive (negative)  $V_G$  induce electrons (holes) for field-effect devices with a 300 nm  $\text{SiO}_2$  layer used as a dielectric [5].

Combining Eqs. 2.4 and 2.5,  $E_{F,SLG}$  can be written as a function of  $V_G$

$$E_{F,SLG} = \hbar v_F \sqrt{\frac{\pi \epsilon_0 \epsilon_r V_G}{ed}} \quad (2.6)$$

It is noteworthy that in the configuration of Figure 2.3(a) we assume an ideal pristine SLG, where  $E_F = 0$  at  $V_G = 0$  [7–9]. Figure 2.3(b) shows the rapid decrease in resistivity on adding charge carriers via  $V_G$ , indicating their high mobility (i.e., in this case  $\mu \simeq 5000 \text{cm}^2 \text{V}^{-1} \text{s}^{-1}$ ).

### 2.1.3 Optical Properties of Graphene - Optical conductivity

The optical response of graphene is governed by its optical conductivity  $\sigma_{SLG}$ . This is constituted of two components, one corresponding to intraband transitions and the other to interband transitions as

$$\sigma_{SLG}(\omega, \mu, T_{e,SLG}) = \sigma_{intra,SLG}(\omega, \mu, T_{e,SLG}) + \sigma_{inter,SLG}(\omega, \mu, T_{e,SLG}) \quad (2.7)$$

These intra- and inter- terms can be described by the Kubo formula [10, 11] and written, respectively, as

$$\sigma_{intra,SLG} = \frac{ie^2}{\pi \hbar^2 \Omega} \int_0^\infty \epsilon \left[ \frac{\partial f_{FD}(-\epsilon, \mu, T_{e,SLG})}{\partial \epsilon} - \frac{\partial f_{FD}(\epsilon, \mu, T_{e,SLG})}{\partial \epsilon} \right] d\epsilon \quad (2.8)$$

and

$$\sigma_{inter,SLG} = \frac{ie^2\Omega}{\pi\hbar^2} \int_0^\infty \left[ \frac{f_{FD}(-\epsilon, \mu, T_{e,SLG}) - f_{FD}(\epsilon, \mu, T_{e,SLG})}{\Omega^2 - 4\left(\frac{\epsilon}{\hbar}\right)^2} \right] d\epsilon \quad (2.9)$$

where  $\Omega = \omega + i\tau_{opt}^{-1}$ ,  $\tau_{opt}$  the free electron relaxation time, related to charge carrier mobility in SLG, and  $f_{FD} = 1/(e^{\frac{\epsilon-\mu}{k_B T}} + 1)$  the Fermi-Dirac distribution. In case of non-equilibrium photoexcited carriers in graphene, this distribution is modified to  $f_{FD}^*$  distribution, described in subsection 6.2.2. The contribution of both intraband and interband processes depends on graphene's chemical potential  $\mu$ , electronic temperature  $T_{e,SLG}$ , and the photon energy  $\hbar\omega$ . When  $\hbar\omega \leq 2|\mu|$ , interband transitions are not allowed due to energy and momentum conservation, given that the conduction band is already occupied [12]. This limitation on interband conductivity is commonly known as Pauli blocking. Within the intraband domain, the conductivity is primarily affected by the intraband term of Equation 2.8. In the degenerate limit (i.e., when  $k_B T_{e,SLG} \ll |\mu|$ ), it is described by the following Drude-like expression [13, 14]

$$\sigma_{SLG} = \frac{ie^2}{\pi\hbar^2} \frac{\mu}{\omega + i\tau_{opt}^{-1}} \quad (2.10)$$

When  $\hbar\omega \geq 2|\mu|$ , Pauli blocking threshold is surpassed and interband transitions are permitted governing graphene's optical response [15]. Figure 2.4 illustrates the optical conductivity spectrum of graphene in the cases of zero temperature  $T_{e,SLG}$  (continuous lines) and a finite temperature  $T_{e,SLG} > 0$  (dashed lines), assuming a scattering time  $\tau_{opt} = 200$  fs. The conductivity is calculated based on Equation 2.7, for undoped graphene ( $2E_{F,SLG}=0$  eV) (black line) and Fermi energy  $2E_{F,SLG}=0.4$  eV (red line).

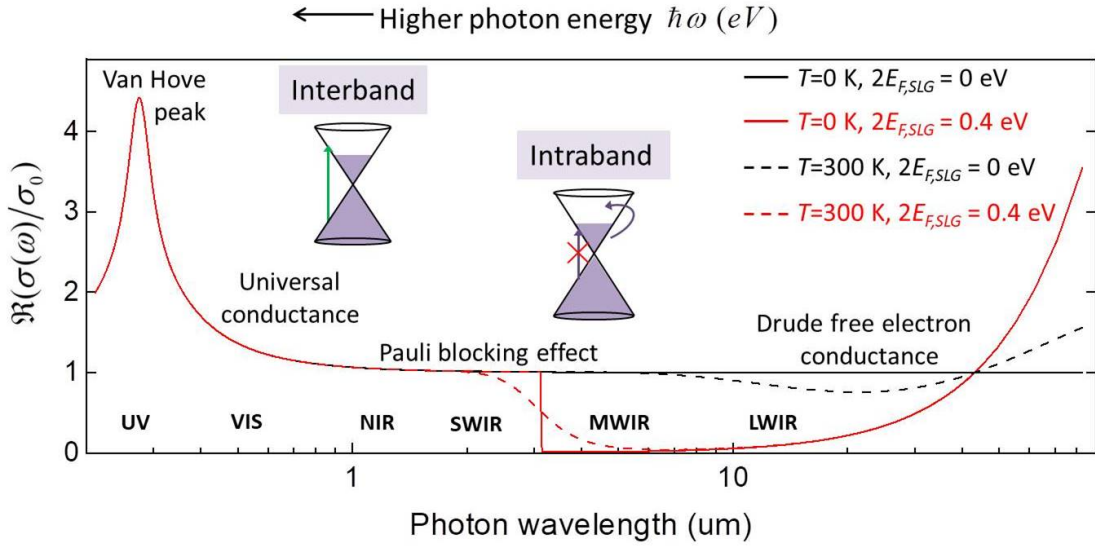


Figure 2.4: The conductivity spectrum of graphene. The real part of the theoretical optical conductivity of graphene normalized to the “universal” conductance  $\sigma_0 = e^2/4\hbar$  is plotted as a function of the photon wavelength (conversely proportional to the photon energy  $\hbar\omega$ ). The conductivity is calculated using Equation 2.7, for undoped graphene ( $2E_{F,SLG}=0$  eV) (black line) and Fermi energy  $2E_{F,SLG}=0.4$  eV (red line). We assume a zero graphene temperature  $T_{e,SLG}$  and a scattering time  $\tau_{opt} = 200$  fs. The dashed lines represent the conductivity for a finite temperature  $T_{e,SLG}=300$  K. In the inset, the illustrated Dirac cones show the two types of transition process. The interband transition process is allowed at  $\hbar\omega > 2E_{F,SLG}$  (marked with a green cross) [15], but prohibited at  $\hbar\omega < 2E_{F,SLG}$  due to Pauli blocking, where only intraband transitions (indicated by a curved purple arrow) are permitted [12]. The spectral position of Pauli blocking can be tuned through the change of electrostatic doping (as detailed in subsection 2.1.2), ranging from near-infrared (NIR) for high  $E_{F,SLG}$  to mid-wavelength infrared (MWIR) for low  $E_{F,SLG}$ .

The real part of  $\sigma_{SLG}$  converges to the universal frequency-independent optical conductivity  $\sigma_0 = \frac{e^2}{4\hbar}$  [16], characteristic for SLG Dirac fermions [17]. The spectral location of this transition region can be conveniently tuned through electrostatic gating, while its spectral extent is dictated by the temperature. For practical doping levels ( $E_{F,SLG}=0.1-0.4$  eV), this corresponds to the spectral range from near-infrared (NIR) for high  $E_{F,SLG}$  to mid-wavelength infrared (MWIR) for low  $E_{F,SLG}$ . At an absolute temperature of  $T_{e,SLG}=0$  K, the conductivity exhibits a step-function profile. However, at finite temperatures  $T_{e,SLG}$ , it becomes broadened around  $\hbar\omega = 2|\mu|$ , as illustrated in Figure 2.4.

### 2.1.4 Dielectric function and Light Absorption in Graphene

Graphene’s bandstructure, described in subsection 2.1.1, gives rise to its unique optical properties and the variety of graphene-light interactions [14, 18, 19]. Specifically, its gapless energy dispersion results in an exceptionally broadband absorption spectrum, making it a compelling material for optoelectronic applications.

Once the optical conductivity is determined (see Eqs. 2.7-2.9), the dielectric function of graphene is derived as follows [20, 21]

$$\epsilon_{SLG} = \epsilon_{\infty,SLG} + \frac{i\sigma_{SLG}(\omega, \mu, T_{e,SLG})}{\epsilon_0\omega d_{SLG}} \quad (2.11)$$

where  $\epsilon_{SLG}=5.7$  is the frequency independent part of the dielectric function at high frequencies [21],  $\epsilon_0$  is the vacuum permittivity and  $d_{SLG}=0.335$  nm corresponds to the thickness of SLG [22, 23]. Conclusively, the complex refractive index of graphene  $n_{SLG} = n + ik$  is given by

$$\Re\epsilon_{SLG} = n^2 - \kappa^2, \Im\epsilon_{SLG} = 2n\kappa \quad (2.12)$$

The optical absorption of suspended graphene is determined by the real part of the optical conductivity as

$$A_{SLG} = \frac{\Re\sigma_{SLG}}{\epsilon_0 c} \quad (2.13)$$

where  $c$  is the speed of light. As mentioned in previous subsection for the optical conductivity, graphene absorption is governed by the two types of transition, the intraband and the interband (see Figure 2.4) [14]. In intraband transition regime ( $\hbar\omega < 2E_{F,SLG}$ ), the absorption is a result of the free-carrier response and can therefore be well described by the Drude model, which takes into account the scattering time of free carriers, as extensively described in subsection 3.1.1 [12, 24].

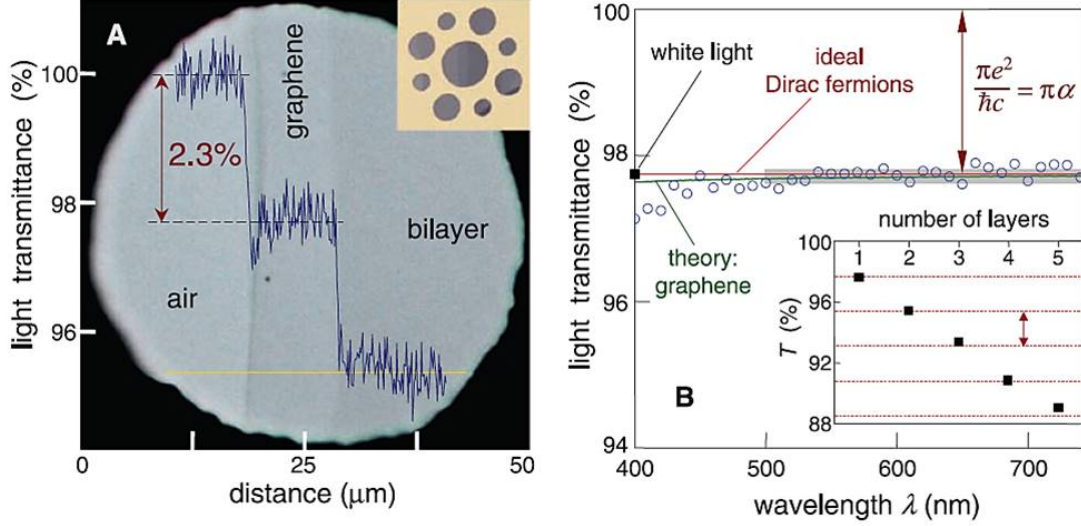


Figure 2.5: Optical absorption of graphene. (a) Image of an 50 mm aperture partially covered by monolayer and bilayer graphene, respectively, as captured by Nair et al [16]. The transmitted white light, measured along the yellow line, reveals distinct steps of 2.3%, aligning with theoretical predictions. (b) Experimental transmittance of a single-layer graphene (open circles) in visible spectrum, measured by [16]. The theoretical transmittance given by  $T = (1 - 0.5\pi\alpha)^{-2}$  for 2D Dirac fermions is represented by the red line, whereas the green curve incorporates nonlinearity and triangular warping in graphene’s electronic spectrum. The shaded gray area indicates the standard error associated with measurements. In the inset, the transmittance of white light is shown as a function of the number of graphene layers, depicted by black squares. The dashed lines illustrate an intensity reduction by the ”universal” absorbance value  $\pi\alpha$  with each additional layer.

Beyond this energy threshold ( $\hbar\omega > 2E_{F,SLG}$ ), interband transitions become dominant in the optical response. Notably, in the linear dispersion regime of graphene, the theoretical interband absorption is independent of photon energy and specific material parameters of graphene (i.e. scattering time). It is entirely determined by universal constants and expressed as  $A = \frac{e^2}{4\epsilon_0\hbar c} = \pi\alpha = 2.3\%$ , where  $\alpha = \frac{e^2}{4\pi\epsilon_0\hbar c}$  is the fine-structure constant [16] (see Figure 2.5). This ”universal” absorbance is a consequence of graphene’s 2D nature and has been also observed in other 2D systems, such as InAs thin films [25]. In practical terms, the measured absorbance aligns well with  $\pi\alpha$  for photon energies ranging from approximately 0.5 to 2 eV (from MWIR to VIS) [16, 24], which corresponds to the spectral region that is relevant for this thesis. However, deviations from the ”universal values” occur in the ultraviolet region as interband transitions move away from the linear dispersion regime and approach the saddle-point singularity at the M point of the Brillouin zone. Within this range, excitonic effects induce a notable Fano resonance (Van Hove peak) at  $\hbar\omega=4.6$  eV or  $\lambda_0=270$  nm [26] (see Figure 2.4).

The operational range of many applications falls within  $\pi\alpha$  spectral region, prompting a crucial question if an absorbance of 2.3% could be considered substantial or negligible. In reality, both perspectives can be justified. On one side, it’s undeniably noteworthy that a single atomic layer can absorb 2.3% of light, in comparison with silicon with 25 nm thickness of silicon (almost 50 atomic layers) required to achieve a comparable absorbance in the visible spectrum. On the other side, the relatively small absolute ab-

sorbance of monolayer graphene poses a significant challenge for numerous applications, particularly photodetectors and solar cells that demand perfect absorption. To address this concern, diverse approaches have been developed to enhance light-matter interactions in SLG-based optoelectronic devices (some of them are described in Chapters 5 and 6). These approaches include the utilization of plasmonics, integrated dielectric waveguides, reflector microcavities and photonic crystals [19, 25, 27].

Finally, it is important to highlight that the presence of a substrate can significantly influence the absorption spectrum of 2D materials, such as graphene. This influence arises from the potential for multiple light reflections and interferences, as discussed in Chapters 5 and 6. Interestingly, this effect can be utilized to enhance the contrast of 2D materials [28] and Surface-Enhanced Raman Spectroscopy (SERS) [29], making their identification more straightforward, as detailed for graphene on top of 3D substrates in Chapter 5.

### 2.1.5 Surface-Enhanced Raman Scattering in Graphene

Raman spectroscopy serves as a valuable tool for rapidly, accurately, and reliably identifying molecules [30]. However, a significant challenge arises from the relatively small cross-section of common molecules and the weak Raman signal. The utilization of Surface-Enhanced Raman Spectroscopy (SERS) [31, 32] addresses this limitation by significantly enhancing the Raman fingerprints of molecules. This enhancement facilitates highly sensitive detection, even down to the single molecule level [33, 34], while maintaining molecular selectivity. Over the past decades, considerable studies have been dedicated to comprehending the origin of SERS effects and developing an improved SERS substrate, resulting in continuing theoretical and experimental progress. However, despite these steps, SERS has not been applied to a widespread of real-world applications. The main challenge stems from the difficulty of achieving a quantitative understanding of the SERS mechanism and develop a convenient SERS method that can fulfill the following criteria [35, 36], such as high SERS sensitivity, uniformity, high selectivity (clear SERS features), rapid sample pretreatments and compatibility under various conditions.

In addition to the considerable theoretical and experimental interest in graphene's unique structure of electrons and phonons [5], monolayer graphene has also exhibited exciting Raman scattering properties, that can be utilized in terms of SERS. Graphene plays various roles in SERS, owing to its distinctive structural features and properties, such as its unique electron and phonon structures, atomic uniformity, atomic thickness, biological compatibility etc., which provide unique advantages for SERS. Figure 2.6 illustrates a typical Raman spectrum obtained from graphene containing defects, measured using a 514.5 nm laser. Two distinct peaks, namely the G band (around  $1585\text{ cm}^{-1}$ ) and the G' band (approximately  $2685\text{ cm}^{-1}$ ), sometimes referred to as the 2D band, represent intrinsic vibrations of defect-free graphene. In cases where the Raman spectrum is obtained from disordered graphene or its edges, additional peaks may become evident, such as around  $1345\text{ cm}^{-1}$  (D band) and  $1625\text{ cm}^{-1}$  (D' band). The appearance of peaks at  $1450\text{ cm}^{-1}$  (D<sub>2</sub> band) and  $1500\text{ cm}^{-1}$  (D<sub>3</sub> band) has also been reported [37].

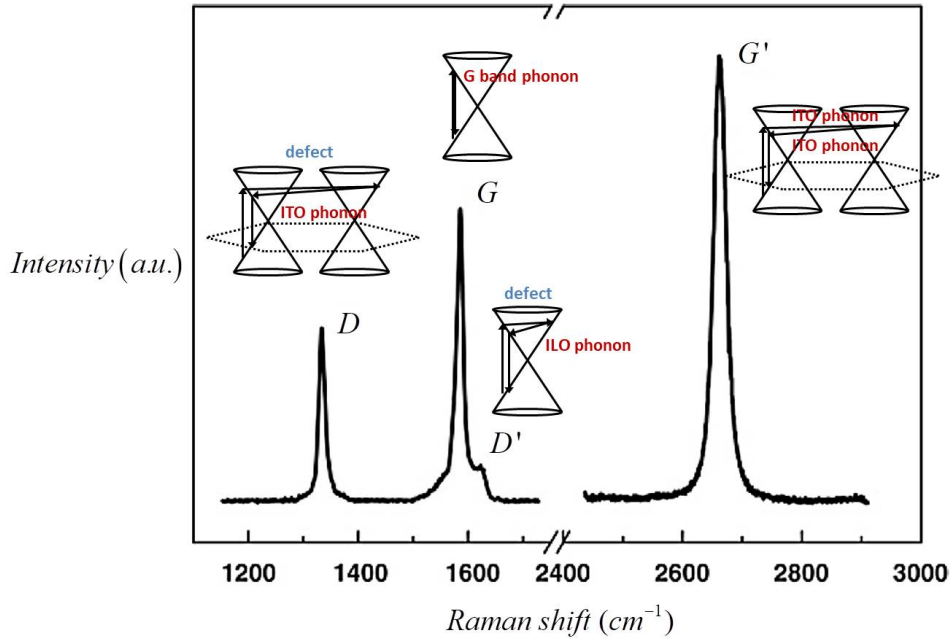


Figure 2.6: Typical Raman spectrum of defect-containing graphene, showing the main Raman features, the G, G', D and D' bands measured under laser excitation of 514.5 nm [38]. Inset: Illustrations of the first-order G-band scattering process in graphene (center-top), the two-phonon second-order G'-band process (right) and D (left) and D'-bands (center-bottom), for the intervalley and intravalley processes.

Raman spectroscopy stands out as a versatile tool to investigate the structure of graphene and identify its properties. The Raman features of graphene itself can be interesting and informative. Exploiting these Raman fingerprints allows us to determine the number of graphene layers, investigate the nature of edges (including defects), and directly monitor the degree of doping. For varying number of graphene layers ( $n$ ), the 2D band exhibits distinct characteristics in terms of shape, position, and intensity. Based on these variations, Ferrari et al. [39] proposed a method to accurately determine the number of layers in few-layer graphene samples. As depicted in Figure 2.7, monolayer graphene exhibits a G' peak characterized by a singular Lorentzian feature. In contrast, the G' peak of bilayer graphene reveals a broad band comprising four components [38–40].

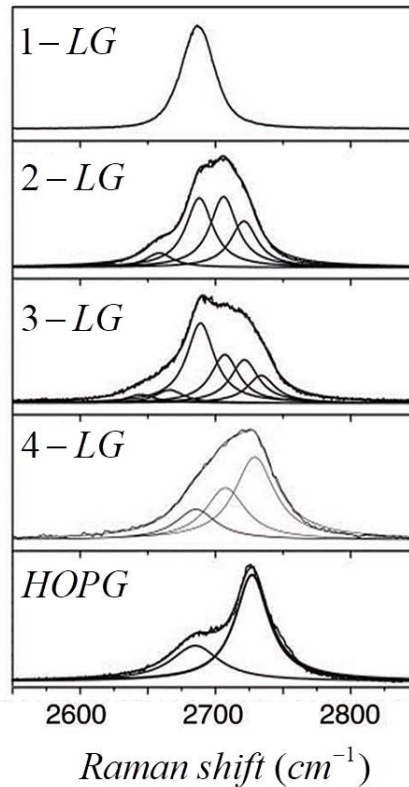


Figure 2.7: Layer-dependent experimental G' band (and fitted Lorentzians) of 1, 2, 3, 4-layer graphene and highly oriented pyrolytic graphite (HOPG), under 514.5 nm laser excitation. The splitting of G'-band opens up in going from 1 to 3-layer graphene and closes up in going from 4-LG to HOPG [38].

For a three-layer graphene, the G' band necessitates the incorporation of additional Lorentzians for fitting [38]. As the layer count ( $n$ ) reaches five or more, the G' band exhibits similar features with graphite, making it challenging to differentiate between the two. This observation can be explained by a double resonance mechanism, where the electronic structure of graphene sheets varies with the layer count ( $n$ ) [38, 39, 41]. Simultaneously, with the increase in  $n$ , the G band experiences a frequency downshift [37], and its intensity demonstrates an almost linear trend across the range of 1–10 layers.

The effectiveness of graphene in numerous applications, such as photovoltaic and photodetection devices, is highly dependent on its structure. As previously discussed, the unique properties of graphene become apparent in its Raman spectrum. Therefore, there is a notable interest in enhancing the Raman signal of graphene, by selecting the appropriate substrate, a key factor that affects Raman intensity [42].

### 2.1.6 Thermal Properties of Graphene - Photocarrier Dynamics

Absorption of photons in graphene through interband transitions results in the generation of photo-excited electron-hole pairs, commonly referred to as photocarriers. The dynamic relaxation of energy in these photocarriers has been extensively explored in literature [43–49]. In this subsection, we provide an overview of the main relaxation processes, as illustrated in Figure 2.8.

As previously discussed, photons with energy of  $\hbar\omega > 2E_F$  are absorbed in graphene through interband transitions. This leads to the creation of an electron-hole pair with re-

spect to the Dirac point (Figure 2.8). Typically, photo-excited carriers can dissipate their excess of energy either through thermalization, redistributing it among other carriers via Coulomb interactions, or by emitting massless bosons, such as photons or phonons. Numerous experiments have indicated that the dominant relaxation pathway is the thermalization process, commonly referred to as the carrier heating, occurring within a few tens of femtoseconds [43, 46, 49, 50].

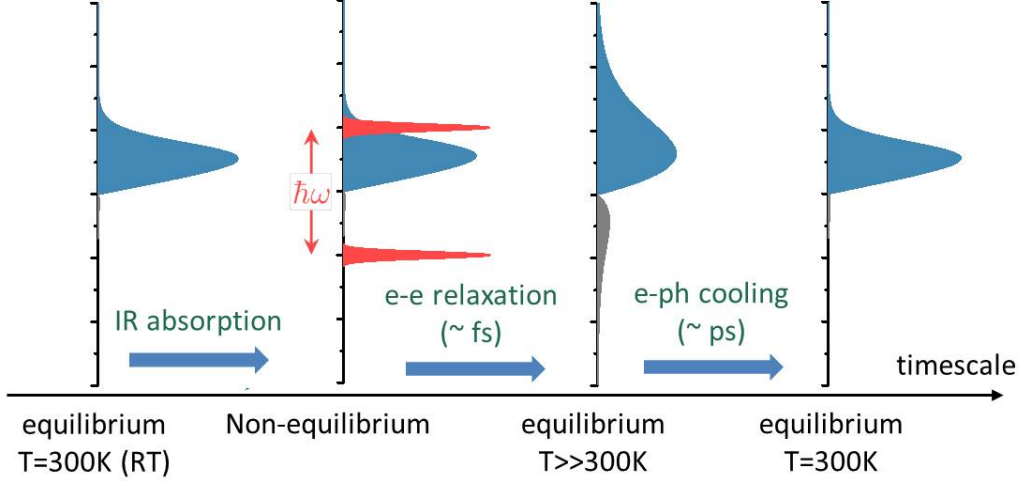


Figure 2.8: SLG carrier distribution for  $E_{F,SLG}=0.15$  eV. (a) Before the photoexcitation at  $T_{e,SLG}=300$  K, (b) immediately after illumination, assuming excitation with photon energy  $\hbar\omega=0.4$  eV, where the red peaks represent non-equilibrium photo-excited carriers, (c) after the relaxation of hot carriers into a Fermi-Dirac distribution at an increased  $T_{e,SLG}\gg 300$  K, (d) after electron-phonon relaxation process, cooled back to RT [51].

Figure 2.8 illustrates the increase in carrier temperature, resulting from pulsed photoexcitation. Once the formation of non-equilibrium carrier distribution occurs (red peaks) and attains equilibrium in approximately a few femtoseconds, carriers undergo a slow (1-20 ps) electron-phonon relaxation process (with lattice and the surrounding medium), before eventually cooling down to room temperature. Both experimental observations and theoretical analysis indicate that carriers dissipate their excess heat through mechanisms, such as optical phonon scattering [52–54] and disorder-assisted supercollisions [47, 55–57].

The fast thermalization of carriers in graphene, occurring within tens of femtoseconds and their slow picosecond cooling, through interactions with phonon modes, enables modeling of carrier temporal dynamics using a two-temperature approach [58, 59]. Here, two distinct rate equations govern  $T_{e,SLG}$  and  $T_{l,SLG}$ . When pumped with pulsed light (time-dependent power density  $P_{in}(t)$ ), these rate equations are written as

$$c_{e,SLG}\dot{T}_{e,SLG} = \alpha_{SLG}P_{in}(t) - J_{e-ph} \quad (2.14)$$

for graphene's electronic temperature  $T_{e,SLG}$  and

$$c_{l,SLG}\dot{T}_{l,SLG} = J_{e-ph} - \Gamma_{SLG-sub}(T_{l,SLG} - T_{sub}) \quad (2.15)$$

for graphene's lattice temperature  $T_{l,SLG}$ . In Eqs. 2.14 and 2.15,  $c_{e,SLG}(\mu, T_{e,SLG}, \delta n_{SLG})$  is the electronic heat capacity of graphene,  $\alpha_{SLG}(T_{e,SLG}, \delta n_{SLG})$  is SLG's optical absorbance and  $J_{e,ph}(\mu_{c,SLG}, \mu_{v,SLG}, T_{e,SLG}, T_{l,SLG}) \equiv J_{op} + J_{sc}$  the electron-phonon thermal

current density, owing to optical phonons and disorder-assisted supercollision scattering (see Appendix B.2). Moreover,  $c_{l,SLG}$  is SLG's lattice heat capacity, found to linearly scale with lattice temperature  $T_{l,SLG}$  up to  $\sim 600$  K, following the linear parametrization expression  $c_{l,SLG} = -1.4 \times 10^{-5} + 1.9 \times 10^{-6} T_{l,SLG}$  in  $\text{Jm}^{-2}\text{K}^{-1}$  units, extracted from experimental data [60]. The thermal energy, accumulated within the lattice of graphene, disperses into the surrounding air (for free-standing graphene) or to a substrate (in case of supported graphene) through a rate denoted as  $\Gamma_{SLG-sub}$ . This rate depends on both  $T_{l,SLG}$  and the temperature of substrate ( $T_{sub}$ ). The values for  $\Gamma_{SLG-sub}$ , in case of graphene supported by a substrate, have been extensively investigated in various studies, typically found within the range of 10 to 1000  $\text{MWm}^{-2}\text{K}^{-1}$  [60, 61].

For a comprehensive and precise description of temperature dynamics, it is essential to consider the non-equilibrium photoexcited carrier density  $\delta n_{SLG}$ , particularly in case of interband photoexcitation. The temporal change in  $\delta n_{SLG}$  is determined through the addition of a third rate equation [62]

$$\dot{\delta n}_{SLG} = \frac{\alpha_{inter,SLG} P_{in}(t)}{\hbar\omega} - \frac{\delta n_{SLG}}{\tau_{e-e}} \quad (2.16)$$

where  $\tau_{e-e} \sim \text{fs}$  [50, 63] representing the time required for carriers to relax into a thermal distribution through electron-electron scattering,  $\hbar\omega$  denotes the energy of exciting photons (assuming  $\hbar\omega > 2E_{F,SLG}$ ), and  $\alpha_{inter,SLG}$  signifies interband graphene's absorption. Given that the overall SLG is directly proportional to  $\Im\epsilon_{SLG}$  (see Eqs. 2.11-2.13) (i.e., to  $\Re\sigma_{SLG}$ ), the interband optical absorption is given by

$$\alpha_{inter,SLG} = \alpha_{SLG} \frac{\Re\sigma_{inter,SLG}}{\Re(\sigma_{inter,SLG} + \sigma_{intra,SLG})} \quad (2.17)$$

The three coupled rate equations 2.14-2.16, can be used to obtain the temporal change of graphene's carrier dynamics, under the influence of a pulsed light source. When the pulse duration exceeds all relevant timescales (i.e.,  $\tau_{pulse} \gg \tau_{e-e}, \tau_{e-ph}$ ), or in case of continuous-wave (CW) illumination, these rate equations can be solved using the quasi-CW approach and determined by

$$\delta n_{SLG} = \frac{\tau_{e-e} \alpha_{inter,SLG} P_{in}}{\hbar\omega} \quad (2.18)$$

for non-equilibrium carrier density  $\delta n_{SLG}$  (setting  $\dot{\delta n}_{SLG} = 0$ ),

$$T_{l,SLG} = T_{sub} + \Gamma_{SLG-sub}^{-1} J_{e-ph} \quad (2.19)$$

for lattice temperature  $T_{l,SLG}$  and

$$\alpha_{SLG} P_{in} = J_{e-ph} \quad (2.20)$$

for electronic temperature  $T_{e,SLG}$ , since both  $\alpha_{SLG}$  and  $J_{e-ph}$  are  $T_{e,SLG}$  dependent.

## 2.1.7 Graphene-based Optical Modulation

Optical modulators stand as crucial components within optoelectronic devices, serving to manipulate the fundamental characteristics of an optical signal as it traverses through free space or within an optical waveguide, under the effect of external electronic, photonic, or alternative inputs [19, 64, 65]. Modulators, used for free-space operation, hold pivotal

role in pulse-shaping applications [66, 67], free-space optical communication networks [68–70], radar systems [71] etc., while they are promising to significantly contribute to emerging 5 G and 6 G technologies [72, 73].

Graphene is a compelling material for the realization of optical modulators, owing to its electrostatically tunable optical performance and ultrafast carrier dynamics, alongside its compatibility with CMOS/Si technologies and broad-spectrum optical absorption capabilities. Therefore, considerable research efforts have been directed towards graphene-based optical modulators [74–78], demonstrating competitive performances across near-infrared (NIR), mid-infrared (midIR) or terahertz (THz) spectral ranges. Optical modulators stand out in various categories, based on the specific light property they manipulate. They can be classified into amplitude, phase, polarization, or wavelength modulators, depending on the characteristic of light they modulate. Alternatively, optical modulators can be categorized based on their operating principles, leading to distinctions such as optical [78, 79], electro-optic [80, 81], magneto-optic [82], acousto-optic [83, 84], thermo-optic [85] modulators, among others.

Furthermore, optical modulators can also be classified based on the optical property of the material used for modulation, resulting in absorptive and refractive modulators. Absorptive modulators operate by varying the absorption coefficient (i.e., the imaginary part of the refractive index). In case of graphene, this can be achieved by tuning the Fermi level through electrostatic gating, using substrates such as optical resonant cavities [86] (see section 6.1). In graphene, electro-absorption modulation is achieved through hot-carrier-induced changes in optical conductivity, resulting from the absorption of an input pulse [58, 87]. Finally, refractive modulators operate by varying the real part of the refractive index. This can be achieved through methods such as utilizing the Kerr effect [88], thermally modulating the refractive index, or via electrostatic gating. The latter method, known as electro-refractive modulation, is commonly applied in Mach-Zehnder interferometers within integrated schemes [65]. It is important to note that a modulator can induce changes in multiple optical properties simultaneously. For instance, in a graphene-based pulse-shaper (see section 6.2), varying the SLG Fermi level under high power affects both the real and imaginary parts of the refractive index.

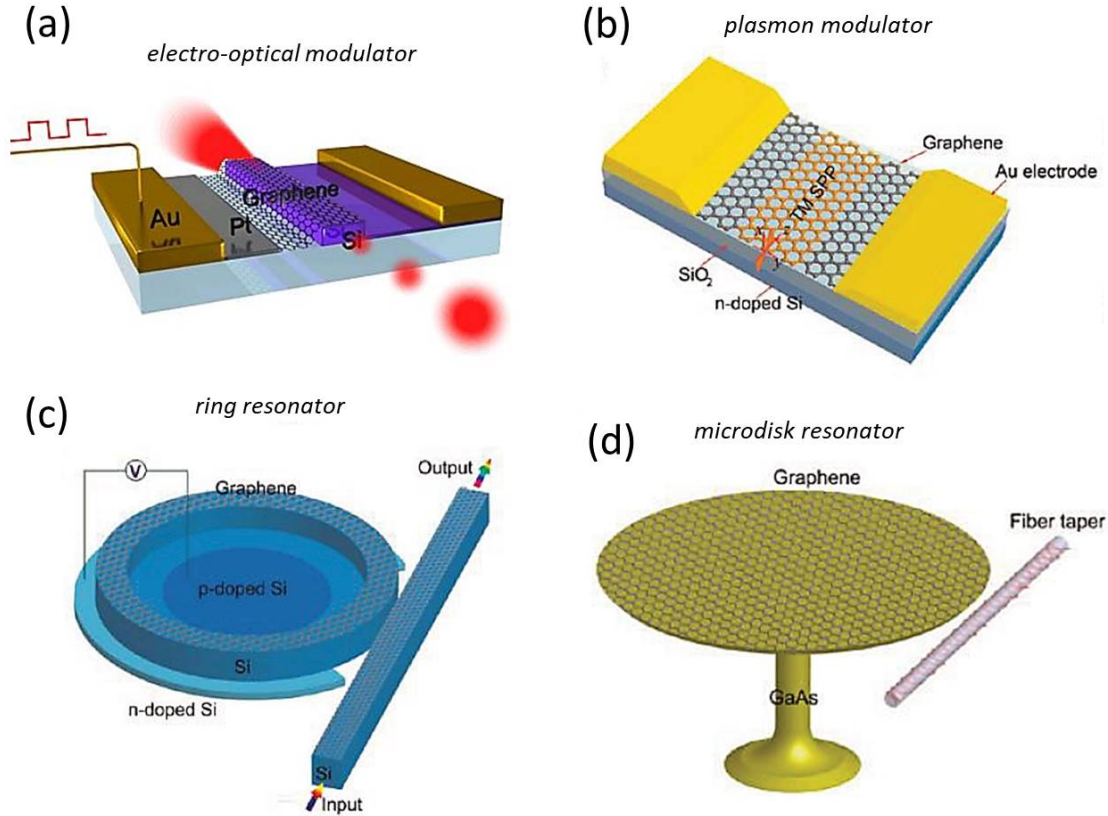


Figure 2.9: Graphene-based optical modulators [19]: (a) Graphene-based electro-optical modulator [89]. (b) Schematic of graphene plasmon modulator [90]. (c) Schematic of a graphene-based ring resonator. (d) Graphene-based microdisk resonator.

The mechanisms mentioned above have been extensively employed in various studies to develop graphene-based optical modulators across a broad spectrum, spanning from visible [91] to IR [80, 81, 92], and up to THz spectral region [93, 94].

## 2.2 Properties of 2D TMDs

As discussed in section 2.1, graphene's linear dispersion relation gives rise to distinctive optical and electrical properties. However, its lack of a bandgap restricts its applicability in cases where semiconductors are essential. The need for alternative 2D materials with a bandgap has led to the identification of monolayer (group-VI) transition metal dichalcogenides (TMDs), notably including  $\text{MoS}_2$ ,  $\text{WS}_2$ ,  $\text{MoSe}_2$ , and  $\text{WSe}_2$ . While TMDs in their layered bulk form have been under research for decades [95–99], the investigation into the properties of their single and few layers has occurred more recently [100, 101].

In the monolayer form, TMDs exhibit a direct bandgap in the visible to near-infrared range [102, 103], making them suitable for various electrical and optoelectronic applications. Together with their relatively high mobility at room temperature ( $1\text{--}100\text{ cm}^2/\text{Vs}$ ) [104], their bandgap makes them appealing as channel materials in logic transistors [4, 105, 106]. TMDs have also generated considerable interest due to their unique optical properties [107, 108], governed, as discussed below, by strong light-exciton interactions.

### 2.2.1 Electronic properties of TMDs

Transition metal dichalcogenides (TMDs) of group VI includes compounds with the  $\text{MX}_2$  formula, where M represents the transition metals VI (Mo, W) and X represents a chalcogen (S, Se). Each monolayer is composed of two planes of chalcogen atoms sandwiching a plane of metal atoms, forming a trigonal prismatic structure [97] (see Figure 2.10(a)). Possessing out-of-plane mirror symmetry and broken in-plane inversion symmetry [109], unlike graphene, these monolayers stack in an ABAB sequence, constituting the 2H polytype in bulk structures. Figure 2.10(a) also shows the 2D Brillouin zone for atomically thin TMDs.

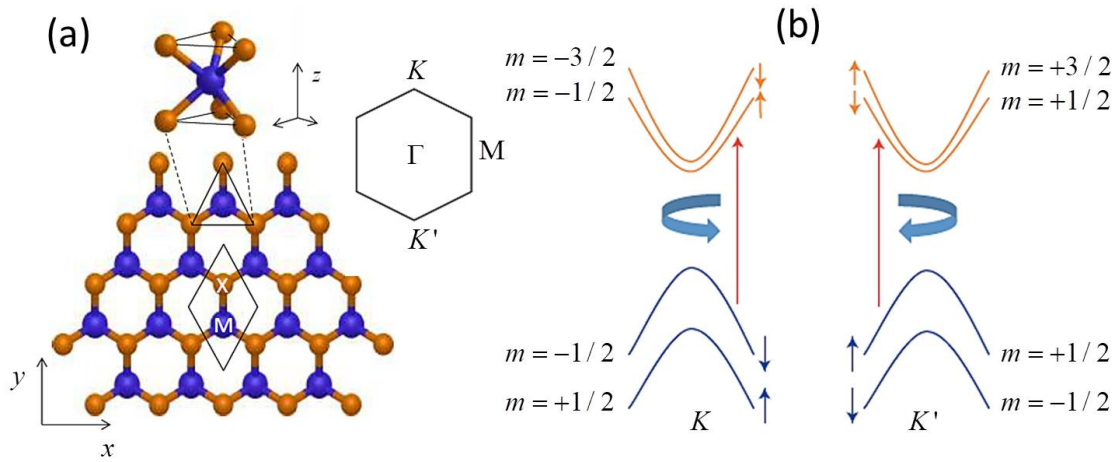


Figure 2.10: Structural and electronic properties of TMDs: (a) Structure of a monolayer TMD. The elementary cell (black rhombus) is composed of a transition metal atom (blue) and two chalcogen atoms (orange) [110]. The 2D Brillouin zone for atomically thin TMDs is also shown in the inset. (b) Schematics of the electronic bands (i.e., W compounds) emerge around the K and K' points, due to spin-splitting caused by spin-orbit interactions. The spin (up and down arrows) and valley degrees of freedom (K and K') are interconnected. The azimuthal quantum number ( $m$ ) is indicated for each band, and the valley-dependent optical selection rules are illustrated [108].

In bulk TMDs, there is an indirect bandgap ( $E_G \sim 1.1\text{-}1.4$  eV), with a valence band (VB) maximum occurring at  $\Gamma$  point and a conduction band (CB) minimum positioned between K and  $\Gamma$  points. However, as the number of layers decreases, TMDs transform into direct bandgap semiconductors in the monolayer form [102, 103, 111–113]. This transformation is a consequence of alterations in orbital hybridization through quantum confinement effects [114].

Furthermore, changing the number of layers significantly affects the states at the  $\Gamma$  point, whereas those at the K points experience comparatively minimal changes. This results in a larger direct band-gap ( $E_G \sim 1.7\text{-}2.1$  eV) at the K and K' points for monolayer TMDs. Due to their identical atomic structure, these TMDs exhibit a similar band structure and, therefore, share electrical and optical properties. The electronic band structure of monolayer TMDs, close to Fermi energy (see Figure 2.10(b)), can be characterized by two sets of degenerate conduction and valence bands around the K and K' points, featuring parabolic dispersion relations as,

$$E(k) = \pm \frac{\hbar^2 |k|^2}{2m^*} \quad (2.21)$$

where  $m^*$  represents the effective mass of either electrons or holes (typically falling within the range of  $0.4m_0$ - $0.6m_0$ , where  $m_0$  is the rest mass of electrons) [108], and  $k$  signifies the wave vector measured from either K or K' point. Notably, this relation is similar to the spectrum of a 2D Dirac Hamiltonian for massive Dirac fermions, which also characterizes carriers in graphene [115]. Moreover, the presence of spin-orbit interactions results in the breaking of spin degeneracy in both conduction and valence bands. It's worth noting that the spin splitting is considerably smaller in the conduction band ( $\sim 3$ - $30$  meV) compared to the valence band ( $\sim 150$ - $500$  meV).

Theoretical calculations have predicted very large exciton binding energies  $E_B \sim 0.5$ – $1$  eV for monolayer TMDs [108]. Recent experimental measurements, using optical and scanning tunneling spectroscopy, have also reported the large binding energies of  $\sim 0.2$ - $0.7$  eV [116–120], although divergence exists in terms of accurate values from different calculations and experiments, as shown in Table 1.

Table 1: Electronic properties of 2D TMDs

2D TMD	MoS <sub>2</sub>	MoSe <sub>2</sub>	WS <sub>2</sub>	WSe <sub>2</sub>
Band masses (in $m_0$ )	$\sim 0.5$	$\sim 0.6$	$\sim 0.4$	$\sim 0.4$
Optical gap $E_g$ (eV)	$\sim 2$	$\sim 1.7$	$\sim 2.1$	$\sim 1.75$
Exciton binding energy (eV)	$\sim 0.2$ - $0.9$	$\sim 0.5$ - $0.6$	$\sim 0.4$ - $0.7$	$\sim 0.4$ - $0.45$
CB spin-orbit splitting (meV)	$\sim -3$	$\sim -20$	$\sim -30$	$\sim -35$
VB spin-orbit splitting (meV)	$\sim 150$	$\sim 180$	$\sim 430$	$\sim 470$

The large binding energies observed in these excitons arise from the two factors related to their 2D nature, the quantum confinement and reduced dielectric screening. In contrast to traditional bulk semiconductors, TMDs' excitons experience strong confinement within the monolayer's plane. Notably, their Bohr radius ( $a_0 \simeq 1$ - $3$  nm) surpasses the layer thickness ( $\simeq 0.6$  nm), following the requirements for real two-dimensionality [25]. Due to this quantum confinement effect, the exciton binding energy is 4 times larger than in 3D [121]. Moreover, the excitons undergo reduced Coulomb screening, as the electric field connecting the electron and hole, extends beyond the monolayer. The reduction in screening enhances the electron-hole Coulomb interaction, resulting in an increased exciton binding energy. Consequently, the dielectric surrounding environment around monolayer plays a significant role in affecting exciton and governing its properties [119, 122, 123].

## 2.2.2 Optical Properties of TMDs: Light Absorption and Emission

Owing to their electronic bandgap, TMDs exhibit optical properties that differ from those of graphene. While they are transparent at longer wavelengths, TMDs exhibit high optical absorption and emission within the near-infrared and visible spectral range [108]. These strong light-matter interactions stem from enhanced carrier-carrier interactions, leading to strong excitonic effects [124]. An exciton is a neutral quasiparticle formed by the binding of an electron and a hole, held together by their Coulomb interaction. In 3D bulk semiconductors, the properties of excitons can be described by the hydrogenic model [125]. Conversely, 2D TMDs host excitons with binding energies reaching about  $\sim 1$  eV (see Table 1) and featuring different excitation spectra, than that described by the conventional 2D hydrogenic model [126–130].

In the absence of excitonic effects, the absorption spectrum would theoretically showcase a step-like function, which is characteristic of 2D semiconductors, shown in Figure 2.11 (blue dashed line) [121].

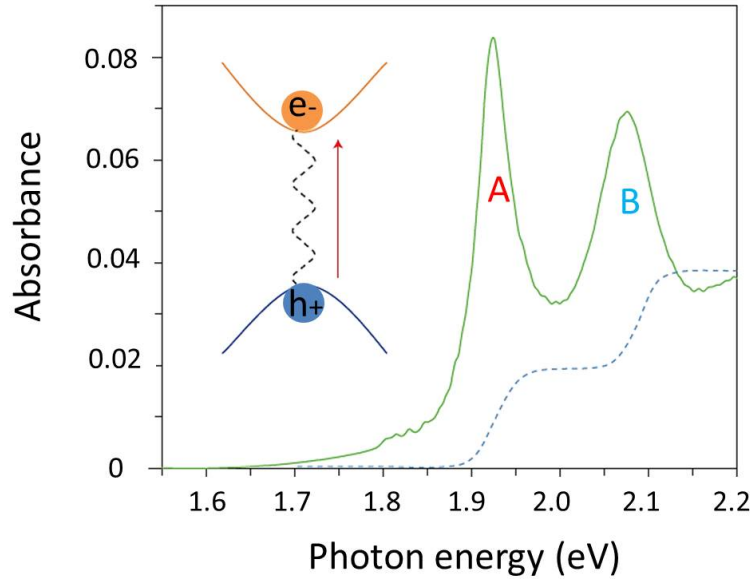


Figure 2.11: Absorbance spectrum of monolayer  $\text{MoS}_2$  at 10 K (green line) [131]. Exciton resonances, labelled A and B, signify transitions from the two spin-split valence bands to the conduction bands. The blue dashed line shows the absorbance (arbitrary units) without the excitonic effects. In the inset, the Coulomb interaction between an optically generated electron–hole pair is depicted, forming a bound exciton.

As depicted in Figure 2.11 (green line), the experimental absorption spectra present distinct and well-defined resonance features, proving the existence of strong excitonic effects. Suspended monolayer TMDs can exhibit a very high absorbance (reaching up to  $A \simeq 15\%$ ) at the exciton resonances [102, 132]. This underscores the strong light-matter interactions in these materials. Figure 2.12 shows the complex refractive index of suspended monolayer  $\text{WS}_2$  in the visible spectrum (utilized in Chapter 7). Within TMDs, the main excitonic peaks, labeled as A and B (see Figs. 2.11 and 2.12), signify transitions originating from the two spin-split valence bands to the conduction bands [95, 96].

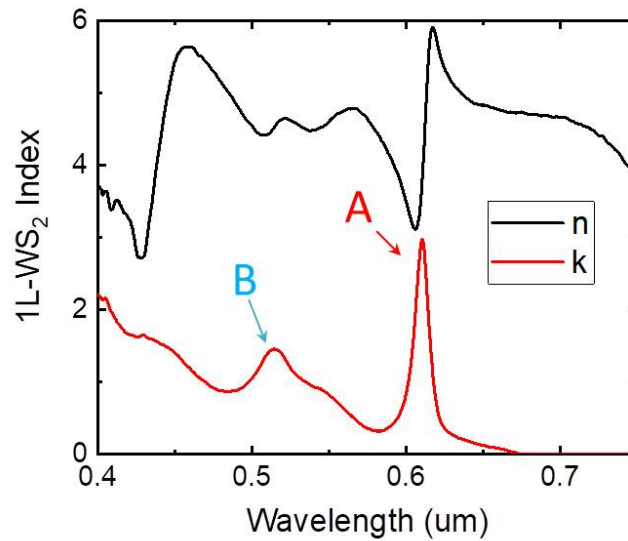


Figure 2.12: Complex refractive index of monolayer WS<sub>2</sub> in visible spectrum. Labels A and B correspond to the A and B excitons, that will be consequently described in the main text. Adapted to experimental measurements in [133].

The significance of these excitonic states extends to the photoluminescence (PL) of monolayer TMDs. Monolayer TMDs exhibit enhanced PL levels (owing to the crossover from an indirect to a direct bandgap) reaching up to a factor of  $10^4$ , when compared to their bulk counterparts [102, 113]. Experimental findings show that in pristine and undoped TMDs, the PL spectrum is characterized by emission from the neutral A exciton. In contrast, emissions from charged A trions become more prominent in highly doped samples [131, 134]. Recently, PL quantum yields approaching 100% have been reported for chemically-treated MoS<sub>2</sub> samples, underscoring the potential of TMDs for applications in light-emitting devices [135].

### 2.3 Hexagonal boron nitride (hBN)

Hexagonal boron nitride (hBN) is a layered atomic structure, similar to that of graphene. In this honeycomb lattice, boron and nitrogen atoms are arranged with a lattice constant only 1.8% larger than graphene [136, 137]. Few-layer hBN, distinguished by different on-site energies of B and N atoms, exhibits an indirect bandgap of approximately  $\sim 6$  eV [138], making it an electrical insulator.

Benefiting from its chemical and mechanical stability, hBN stands out as an ideal material for encapsulating or supporting other 2D materials, providing an atomically flat surface. Notably, research by Dean et al. [139] demonstrated that, compared to SiO<sub>2</sub>, hBN substrates reduce disorder and charge inhomogeneity in graphene, while significantly enhancing its carrier mobility. Additionally, hBN has proven to be an excellent tunnelling barrier, with a high dielectric breakdown field of up to 0.8 V/nm [140, 141].

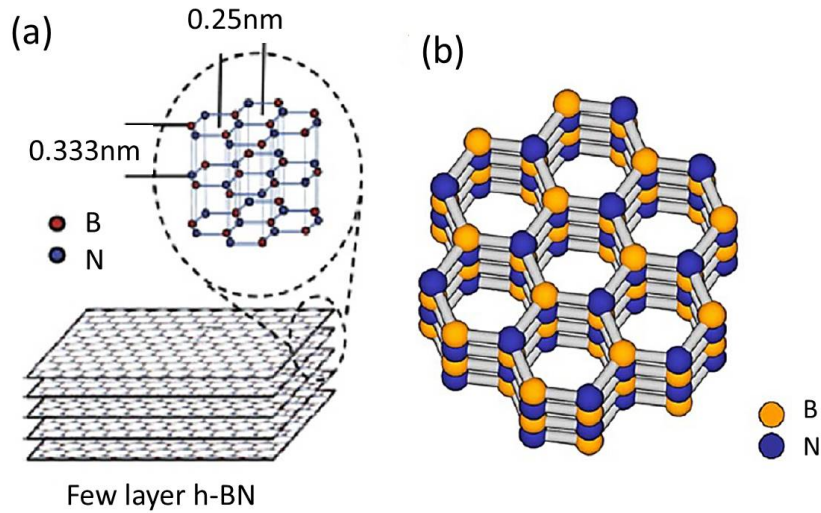


Figure 2.13: (a) Schematics of the structure of hBN nanosheets [142, 143]. (b) The lattice of hBN with an AAA stacking. Boron and nitrogen atoms are alternately stacked on each other [143, 144].

In the field of optics, hBN is a transparent material across all wavelengths below the ultraviolet region. It also hosts indirect Wannier excitons, characterized by a binding energy of approximately 100 meV [138]. The recent identification of room-temperature single-photon emission from point defects within hBN introduces intriguing possibilities for applications in quantum photonics [145]. Notably, phonon-polariton modes in the mid-infrared spectrum have been observed in thin hBN flakes [146] (see Figure 2.14(b)). These polaronic waves come from the hyperbolic nature of the hBN dielectric function, featuring two Reststrahlen bands positioned at around 100 and 180 meV ( $\sim 12.4$  and  $\sim 6.9$   $\mu\text{m}$ , respectively), as shown in Figure 2.14(a).

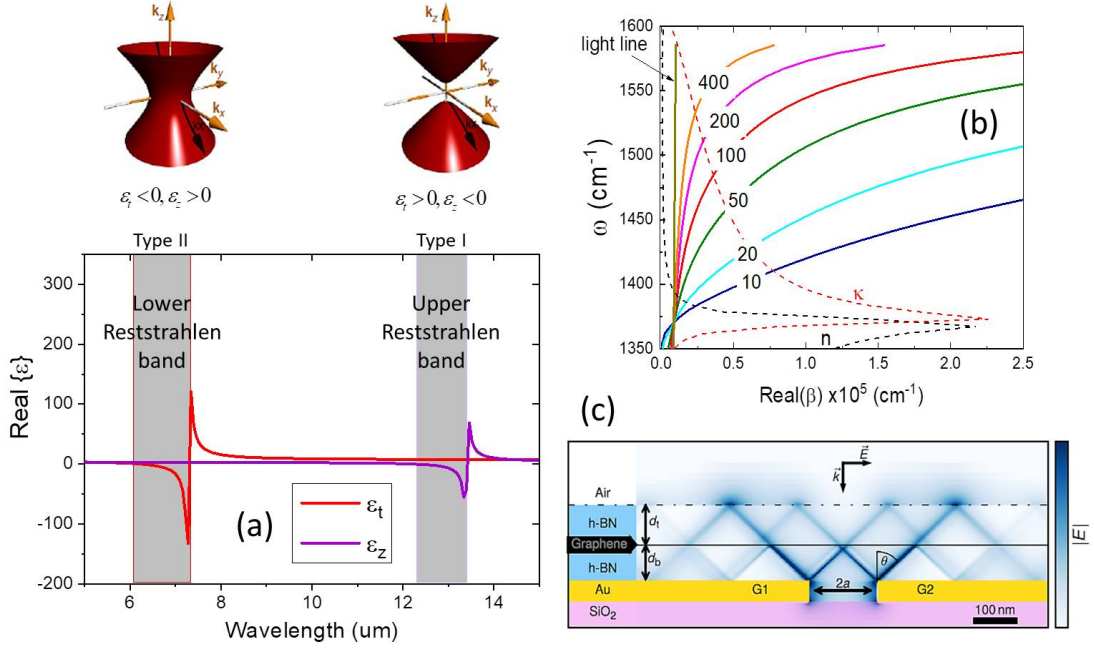


Figure 2.14: (a) Real parts of the permittivity tensor components for hBN. The shaded areas correspond to (Type I) upper and (Type II) lower Reststrahlen bands. On top schematics of isofrequency surfaces for Type I (right) and Type II (left) hyperbolic media are illustrated. (b) Calculated dispersion relation of the fundamental hyperbolic phonon polariton mode in hBN for various crystal thicknesses (10-400 nm) with FDE solver (described in section 4.3). (c) Side view of the propagating hyperbolic phonon polaritons, simulated by FDTD, for an hBN encapsulated graphene pn-junction device [147].

Within the upper Reststrahlen band, hBN demonstrates type I hyperbolicity ( $\Re\epsilon_t = \Re\epsilon_x = \Re\epsilon_y > 0$  and  $\Re\epsilon_z < 0$ ). In contrast, in the lower Reststrahlen band, hBN exhibits type II hyperbolicity, featuring  $\Re\epsilon_t = \Re\epsilon_x = \Re\epsilon_y < 0$  and  $\Re\epsilon_z > 0$ . The dispersion relation of hyperbolic phonon polaritons (HPPs) within these Reststrahlen Bands can be obtained using equation [148]

$$\frac{k_t^2}{\epsilon_z(\omega)} + \frac{k_z^2}{\epsilon_t(\omega)} = \frac{\omega^2}{c^2} = k_0^2 \quad (2.22)$$

Where  $c$  represents the speed of light, and  $\omega$  denotes the frequency of the incident light. The incident light momentum is denoted by  $k_0$ , while  $k = (k_t, k_z)$  represents the momenta of HPPs. The in-plane ( $k_t$ ) and incident light  $k_0$  momenta are correlated with their respective propagation wavelengths  $\lambda_{HPP}$  and  $\lambda_0$ . Solving Equation 2.22 under the large  $k$  approximation, where  $k_0 \ll k \ll 1/\alpha$  with  $\alpha$  the unit cell lattice constant of hBN, yields a single hyperboloid isofrequency surface for the upper Reststrahlen band and a double hyperboloid for the lower Reststrahlen band (see top schematics of Figure 2.14(a)).

In thin films of hBN with limited extent in the  $z$  direction, the hyperbolic dispersion is affected by the confinement of polaritonic fields within the volume. The finite thickness of hBN film gives rise to confined Fabry-Perot resonances, that appear between the two interfaces of the hBN crystal. hBN phonon polaritons enable the confinement and control of electromagnetic energy at the nanoscale limit. They exhibit extraordinary modal confinements ( $\lambda_0/\lambda_{HPP}$ ) that can reach values beyond 100 for higher order modes and small

crystal thicknesses (see Figure 2.14(b)). These confinements surpass the highest achieved confinement in hyperbolic metamaterial structures [149].

The significant increase in the optical density of states, due to the hyperbolic dispersion, which expands the range of supported wavevectors at a given frequency, introduces a limitation on the propagation of polaritons. Specifically, polariton propagation is limited to a frequency-dependent angle [150]. The propagation angle  $\theta(\omega)$  (the angle between the Poynting vector and the z-axis, as illustrated in Figure 2.14(c)) can be roughly estimated by  $\theta(\omega) = \pi/2 - \arctan\left(\frac{\sqrt{\epsilon_z(\omega)}}{i\sqrt{\epsilon_t(\omega)}}\right)$ . This angle remains constant through multiple reflections. Moreover, at a specific frequency, both the fundamental and higher-order modes propagate at the same angle relative to the surface normal.

## 2.4 Van der Waals Heterostructures (vdWHs)

As explored in previous sections, 2D layered materials like graphene, TMDs, and hBN exhibit a wide range of complementary properties. Notably, the weak van der Waals forces that facilitate the exfoliation of these bulk materials into individual layers can also be used to stack them one on top of the other in the desired layer sequence. The absence of lattice matching limitations provides a lot of freedom in creating these heterostructures. Due to the variety of 2D materials, the creation of an extensive array of vdWHs becomes possible (see Figure 2.15). Parameters, such as sequence, layer thickness and rotational alignment, become tunable in their fabrication.

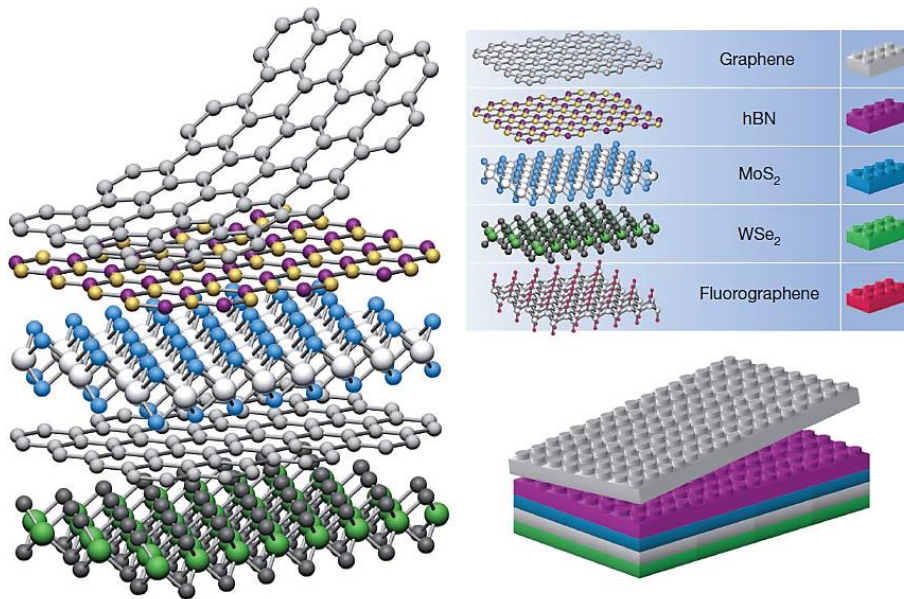


Figure 2.15: Creating van der Waals heterostructures seems like assembling Lego blocks, when 2D crystals can be assumed as an analog, as shown in the right panel. This allows for the creation of an extensive array of layered structures [151].

Van der Waals heterostructures (vdWHs), not only combine their constituent layers' unique properties, but also introduce novel physical effects and possibilities for engineering their optoelectronic properties.

### 2.4.1 Electronic and Optical properties

Combining different materials in a stack can yield various effects on both individual layers' electronic properties and overall vdWH. These effects depend on the electronic band alignment, between the layers and the strength of interlayer coupling, affected by the rotational alignment and lattice mismatch of the layers. When interlayer coupling is weak, individual layers keep their two-dimensional properties. Interactions between neighboring layers occur primarily through electrostatic coupling. In this case, the electronic behavior of vdWH is governed by the contributions of individual layers and the heterojunctions they form. These heterojunctions introduce discontinuities in the band diagram and fall into various categories based on the different 2D materials involved and their band alignment.

Owing to the absence of dangling bonds on surface of layered materials, their alignment typically follows the predictions from simple electrostatic models, such as Schottky-Mott and Anderson's rules [152, 153]. For example, graphene/TMD junction typically establish Schottky metal-semiconductor junction, characterized by a Schottky barrier height approximately determined by  $\Phi_B = W_G - \chi$ , where  $W_G$  is the work function of graphene, and  $\chi$  is the electron (or hole) affinity of TMDs. In contrast, graphene/hBN junction form metal-insulator interface, where the Dirac point of graphene is situated well above the edge of hBN valence band ( $\Phi_0 \simeq 1.3$  eV) [137]. Heterojunctions involving TMD/TMD combinations usually exhibit a band alignment, featuring valence or conduction band offsets in the range of  $\sim 0.1$ - $0.3$  eV [154–157].

While principles associated with 3D bulk junctions are often relevant to those formed with 2D materials, there are some limitations. Typically, combining two materials with different work functions results in a transfer of charges between them. In 3D bulk junctions, this charge transfer induces an internal electric field, leading to a depletion region that extends from the junction. However, in the field of 2D materials, the depletion region becomes less applicable, as the charges are localized within the two layers. Instead, 2D junctions are more accurately described as parallel plate capacitors separated by a small vdW gap. This simple model effectively explains charge doping and Fermi level shift observed in 2D junctions [154, 158]. Recently, a comprehensive model, predicting the spatial and dynamic dielectric properties of a given vdWH, is proposed in ref. [159], based on the dielectric properties of its constituent 2D layers and their long-range Coulomb interactions. It's worth noting that in specific cases, especially when two crystals are rotationally aligned, the interlayer coupling can be strong enough to significantly modify the band structure of individual layers. This effect can arise from various hybridization effects [155, 160] or the creation of moiré super-lattices [161, 162].

Owing to the weak electronic interactions between layers, the optical properties of vdWHs can be described by combining the properties of their individual layers [163]. On the other side, recent research indicates a notable modification in the dynamics of photo-generated charges, due to the electronic states of the surrounding layers. Graphene/TMD heterojunctions [164, 165] serve as an example of this effect. Photocarriers generated in the TMD swiftly transfer to graphene within picosecond timescale, resulting in a strong quenching of TMD photoluminescence. The mechanisms for this energy transfer can be either radiative or non-radiative (due to dipole-dipole coupling) [166]. The latter has been observed not only in graphene/quantum dot systems [167], but also in certain TMD/TMD heterostructures [168].

## 2.4.2 Optoelectronic applications based on vdWHs

Recently, the rapid increase of interest in vdWHs has led to enormous progress in this field, which is presented in several review articles [108, 151, 169–173]. Here we give an overview of the main applications of vdWHs, with an emphasis on those relevant for this thesis. Namely, in Chapter 7, we study TMD/hBN/graphene heterostructures for photonic cavity and plasmonic antenna enhanced nanoscale Light Emitting Diodes (LEDs), for both free-space and integrated devices.

### Photodetectors based on vdWHs

Photodetection, based on the photovoltaic effect, follows two different operations, such as photoconduction and photocurrent. In photoconduction operation, the conductance of the device is increased by the photo-excited carriers, while in photocurrent operation, photo-excited carriers are converted into current, affected by an electric field caused by a symmetry-lowering element like a junction. In case of intrinsic photo-response, an important challenge for photodetectors based on 2D TMDs is the dissociation of excitons by electric fields, whether intrinsic or externally applied, due to their remarkably strong excitonic effects.

Advancements in experimental techniques have been achieved in photodetectors, employing both in-plane and out-of-plane structures of 2D TMDs (see Figure 2.16). In-plane devices offer improved control over material properties through electrostatic gating, while out-of-plane devices can sustain a significantly high bias field. Additionally, they present a reduced excitonic binding energy in multilayer structures [116], promoting more effective exciton dissociation. TMD photodetectors, particularly those based on in-plane photoconduction, are notably affected by extrinsic effects, associated with impurities and defects. Thus, there is a need of future studies in order to showcase the importance of intrinsic and extrinsic mechanisms, aiming to manage structure optimization for enhanced performances.

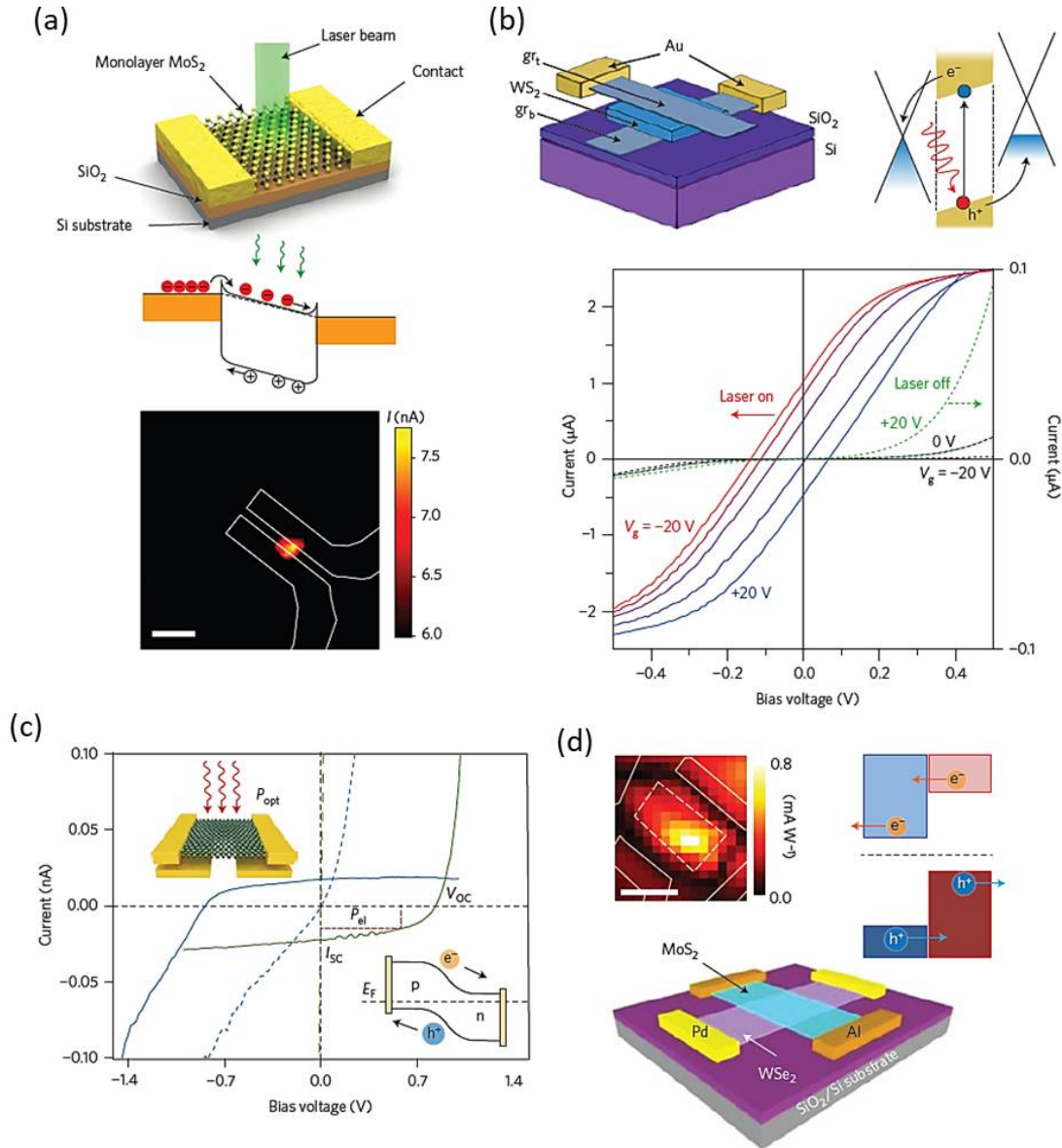


Figure 2.16: Photoconduction (a-b) and photocurrent (c-d) devices, based on lateral and vertical structures [108]. (a) Schematic of monolayer MoS<sub>2</sub> lateral photoconductor [174] (top). In the middle, there is a band diagram (with small Schottky barriers at the contacts) of monolayer MoS<sub>2</sub> photodetector. Photocurrent spatial map with a hot-spot area, corresponding to the location of MoS<sub>2</sub> (bottom). (b) Few-layer WS<sub>2</sub> vertical photoconductor with graphene on top and back electrodes [175]. Band diagram for a graphene/WS<sub>2</sub>/graphene heterostructure, with a built-in electric field to separate the generated electron-hole pair. Electric current as a function of bias voltage with and without light illumination (bottom). (c) Photocurrent as a function of bias voltage of a monolayer WSe<sub>2</sub> device with split gate electrodes (top inset) under different bias voltage [176]. In the bottom inset the band diagram of p-n diode is illustrated. (d) Schematic of a vertical p-n diode device, where the heterojunction is formed by monolayers MoS<sub>2</sub> and WSe<sub>2</sub> (bottom) [177]. Colormap of the photocurrent hot-spot at the heterojunction (top left) and schematic illustration of exciton dissociation (top right).

Following the literature, Mak et al. initially detected weak in-plane photoconduction, when illuminating 2D MoS<sub>2</sub> transistors with a diffraction-limited laser beam [102]. Later investigations have revealed a significant enhancement in photoconduction through illumination, particularly at the semiconductor–metal contacts and in short-channel devices [174, 178–180]. Experiments have identified doping and trapping of photo-generated carriers by impurities as the main mechanisms altering the device conductance in 2D MoS<sub>2</sub>. These extrinsic effects offer an explanation for the significant saturation behavior observed in the excitation power dependence of responsivity. Conversely, vertical TMD devices with graphene as bias electrodes have been reported by Britnell et al. [175] (see Figure 2.16(b)). This device reached an impressive 50% in external quantum efficiency.

A more controllable and efficient category of photodetector relies on the photocurrent operation. These devices incorporate a junction [176, 177, 181–185], establishing a built-in electric field. Both in-plane (see Figure 2.16(c)) and out-of-plane junctions (see Figure 2.16(d)) have been successfully demonstrated. Figure 2.16(c) shows an in-plane p–n diode [176] based on monolayer WSe<sub>2</sub>, where successful achievement of both n- and p-type contacts, along with ambipolar operation, is notable. The relatively small energy gap of WSe<sub>2</sub>, plays an important role in these achievements. However, the efficiency of these devices (i.e., EQE  $\simeq$  0.2% under zero bias) faces limitations due to the challenge of achieving a broad depletion region to capture excitons and a high built-in field for efficient dissociation. Given that limitation, out-of-plane junctions emerge as promising alternatives. These junctions comprise two-layer vertical stacks (see Figure 2.16(d)), with one layer serving as n-type (e.g., monolayer MoS<sub>2</sub>) and the other as p-type (e.g., monolayer WSe<sub>2</sub>) [177]. Electrostatic gates offer additional control over the device doping levels. Due to the very small interlayer separation, these structures can generate remarkably high built-in electric fields. Additionally, these devices provide a large exposure area for efficient optical absorption, eliminating the need for exciton diffusion to the depletion region. Lee et al. reported an external quantum efficiency of  $\sim$ 10–30% for graphene-encapsulated vertical TMD p–n diodes [177]. This study underscores the potential for effective photodetection in out-of-plane p–n diodes based on 2D vdW materials, benefiting from unique layer-by-layer control at the atomic level. Nevertheless, further investigations are needed to explore the role of tunnelling contributions in these diodes with atomic-scale depletion regions, as well as to assess their operational bandwidths.

### LEDs on lateral vdWH p–n junction

While the bulk TMDs exhibit an indirect bandgap, their conversion to single layer transforms it into a direct bandgap [102]. This modification satisfies a fundamental requirement, essential for effective utilization in light emission applications. The wide range of TMDs, with distinct bandgaps and working functions, offers dual benefits. Firstly, it enables tunable emissions across a broad spectrum of wavelengths and secondly it presents numerous opportunities for bandgap engineering of heterostructures [157].

The p–n junction serves as a key element in various optoelectronic applications, such as photodetectors and LEDs. Ultra-thin TMDs are inherently responsive to their surrounding dielectric environment. This sensitivity facilitates the possibility for electrostatic gating control of monolayer TMDs' doping, offering a pathway for precise modulation. Creating a p–n junction involves the application of two split gates beneath the monolayer TMDs. This approach has been utilized in the production of monolayer WSe<sub>2</sub> LED devices (see Figs 2.17(a–b)). These devices exhibited a remarkable total photon emission

rate (one emitted photon per  $10^4$  injected electron–hole pairs [181]), under the highest applied current ( $\sim 35$  nA). While the total estimated quantum efficiency remains at 0.01%, the emission wavelength can be finely tuned between regimes, such as impurity-bound, charged, and neutral excitons, as depicted in the colormap of Figure 2.17(c). The electrical control enables a single device to have multiple functionalities. For instance, ambipolar monolayer WSe<sub>2</sub> devices, equipped with local splitting gates, have achieved both p-n and n-p configurations. The estimated electroluminescence quantum efficiency has reached approximately 1% [184].

To achieve light emission from monolayer TMDs, the ambipolar field-effect transistor (FET) is an alternative structure to establish p-n junction within 2D materials [186]. TMDs can undergo effective neutral doping, by applying gate voltage. Consequently, TMD-based FET devices can function within the ambipolar injection regime, facilitating the injection of holes and electrons at opposing contacts. This operation enables the observation of light emission from the FET channel. Such a light-emitting transistor, based on monolayer WSe<sub>2</sub>, has been successfully realized, as depicted in Figure 2.17(d) [187]. Circularly polarized electroluminescence from p-n junctions are electrostatically formed within transistor channels (see Figure 2.17(e)). This property can be described by hole-electron overlap through the in-plane electric field. The external quantum efficiency (EQE) varies across samples, ranging from 0.002% to 0.06%, as illustrated in Figure 2.17(f).

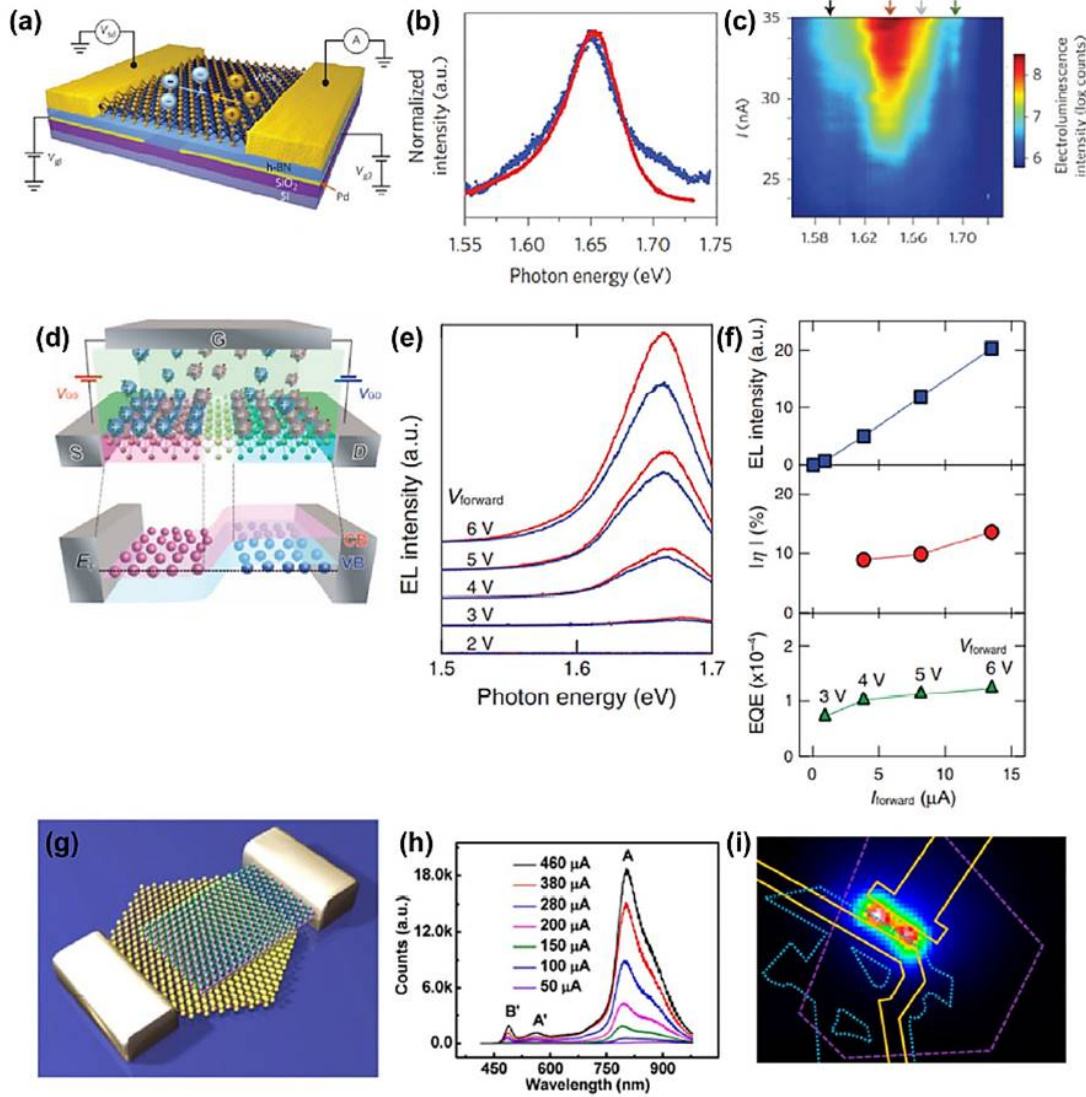


Figure 2.17: LEDs based on TMDs p-n junction [169]: (a) Schematic of multiple monolayer  $\text{WSe}_2$  p-n junction device with back gates and source-drain contacts. The source–drain voltage is applied to one contact and the current is read out of the other. During electroluminescence in the  $\text{WSe}_2$ , electrons and holes move towards each other and recombine. The device is placed on top of a typical  $\text{SiO}_2/\text{Si}$  substrate [181]. (b) Electroluminescence (EL) spectrum (blue line), generated by a nA current, converges to the photoluminescence (PL) spectrum (red line) at 300 K [181]. (c) EL intensity plot as a function of bias current and photon energy. The impurity-bound exciton XI (black arrow), the charged excitons  $X^-$  (red arrow) and  $X^+$  (yellow arrow) and the neutral exciton  $X_0$  (green arrow) [181]. (d) Schematic of TMD electric-double-layer transistor (EDLT), under ambipolar charge accumulation (top panel). The bottom panel shows a schematic of the band structure of EDLT induced p-n junction under equilibrium [187]. (e) EL intensity spectra of the device for voltage (2–6 V) [187]. (f) Extracted from (e): Total EL intensity as a function of forward current (top). EL polarization as a function of forward current (middle). External quantum efficiency as a function of forward current (bottom) [187]. (g) Schematic illustration of the  $\text{WSe}_2/\text{MoS}_2$  vertical heterojunction p-n diode [182]. (h) EL spectra of a ML- $\text{WSe}_2/\text{MoS}_2$  heterojunction at variable injection currents [182]. (i) Colored EL image of the heterojunction device under an injection current of 100  $\mu\text{A}$  [182].

Nevertheless, the light emission capability of lateral p-n junction devices is limited by the narrow interface of 1D junction, resulting in low LED efficiency. Consequently, the vertical stacking of TMDs to create p-n junctions is more efficient, as it expands the optical active area from 1D line to 2D overlapping region. MoS<sub>2</sub> and WSe<sub>2</sub> vertical p-n junction LEDs (see Figure 2.17(g)), demonstrate this extension, with the p-n junction covering the entire MoS<sub>2</sub>/WSe<sub>2</sub> overlapping area [182]. The EL from such devices exhibits noticeable band-edge excitonic emission alongside significantly enhanced hot-electron luminescence, as depicted in Figure 2.17(h). However, the emitted light is localized at the overlapping region closer to the electrodes rather than across the entire overlapping area (Figure 2.17(i)). This effect can be attributed to the current injection limitations within these p-n junctions, limited by lateral contacts and lateral carrier transport, due to the depletion of the ultra-thin TMDs.

### LEDs on vertical vdWHs

Efficient and expansive light emission from LEDs is useful for numerous applications. Due to the limitations of traditional p-n junction structures, described previously, a novel design has emerged, including vertically chip-based LEDs, constructed by layering 2D materials. This innovative approach typically involves graphene, hBN, and TMDs. In the configuration of Figure 2.18(a) [188], two graphene layers serve as transparent uniform electrode contacts, separated by an hBN/MoS<sub>2</sub>/hBN sandwich quantum well. The important element in this setup is the hBN layer. Acting as a tunnelling barrier, the few-layer hBN diminishes leakage current during device operation, when current flows from the top to the bottom layers. Specifically, the important parameter is the thickness of the hBN layer. When hBN flake exceeds one atomic layer thickness, it effectively extends the carrier lifetime, facilitating the formation of excitons, that recombine to produce efficient light emission, as depicted in Figure 2.18(b) [188]. Nevertheless, as the thickness of the hBN increases, the current tunnelling through it experiences a sharp decline [140, 189], resulting in very weak LED emission, as illustrated in Figure 2.18(c).

A single hBN/MoS<sub>2</sub>/hBN quantum well (QW) LED device showcases a quantum efficiency of approximately 1% [188]. This efficiency can be elevated to 8.4% by incorporating four QWs, attributed to enhanced radiative recombination [188]. Vertical stacking structure significantly enhances light-emitting quantum efficiency by several orders of magnitude compared to LEDs employing p-n junction geometry. Furthermore, the emission spectrum can be finely tuned by combining different 2D semiconductors. Combinational devices exhibit a quantum efficiency of ~5%, comparable to current organic LEDs and state-of-the-art quantum dot LEDs.

Recent research has focused on further optimizing quantum efficiency through substrate modulation and integration with photonic crystal cavities. Vertical stacking LEDs utilizing WSe<sub>2</sub> with high efficiency at room temperature have been reported, employing refractive distributed Bragg reflector (DBR) substrates, illustrated in Figs 2.18(d) and (e). The DBR's role is to minimize light scattering into SiO<sub>2</sub>/Si substrates, while enhancing light collection. Based on these DBRs, up to 30% of the emitted light can be effectively collected, in contrast to a 2% collected from conventional Si/SiO<sub>2</sub> substrates. The EQE efficiency of WSe<sub>2</sub> devices is improved with temperature (see Figure 2.18(f)). At room temperature, EQE reaches 5% [190], marking a significant improvement compared to the MoS<sub>2</sub> quantum wells under ambient conditions, which have achieved only ~250 times less in EQE so far [188].

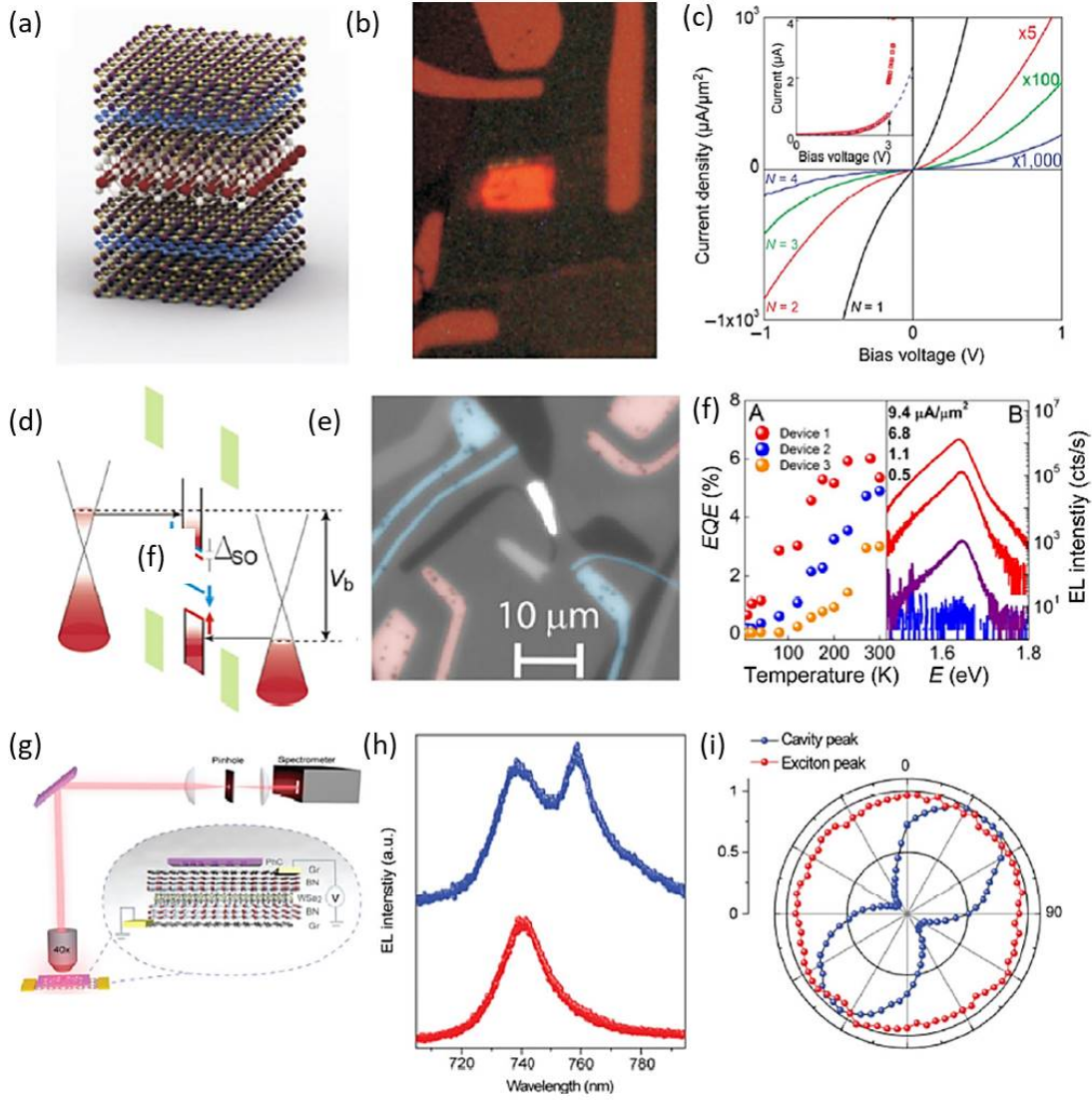


Figure 2.18: LEDs based on TMDs vertical stacking [169]: (a) Schematic of the hBN/Gr/2hBN/WS<sub>2</sub>/2hBN/Gr/hBN heterostructure [188]. (b) Optical image of EL from the same device ( $V_b=2.5$  V,  $T=300$  K) [188]. (c) Characteristic I-V curves for graphite/BN/graphite devices with different BN insulating layer thicknesses, such as monolayer of BN (black line), bilayer (red line), triple layer (green line) and quadruple layer (blue line) [140]. The inset shows a typical I-V curve, where the breakdown in the BN is observed at +3 V (4-layer thickness of BN is 1.3 nm). (d) Band alignment at high bias of a WSe<sub>2</sub> LEQW device [190]. (e) Image of a WSe<sub>2</sub> LEQW device with an applied bias of  $V_b=2$  V and current of 2 uA. The central white area corresponds to strong electroluminescence, in red areas are the Au contacts to bottom graphene and in blue the Au contacts to top graphene [190]. (f) Temperature dependence of the quantum efficiency for three typical WSe<sub>2</sub> LED devices (left panel). EL intensity spectra plotted for four different injection current densities for device 3 [190] (right panel). (g) Schematic of the EL measurement device's set-up [191]. (h) EL measurements from (blue dots) and away (red dots) from the cavity area with  $V_b=2$  V [191]. (i) Cavity-enhanced peak intensity (blue dots) and exciton peak intensity (red dots) as a function of polarization detection angle [191].

Figs 2.18(g) and (h) show integrated WSe<sub>2</sub> vertical stacking LEDs with an incorporated photonic crystal cavity, as reported in recent studies. The EL emission efficiency has a remarkable 4-fold enhancement compared to LEDs on bare SiO<sub>2</sub>/Si substrates [191]. This enhancement is attributed to the strong coupling between the photonic crystal mode and exciton EL in WSe<sub>2</sub>, resulting in an enhanced emission rate. Furthermore, the emission at the cavity resonance exhibits single-mode operation and high linear polarization (84%) along the cavity mode axis, as illustrated in Figure 2.18(i). The implementation of photonic crystal cavity has enabled the realization of electrically pumped single-mode light sources, marking significant advancement towards on-chip optical information technologies. This underscores the advantage offered by vertical stacking LED structures.

### Single-photon emitters based on vdWHs

The integration of high quality and enhanced efficiency single-photon sources into optoelectronic circuits represents a important challenge in advancing scalable quantum communication technologies [192]. In monolayer WSe<sub>2</sub>, single-photon emitters have been optically observed, due to crystal structure imperfections that serve as efficient carrier trapping centers [193]. As a complement to optical pumping, electrically pumped single-photon emission holds promise for the development of future quantum light-generating devices.

Atomically thin quantum LEDs, utilizing WSe<sub>2</sub> and WS<sub>2</sub> have been reported [194], from successful techniques employing TMD-based vertical stacking LEDs. These quantum LEDs create a graphene/hBN/TMD structure, designed to facilitate carrier injections by modulating the Fermi level in graphene, as depicted in Figs. 2.19(a) and 2.19(b). During device operation, uniform light emission is generated across the entire WSe<sub>2</sub> area. However, both monolayer and bilayer WSe<sub>2</sub> samples exhibit a distinct hot spot, as observed in Figure 2.19(d). Spectrum analysis reveals distinct emission performance, compared to free exciton recombination. Notably, in Figure 2.19(c), remarkably sharp peaks are identified in the near-IR, with linewidths ranging between 0.8 and 3 nm, indicating quantum emission. To verify them as single-photon sources, the intensity correlation function of EL emission, denoted as  $g(2)(\tau)$ , from WSe<sub>2</sub>-based quantum LEDs was plotted (see Figure 2.19(e)). The normalized value of  $g(2)(0)$  was found to decrease to  $\simeq 0.29$ , below the threshold value of 0.5, expected for a single-photon source [195]. Similarly, in WS<sub>2</sub>-based quantum LEDs, a quantum emitter was also identified, with  $g(2)(0) \simeq 0.31$ . This observation shows the stable operation of WS<sub>2</sub>-based quantum LEDs, capable of generating single photons in the visible spectral range, as illustrated in Figs. 2.19(f) and 2.19(g).

It is important to mention that single-photon emission can also be achieved in WSe<sub>2</sub> LEDs featuring lateral structures (see Figure 2.19(h)) [196]. These devices exhibit three different single defects within a narrow p-i-n junction area, as depicted in Figure 2.19(i). The emissions from these defects appear as a doublet with characteristic exchange splitting and linearly polarized selection rules, aligning with properties of previously reported single-photon emitters observed through optical measurements. In comparison to traditional bulk materials, 2D materials offer greater suitability for on-chip integration with electronic circuits due to their ultra-thin nature. However, the limited research on single-photon emitters in 2D materials remains a significant challenge. Controlling the defects in TMDs to create single-photon emitters is the future step in advancing TMD-based single-photon emitter technology.

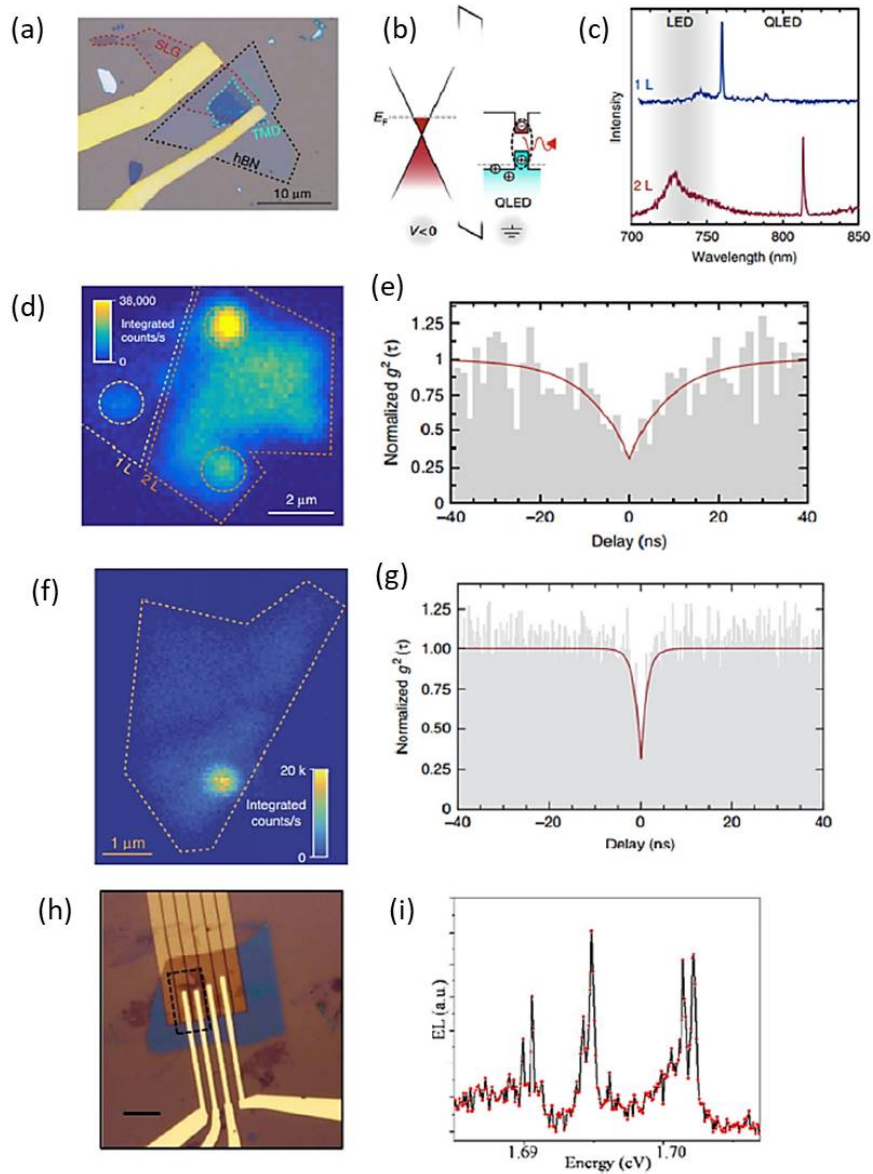


Figure 2.19: Single-photon emitters based on vdWHs: (a) Optical microscope image of a typical experimental device. The dotted lines represent the areas of SLG (red), hBN (black) and the TMD layers (light blue), respectively [194]. The electrical bias is provided by Cr/Au electrodes contacting both the SLG and TMD layers. (b) The heterostructure band diagram illustrates the case where a finite negative bias is applied to the SLG [194]. (c) EL emission spectra for quantum dots in monolayer (top) and bilayer (bottom)  $\text{WSe}_2$ . The shaded area denotes the spectral window for LED emission caused by bulk  $\text{WSe}_2$  excitons, while QLED operation appears at longer wavelengths [194]. (d) Raster-scan map of integrated EL intensity from monolayer and bilayer  $\text{WSe}_2$  regions of the QLED at an injection current of 3 mA. The dotted circles show the localized emission observed in this device [194]. (e) Intensity-correlation function  $g^{(2)}(\tau)$  revealing the anti-bunched nature of the EL signal with  $g^{(2)}(0) \simeq 0.29$  and width-time of  $\simeq 9.4$  ns [194]. (f) Raster-scan map illustrating the integrated EL intensity from the monolayer  $\text{WS}_2$  region of the device at 0.57 mA, where the highly localized QLED emission becomes dominant over the unbound  $\text{WS}_2$  exciton emission [194]. (g) Intensity-correlation function, for the same quantum dot, showcasing the anti-bunched nature of the EL signal with  $g^{(2)}(0) \simeq 0.31$  and width-time of  $\simeq 1.4$  ns. (h) Optical image of a lateral LED device [196]. (i) EL spectrum for a lateral LED device, illustrating emission from three distinct single defects [196].

## References

- [1] P. R. Wallace, “The band theory of graphite,” *Physical review*, vol. 71, no. 9, p. 622, 1947.
- [2] A. C. Neto, F. Guinea, N. M. Peres, K. S. Novoselov, and A. K. Geim, “The electronic properties of graphene,” *Reviews of modern physics*, vol. 81, no. 1, p. 109, 2009.
- [3] Y. Zhang, Y.-W. Tan, H. L. Stormer, and P. Kim, “Experimental observation of the quantum hall effect and berry’s phase in graphene,” *nature*, vol. 438, no. 7065, pp. 201–204, 2005.
- [4] K. S. Novoselov, A. K. Geim, S. V. Morozov, D. Jiang, M. I. Katsnelson, I. V. Grigorieva, S. Dubonos, Firsov, and AA, “Two-dimensional gas of massless dirac fermions in graphene,” *nature*, vol. 438, no. 7065, pp. 197–200, 2005.
- [5] A. K. Geim and K. S. Novoselov, “The rise of graphene,” *Nature materials*, vol. 6, no. 3, pp. 183–191, 2007.
- [6] K. S. Novoselov, A. K. Geim, S. V. Morozov, D.-e. Jiang, Y. Zhang, S. V. Dubonos, I. V. Grigorieva, and A. A. Firsov, “Electric field effect in atomically thin carbon films,” *science*, vol. 306, no. 5696, pp. 666–669, 2004.
- [7] N. Kakenov, O. Balci, T. Takan, V. A. Ozkan, H. Altan, and C. Kocabas, “Observation of gate-tunable coherent perfect absorption of terahertz radiation in graphene,” *Acs Photonics*, vol. 3, no. 9, pp. 1531–1535, 2016.
- [8] N. Kakenov, O. Balci, E. O. Polat, H. Altan, and C. Kocabas, “Broadband terahertz modulators using self-gated graphene capacitors,” *JOSA B*, vol. 32, no. 9, pp. 1861–1866, 2015.
- [9] O. Balci, E. O. Polat, N. Kakenov, and C. Kocabas, “Graphene-enabled electrically switchable radar-absorbing surfaces,” *Nature communications*, vol. 6, no. 1, p. 6628, 2015.
- [10] L. A. Falkovsky, “Optical properties of graphene,” in *Journal of Physics: conference series*, vol. 129, p. 012004, IOP Publishing, 2008.
- [11] G. W. Hanson, “Dyadic green’s functions and guided surface waves for a surface conductivity model of graphene,” *Journal of Applied Physics*, vol. 103, no. 6, 2008.
- [12] Z. Li, E. A. Henriksen, Z. Jiang, Z. Hao, M. C. Martin, P. Kim, H. L. Stormer, and D. N. Basov, “Dirac charge dynamics in graphene by infrared spectroscopy,” *Nature physics*, vol. 4, no. 7, pp. 532–535, 2008.
- [13] J. Horng, C.-F. Chen, B. Geng, C. Girit, Y. Zhang, Z. Hao, H. A. Bechtel, M. Martin, A. Zettl, M. F. Crommie, *et al.*, “Drude conductivity of dirac fermions in graphene,” *Physical Review B*, vol. 83, no. 16, p. 165113, 2011.
- [14] K. F. Mak, L. Ju, F. Wang, and T. F. Heinz, “Optical spectroscopy of graphene: From the far infrared to the ultraviolet,” *Solid State Communications*, vol. 152, no. 15, pp. 1341–1349, 2012.

- [15] V. Kravets, A. Grigorenko, R. Nair, P. Blake, S. Anissimova, K. Novoselov, and A. Geim, "Spectroscopic ellipsometry of graphene and an exciton-shifted van hove peak in absorption," *Physical Review B*, vol. 81, no. 15, p. 155413, 2010.
- [16] R. R. Nair, P. Blake, A. N. Grigorenko, K. S. Novoselov, T. J. Booth, T. Stauber, N. M. Peres, and A. K. Geim, "Fine structure constant defines visual transparency of graphene," *science*, vol. 320, no. 5881, pp. 1308–1308, 2008.
- [17] S. D. Sarma, S. Adam, E. Hwang, and E. Rossi, "Electronic transport in two-dimensional graphene," *Reviews of modern physics*, vol. 83, no. 2, p. 407, 2011.
- [18] F. Bonaccorso, Z. Sun, T. Hasan, and A. Ferrari, "Graphene photonics and optoelectronics," *Nature photonics*, vol. 4, no. 9, pp. 611–622, 2010.
- [19] Q. Bao and K. P. Loh, "Graphene photonics, plasmonics, and broadband optoelectronic devices," *ACS nano*, vol. 6, no. 5, pp. 3677–3694, 2012.
- [20] E. Lidorikis and A. C. Ferrari, "Photonics with multiwall carbon nanotube arrays," *ACS nano*, vol. 3, no. 5, pp. 1238–1248, 2009.
- [21] T. Echtermeyer, S. Milana, U. Sassi, A. Eiden, M. Wu, E. Lidorikis, and A. Ferrari, "Surface plasmon polariton graphene photodetectors," *Nano Letters*, vol. 16, no. 1, pp. 8–20, 2016.
- [22] M. S. Dresselhaus, G. Dresselhaus, and P. C. Eklund, *Science of fullerenes and carbon nanotubes: their properties and applications*. Elsevier, 1996.
- [23] C. Casiraghi, A. Hartschuh, E. Lidorikis, H. Qian, H. Harutyunyan, T. Gokus, K. S. Novoselov, and A. Ferrari, "Rayleigh imaging of graphene and graphene layers," *Nano letters*, vol. 7, no. 9, pp. 2711–2717, 2007.
- [24] K. F. Mak, M. Y. Sfeir, Y. Wu, C. H. Lui, J. A. Misewich, and T. F. Heinz, "Measurement of the optical conductivity of graphene," *Physical review letters*, vol. 101, no. 19, p. 196405, 2008.
- [25] H. Fang, H. A. Bechtel, E. Plis, M. C. Martin, S. Krishna, E. Yablonovitch, and A. Javey, "Quantum of optical absorption in two-dimensional semiconductors," *Proceedings of the National Academy of Sciences*, vol. 110, no. 29, pp. 11688–11691, 2013.
- [26] K. F. Mak, J. Shan, and T. F. Heinz, "Seeing many-body effects in single-and few-layer graphene: observation of two-dimensional saddle-point excitons," *Physical review letters*, vol. 106, no. 4, p. 046401, 2011.
- [27] F. Xia, H. Wang, D. Xiao, M. Dubey, and A. Ramasubramaniam, "Two-dimensional material nanophotonics," *Nature Photonics*, vol. 8, no. 12, pp. 899–907, 2014.
- [28] P. Blake, E. Hill, A. Castro Neto, K. Novoselov, D. Jiang, R. Yang, T. Booth, and A. Geim, "Making graphene visible," *Applied physics letters*, vol. 91, no. 6, 2007.
- [29] M. Kanidi, A. Dagkli, N. Kelaidis, D. Palles, S. Aminalragia-Giamini, J. Marquez-Velasco, A. Colli, A. Dimoulas, E. Lidorikis, M. Kandyla, *et al.*, "Surface-enhanced raman spectroscopy of graphene integrated in plasmonic silicon platforms

- with three-dimensional nanotopography,” *The Journal of Physical Chemistry C*, vol. 123, no. 5, pp. 3076–3087, 2019.
- [30] W. Xu, N. Mao, and J. Zhang, “Graphene: a platform for surface-enhanced raman spectroscopy,” *Small*, vol. 9, no. 8, pp. 1206–1224, 2013.
- [31] M. G. Albrecht and J. A. Creighton, “Anomalously intense raman spectra of pyridine at a silver electrode,” *Journal of the american chemical society*, vol. 99, no. 15, pp. 5215–5217, 1977.
- [32] D. L. Jeanmaire and R. P. Van Duyne, “Surface raman spectroelectrochemistry: Part i. heterocyclic, aromatic, and aliphatic amines adsorbed on the anodized silver electrode,” *Journal of electroanalytical chemistry and interfacial electrochemistry*, vol. 84, no. 1, pp. 1–20, 1977.
- [33] K. Kneipp, Y. Wang, H. Kneipp, L. T. Perelman, I. Itzkan, R. R. Dasari, and M. S. Feld, “Single molecule detection using surface-enhanced raman scattering (sers),” *Physical review letters*, vol. 78, no. 9, p. 1667, 1997.
- [34] S. Nie and S. R. Emory, “Probing single molecules and single nanoparticles by surface-enhanced raman scattering,” *science*, vol. 275, no. 5303, pp. 1102–1106, 1997.
- [35] M. J. Natan, “Concluding remarks surface enhanced raman scattering,” *Faraday Discussions*, vol. 132, pp. 321–328, 2006.
- [36] X.-M. Lin, Y. Cui, Y.-H. Xu, B. Ren, and Z.-Q. Tian, “Surface-enhanced raman spectroscopy: substrate-related issues,” *Analytical and bioanalytical chemistry*, vol. 394, pp. 1729–1745, 2009.
- [37] A. Gupta, G. Chen, P. Joshi, S. Tadigadapa, and Eklund, “Raman scattering from high-frequency phonons in supported n-graphene layer films,” *Nano letters*, vol. 6, no. 12, pp. 2667–2673, 2006.
- [38] L. M. Malard, M. A. Pimenta, G. Dresselhaus, and M. S. Dresselhaus, “Raman spectroscopy in graphene,” *Physics reports*, vol. 473, no. 5-6, pp. 51–87, 2009.
- [39] A. C. Ferrari, J. C. Meyer, V. Scardaci, C. Casiraghi, M. Lazzeri, F. Mauri, S. Piscanec, D. Jiang, K. S. Novoselov, S. Roth, *et al.*, “Raman spectrum of graphene and graphene layers,” *Physical review letters*, vol. 97, no. 18, p. 187401, 2006.
- [40] L. Malard, J. Nilsson, D. Elias, J. Brant, F. Plentz, E. Alves, A. C. Neto, and M. Pimenta, “Probing the electronic structure of bilayer graphene by raman scattering,” *Physical Review B*, vol. 76, no. 20, p. 201401, 2007.
- [41] A. C. Ferrari, “Raman spectroscopy of graphene and graphite: Disorder, electron-phonon coupling, doping and nonadiabatic effects,” *Solid state communications*, vol. 143, no. 1-2, pp. 47–57, 2007.
- [42] A. Khan, R. R. Kumar, J. Cong, M. Imran, D. Yang, and X. Yu, “Cvd graphene on textured silicon: An emerging technologically versatile heterostructure for energy and detection applications,” *Advanced Materials Interfaces*, vol. 9, no. 1, p. 2100977, 2022.

- [43] M. Breusing, S. Kuehn, T. Winzer, E. Malić, F. Milde, N. Severin, J. Rabe, C. Ropers, A. Knorr, and T. Elsaesser, “Ultrafast nonequilibrium carrier dynamics in a single graphene layer,” *Physical Review B*, vol. 83, no. 15, p. 153410, 2011.
- [44] A. H. C. Neto, “The carbon new age,” *Materials today*, vol. 13, no. 3, pp. 12–17, 2010.
- [45] P. A. George, J. Strait, J. Dawlaty, S. Shivaraman, M. Chandrashekar, F. Rana, and M. G. Spencer, “Ultrafast optical-pump terahertz-probe spectroscopy of the carrier relaxation and recombination dynamics in epitaxial graphene,” *Nano letters*, vol. 8, no. 12, pp. 4248–4251, 2008.
- [46] I. Gierz, J. C. Petersen, M. Mitrano, C. Cacho, I. E. Turcu, E. Springate, A. Stöhr, A. Köhler, U. Starke, and A. Cavalleri, “Snapshots of non-equilibrium dirac carrier distributions in graphene,” *Nature materials*, vol. 12, no. 12, pp. 1119–1124, 2013.
- [47] M. W. Graham, S.-F. Shi, D. C. Ralph, J. Park, and P. L. McEuen, “Photocurrent measurements of supercollision cooling in graphene,” *Nature Physics*, vol. 9, no. 2, pp. 103–108, 2013.
- [48] S. A. Jensen, Z. Mics, I. Ivanov, H. S. Varol, D. Turchinovich, F. Koppens, M. Bonn, and K.-J. Tielrooij, “Competing ultrafast energy relaxation pathways in photoexcited graphene,” *Nano Letters*, vol. 14, no. 10, pp. 5839–5845, 2014.
- [49] J. C. Johannsen, S. Ulstrup, F. Cilento, A. Crepaldi, M. Zacchigna, C. Cacho, I. E. Turcu, E. Springate, F. Fromm, C. Roidel, *et al.*, “Direct view of hot carrier dynamics in graphene,” *Physical Review Letters*, vol. 111, no. 2, p. 027403, 2013.
- [50] D. Brida, A. Tomadin, C. Manzoni, Y. J. Kim, A. Lombardo, S. Milana, R. R. Nair, K. S. Novoselov, A. C. Ferrari, G. Cerullo, *et al.*, “Ultrafast collinear scattering and carrier multiplication in graphene,” *Nature communications*, vol. 4, no. 1, p. 1987, 2013.
- [51] S. Doukas, P. Mensz, N. Myoung, A. Ferrari, I. Goykhman, and E. Lidorikis, “Thermionic graphene/silicon schottky infrared photodetectors,” *Physical Review B*, vol. 105, no. 11, p. 115417, 2022.
- [52] R. Bistritzer and A. H. MacDonald, “Electronic cooling in graphene,” *Physical Review Letters*, vol. 102, no. 20, p. 206410, 2009.
- [53] J. Viljas and T. Heikkilä, “Electron-phonon heat transfer in monolayer and bilayer graphene,” *Physical Review B*, vol. 81, no. 24, p. 245404, 2010.
- [54] E. A. Pogna, X. Jia, A. Principi, A. Block, L. Banszerus, J. Zhang, X. Liu, T. Sohier, S. Forti, K. Soundarapandian, *et al.*, “Hot-carrier cooling in high-quality graphene is intrinsically limited by optical phonons,” *ACS nano*, vol. 15, no. 7, pp. 11285–11295, 2021.
- [55] J. C. Song and L. S. Levitov, “Energy flows in graphene: hot carrier dynamics and cooling,” *Journal of Physics: Condensed Matter*, vol. 27, no. 16, p. 164201, 2015.

- [56] J. C. Song, M. Y. Reizer, and L. S. Levitov, “Disorder-assisted electron-phonon scattering and cooling pathways in graphene,” *Physical review letters*, vol. 109, no. 10, p. 106602, 2012.
- [57] A. Betz, S. H. Jhang, E. Pallecchi, R. Ferreira, G. Fève, J.-M. Berroir, and B. Plaçais, “Supercollision cooling in undoped graphene,” *Nature Physics*, vol. 9, no. 2, pp. 109–112, 2013.
- [58] M. Massicotte, G. Soavi, A. Principi, and K.-J. Tielrooij, “Hot carriers in graphene—fundamentals and applications,” *Nanoscale*, vol. 13, no. 18, pp. 8376–8411, 2021.
- [59] M. Massicotte, P. Schmidt, F. Violla, K. Watanabe, T. Taniguchi, K.-J. Tielrooij, and F. H. Koppens, “Photo-thermionic effect in vertical graphene heterostructures,” *Nature communications*, vol. 7, no. 1, p. 12174, 2016.
- [60] E. Pop, V. Varshney, and A. K. Roy, “Thermal properties of graphene: Fundamentals and applications,” *MRS bulletin*, vol. 37, no. 12, pp. 1273–1281, 2012.
- [61] A. A. Balandin, “Thermal properties of graphene and nanostructured carbon materials,” *Nature materials*, vol. 10, no. 8, pp. 569–581, 2011.
- [62] G. Soavi, G. Wang, H. Rostami, D. G. Purdie, D. De Fazio, T. Ma, B. Luo, J. Wang, A. K. Ott, D. Yoon, *et al.*, “Broadband, electrically tunable third-harmonic generation in graphene,” *Nature nanotechnology*, vol. 13, no. 7, pp. 583–588, 2018.
- [63] A. Tomadin, D. Brida, G. Cerullo, A. C. Ferrari, and M. Polini, “Nonequilibrium dynamics of photoexcited electrons in graphene: Collinear scattering, auger processes, and the impact of screening,” *Physical Review B*, vol. 88, no. 3, p. 035430, 2013.
- [64] G. T. Reed, G. Mashanovich, F. Y. Gardes, and D. Thomson, “Silicon optical modulators,” *Nature photonics*, vol. 4, no. 8, pp. 518–526, 2010.
- [65] G. Sinatkas, T. Christopoulos, O. Tsilipakos, and E. E. Kriezis, “Electro-optic modulation in integrated photonics,” *Journal of Applied Physics*, vol. 130, no. 1, 2021.
- [66] Z. Sun, T. Hasan, and A. Ferrari, “Ultrafast lasers mode-locked by nanotubes and graphene,” *Physica E: Low-dimensional Systems and Nanostructures*, vol. 44, no. 6, pp. 1082–1091, 2012.
- [67] A. Martinez and Z. Sun, “Nanotube and graphene saturable absorbers for fibre lasers,” *Nature Photonics*, vol. 7, no. 11, pp. 842–845, 2013.
- [68] A. K. Majumdar and J. C. Ricklin, *Free-space laser communications: principles and advances*, vol. 2. Springer Science & Business Media, 2010.
- [69] H. Kaushal and G. Kaddoum, “Optical communication in space: Challenges and mitigation techniques,” *IEEE communications surveys & tutorials*, vol. 19, no. 1, pp. 57–96, 2016.
- [70] A. Malik, P. Singh, *et al.*, “Free space optics: current applications and future challenges,” *International journal of optics*, vol. 2015, 2015.

- [71] M. Flood, "Laser altimetry: From science to commercial lidar mapping," *Photogrammetric engineering and remote sensing*, vol. 67, no. 11, 2001.
- [72] G. C. Gilbreath, W. S. Rabinovich, T. J. Meehan, M. J. Vilcheck, M. Stell, R. Mahon, P. G. Goetz, E. Oh, J. A. Vasquez, K. Cochrell, *et al.*, "Progress in development of multiple-quantum-well retro modulators for free-space data links," *Optical Engineering*, vol. 42, no. 6, pp. 1611–1617, 2003.
- [73] I. F. Akyildiz, A. Kak, and S. Nie, "6g and beyond: The future of wireless communications systems," *IEEE access*, vol. 8, pp. 133995–134030, 2020.
- [74] S. Luo, Y. Wang, X. Tong, and Z. Wang, "Graphene-based optical modulators," *Nanoscale research letters*, vol. 10, pp. 1–11, 2015.
- [75] Z. Sun, A. Martinez, and F. Wang, "Optical modulators with 2d layered materials," *Nature Photonics*, vol. 10, no. 4, pp. 227–238, 2016.
- [76] S. Yu, X. Wu, Y. Wang, X. Guo, and L. Tong, "2d materials for optical modulation: challenges and opportunities," *Advanced Materials*, vol. 29, no. 14, p. 1606128, 2017.
- [77] J. Liu, Z. U. Khan, C. Wang, H. Zhang, and S. Sarjoghian, "Review of graphene modulators from the low to the high figure of merits," *Journal of Physics D: Applied Physics*, vol. 53, no. 23, p. 233002, 2020.
- [78] C. Zhong, J. Li, and H. Lin, "Graphene-based all-optical modulators," *Frontiers of Optoelectronics*, vol. 13, pp. 114–128, 2020.
- [79] W. Li, B. Chen, C. Meng, W. Fang, Y. Xiao, X. Li, Z. Hu, Y. Xu, L. Tong, H. Wang, *et al.*, "Ultrafast all-optical graphene modulator," *Nano letters*, vol. 14, no. 2, pp. 955–959, 2014.
- [80] M. Liu, X. Yin, E. Ulin-Avila, B. Geng, T. Zentgraf, L. Ju, F. Wang, and X. Zhang, "A graphene-based broadband optical modulator," *Nature*, vol. 474, no. 7349, pp. 64–67, 2011.
- [81] C.-C. Lee, S. Suzuki, W. Xie, and T. Schibli, "Broadband graphene electro-optic modulators with sub-wavelength thickness," *Optics express*, vol. 20, no. 5, pp. 5264–5269, 2012.
- [82] M. Shah and M. S. Anwar, "Magneto-optic modulation of lateral and angular shifts in spin-orbit coupled members of the graphene family," *OSA Continuum*, vol. 3, no. 4, pp. 878–892, 2020.
- [83] M. Farhat, S. Guenneau, and H. Bağcı, "Exciting graphene surface plasmon polaritons through light and sound interplay," *Physical review letters*, vol. 111, no. 23, p. 237404, 2013.
- [84] B. Gulbahar and G. Memisoglu, "Csstag: Optical nanoscale radar and particle tracking for in-body and microfluidic systems with vibrating graphene and resonance energy transfer," *IEEE Transactions on NanoBioscience*, vol. 16, no. 8, pp. 905–916, 2017.

- [85] X. Gan, C. Zhao, Y. Wang, D. Mao, L. Fang, L. Han, and J. Zhao, "Graphene-assisted all-fiber phase shifter and switching," *Optica*, vol. 2, no. 5, pp. 468–471, 2015.
- [86] R. Yu, V. Pruneri, and F. J. García de Abajo, "Resonant visible light modulation with graphene," *ACS Photonics*, vol. 2, no. 4, pp. 550–558, 2015.
- [87] A. C. Tasolamprou, A. D. Koulouklidis, C. Daskalaki, C. P. Mavidis, G. Kenanakis, G. Deligeorgis, Z. Viskadourakis, P. Kuzhir, S. Tzortzakis, M. Kafesaki, *et al.*, "Experimental demonstration of ultrafast thz modulation in a graphene-based thin film absorber through negative photoinduced conductivity," *ACS photonics*, vol. 6, no. 3, pp. 720–727, 2019.
- [88] R. Shimano, G. Yumoto, J. Yoo, R. Matsunaga, S. Tanabe, H. Hibino, T. Morimoto, and H. Aoki, "Quantum faraday and kerr rotations in graphene," *Nature communications*, vol. 4, no. 1, p. 1841, 2013.
- [89] Q. Bao, H. Zhang, B. Wang, Z. Ni, C. H. Y. X. Lim, Y. Wang, D. Y. Tang, and K. P. Loh, "Broadband graphene polarizer," *Nature photonics*, vol. 5, no. 7, pp. 411–415, 2011.
- [90] D. R. Andersen, "Graphene-based long-wave infrared tm surface plasmon modulator," *JOSA B*, vol. 27, no. 4, pp. 818–823, 2010.
- [91] E. O. Polat and C. Kocabas, "Broadband optical modulators based on graphene supercapacitors," *Nano letters*, vol. 13, no. 12, pp. 5851–5857, 2013.
- [92] C.-C. Lee, C. Mohr, J. Bethge, S. Suzuki, M. Fermann, I. Hartl, and T. Schibli, "Frequency comb stabilization with bandwidth beyond the limit of gain lifetime by an intracavity graphene electro-optic modulator," *Optics Letters*, vol. 37, no. 15, pp. 3084–3086, 2012.
- [93] B. Sensale-Rodriguez, R. Yan, M. M. Kelly, T. Fang, K. Tahy, W. S. Hwang, D. Jena, L. Liu, and H. G. Xing, "Broadband graphene terahertz modulators enabled by intraband transitions," *Nature communications*, vol. 3, no. 1, p. 780, 2012.
- [94] L. Ren, Q. Zhang, J. Yao, Z. Sun, R. Kaneko, Z. Yan, S. Nanot, Z. Jin, I. Kawayama, M. Tonouchi, *et al.*, "Terahertz and infrared spectroscopy of gated large-area graphene," *Nano letters*, vol. 12, no. 7, pp. 3711–3715, 2012.
- [95] J. A. Wilson and A. Yoffe, "The transition metal dichalcogenides discussion and interpretation of the observed optical, electrical and structural properties," *Advances in Physics*, vol. 18, no. 73, pp. 193–335, 1969.
- [96] A. Beal, J. Knights, and W. Liang, "Transmission spectra of some transition metal dichalcogenides. ii. group via: trigonal prismatic coordination," *Journal of Physics C: Solid State Physics*, vol. 5, no. 24, p. 3540, 1972.
- [97] L. F. Mattheiss, "Band structures of transition-metal-dichalcogenide layer compounds," *Physical Review B*, vol. 8, no. 8, p. 3719, 1973.
- [98] V. Grasso, "Electronic structure and electronic transitions in layered materials," 2012.

- [99] W. Kautek, “Electronic mobility anisotropy of layered semiconductors: transversal photoconductivity measurements at n-mos<sub>2</sub>,” *Journal of Physics C: Solid State Physics*, vol. 15, no. 16, p. L519, 1982.
- [100] Q. H. Wang, K. Kalantar-Zadeh, A. Kis, J. N. Coleman, and M. S. Strano, “Electronics and optoelectronics of two-dimensional transition metal dichalcogenides,” *Nature nanotechnology*, vol. 7, no. 11, pp. 699–712, 2012.
- [101] X. Duan, C. Wang, A. Pan, R. Yu, and X. Duan, “Two-dimensional transition metal dichalcogenides as atomically thin semiconductors: opportunities and challenges,” *Chemical Society Reviews*, vol. 44, no. 24, pp. 8859–8876, 2015.
- [102] K. F. Mak, C. Lee, J. Hone, J. Shan, and T. F. Heinz, “Atomically thin mos<sub>2</sub>: a new direct-gap semiconductor,” *Physical review letters*, vol. 105, no. 13, p. 136805, 2010.
- [103] A. Splendiani, L. Sun, Y. Zhang, T. Li, J. Kim, C.-Y. Chim, G. Galli, and F. Wang, “Emerging photoluminescence in monolayer mos<sub>2</sub>,” *Nano letters*, vol. 10, no. 4, pp. 1271–1275, 2010.
- [104] H. Schmidt, F. Giustiniano, and G. Eda, “Electronic transport properties of transition metal dichalcogenide field-effect devices: surface and interface effects,” *Chemical Society Reviews*, vol. 44, no. 21, pp. 7715–7736, 2015.
- [105] V. Podzorov, M. Gershenson, C. Kloc, R. Zeis, and E. Bucher, “High-mobility field-effect transistors based on transition metal dichalcogenides,” *Applied Physics Letters*, vol. 84, no. 17, pp. 3301–3303, 2004.
- [106] B. Radisavljevic, A. Radenovic, J. Brivio, V. Giacometti, and A. Kis, “Single-layer mos<sub>2</sub> transistors,” *Nature nanotechnology*, vol. 6, no. 3, pp. 147–150, 2011.
- [107] U. Wurstbauer, B. Miller, E. Parzinger, and A. W. Holleitner, “Light–matter interaction in transition metal dichalcogenides and their heterostructures,” *Journal of Physics D: Applied Physics*, vol. 50, no. 17, p. 173001, 2017.
- [108] K. F. Mak and J. Shan, “Photonics and optoelectronics of 2d semiconductor transition metal dichalcogenides,” *Nature Photonics*, vol. 10, no. 4, pp. 216–226, 2016.
- [109] D. Xiao, G.-B. Liu, W. Feng, X. Xu, and W. Yao, “Coupled spin and valley physics in monolayers of mos<sub>2</sub> and other group-vi dichalcogenides,” *Physical review letters*, vol. 108, no. 19, p. 196802, 2012.
- [110] G.-B. Liu, D. Xiao, Y. Yao, X. Xu, and W. Yao, “Electronic structures and theoretical modelling of two-dimensional group-vib transition metal dichalcogenides,” *Chemical Society Reviews*, vol. 44, no. 9, pp. 2643–2663, 2015.
- [111] S. Lebegue and O. Eriksson, “Electronic structure of two-dimensional crystals from ab initio theory,” *Physical Review B*, vol. 79, no. 11, p. 115409, 2009.
- [112] A. Kuc, N. Zibouche, and T. Heine, “Influence of quantum confinement on the electronic structure of the transition metal sulfide t s<sub>2</sub>,” *Physical review B*, vol. 83, no. 24, p. 245213, 2011.

- [113] W. Zhao, Z. Ghorannevis, L. Chu, M. Toh, C. Kloc, P.-H. Tan, and G. Eda, “Evolution of electronic structure in atomically thin sheets of  $\text{ws}_2$  and  $\text{wse}_2$ ,” *ACS nano*, vol. 7, no. 1, pp. 791–797, 2013.
- [114] W. Zhao, R. M. Ribeiro, M. Toh, A. Carvalho, C. Kloc, A. Castro Neto, and G. Eda, “Origin of indirect optical transitions in few-layer  $\text{mos}_2$ ,  $\text{ws}_2$ , and  $\text{wse}_2$ ,” *Nano letters*, vol. 13, no. 11, pp. 5627–5634, 2013.
- [115] D. Xiao, W. Yao, and Q. Niu, “Valley-contrasting physics in graphene: magnetic moment and topological transport,” *Physical review letters*, vol. 99, no. 23, p. 236809, 2007.
- [116] A. Chernikov, T. C. Berkelbach, H. M. Hill, A. Rigosi, Y. Li, B. Aslan, D. R. Reichman, M. S. Hybertsen, and T. F. Heinz, “Exciton binding energy and nonhydrogenic rydberg series in monolayer  $\text{ws}_2$ ,” *Physical review letters*, vol. 113, no. 7, p. 076802, 2014.
- [117] Z. Ye, T. Cao, K. O’Brien, H. Zhu, X. Yin, Y. Wang, S. G. Louie, and X. Zhang, “Probing excitonic dark states in single-layer tungsten disulphide,” *Nature*, vol. 513, no. 7517, pp. 214–218, 2014.
- [118] M. M. Ugeda, A. J. Bradley, S.-F. Shi, F. H. Da Jornada, Y. Zhang, D. Y. Qiu, W. Ruan, S.-K. Mo, Z. Hussain, Z.-X. Shen, *et al.*, “Giant bandgap renormalization and excitonic effects in a monolayer transition metal dichalcogenide semiconductor,” *Nature materials*, vol. 13, no. 12, pp. 1091–1095, 2014.
- [119] A. V. Stier, N. P. Wilson, G. Clark, X. Xu, and S. A. Crooker, “Probing the influence of dielectric environment on excitons in monolayer  $\text{wse}_2$ : insight from high magnetic fields,” *Nano letters*, vol. 16, no. 11, pp. 7054–7060, 2016.
- [120] K. He, N. Kumar, L. Zhao, Z. Wang, K. F. Mak, H. Zhao, and J. Shan, “Tightly bound excitons in monolayer  $\text{wse}_2$ ,” *Physical review letters*, vol. 113, no. 2, p. 026803, 2014.
- [121] E. Rosencher and B. Vinter, *Optoelectronics*. Cambridge University Press, 2002.
- [122] S. Latini, T. Olsen, and K. S. Thygesen, “Excitons in van der waals heterostructures: The important role of dielectric screening,” *Physical Review B*, vol. 92, no. 24, p. 245123, 2015.
- [123] A. Raja, A. Chaves, J. Yu, G. Arefe, H. M. Hill, A. F. Rigosi, T. C. Berkelbach, P. Nagler, C. Schüller, T. Korn, *et al.*, “Coulomb engineering of the bandgap and excitons in two-dimensional materials,” *Nature communications*, vol. 8, no. 1, p. 15251, 2017.
- [124] T. Low, A. Chaves, J. D. Caldwell, A. Kumar, N. X. Fang, P. Avouris, T. F. Heinz, F. Guinea, L. Martin-Moreno, and F. Koppens, “Polaritons in layered two-dimensional materials,” *Nature materials*, vol. 16, no. 2, pp. 182–194, 2017.
- [125] S. Koch, M. Kira, G. Khitrova, and H. Gibbs, “Semiconductor excitons in new light,” *Nature materials*, vol. 5, no. 7, pp. 523–531, 2006.

- [126] A. Ramasubramaniam, “Large excitonic effects in monolayers of molybdenum and tungsten dichalcogenides,” *Physical Review B*, vol. 86, no. 11, p. 115409, 2012.
- [127] D. Y. Qiu, F. H. Da Jornada, and S. G. Louie, “Optical spectrum of mos 2: many-body effects and diversity of exciton states,” *Physical review letters*, vol. 111, no. 21, p. 216805, 2013.
- [128] H.-P. Komsa and A. V. Krasheninnikov, “Effects of confinement and environment on the electronic structure and exciton binding energy of mos 2 from first principles,” *Physical Review B*, vol. 86, no. 24, p. 241201, 2012.
- [129] T. C. Berkelbach, M. S. Hybertsen, and D. R. Reichman, “Theory of neutral and charged excitons in monolayer transition metal dichalcogenides,” *Physical Review B*, vol. 88, no. 4, p. 045318, 2013.
- [130] K. S. Thygesen, “Calculating excitons, plasmons, and quasiparticles in 2d materials and van der waals heterostructures,” *2D Materials*, vol. 4, no. 2, p. 022004, 2017.
- [131] K. F. Mak, K. He, C. Lee, G. H. Lee, J. Hone, T. F. Heinz, and J. Shan, “Tightly bound trions in monolayer mos<sub>2</sub>,” *Nature materials*, vol. 12, no. 3, pp. 207–211, 2013.
- [132] Y. Li, A. Chernikov, X. Zhang, A. Rigosi, H. M. Hill, A. M. Van Der Zande, D. A. Chenet, E.-M. Shih, J. Hone, and T. F. Heinz, “Measurement of the optical dielectric function of monolayer transition-metal dichalcogenides: Mos 2, mo s e 2, ws 2, and ws e 2,” *Physical Review B*, vol. 90, no. 20, p. 205422, 2014.
- [133] C. Hsu, R. Frisenda, R. Schmidt, A. Arora, S. M. De Vasconcellos, R. Bratschitsch, H. S. van der Zant, and A. Castellanos-Gomez, “Thickness-dependent refractive index of 1l, 2l, and 3l mos<sub>2</sub>, mose<sub>2</sub>, ws<sub>2</sub>, and wse<sub>2</sub>,” *Advanced optical materials*, vol. 7, no. 13, p. 1900239, 2019.
- [134] J. S. Ross, S. Wu, H. Yu, N. J. Ghimire, A. M. Jones, G. Aivazian, J. Yan, D. G. Mandrus, D. Xiao, W. Yao, *et al.*, “Electrical control of neutral and charged excitons in a monolayer semiconductor,” *Nature communications*, vol. 4, no. 1, p. 1474, 2013.
- [135] M. Amani, D.-H. Lien, D. Kiriya, J. Xiao, A. Azcatl, J. Noh, S. R. Madhvapathy, R. Addou, S. Kc, M. Dubey, *et al.*, “Near-unity photoluminescence quantum yield in mos<sub>2</sub>,” *Science*, vol. 350, no. 6264, pp. 1065–1068, 2015.
- [136] G. Giovannetti, P. A. Khomyakov, G. Brocks, P. J. Kelly, and J. Van Den Brink, “Substrate-induced band gap in graphene on hexagonal boron nitride: Ab initio density functional calculations,” *Physical Review B*, vol. 76, no. 7, p. 073103, 2007.
- [137] N. Kharche and S. K. Nayak, “Quasiparticle band gap engineering of graphene and graphone on hexagonal boron nitride substrate,” *Nano letters*, vol. 11, no. 12, pp. 5274–5278, 2011.
- [138] G. Cassabois, P. Valvin, and B. Gil, “Hexagonal boron nitride is an indirect bandgap semiconductor,” *Nature photonics*, vol. 10, no. 4, pp. 262–266, 2016.

- [139] C. R. Dean, A. F. Young, I. Meric, C. Lee, L. Wang, S. Sorgenfrei, K. Watanabe, T. Taniguchi, P. Kim, K. L. Shepard, *et al.*, “Boron nitride substrates for high-quality graphene electronics,” *Nature nanotechnology*, vol. 5, no. 10, pp. 722–726, 2010.
- [140] L. Britnell, R. V. Gorbachev, R. Jalil, B. D. Belle, F. Schedin, M. I. Katsnelson, L. Eaves, S. V. Morozov, A. S. Mayorov, N. M. Peres, *et al.*, “Electron tunneling through ultrathin boron nitride crystalline barriers,” *Nano letters*, vol. 12, no. 3, pp. 1707–1710, 2012.
- [141] Y.-C. Lin, R. K. Ghosh, R. Addou, N. Lu, S. M. Eichfeld, H. Zhu, M.-Y. Li, X. Peng, M. J. Kim, L.-J. Li, *et al.*, “Atomically thin resonant tunnel diodes built from synthetic van der waals heterostructures,” *Nature communications*, vol. 6, no. 1, p. 7311, 2015.
- [142] G. Bhimanapati, N. Glavin, and J. A. Robinson, “2d boron nitride: synthesis and applications,” in *Semiconductors and semimetals*, vol. 95, pp. 101–147, Elsevier, 2016.
- [143] M. J. Molaei, M. Younas, and M. Rezakazemi, “A comprehensive review on recent advances in two-dimensional (2d) hexagonal boron nitride,” *ACS Applied Electronic Materials*, vol. 3, no. 12, pp. 5165–5187, 2021.
- [144] N. Alem, R. Erni, C. Kisielowski, M. D. Rossell, W. Gannett, and A. Zettl, “Atomically thin hexagonal boron nitride probed by ultrahigh-resolution transmission electron microscopy,” *Physical review B*, vol. 80, no. 15, p. 155425, 2009.
- [145] T. T. Tran, K. Bray, M. J. Ford, M. Toth, and I. Aharonovich, “Quantum emission from hexagonal boron nitride monolayers,” *Nature nanotechnology*, vol. 11, no. 1, pp. 37–41, 2016.
- [146] S. Dai, Z. Fei, Q. Ma, A. Rodin, M. Wagner, A. McLeod, M. Liu, W. Gannett, W. Regan, K. Watanabe, *et al.*, “Tunable phonon polaritons in atomically thin van der waals crystals of boron nitride,” *Science*, vol. 343, no. 6175, pp. 1125–1129, 2014.
- [147] A. Woessner, R. Parret, D. Davydovskaya, Y. Gao, J.-S. Wu, M. B. Lundeberg, S. Nanot, P. Alonso-González, K. Watanabe, T. Taniguchi, *et al.*, “Electrical detection of hyperbolic phonon-polaritons in heterostructures of graphene and boron nitride,” *npj 2D Materials and Applications*, vol. 1, no. 1, p. 25, 2017.
- [148] C. Cortes, W. Newman, S. Molesky, and Z. Jacob, “Quantum nanophotonics using hyperbolic metamaterials,” *Journal of Optics*, vol. 14, no. 6, p. 063001, 2012.
- [149] X. Yang, J. Yao, J. Rho, X. Yin, and X. Zhang, “Experimental realization of three-dimensional indefinite cavities at the nanoscale with anomalous scaling laws,” *Nature Photonics*, vol. 6, no. 7, pp. 450–454, 2012.
- [150] J. D. Caldwell, I. Aharonovich, G. Cassabois, J. H. Edgar, B. Gil, and D. Basov, “Photonics with hexagonal boron nitride,” *Nature Reviews Materials*, vol. 4, no. 8, pp. 552–567, 2019.
- [151] A. K. Geim and I. V. Grigorieva, “Van der waals heterostructures,” *Nature*, vol. 499, no. 7459, pp. 419–425, 2013.

- [152] N. F. Mott, “Note on the contact between a metal and an insulator or semiconductor,” in *Mathematical Proceedings of the Cambridge Philosophical Society*, vol. 34, pp. 568–572, Cambridge University Press, 1938.
- [153] R. Anderson, “Germanium-gallium arsenide heterojunctions,” *IBM Journal of Research and Development*, vol. 4, no. 3, pp. 283–287, 1960.
- [154] C. Zhang, C.-P. Chuu, X. Ren, M.-Y. Li, L.-J. Li, C. Jin, M.-Y. Chou, and C.-K. Shih, “Interlayer couplings, moiré patterns, and 2d electronic superlattices in mos<sub>2</sub>/wse<sub>2</sub> hetero-bilayers,” *Science advances*, vol. 3, no. 1, p. e1601459, 2017.
- [155] N. R. Wilson, P. V. Nguyen, K. Seyler, P. Rivera, A. J. Marsden, Z. P. Laker, G. C. Constantinescu, V. Kandyba, A. Barinov, N. D. Hine, *et al.*, “Determination of band offsets, hybridization, and exciton binding in 2d semiconductor heterostructures,” *Science advances*, vol. 3, no. 2, p. e1601832, 2017.
- [156] H. M. Hill, A. F. Rigosi, K. T. Rim, G. W. Flynn, and T. F. Heinz, “Band alignment in mos<sub>2</sub>/ws<sub>2</sub> transition metal dichalcogenide heterostructures probed by scanning tunneling microscopy and spectroscopy,” *Nano letters*, vol. 16, no. 8, pp. 4831–4837, 2016.
- [157] J. Kang, S. Tongay, J. Zhou, J. Li, and J. Wu, “Band offsets and heterostructures of two-dimensional semiconductors,” *Applied Physics Letters*, vol. 102, no. 1, 2013.
- [158] N. B. Le, T. D. Huan, and L. M. Woods, “Interlayer interactions in van der waals heterostructures: electron and phonon properties,” *ACS applied materials & interfaces*, vol. 8, no. 9, pp. 6286–6292, 2016.
- [159] K. Andersen, S. Latini, and K. S. Thygesen, “Dielectric genome of van der waals heterostructures,” *Nano letters*, vol. 15, no. 7, pp. 4616–4621, 2015.
- [160] H. Coy Diaz, J. Avila, C. Chen, R. Addou, M. C. Asensio, and M. Batzill, “Direct observation of interlayer hybridization and dirac relativistic carriers in graphene/mos<sub>2</sub> van der waals heterostructures,” *Nano letters*, vol. 15, no. 2, pp. 1135–1140, 2015.
- [161] M. Yankowitz, J. Xue, D. Cormode, J. D. Sanchez-Yamagishi, K. Watanabe, T. Taniguchi, P. Jarillo-Herrero, P. Jacquod, and B. J. LeRoy, “Emergence of superlattice dirac points in graphene on hexagonal boron nitride,” *Nature physics*, vol. 8, no. 5, pp. 382–386, 2012.
- [162] O. A. Ajayi, J. V. Ardelean, G. D. Shepard, J. Wang, A. Antony, T. Taniguchi, K. Watanabe, T. F. Heinz, S. Strauf, X. Zhu, *et al.*, “Approaching the intrinsic photoluminescence linewidth in transition metal dichalcogenide monolayers,” *2D Materials*, vol. 4, no. 3, p. 031011, 2017.
- [163] A. F. Rigosi, H. M. Hill, Y. Li, A. Chernikov, and T. F. Heinz, “Probing interlayer interactions in transition metal dichalcogenide heterostructures by optical spectroscopy: Mos<sub>2</sub>/ws<sub>2</sub> and mose<sub>2</sub>/wse<sub>2</sub>,” *Nano letters*, vol. 15, no. 8, pp. 5033–5038, 2015.
- [164] G. Froehlicher, E. Lorchat, and S. Berciaud, “Charge versus energy transfer in atomically thin graphene-transition metal dichalcogenide van der waals heterostructures,” *Physical Review X*, vol. 8, no. 1, p. 011007, 2018.

- [165] J. He, N. Kumar, M. Z. Bellus, H.-Y. Chiu, D. He, Y. Wang, and H. Zhao, “Electron transfer and coupling in graphene–tungsten disulfide van der waals heterostructures,” *Nature communications*, vol. 5, no. 1, p. 5622, 2014.
- [166] C. Manolatou, H. Wang, W. Chan, S. Tiwari, and F. Rana, “Radiative and nonradiative exciton energy transfer in monolayers of two-dimensional group-vi transition metal dichalcogenides,” *Physical Review B*, vol. 93, no. 15, p. 155422, 2016.
- [167] L. Gaudreau, K.-J. Tielrooij, G. Prawiroatmodjo, J. Osmond, F. G. De Abajo, and F. Koppens, “Universal distance-scaling of nonradiative energy transfer to graphene,” *Nano letters*, vol. 13, no. 5, pp. 2030–2035, 2013.
- [168] D. Kozawa, A. Carvalho, I. Verzhbitskiy, F. Giustiniano, Y. Miyauchi, S. Mouri, A. Castro Neto, K. Matsuda, and G. Eda, “Evidence for fast interlayer energy transfer in mose2/ws2 heterostructures,” *Nano letters*, vol. 16, no. 7, pp. 4087–4093, 2016.
- [169] Y. Zhu, X. Sun, Y. Tang, L. Fu, and Y. Lu, “Two-dimensional materials for light emitting applications: Achievement, challenge and future perspectives,” *Nano Research*, vol. 14, pp. 1912–1936, 2021.
- [170] Y. Liu, N. O. Weiss, X. Duan, H.-C. Cheng, Y. Huang, and X. Duan, “Van der waals heterostructures and devices,” *Nature Reviews Materials*, vol. 1, no. 9, pp. 1–17, 2016.
- [171] K. Novoselov, A. Mishchenko, A. Carvalho, and A. Castro Neto, “2d materials and van der waals heterostructures,” *Science*, vol. 353, no. 6298, p. aac9439, 2016.
- [172] W. Xia, L. Dai, P. Yu, X. Tong, W. Song, G. Zhang, and Z. Wang, “Recent progress in van der waals heterojunctions,” *Nanoscale*, vol. 9, no. 13, pp. 4324–4365, 2017.
- [173] D. Jariwala, T. J. Marks, and M. C. Hersam, “Mixed-dimensional van der waals heterostructures,” *Nature materials*, vol. 16, no. 2, pp. 170–181, 2017.
- [174] O. Lopez-Sanchez, D. Lembke, M. Kayci, A. Radenovic, and A. Kis, “Ultrasensitive photodetectors based on monolayer mos2,” *Nature nanotechnology*, vol. 8, no. 7, pp. 497–501, 2013.
- [175] L. Britnell, R. M. Ribeiro, A. Eckmann, R. Jalil, B. D. Belle, A. Mishchenko, Y.-J. Kim, R. V. Gorbachev, T. Georgiou, S. V. Morozov, *et al.*, “Strong light-matter interactions in heterostructures of atomically thin films,” *Science*, vol. 340, no. 6138, pp. 1311–1314, 2013.
- [176] A. Pospischil, M. M. Furchi, and T. Mueller, “Solar-energy conversion and light emission in an atomic monolayer p–n diode,” *Nature nanotechnology*, vol. 9, no. 4, pp. 257–261, 2014.
- [177] C.-H. Lee, G.-H. Lee, A. M. Van Der Zande, W. Chen, Y. Li, M. Han, X. Cui, G. Arefe, C. Nuckolls, T. F. Heinz, *et al.*, “Atomically thin p–n junctions with van der waals heterointerfaces,” *Nature nanotechnology*, vol. 9, no. 9, pp. 676–681, 2014.

- [178] K. F. Mak, K. L. McGill, J. Park, and P. L. McEuen, “The valley hall effect in mos2 transistors,” *Science*, vol. 344, no. 6191, pp. 1489–1492, 2014.
- [179] H. S. Lee, S.-W. Min, Y.-G. Chang, M. K. Park, T. Nam, H. Kim, J. H. Kim, S. Ryu, and S. Im, “Mos2 nanosheet phototransistors with thickness-modulated optical energy gap,” *Nano letters*, vol. 12, no. 7, pp. 3695–3700, 2012.
- [180] D.-S. Tsai, K.-K. Liu, D.-H. Lien, M.-L. Tsai, C.-F. Kang, C.-A. Lin, L.-J. Li, and J.-H. He, “Few-layer mos2 with high broadband photogain and fast optical switching for use in harsh environments,” *Acs Nano*, vol. 7, no. 5, pp. 3905–3911, 2013.
- [181] J. S. Ross, P. Klement, A. M. Jones, N. J. Ghimire, J. Yan, D. Mandrus, T. Taniguchi, K. Watanabe, K. Kitamura, W. Yao, *et al.*, “Electrically tunable excitonic light-emitting diodes based on monolayer wse2 p–n junctions,” *Nature nanotechnology*, vol. 9, no. 4, pp. 268–272, 2014.
- [182] R. Cheng, D. Li, H. Zhou, C. Wang, A. Yin, S. Jiang, Y. Liu, Y. Chen, Y. Huang, and X. Duan, “Electroluminescence and photocurrent generation from atomically sharp wse2/mos2 heterojunction p–n diodes,” *Nano letters*, vol. 14, no. 10, pp. 5590–5597, 2014.
- [183] M. Fontana, T. Deppe, A. K. Boyd, M. Rinzan, A. Y. Liu, M. Paranjape, and P. Barbara, “Electron-hole transport and photovoltaic effect in gated mos2 schottky junctions,” *Scientific reports*, vol. 3, no. 1, p. 1634, 2013.
- [184] B. W. Baugher, H. O. Churchill, Y. Yang, and P. Jarillo-Herrero, “Optoelectronic devices based on electrically tunable p–n diodes in a monolayer dichalcogenide,” *Nature nanotechnology*, vol. 9, no. 4, pp. 262–267, 2014.
- [185] R. Sundaram, M. Engel, A. Lombardo, R. Krupke, A. Ferrari, P. Avouris, and M. Steiner, “Electroluminescence in single layer mos2,” *Nano letters*, vol. 13, no. 4, pp. 1416–1421, 2013.
- [186] S. Jo, N. Ubrig, H. Berger, A. B. Kuzmenko, and A. F. Morpurgo, “Mono-and bilayer ws2 light-emitting transistors,” *Nano letters*, vol. 14, no. 4, pp. 2019–2025, 2014.
- [187] Y. Zhang, T. Oka, R. Suzuki, J. Ye, and Y. Iwasa, “Electrically switchable chiral light-emitting transistor,” *Science*, vol. 344, no. 6185, pp. 725–728, 2014.
- [188] F. Withers, O. Del Pozo-Zamudio, A. Mishchenko, A. Rooney, A. Gholinia, K. Watanabe, T. Taniguchi, S. J. Haigh, A. Geim, A. Tartakovskii, *et al.*, “Light-emitting diodes by band-structure engineering in van der waals heterostructures,” *Nature materials*, vol. 14, no. 3, pp. 301–306, 2015.
- [189] G.-H. Lee, Y.-J. Yu, C. Lee, C. Dean, K. L. Shepard, P. Kim, and J. Hone, “Electron tunneling through atomically flat and ultrathin hexagonal boron nitride,” *Applied physics letters*, vol. 99, no. 24, 2011.
- [190] F. Withers, O. Del Pozo-Zamudio, S. Schwarz, S. Dufferwiel, P. Walker, T. Godde, A. Rooney, A. Gholinia, C. Woods, P. Blake, *et al.*, “Wse2 light-emitting tunneling transistors with enhanced brightness at room temperature,” *Nano letters*, vol. 15, no. 12, pp. 8223–8228, 2015.

- [191] C.-H. Liu, G. Clark, T. Fryett, S. Wu, J. Zheng, F. Hatami, X. Xu, and A. Majumdar, “Nanocavity integrated van der waals heterostructure light-emitting tunneling diode,” *Nano letters*, vol. 17, no. 1, pp. 200–205, 2017.
- [192] A. Politi, J. C. Matthews, and J. L. O’Brien, “Shor’s quantum factoring algorithm on a photonic chip,” *Science*, vol. 325, no. 5945, pp. 1221–1221, 2009.
- [193] M. Koperski, K. Nogajewski, A. Arora, V. Cherkez, P. Mallet, J.-Y. Veillen, J. Marcus, P. Kossacki, and M. Potemski, “Single photon emitters in exfoliated wse2 structures,” *Nature nanotechnology*, vol. 10, no. 6, pp. 503–506, 2015.
- [194] C. Palacios-Berraquero and C. Palacios-Berraquero, “Atomically-thin quantum light emitting diodes,” *Quantum confined excitons in 2-dimensional materials*, pp. 71–89, 2018.
- [195] Z. Yuan, B. E. Kardynal, R. M. Stevenson, A. J. Shields, C. J. Lobo, K. Cooper, N. S. Beattie, D. A. Ritchie, and M. Pepper, “Electrically driven single-photon source,” *science*, vol. 295, no. 5552, pp. 102–105, 2002.
- [196] G. Clark, J. R. Schaibley, J. Ross, T. Taniguchi, K. Watanabe, J. R. Hendrickson, S. Mou, W. Yao, and X. Xu, “Single defect light-emitting diode in a van der waals heterostructure,” *Nano letters*, vol. 16, no. 6, pp. 3944–3948, 2016.

# Chapter 3

## Plasmonics, Photonics and Dipole Emission

The main purpose of this chapter is to present the fundamental concepts governing the interaction between electromagnetic fields and matter, constituting classical electrodynamics of solids (or continuous media) [1–4]. A comprehensive exploration of plasmonic response of metals, photonic material properties, along with the description of dipole emission is detailed. The concepts developed in the following chapter are the basis to analyze optoelectronic devices based on graphene and other 2D materials (such as TMDs), described in Chapter 2.

### 3.1 Plasmonic response of metals

Plasmon polaritons in noble metals are characterized as hybrid electromagnetic waves that emerge from the interaction between free-space photons and dipoles induced by electron oscillations in metals. These hybrid states can manifest as either propagating waves along a metal/dielectric interface or as localized phenomena within finite metal structures. The former is referred to as surface plasmon polaritons (SPPs), while the latter is commonly known as localized surface plasmon polaritons (LSPPs).

#### 3.1.1 Drude Model for metals

To elucidate plasmonics, it is effective to provide a brief derivation of the AC (i.e., frequency-dependent) Drude response model for conductors. In the Drude model [5], metals are treated as a free-electron gas that permeates a background composed of immobile ions constituting the crystal's lattice. Within this framework, the microscopic dynamics of the conduction electrons, when subjected to an external electric field,  $E(t)$ , is classically governed by Newton's second law. This is expressed through the equation of motion [6–9].

$$\frac{d}{dt}p(t) = -eE(t) - \frac{1}{\tau}p(t) \quad (3.1)$$

where  $p$  represents the average momentum of electron and  $\tau$  denotes the momentum relaxation time (i.e., the average time between instantaneous collisions of electrons with phonons, lattice defects, etc.). Consequently, we can identify the scattering rate  $\gamma = \tau^{-1}$ . For a time-dependent field  $E(t) = E^0 e^{-i\omega t}$  and assuming that the momentum follows the same time-dependence with  $E(t)$ , the preceding equation results in:

$$p(t) = \frac{e}{i\omega - \gamma} E(t) \quad (3.2)$$

Given that the current induced by the external field can also be expressed as  $J = -en_e v$ , where  $n_e$  represents the electron density and  $v = p/m$  denotes the average velocity, utilizing Equation 3.2 leads to the following result:

$$J = \frac{e^2 n_e}{m} \frac{1}{\gamma - i\omega} E \quad (3.3)$$

From Equation 3.3 and  $J = \sigma(\omega)E$ , we can easily define the frequency-dependent optical conductivity of the the uniform electron gas [6, 9] as

$$\sigma(\omega) = \frac{e^2 n_e}{m} \frac{1}{\gamma - i\omega} \quad (3.4)$$

Furthermore, the equivalent Drude dielectric function is expressed as [6, 9].

$$\epsilon(\omega) = \epsilon_\infty(\omega) - \frac{\omega_p^2}{\omega^2 + i\gamma\omega} \quad (3.5)$$

where  $\omega_p^2 = e^2 n_e / (\mu\epsilon_0)$  is referred to as the plasma frequency of the electron gas. In the so-called jellium approximation, the contribution of the homogeneous ionic background simply equals  $\epsilon_\infty=1$ . In "real metal" cases the frequency dependence of  $\epsilon_\infty(\omega)$  is retained to incorporate although ad hoc, interband transitions, and background screening originating from lower-lying orbitals (e.g., the d-band of noble metals). A common phenomenological approach to address these effects involves adding a series of Lorentz oscillators [6] to the free-carrier contribution, as described in section 3.3. This adjustment is made in such a way that the resulting dielectric function aligns with the experimental data within a specified frequency range.

Despite its simplicity, the Drude model is quite effective in explaining the key characteristics of metals, especially simple alkali metals, in the infrared and visible regions of the electromagnetic spectrum. This holds true as long as the frequencies of interest remain below the onset of interband transitions. Such effectiveness should not be surprising since this model considers only a single band. Following Drude's groundbreaking work in 1900 [5], Sommerfeld further advanced the model by incorporating Fermi–Dirac statistics and introducing concepts from band theory within a semi-classical description of the electron gas [10].

### 3.1.2 Surface Plasmon Polaritons at Planar Interfaces

In this subsection, we summarize the key characteristics of propagating surface plasmon polaritons maintained at planar dielectric–metal interfaces. Deriving the necessary fundamental knowledge from classical electrodynamics [1–4, 11], combined with that described in subsection 3.1.1, we can introduce the elementary concepts of classical plasmonics.

The plasmonic excitations in a given system can be entirely characterized by applying Maxwell's equations (with the relevant boundary conditions) alongside the specification of the materials' local response. We will derive the dispersion relation of surface plasmon polaritons (SPPs) propagating along flat dielectric–metal interfaces and explore their essential characteristics. Here, for simplicity, we examine a single dielectric–metal interface. We consider a planar interface situated between two distinct media, described by

the boundary separating a dielectric half-space ( $z > 0$ ) and a metal half-space ( $z < 0$ ), as illustrated in schematics of Figure 3.1. The dielectric medium is defined by the dielectric constant  $\epsilon_d$ , which may exhibit frequency dependence, while the electromagnetic properties of the metal are described by its frequency-dependent dielectric function  $\epsilon_m(\omega)$ . We assume that the system is uniform in the  $y$ -direction.

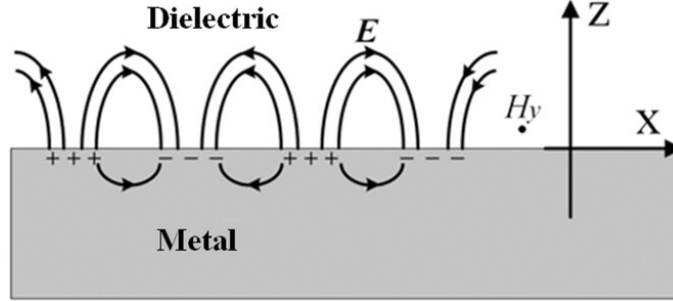


Figure 3.1: Schematic of a planar dielectric-metal interface, defined by  $z=0$  plane. The fields decay exponentially away from the interface.

We explore p-polarized (or transverse-magnetic (TM)) solutions, that resemble surface electromagnetic waves propagating (e.g. along the  $x$ -direction) and showcasing exponential decay along the vertical  $z$ -direction. Specifically, these solutions (whose time-dependence is harmonic and has the form  $e^{-i\omega t}$ ) can be expressed, in the dielectric medium, as

$$E_d(r) = (E_{x,d}\hat{x} + E_{z,d}\hat{z})e^{iqx}e^{-\kappa_d z}, H_d(r) = H_{y,d}e^{iqx}e^{-\kappa_d z}\hat{y} \quad (3.6)$$

and, in the metal half-space, as

$$E_m(r) = (E_{x,m}\hat{x} + E_{z,m}\hat{z})e^{iqx}e^{\kappa_m z}, H_m(r) = H_{y,m}e^{iqx}e^{\kappa_m z}\hat{y} \quad (3.7)$$

where  $q$  denotes the SPP's wavevector (or propagation constant) and  $\kappa_{d,m}$  defines the decay of the fields along the perpendicular direction. The relations between the components of the fields within each medium can be established by incorporating Eqs. 3.6 and 3.7 into Maxwell's equations. This process results in:

$$H_{y,j} = -\frac{\omega}{q}\epsilon_0\epsilon_j E_{z,j}, H_{y,j} = -s_j i \frac{\omega}{\kappa_j}\epsilon_0\epsilon_j E_{x,j}, E_{z,j} = s_j i \frac{q}{\kappa_j} E_{x,j} \quad (3.8)$$

For  $j \in [d, m]$ , we define the auxiliary variable  $s_j = \delta_{jd} - \delta_{jm}$  using delta Kronecker. Furthermore, we derive

$$\kappa_j^2 = q^2 - (\omega/c)^2\epsilon_j \quad (3.9)$$

where  $\epsilon_0$  represents the permittivity of vacuum, and  $c = 1/\sqrt{\epsilon_0\mu_0}$  is the speed of light in free space, with  $\mu_0$  indicating vacuum permeability. Now, the only necessity is to equate the fields on both sides of the interface in alignment with the boundary condition equations  $\hat{n} \times (E_2 - E_1) = 0$  and  $\hat{n} \times (H_2 - H_1) = K$ . These equations express the continuity of the tangential components of the electromagnetic field across the interface and result in

$$E_{x,d} - E_{x,m} = 0, H_{y,d} - H_{y,m} = 0 \quad (3.10)$$

Utilizing the Eqs. 3.8 and 3.9, and incorporating them into the system of equations 3.10, we deduce the implicit condition for the dispersion relation of SPPs [6, 7]

$$\frac{\epsilon_d}{\kappa_d} + \frac{\epsilon_m}{\kappa_m} = 0 \quad (3.11)$$

Moreover, according to Equation 3.11, we can derive an essential condition for the presence of SPPs at the interface of two distinct media. To facilitate the existence of an electromagnetic wave exhibiting decay perpendicular to the interface, it is necessary that  $\text{Re}(\kappa_{d,m}) > 0$ . Consequently, the real parts of  $\epsilon_d$  and  $\epsilon_m$  must have opposite signs. For insulating materials, where  $\epsilon_d = \text{Re}(\epsilon_d) > 0$ , it follows that the medium in the opposing half-space must have  $\text{Re}(\epsilon_m) < 0$  [6, 7]. This condition aligns with the characteristics of most metals for frequencies in the visible/near-infrared and below. Alternatively, using Equation 3.9, we can present the SPP wavevector in a closed-form [6, 12, 13] as

$$q_{SPP} = \frac{\omega}{c} \sqrt{\frac{\epsilon_d \epsilon_m}{\epsilon_d + \epsilon_m}} \quad (3.12)$$

which provides a simple relation between SPP's wavevector and its frequency. According to Equation 3.12, the alteration in the dielectric environment  $\epsilon_d$  impacts the momentum  $q_{SPP}$  of SPPs. Figure 3.2 illustrates the dispersion relation of SPP mode sustained by a planar interface between a dielectric and a lossless Drude metal. We describe the lossless metal material ( $\gamma=0$ ) by the Drude model, i.e., with dielectric function given by Equation 3.5. We further assume that  $\epsilon_\infty=1$  and define the surface plasmon frequency as  $\omega_{SP} = \omega_P / \sqrt{\epsilon_\infty + \epsilon_d}$ .

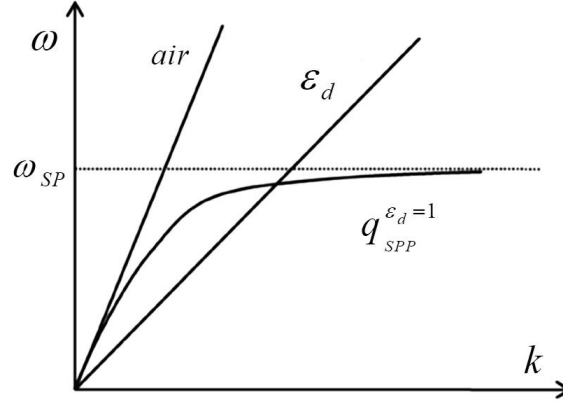


Figure 3.2: Dispersion relation of SPPs at dielectric–metal interfaces ( $\epsilon_d = 1$ ). The dashed horizontal line indicates the surface plasmon frequency and  $k_0 = \omega/c$  and  $k = (\omega/c)\sqrt{\epsilon_d}$  are the light lines inside air and dielectric  $\epsilon_d$ , respectively.

It is worth noting that, SPP dispersion curve for  $\epsilon_d = 1$ , shown in Figure 3.2, is positioned to the right of the light line, defined by  $k_0$ , implying that the electromagnetic field of SPPs is effectively confined near the interface. Moreover, we can determine the ratio between the wavelength of a photon in free space and that of a SPP, oscillating at the same frequency, as  $\lambda_0/\lambda_{SPP} = \sqrt{\epsilon_d \epsilon_m / (\epsilon_d + \epsilon_m)}$ . This reveals a particularly captivating characteristic of SPPs: given that  $\lambda_{SPP}/\lambda_0 < 1$ , these polaritons can confine the electromagnetic field below the diffraction limit [6, 11, 12, 14, 15]. In specific systems, this effect can be notably substantial, with  $\lambda_{SPP}/\lambda_0 \ll 1$  [6, 12, 16–18]. It becomes evident that this characteristic plays a pivotal role in manipulating electromagnetic fields at the

nanoscale and enhancing light–matter interactions, leading to promising applications in nanophotonics.

### 3.1.3 Localized Surface Plasmons in metallic nanoparticles

While the planar dielectric–metal interface serves as the simplest system supporting SPPs, other nanogeometries provide valuable insights. In this subsection we outline the optical response of metallic nanoparticles, such as nanospheres used on SERS of graphene in Chapter 5. Surface plasmons can also be excited in metallic nanostructures, where the electric field of incident light excites oscillations of the conduction electrons. Plasmonic resonances in finite-sized structures, such as nanospheres, are commonly referred to as Localized Surface Plasmons (LSPs) [7, 12].

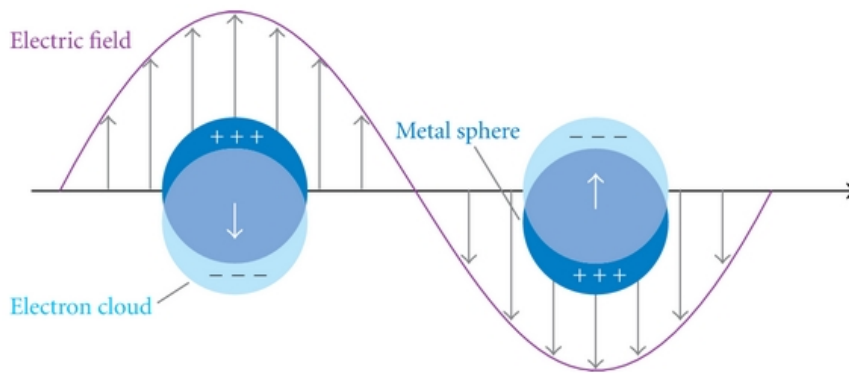


Figure 3.3: Schematic of localized surface plasmon resonance (LSPR), resulting from the collective oscillations of delocalized electrons in response to an external electric field [19].

In Figure 3.3 is illustrated the oscillation of charge due to the external field. In this case, the nanoparticle is assumed to be significantly smaller than the wavelength of the incident light. The electric field of the incoming light generates an electric dipole in the metal particle by displacing numerous delocalized electrons in one direction away from the rest of the metal particle, resulting in a net negative charge on one side and a net positive charge on the opposite side. While LSPs are well-known as dipole plasmons, it is noteworthy that the oscillating field of the incident light can induce quadrupole resonances as well, especially for particles exceeding 30 nm in diameter [20, 21].

Analyzing LSPs typically involves considering a sub-wavelength metallic sphere with a diameter  $d \ll \lambda$ , and employing the quasi-static approximation. This approximation assumes a uniform incident electric field across the entire metallic nanoparticle. We consider a uniform, isotropic sphere with a radius  $a$ , situated within a uniform, static electric field ( $\mathbf{E} = E_0 \hat{z}$ ) aligned along the  $z$ -axis (see Figure 3.4). The surrounding medium  $\epsilon_d$  is isotropic and has no absorption losses. The optical response of the nanosphere is further described by the complex dielectric function  $\epsilon_m(\omega)$ .

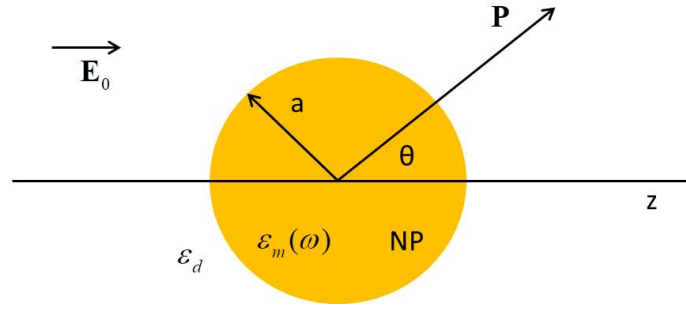


Figure 3.4: Schematic of a homogeneous, isotropic nanosphere placed into an electrostatic field [7].

By applying simple electrostatics, solving the Laplace equation for the potential  $\nabla^2\Phi = 0$ , we are able to derive the electric field  $\mathbf{E} = -\nabla\Phi$ . The general solution for the potential in azimuthal symmetry is [1]

$$\Phi(r, \theta) = \sum_{l=0}^{\infty} [A_l r^l + B_l r^{-(l+1)}] P_l(\cos\theta) \quad (3.13)$$

where  $P_l \cos(\theta)$  are the Legendre polynomials of order  $l$ , and  $\theta$  is the angle formed by the position vector  $\mathbf{r}$  at point  $\mathbf{P}$  and the  $z$ -axis (see Figure 3.4). To ensure the potential remains finite at the origin and by equating the tangential components of the electric field to the normal components of the displacement field, the expressions for the potentials inside and out of the sphere [1] can be expressed as

$$\Phi_{in} = -\frac{3\epsilon_m}{\epsilon + 2\epsilon_m} E_0 r \cos\theta, \quad \Phi_{out} = -E_0 r \cos\theta + \frac{\epsilon - \epsilon_m}{\epsilon + 2\epsilon_m} a^3 \frac{\cos\theta}{r^2} \quad (3.14)$$

It is interesting that  $\Phi_{out}$  describes the superposition of the applied external field and the field created by a dipole located in the center of nanosphere. To introduce the dipole moment  $\mathbf{p}$  we can write

$$\mathbf{p} = 4\pi\epsilon_0\epsilon_m a^3 \frac{\epsilon - \epsilon_m}{\epsilon + 2\epsilon_m} \mathbf{E}_0 \quad (3.15)$$

and re-write outside potential  $\Phi_{out}$  as

$$\Phi_{out} = -E_0 r \cos\theta + \frac{\mathbf{p} \cdot \mathbf{r}}{4\pi\epsilon_0\epsilon_m r^3} \quad (3.16)$$

Hence, we observe that the applied field generates a dipole moment within the sphere, the magnitude of which is directly proportional to  $|\mathbf{E}_0|$ . Defining that  $\mathbf{p} = \epsilon_0\epsilon_m\alpha\mathbf{E}_0$  we can write the polarizability  $\alpha$  as

$$\alpha = 4\pi a^3 \frac{\epsilon - \epsilon_m}{\epsilon + 2\epsilon_m} \quad (3.17)$$

The final expression 3.17 represents the key outcome of this section, which is the complex polarizability of a nanosphere, with a diameter smaller than the wavelength, within the electrostatic approximation.

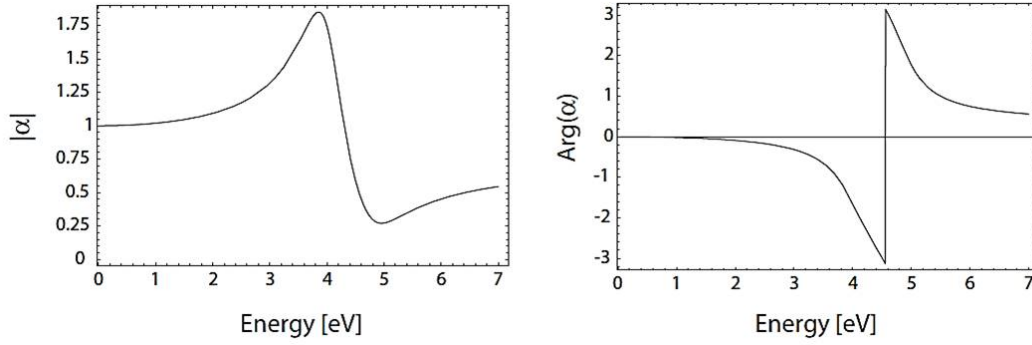


Figure 3.5: Absolute value and phase of the polarizability  $\alpha$  of a sub-wavelength silver nanoparticle with respect to the frequency of the driving field [7, 22].

Figure 3.5 shows the magnitude and phase of  $\alpha$ , for frequency  $\omega$  (in eV) and dielectric constant  $\epsilon(\omega)$ , following the Drude formula (in this case for silver [7, 22]). It is evident that the polarizability has a resonance when  $|\epsilon + 2\epsilon_m|$  is minimized, which, in case of small (or gradually changing)  $\text{Im}[\epsilon]$  around the resonance, can be simplified to

$$\text{Re}[\epsilon(\omega)] = -2\epsilon_m \quad (3.18)$$

This relation is known as the Fröhlich condition, and the corresponding mode (under an oscillating field) is termed the dipole surface plasmon of the metal nanoparticle. For a Drude metal sphere situated in air, the Fröhlich condition is satisfied at frequency  $\omega_0 = \omega_p/\sqrt{3}$ , further highlighting the strong dependence of resonance frequency on the dielectric environment. When  $\epsilon_m$  increases, this resonance experiences a red-shift. Therefore, metal nanoparticles serve as ideal platforms for optical sensing, when the refractive index of the surrounding medium changes.

Electric field distribution  $E = -\nabla\Phi$  can be derived by the Equations 3.14 as

$$\mathbf{E}_{in} = \frac{3\epsilon_m}{\epsilon + 2\epsilon_m}\mathbf{E}_0, \mathbf{E}_{out} = \mathbf{E}_0 + \frac{3\mathbf{n}(\mathbf{n}\cdot\mathbf{p} - \mathbf{p})}{4\pi\epsilon_0\epsilon_m} \frac{1}{r^3} \quad (3.19)$$

Where  $\mathbf{n}$  is the unit vector in the same direction as  $\mathbf{P}$  (in Figure 3.4). We observe that the resonance in  $\alpha$  also signifies a resonant enhancement of both the internal and dipolar fields. This field enhancement at the plasmon resonance forms the basis for many prominent applications of metal nanoparticles in optical devices and sensors. Optically, it is interesting to notice that another outcome of the resonantly enhanced polarization  $\alpha$  is a strong increase in the efficiency with which a metal nanoparticle scatters and absorbs light. The corresponding cross-sections for scattering and absorption, which can be calculated using the Poynting vector  $\mathbf{S}$  [1, 7, 22], are, respectively,

$$C_{sca} = \frac{k^4}{6\pi}|\alpha|^2 = \frac{8\pi}{3}k^4 a^6 \left| \frac{\epsilon - \epsilon_m}{\epsilon + 2\epsilon_m} \right| \quad (3.20)$$

and

$$C_{abs} = k\text{Im}[\alpha] = 4\pi k a^3 \text{Im}\left[ \frac{\epsilon - \epsilon_m}{\epsilon + 2\epsilon_m} \right] \quad (3.21)$$

Finally, for a sphere of volume  $V$  and dielectric function  $\epsilon = \epsilon_1 + i\epsilon_2$  in the quasi-static limit, the extinction cross-section  $C_{ext} = C_{sca} + C_{abs}$  can be written as

$$C_{ext} = 9 \frac{\omega}{c} \epsilon_m^{3/2} V \frac{\epsilon_2}{[\epsilon_1 + 2\epsilon_m]^2 + \epsilon_2^2} \quad (3.22)$$

There is a variety of different nanoparticles capable of supporting LSP resonances [12, 23]. Apart from the metal nanosphere, studied in this subsection, numerous investigations of LSPs have been made in plasmonic disks [24–26], triangles [27, 28], cubes [29–31], and nanorods [32], among others [33–35]. Furthermore, coupling these plasmonic particles could be exploited to form new coupled structures, broadening the library of plasmon resonances. This is achieved using plasmonic dimers [36–40], including bow-ties [41–44] (studied in Chapter 7) and oligomers [45–48], or multi-layered nanoparticles [49–51]. Alternatively, individual plasmonic particles can be periodically assembled into plasmonic lattices [52–56], capable of sustaining surface plasmon lattice resonances resulting from diffractively coupled LSP resonances.

## 3.2 Optical response of dielectrics

The classical theory for absorption and dispersion is attributed to Drude, described in subsection 3.1.1, and Lorentz [57] models. The Drude model is applicable to free electron metals, and its quantum analog involves intraband transitions, i.e. transitions of free electrons within the conduction band. In contrast, Lorentz model can be applied in case of insulators, and its quantum mechanical analog includes all direct interband transitions, i.e. transitions of bound electrons whose final states appear in a different band. Notably, we can observe that various characteristics of these classical models find quantum mechanical counterparts, which are easily understood as generalizations of their classical analogs. The arrangement of bound electrons within an atom typically forms orbitals around the positive nucleus. In the absence of an external electric field, this electron cloud exhibits a spherical symmetry centered around the nucleus. However, under an external electric field, the electron cloud shifts in the opposite direction of the field, appearing like a dipole. This induced dipole is oscillating, as a response to the external electric field. This forced oscillation of electrons bound to the nucleus, is a mechanical analog to a small mass bound to a larger mass by a spring. This is known as the Lorentz model and will be described in the following paragraphs.

### 3.2.1 Lorentz oscillator

In order to explain the Lorentz model, we assume a single atom consisted of one electron bound to the nucleus. We initially apply the classical Hooke's law for the clarification of the forced oscillation within the Lorentz model. Subsequently, by substituting the different forces into Newton's law, we derive the equation of motion, the polarization and the final dielectric function for dielectrics. The Lorentz oscillator model assumes a force ( $F_H$ ) applied to an orbital by the atomic nucleus, according to the Hooke's law  $F_H = -kr$ , where  $k$  represents the spring constant and  $r$  is the orbital displacement (see Figure 3.6).

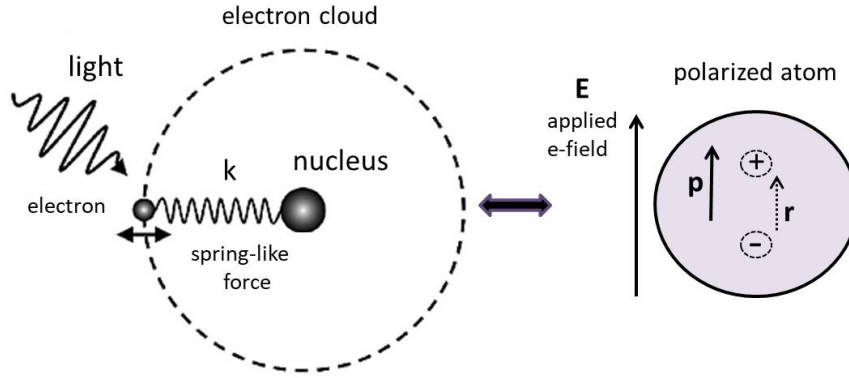


Figure 3.6: Schematics of a Lorentz oscillator, where electrons are bound to the atomic nucleus, analogously to springs of different strength.

Despite the fact that the forces between charges follow Coulomb's law  $F_C \sim 1/r^2$ , we adopt Hooke's law, due to its validity as an approximation for small perturbations around equilibrium (where the force equals to zero). Expressing this, in terms of potential energy  $V$ , if  $F = -\partial V/\partial r = -\partial V/\partial x$  at  $x = x_0$ , when  $x_0$  is the minimum energy, we get  $F = 0$ . The general form of potential energy can be written, as a Taylor expansion around  $x = x_0$ , as

$$V = V(x_0) + V'|_{x=x_0}(x - x_0) + \frac{1}{2!}V''|_{x=x_0}(x - x_0)^2 + \frac{1}{3!}V'''|_{x=x_0}(x - x_0)^3 \quad (3.23)$$

In case of  $x_0$  equals to 0, the force can be written as

$$F = -\frac{\partial V}{\partial x} = V''(x - x_0) \quad (3.24)$$

which seems like Hooke's law formula with  $V'' = k$ . As a result, the force has a linear relationship with the displacement. According to Hooke's law, the restoring force of oscillation is defined as  $F_H = -m\omega_0^2 r$ , where  $m$  is electron effective mass and  $\omega_0 = \sqrt{k/m}$  the eigenfrequency of the oscillator. Additionally, there is a friction force ( $F_F$ ), which, in the simplest approximation, is proportional to the velocity ( $v$ ) and is defined as  $F_F = -m\Gamma v = -m\Gamma(dr/dt)$ , where  $\Gamma$  is a friction constant in units of inverse time ( $sec^{-1}$ ), representing the energy loss rate from the oscillator. While radiation damping is the dominant energy loss mechanism in a free atom, various scattering mechanisms in a solid, like electron-phonon scattering, contribute to it. Finally, the external force ( $F_E$ ) from the applied electric field ( $E$ ) is defined as  $F_E = -eE$ . Substituting all these forces into Newton's law, we can express the equation of motion as

$$m\frac{d^2 r}{dt^2} + m\Gamma\frac{dr}{dt} + m\omega_0^2 r = -eE \quad (3.25)$$

In the classical description, Equation 3.25 involves two approximations. Firstly, the nucleus is assumed to have infinite mass, which stays stationary during the electron's motion. Secondly, we neglect the magnetic force ( $\mathbf{F}_M$ ) arising from the magnetic field ( $\mathbf{B}$ ) acting on the electron, defined as  $\mathbf{F}_M = -ev \times \mathbf{B}/c$ . The magnetic force can be negligible, due to the small collective electron velocity (significantly smaller than  $c$ ) under the effect of an external field. Considering that the electric field has a temporal harmonic dependence as

$E = Ee^{-i\omega t}$ , the electron cloud displacement  $r = re^{-i\omega t}$ . Substituting E and r to Equation 3.25 we get

$$\mathbf{r} = -\frac{e\mathbf{E}}{m} \frac{1}{\omega_0^2 - \omega^2 - i\Gamma\omega} \quad (3.26)$$

The induced dipole moment, as a result of the displacement  $\mathbf{r}$  of the electron cloud, is  $p = -e\mathbf{r}$  and using Equation 3.26

$$\mathbf{p} = \frac{e^2\mathbf{E}}{m} \frac{1}{\omega_0^2 - \omega^2 - i\Gamma\omega} \quad (3.27)$$

Supposing that the electric field and displacement are quite small, have no dependency. Assuming small electric field and displacement, with  $\omega_0$  and  $\Gamma$  being independent of the electric field intensity, a linear relationship exists between the dipole moment and the electric field, given by  $\mathbf{p} = \alpha(\omega)\mathbf{E}$ , where

$$\alpha = \frac{e^2}{m} \frac{1}{\omega_0^2 - \omega^2 - i\Gamma\omega} \quad (3.28)$$

is the atomic polarizability in case of a one electron atom. This parameter is frequency-dependent and as a complex parameter, has an imaginary term which provides that there is a phase difference between electric field and the dipole moment. In a real material of many atoms, all the dipole moments together consist the macroscopic polarization:

$$\mathbf{P} = n\alpha\mathbf{E} = \chi_e\mathbf{E} \quad (3.29)$$

where N is the number of atoms per unit volume, and  $\chi_e$  the electric susceptibility. We can now define, from the electric displacement, the dielectric function  $\epsilon(\omega)$  as

$$\epsilon(\omega) = 1 + \frac{4\pi N e^2}{m} \frac{1}{\omega_0^2 - \omega^2 - i\Gamma\omega} \quad (3.30)$$

Considering classical atoms with more than one electron per atom, we can extend the previous expression to N types of electrons with the corresponding orbitals. Finally combining the contribution of free-electrons (intraband transitions which are described by Drude model) and the contribution of bound electrons (interband transitions which are described by Lorentz-model, we result to the Drude-Lorentz model for the dielectric function

$$\epsilon(\omega) = 1 + \frac{4\pi e^2 N_{free}}{m} \frac{1}{\omega^2 + i\gamma\omega} + \frac{4\pi e^2 N_{bound}}{m} \sum_{j=1}^N \frac{f_j}{\omega_{0j}^2 - \omega^2 - i\Gamma_j\omega} \quad (3.31)$$

where  $\gamma$  is to the friction of free electrons, due to the scattering with phonons and impurities, and  $f_j$  the oscillator strength, which is the partial contribution of each type of electron and satisfies  $\sum_{j=1}^N f_j = 1$  for free electrons. In practice, there are numerous orbitals and transitions, but there is no need to explicitly consider each one. Instead, fitting and focusing on a selective group of characteristic Lorentzians could be a good approximation. The dielectric function then takes the common form

$$\epsilon(\omega) = \epsilon_\infty + \frac{\omega_p^2}{\omega^2 + \frac{i\omega}{\tau}} + \sum_{j=1}^N \frac{\Delta\epsilon_j \Omega_j^2}{\Omega_j^2 - \omega^2 - i\Gamma_j\omega} \quad (3.32)$$

Where  $\epsilon_\infty$  represents the dielectric function at much higher frequencies, the plasma frequency ( $\omega_p$ ) is given by  $\omega_p = \sqrt{\frac{4\pi e^2 N_{free}}{m}}$ , where  $N_{free}$  is the free electron density,  $e$  is the elementary charge, and  $m$  is the electron mass. The free electrons' relaxation time is  $\tau = 1/\gamma$ , while the oscillation strength is determined by  $\Delta\epsilon_j = 4\pi e^2 N_{bound} f_j / (m\Omega_j)$ , where  $\Omega_j$  is the transition frequency and  $\Gamma_j$  is the decay rate of each Lorentz term, respectively. All these parameters are fitted to experimental refractive index ( $n$ ) data, obtained from ellipsometry measurements. For non-magnetic materials, the dielectric function is  $\epsilon = n^2$  and thus,  $\epsilon = \epsilon_1 + i\epsilon_2$ , where  $\epsilon_1$  and  $\epsilon_2$  are the real and imaginary parts of refractive index and  $n$  and  $k$  are the real and imaginary parts of dielectric function.

Figure 3.7 illustrates the dielectric functions of gold (Au) and silver (Ag), used in Chapters 5, 6 and 7 of this thesis. The associated Drude-Lorentz fits, referring to Equation 3.32, are depicted as continuous lines, and the fitting parameters are specified in the paragraph below.

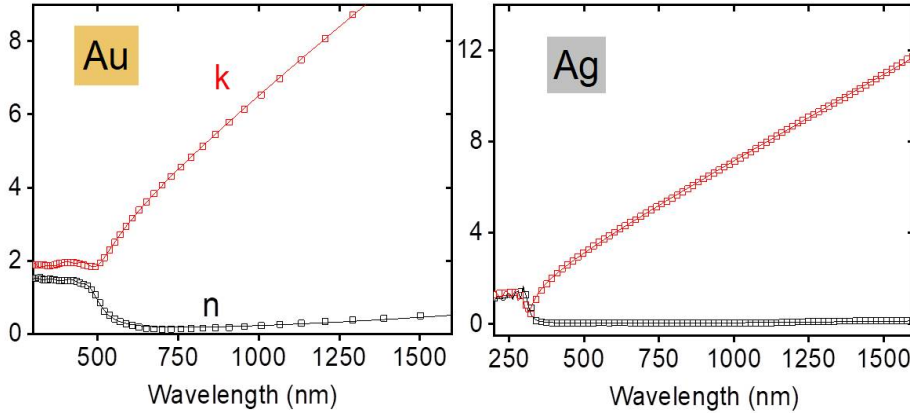


Figure 3.7: Drude-Lorentz fits of gold (left) and silver (right) dielectric functions for selected noble metals (typically used as plasmonic materials). The colored points correspond to experimentally determined values (from Johnson and Christy [22]).

We fitted Johnson and Christy's experimental data [22], represented in the same figure as colored squares. The fitting parameters for Au are  $N=4$ , and  $\epsilon_\infty=4.054$ ,  $\Delta\epsilon_j=(0.43, 0.634, 0.755, 1.059)$ ,  $\hbar\omega_p=8.76$  eV,  $\hbar\gamma=0.068$  eV,  $\hbar\Omega_j=(2.67, 3.03, 3.54, 4.23)$  eV, and  $\hbar\Gamma_j=(0.458, 0.641, 0.892, 0.959)$  eV. Respectively, in case of Ag, we use  $N=4$ , and  $\epsilon_\infty=2.492$ ,  $\Delta\epsilon_j=(0.119, 0.188, 0.266, 0.605)$ ,  $\hbar\omega_p=9.189$  eV,  $\hbar\gamma=0.0167$  eV,  $\hbar\Omega_j=(1.45, 1.98, 2.62, 4.73)$  eV, and  $\hbar\Gamma_j=(0.165, 0.281, 0.511, 1.231)$  eV. Still, the simplicity and straightforward applicability of the Drude-Lorentz model, as discussed above, remains an important tool to model the optical response of materials in nanophotonics.

### 3.2.2 Distributed Bragg Reflector (DBR) - Optical Cavity

Distributed Bragg Reflectors (DBRs), also referred to as one-dimensional photonic crystals or dielectric mirrors, are an excellent alternative to metallic mirrors, exhibiting low losses in the visible and infrared radiation range [58–61]. Conversely, metallic mirrors exhibit a broader reflection bandwidth, compared to dielectric mirrors, reflecting almost all incident light angles. Nevertheless, omnidirectional dielectric mirrors have also been developed recently [62]. DBR omnidirectionality is explored in Chapter 7. Here, we

consider only the normal-incidence case. The appropriate combination of a number of dielectric layers offers the possibility of effectively implementing a variety of basic optical structures, such as Bragg reflectors. Specifically, a DBR consists of identical alternating layers of high ( $h$ ) and low ( $l$ ) refractive indices, as shown in Figure 3.8.

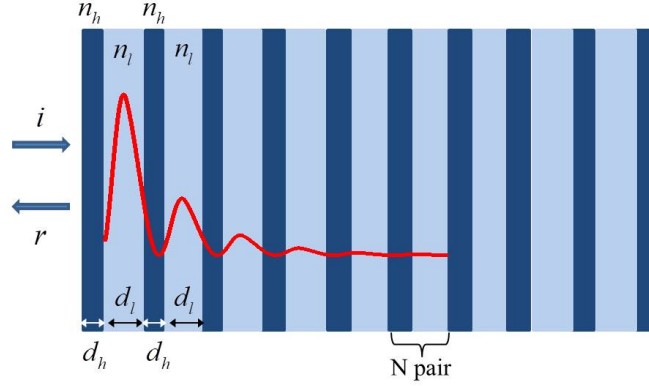


Figure 3.8: Schematics of a single DBR reflector, consisted of  $N$  dielectric pairs, in normal incidence.

The optical thicknesses are typically chosen to be quarter-wavelength long, i.e.,  $n_h d_h = n_l d_l = \lambda_0/4$  (following the condition for maximum reflection) at some operating wavelength  $\lambda_0$ . The standard arrangement is to have an odd number of layers, with the high index layer being the first and last layer. The quantitative description of the propagation of electromagnetic waves is performed using the Transfer Matrix Method, which is analyzed in Chapter 4. In this chapter, we will examine a system of multiple pairs of dielectric layers. We will proceed to calculate the reflection and transmission coefficients, but in this case for an arrangement as shown in Figure 3.8 with a number of periods  $N$ . The alternating placement of dielectric layers is periodic, with a period  $a = d_h + d_l$ , for  $N$  pairs of dielectric layers. The variation of fields along period  $a$  is found as generally described in Chapter 4.

$$E^a = P_{n_l, d_l} I_{n_l, n_2} P_{n_2, d_2} I_{n_2, n_1} E^0 = M \cdot E^0 \quad (3.33)$$

Transfer Matrix ( $M$ ) of the unit cell is similar with that of a single layer, with the only difference that the first and last elements change. Matrix  $M$  can be written as

$$\begin{aligned} M_{11} &= e^{ik_1(a-d_2)} \left[ \cos(k_2 d_2) + \frac{i}{2} \left( \frac{n_2}{n_1} + \frac{n_1}{n_2} \right) \sin(k_2 d_2) \right] \\ M_{12} &= \frac{i}{2} \left( \frac{n_2}{n_1} - \frac{n_1}{n_2} \right) \sin(k_2 d_2) \\ M_{22} &= e^{-ik_1(a-d_2)} M_{11}^* \\ M_{21} &= M_{12}^* \end{aligned} \quad (3.34)$$

The dielectric function is the periodical function of distance with period  $a$

$$\epsilon(x + a) = \epsilon(x) \quad (3.35)$$

Considering Bloch-Floquet theorem, we know that the solutions of Equation 3.33 are

$$E_q(x) = e^{iqx} u(x) \quad (3.36)$$

where the vector function  $u(x)$  is periodic,  $u(x + a) = u(x)$ , and  $q$  is the wave vector describing the spatial properties of the solution. The fundamental property of Equation 3.36 is that if it is shifted by one period  $a$ , the solution remains unchanged, except for an additional phase, and can be written as

$$E_q(x + a) = e^{iqa} E(x) \quad (3.37)$$

By combining Equation 3.33 with Equation 3.37 and writing E in detail,

$$M \begin{pmatrix} A \\ B \end{pmatrix} = e^{iqa} \begin{pmatrix} A \\ B \end{pmatrix} \quad (3.38)$$

which is a classical eigenvalue problem, and its solution is obtained by diagonalizing M.

For frequencies within the gap,  $q$  is imaginary, and thus instead of propagating waves, the solution consists of waves that exponentially decay in space. In a finite system like this, every incident wave with the appropriate frequency will be reflected. The greater the number of layers, the higher the reflection. Such a system constitutes a perfect mirror, despite being composed of a periodic arrangement of transparent layers, and as mentioned above is a dielectric (or Bragg) mirror. The reflection and transmission for such a system with  $N$  periods, can be calculated by transfer matrix M of unit cell, whose elements are shown in Equation 3.34.

$$\begin{pmatrix} A^N \\ B^N \end{pmatrix} = M^N \begin{pmatrix} A^1 \\ B^1 \end{pmatrix} \quad (3.39)$$

Calculating  $M^N$  matrix, it will be easy to derive the optical parameters of reflection and transmission. Continuing from Equation 3.37, we write matrix M as a function of its eigenvalues and eigenvectors

$$M = \Psi \begin{pmatrix} e^{iqa} & 0 \\ 0 & e^{-iqa} \end{pmatrix} = \Psi \Phi \Psi^{-1} \quad (3.40)$$

where the columns of the matrix  $\Psi$  are the eigenvectors of M. Finally,

$$M = [\Psi \Phi \Psi^{-1}]^N = \Psi \Phi^N \Psi^{-1} \quad (3.41)$$

So the solution is found after multiplying three matrices. After a bit of algebra matrix M becomes

$$M^N = \begin{pmatrix} \frac{M_{11} \sin Nqa - \sin(N-1)qa}{\sin qa} & \frac{M_{12} \sin Nqa}{\sin qa} \\ \frac{M_{21} \sin Nqa}{\sin qa} & \frac{M_{22} \sin Nqa - \sin(N-1)qa}{\sin qa} \end{pmatrix} \quad (3.42)$$

and transmission  $T = 1/(1 + R/T) = 1/(1 + |M_{12}|^2)$  can be derived by

$$T = \frac{1}{1 + |M_{12}|^2 \frac{\sin^2 Nqa}{\sin^2 qa}} \quad (3.43)$$

In Figure 3.9 (black curve), the transmittance coefficient of the dielectric Bragg mirror is plotted for  $N = 10$  periods.

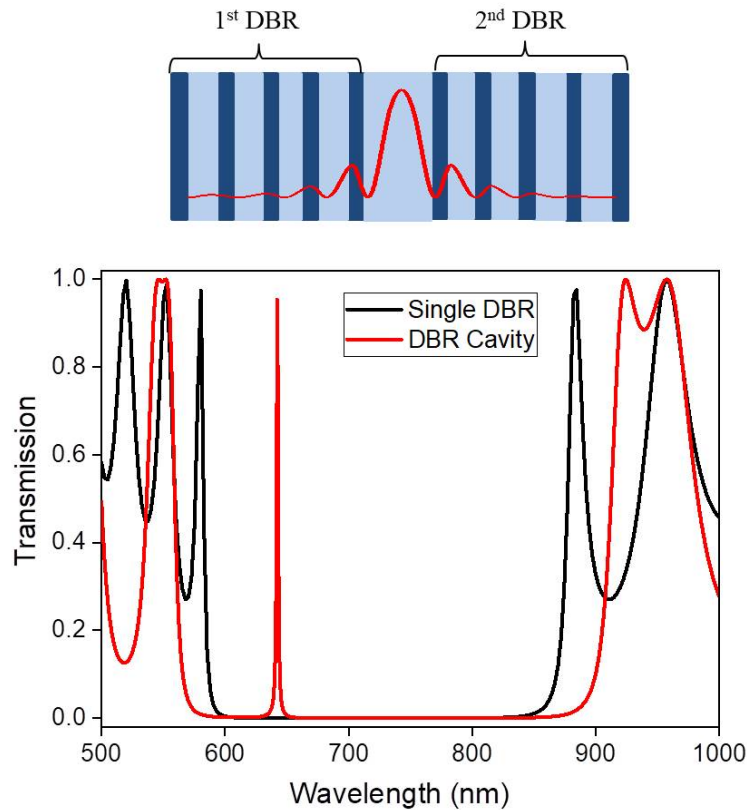


Figure 3.9: Optical transmission as a function of incident wavelength in case of a single DBR (black line) and a double DBR optical cavity (red line). On top inset is illustrated a schematic of the double DBR cavity; moreover the red curves correspond to e-field intensity partial distribution (1st cavity order).

It is noteworthy that the minimum value of transmission within the gap decreases exponentially as the number of periods increases. For each new period added, the transmission coefficient decreases by a factor of 10. This is an interesting, and well-known result, considering that the materials composing the alternating layers are completely transparent.

In the case where periodicity is broken, e.g. by changing central layer dimensions, a disturbance appears in the optical response creating an imperfection, as schematically shown in the top inset of Figure 3.9. Transmission of a DBR imperfection is also shown in Figure 3.9, where we can observe a slight change in the shape of transmission around the gap, and a dramatic change within the gap. A high transmission coefficient is noticeable, which appears in a very narrow frequency range inside the gap (red curve). Another way to think about this device is as consisting of two individual mirror segments, which are spaced apart by a distance  $d$ . In this case, light can be trapped between them, just like in any cavity formed by two mirrors. So, we notice the creation of a cavity with a characteristic frequency inside the gap. Light can pass through the entire system only if its frequency coincides with the frequency of the cavity. This mechanism is similar to the resonance in quantum tunneling, where light passes through using the cavity as an intermediate pathway. Such arrangements function as excellent spectral filters for isolating specific frequencies.

The position of cavity frequency within the gap depends on thickness  $d$  of the cavity. If there is a match of imperfection to  $\lambda/2$  condition of maximum transmission (i.e.,  $d = \lambda/2n_{cavity}$ ), the resonance will appear near the center of the gap. The closer it appears

to the center of the gap, the higher are the reflections from the mirrors, and thus the more precisely localized it will be. The spectral width of the cavity resonance depends on the "depth" of the gap, and thus, both on its position in the gap and the number of periods on each side. Better mirrors are assumed to have a larger  $N$  number, and thus narrower spectral width. The ratio of frequency  $\omega$ , at which cavity resonance appears, to the frequency range  $\Delta\omega$  (as measured at half of its maximum value) is known as the quality factor  $Q$  of the cavity

$$Q = \frac{\omega}{\Delta\omega} = 2\pi \frac{\text{stored energy}}{\text{decaying energy per cycle}} \quad (3.44)$$

The physical significance of this is that the lower quality factor  $Q$  (larger spectral width of initial and final states), corresponds to the faster rate of de-excitation (atomic excitation).

### 3.2.3 Optical Waveguides

Optical waveguides consist of dielectric material structures with a core region, possessing a higher refractive index compared to its surroundings. Electromagnetic waves guided by these structures propagate within and around the core. The core's transverse dimensions are either comparable to or smaller than the optical wavelength [63, 64]. The simplest optical waveguide is the planar type, depicted in Figure 3.10(a).

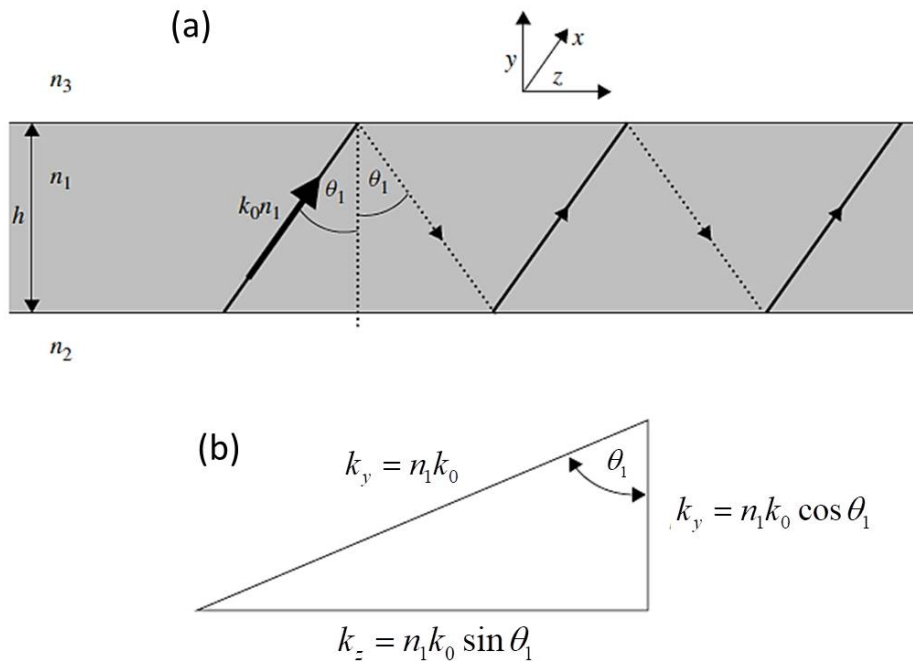


Figure 3.10: (a) Electromagnetic wave propagation in a planar waveguide. (b) The relations between propagation constants in  $y$ ,  $z$  and wave-normal directions.[64]

Considering the waveguide height as  $h$ , we assume that propagation occurs in the  $z$  direction, while light is confined in the  $y$  direction due to total internal reflection. The zig-zag path, depicted in the above figure, gains significance as it represents the wave-normal direction of light propagating through the waveguide with wavevector  $k = k_0 n_1$ . Further

explanation could be provided using an associated diagram (Figure 3.10(b)), where there is a decomposition of wavevector  $k$  into two components in the  $y$  and  $z$  directions. This decomposition can be analyzed using simple trigonometry as

$$\begin{aligned} k_z &= n_1 k_0 \sin(\theta_1) \\ k_y &= n_1 k_0 \cos(\theta_1) \end{aligned} \quad (3.45)$$

Once the propagation constant in the  $y$  direction is determined, we can assume a wave propagating in that direction. As this theoretical wave encounters reflections at each interface, there is a possibility of a standing wave forming across the waveguide in the same direction. Consequently, we can sum all the phase shifts, introduced during one complete 'round trip' across the waveguide and back again. For a waveguide of thickness  $h$  (resulting in a traversed distance  $2h$ ), a phase shift is introduced as follows

$$\phi_h = 2k_y h = 2k_0 n_1 h \cos\theta_1 \quad (3.46)$$

It is evident that phase changes occur upon reflection at both the upper and lower boundaries of the waveguide. Therefore, denoting these phase shifts as  $\phi_u$  and  $\phi_l$ , respectively, we derive the total phase shift by

$$\phi_{total}^* = 2k_y h = 2k_0 n_1 h \cos\theta_1 - \phi_u - \phi_l \quad (3.47)$$

To ensure the preservation of a wave across the waveguide, the total phase shift must be a multiple of  $2\pi$ . Hence,

$$2k_y h = 2k_0 n_1 h \cos\theta_1 - \phi_u - \phi_l = 2m\pi \quad (3.48)$$

where integer  $m = 0, 1, 2, \dots$ . It is noteworthy that since  $m$  is an integer, a series of discrete angles  $\theta$  will exist for which Equation 3.48 can be solved, corresponding to integral values of  $m$ . For each solution, there will consequently be a corresponding propagation constant in the  $y$  and  $z$  directions for each polarization. This highlights that light cannot propagate at just any angle  $\theta$ , but only at one of the permitted discrete angles. Each permitted solution is a mode of propagation, with the mode number being determined by the integer value of  $m$ . The first TE mode, also known as the fundamental mode, is described as TE<sub>0</sub>. Higher-order modes are similarly described using the appropriate  $m$  value. Moreover, a further limitation on  $m$  is noticeable, indicating a restriction on the number of modes that can propagate within a given waveguide structure. These limiting conditions arise when the propagation angle  $\theta_1$  falls below the critical angle at either the upper or lower waveguide interface.

Next, we can solve Equation 3.48, which describes the discrete nature of waveguide modes. The planar waveguide, depicted in Figure 3.10(a), consists of an upper cladding with a refractive index of  $n_3$  and a lower cladding with a refractive index of  $n_2$ . In case where  $n_2 = n_3$ , the waveguide is termed symmetrical since identical boundary conditions apply at both the upper and lower interfaces. Considering the slightly more intricate asymmetrical planar waveguide where  $n_2 \neq n_3$ . We can approach a simplified analysis where the phase change upon reflection at the upper and lower waveguide boundaries will not be identical. The eigenvalue equation for TE modes becomes

$$[k_0 n_1 h \cos\theta_1 - m\pi] = \tan^{-1}\left[\frac{\sqrt{\sin^2\theta_1 - (n_2/n_1)^2}}{\cos\theta_1}\right] + \tan^{-1}\left[\frac{\sqrt{\sin^2\theta_1 - (n_3/n_1)^2}}{\cos\theta_1}\right] \quad (3.49)$$

Equation 3.49 can be solved either numerically or graphically to determine the propagation angle  $\theta_1$  for a given value of  $m$ . However, it is noteworthy that there might not always be a solution to this equation ( $m = 0$ ), because one of the terms within the square roots on the right-hand side could potentially be negative. This occurs because the critical angle for the waveguide is determined by the larger of the critical angles of the two waveguide boundaries. It is obvious that, for total internal reflection at both waveguide boundaries, the propagating mode angle have to surpass both critical angles. However, the mode angle of the waveguide may not meet the condition for both critical angles, if the guide is too thin (i.e.,  $h$  is small) or if the refractive index difference between the core and claddings is too small.

In some applications, it is desirable for a waveguide to exclusively support a single mode for a specific polarization of light (as needed in integrated TMD-based LEDs of section 7.6). Such a waveguide is commonly referred to as single-mode. Figure 3.11 shows a dispersion diagram for a planar single-mode SiN waveguide at around  $\lambda_0=700$  nm.

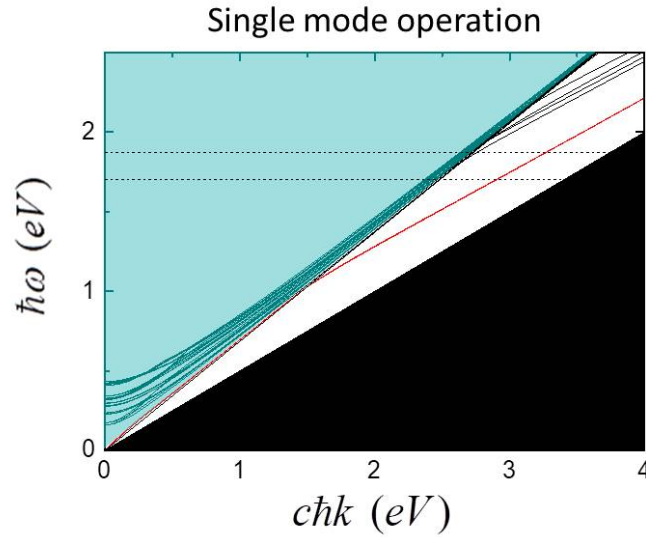


Figure 3.11: Dispersion diagram of a planar single-mode SiN waveguide.

In order to derive a single-mode angle condition, we consider TE polarization eigenvalue solution for a symmetrical waveguide (for simplicity), produced below

$$\tan\left[\frac{k_0 n_1 h \cos\theta_1 - m\pi}{2}\right] = \left[\frac{\sqrt{\sin^2\theta_1 - (n_1/n_2)^2}}{\cos\theta_1}\right] \quad (3.50)$$

Considering the second mode ( $m = 1$ ), the limiting condition for this mode is that the propagation angle equals the critical angle. In this case, the square-root term in the equation reduces to zero. Since the propagation angle for the second mode will be less than for the fundamental mode ( $m = 0$ ), for all angles greater than this critical angle, the waveguide will be single-mode. Equation 3.50 reduces to

$$\tan\left[\frac{k_0 n_1 h \cos\theta_c - \pi}{2}\right] = 0 \quad (3.51)$$

where  $\cos\theta_c = \frac{\pi}{k_0 n_1 h} = \frac{\lambda_0}{2n_1 h}$ . So, the single-mode condition will be

$$\theta_c < \cos^{-1}\left(\frac{\lambda_0}{2n_1h}\right) \quad (3.52)$$

Similar expression can be derived from TM eigenvalue equation.

### 3.3 Dipole Emission: Spontaneous decay rate and Optical Local Density of States (LDOS)

The radiation emission from a classical oscillating electric dipole serves as a classic example for elucidating the principles of LED emission, studied for planar cavity and antenna-coupled devices in Chapter 7. Notably, the expression for power emitted by a classical dipole shares the same mathematical formula as the spontaneous emission rate of a (two-level) quantum emitter, derived by quantum electrodynamics (QED) [11, 65–67]. Despite this, a purely classical description of the optical interaction between a dipole and its surroundings proves valuable, concerning the optical local density of states (LDOS), the Purcell enhancement [6, 11, 68] e.t.c.

#### 3.3.1 Electric Dipole in homogeneous medium

Power radiated by a classical dipole can be calculated considering a current distribution with harmonic time-dependence in a linear and homogeneous medium. We assume two point charges  $+q$  and  $-q$  performing linear oscillations with frequency  $\omega$ , as illustrated in Figure 3.12 [1].

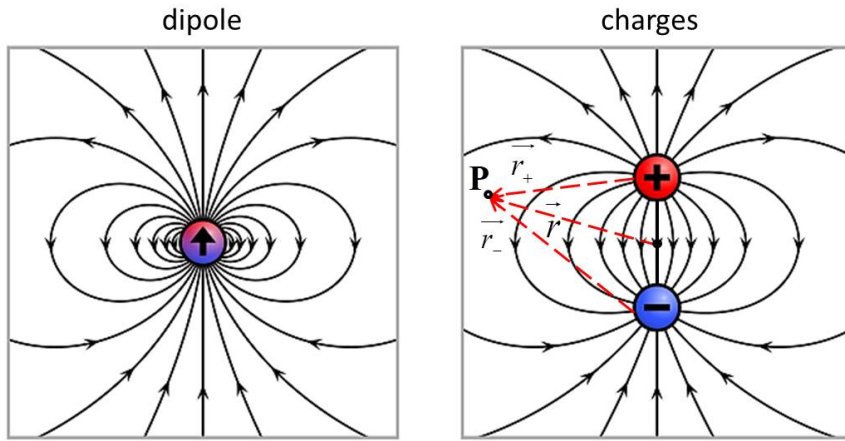


Figure 3.12: Schematic of an oscillating point dipole with frequency  $\omega$  (left). Schematic of dipole charges with distance  $d$  (right).  $P$  represents the emitted power in distance  $r$  from the center of the charge distance.

Specifically, the instantaneous positions of the charges are  $\vec{\rho}_+ = \hat{z}a\cos(\omega t)$  and  $\vec{\rho}_- = -\hat{z}a\cos(\omega t)$  and the electric charge density can be written

$$\rho(\vec{r}, t) = q\delta(\vec{r} - \vec{r}_+(t)) - q\delta(\vec{r} - \vec{r}_+(-)) \quad (3.53)$$

or

$$\rho(\vec{r}, t) = q\delta(x)\delta(y)(\delta(z - a\cos\omega t) - \delta(z + a\cos\omega t)) \quad (3.54)$$

The current density corresponding to the above charge density is

$$\vec{J} = -\hat{z}qa\omega\delta(x)\delta(y)(\delta(z - a\cos\omega t) - \delta(z + a\cos\omega t)) \quad (3.55)$$

The respective electric dipole moment follows the expression

$$\vec{p} = 2\hat{z}qa\cos\omega t \quad (3.56)$$

The above system of two charges is the simplest version of an oscillating electric dipole. In the following we study any electric dipole moment system with  $\vec{p} = \vec{p}_0\cos(\omega t)$ . The dipole radiation potentials are

$$\phi(\vec{r}, t) = \frac{hatr\dot{\vec{p}}}{4\pi\epsilon_0cr} = -\frac{qa\omega}{2\pi\epsilon_0c}\sin(\omega t_R)\frac{\hat{z}\hat{r}}{r} \quad (3.57)$$

and

$$\vec{A}(\vec{r}, t) = \frac{\mu_0\dot{\vec{p}}}{4\pi r} = -\frac{\mu_0qa\omega}{2\pi}\sin(\omega t_R)\frac{\hat{z}}{r} \quad (3.58)$$

where  $t_R = t - (r/c)$  the retarded time. The respective radiation fields can be produced, substituting Equations 3.57 and 3.58 in the general equations  $\vec{E} = -\nabla V - (\partial\vec{A}/\partial t)$  and  $\vec{B} = \nabla \times \vec{A}$ , as

$$\vec{E} = -\frac{\mu_0\omega^2 p_0}{4\pi}\hat{r} \times \left(\frac{\hat{r} \times \hat{z}}{r}\right)\cos(\omega t_R), \quad (3.59)$$

and

$$\vec{B} = \frac{\mu_0\omega^2 p_0}{4\pi c}\left(\frac{\hat{r} \times \hat{z}}{r}\right)\cos(\omega t_R) \quad (3.60)$$

The Poynting vector  $\vec{S} = \frac{1}{\mu_0}(\vec{E} \times \vec{B})$  for this system takes the form

$$\vec{S} = \frac{\mu_0\omega^4 p_0^2}{16\pi^2 c}\left(\frac{\cos^2(\omega t_R)}{r^2}\right)\sin^2\theta\hat{r} \quad (3.61)$$

According to the Poynting theorem, the emitted power through a spherical surface can be derived using the following expression [1, 11, 65]

$$P = \oint \vec{d}a\vec{S} = \frac{\mu_0\omega^4 p_0^2}{6\pi c}\cos^2(\omega t_R) \quad (3.62)$$

While the time-averaged dissipated power can be calculated by

$$\langle P \rangle = \frac{1}{T} \int_0^T dt P(t) = \frac{\omega}{2\pi} \left(\frac{\mu_0\omega^4 p_0^2}{6\pi c}\right) \int_0^T dt \cos^2(\omega t_R) \quad (3.63)$$

where  $\langle \cos^2(\omega t_R) \rangle = 1/2$  and finally, we obtain

$$\langle P \rangle = \frac{\mu_0\omega^4 p_0^2}{12\pi c} \quad (3.64)$$

which is the well-known Larmor formula for the power radiated by a classical oscillating electric dipole [1, 11, 69].

### 3.3.2 Electric Dipole in inhomogeneous medium: Spontaneous emission rate, LDOS and Purcell enhancement

When considering a inhomogeneous environment, it is useful to decompose the total electric field at the dipole's origin. Specifically, the field, involved in Equation 3.59, into a primary field  $E_0$  and an additional scattered component  $E_{scat}$ .

$$E = E_0 + E_{scat} \quad (3.65)$$

We can notice, from the description of dipole emission in the previous subsection, that the presence of an inhomogeneity in the medium changes the rate of energy's dissipation. This arises from the fact that the total field at the position  $\vec{r}$  (see Figure 3.12) is the combination of the dipole's primary field along with the dipole's field, generated at an earlier time, after scattering in the non-uniform environment. The normalized spontaneous decay rate of a quantum emitter  $\gamma$ , relative to its value in the vacuum  $\gamma_0$ , equals the power radiated by a classical dipole P, normalized with  $P_0$  [11]. This relationship can be expressed as

$$\frac{\gamma}{\gamma_0} = \frac{P}{P_0} \quad (3.66)$$

In the weak-coupling regime, the decay of the excited state population of a quantum emitter decays exponentially over time, characterized by a fluorescence lifetime ( $\tau$ ) equal to ( $\gamma^{-1}$ ), where  $\gamma$  represents the spontaneous decay rate. We study a two-level system with an excited state  $|i\rangle$  and ground state  $|j\rangle$ , Bohr frequency  $\omega_{ij}$ , and dipole transition  $p_{ij} = \langle i|M|j\rangle$ , where M is the electric dipole operator. Starting from the time-averaged power emitted by a classical dipole equation (Equation 3.64) [70], with  $\omega$  replaced by the Bohr frequency  $\omega_{ij}$ , we can derive the decay rate (average number of quantum transitions per unit time) by dividing the power by the quantum energy  $\hbar\omega_{ij}$  and replacing the classical dipole moment  $p_0$  with the transition dipole  $p_{ij}$ . It is noteworthy that a quantum mechanical computation of the spontaneous emission rate through Fermi's golden rule establishes a link between  $\gamma$  rate and the local density of states (LDOS), denoted as  $D(r, \omega_{ij})$ . Specifically, the relationship [11] is expressed as

$$\gamma = \frac{\pi\omega_{ij}}{3\hbar\epsilon_0} p_{ij}^2 D(r, \omega_{ij}) \quad (3.67)$$

Specifically, in vacuum, the LDOS is given by

$$D_0(r, \omega) = \frac{\omega^2}{\pi^2 c^3} \quad (3.68)$$

and the spontaneous decay rate follows the expression

$$\gamma_0 = \frac{\omega_{ij}^3}{3\pi\hbar\epsilon_0 c^3} p_{ij}^2 \quad (3.69)$$

The change in spontaneous decay rate  $\gamma/\gamma_0$ , due to the structured environment was originally calculated by Purcell in the simple case of a single-mode cavity [71]. Using the expression of Equation 3.69 for the spontaneous decay rate in vacuum, the normalized decay rate can be written as

$$\frac{\gamma}{\gamma_0} = \frac{3}{4\pi^2} \lambda_{ij}^3 \frac{Q}{V} \quad (3.70)$$

where  $\lambda_{ij} = 2\pi c/\omega_{ij}$  and  $Q =$  the quality factor. This is the result given by Purcell [71] and the right-hand side is usually referred to as the Purcell factor.

As established in Purcell's work, the rate of spontaneous emission is not an intrinsic characteristic of the emitter and can be altered by the environment [11, 65, 72–74]. Notably, the dynamics of emitter decay rates can be significantly enhanced close to material interfaces. In the case of plasmonics, the LDOS of an emitter can be exceedingly amplified by orders of magnitude, due to the presence of plasmon resonances [29, 75, 76]. This plasmon-assisted Purcell enhancement stands out as a distinctive feature of plasmonics, and will be discussed in case of planar cavity and/or antenna-coupled light emission in Chapter 7.

## References

- [1] J. D. Jackson, "Classical electrodynamics," 1998.
- [2] M. Born and E. Wolf, "Principles of optics 7th edn (cambridge: Cambridge university)," 1999.
- [3] J. A. Stratton, *Electromagnetic theory*, vol. 33. John Wiley & Sons, 2007.
- [4] L. D. Landau, J. S. Bell, M. Kearsley, L. Pitaevskii, E. Lifshitz, and J. Sykes, *Electrodynamics of continuous media*, vol. 8. elsevier, 2013.
- [5] P. Drude, "Zur elektronentheorie der metalle," *Annalen der physik*, vol. 306, no. 3, pp. 566–613, 1900.
- [6] P. A. D. Gonçalves and N. M. Peres, *An introduction to graphene plasmonics*. World Scientific, 2016.
- [7] S. A. Maier *et al.*, *Plasmonics: fundamentals and applications*, vol. 1. Springer, 2007.
- [8] T. V. Shahbazyan and M. I. Stockman, *Plasmonics: theory and applications*, vol. 15. Springer, 2013.
- [9] N. W. Ashcroft and N. Mermin, "Solid state," *Physics (New York: Holt, Rinehart and Winston) Appendix C*, 1976.
- [10] A. Sommerfeld, "Zur elektronentheorie der metalle auf grund der fermischen statistik: I. teil: Allgemeines, strömungs-und austrittsvorgänge," *Zeitschrift für Physik*, vol. 47, pp. 1–32, 1928.
- [11] L. Novotny and B. Hecht, *Principles of nano-optics*. Cambridge university press, 2012.
- [12] A. A. Maradudin, J. R. Sambles, and W. L. Barnes, *Modern plasmonics*. Elsevier, 2014.
- [13] H. Raether *et al.*, "Surface plasmons on smooth and rough surfaces and on gratings [electronic resource],"

- [14] O. Graydon, “Polymer yields 3d video,” *Nature Photonics*, vol. 4, no. 12, pp. 811–811, 2010.
- [15] W. L. Barnes, A. Dereux, and T. W. Ebbesen, “Surface plasmon subwavelength optics,” *nature*, vol. 424, no. 6950, pp. 824–830, 2003.
- [16] E. Ozbay, “Plasmonics: merging photonics and electronics at nanoscale dimensions,” *science*, vol. 311, no. 5758, pp. 189–193, 2006.
- [17] T. Low, A. Chaves, J. D. Caldwell, A. Kumar, N. X. Fang, P. Avouris, T. F. Heinz, F. Guinea, L. Martin-Moreno, and F. Koppens, “Polaritons in layered two-dimensional materials,” *Nature materials*, vol. 16, no. 2, pp. 182–194, 2017.
- [18] F. J. Garcia de Abajo, “Graphene plasmonics: challenges and opportunities,” *Acs Photonics*, vol. 1, no. 3, pp. 135–152, 2014.
- [19] K. A. Willets and R. P. Van Duyne, “Localized surface plasmon resonance spectroscopy and sensing,” *Annu. Rev. Phys. Chem.*, vol. 58, pp. 267–297, 2007.
- [20] K. L. Kelly, E. Coronado, L. L. Zhao, and G. C. Schatz, “The optical properties of metal nanoparticles: the influence of size, shape, and dielectric environment,” 2003.
- [21] E. Hutter and J. H. Fendler, “Exploitation of localized surface plasmon resonance,” *Advanced materials*, vol. 16, no. 19, pp. 1685–1706, 2004.
- [22] P. B. Johnson and R.-W. Christy, “Optical constants of the noble metals,” *Physical review B*, vol. 6, no. 12, p. 4370, 1972.
- [23] M. Pelton and G. W. Bryant, *Introduction to metal-nanoparticle plasmonics*. John Wiley & Sons, 2013.
- [24] M. Geisler, X. Cui, J. Wang, T. Rindzevicius, L. Gammelgaard, B. S. Jessen, P. A. D. Gonçalves, F. Todisco, P. Bøggild, A. Boisen, *et al.*, “Single-crystalline gold nanodisks on ws2 mono- and multilayers for strong coupling at room temperature,” *Acs Photonics*, vol. 6, no. 4, pp. 994–1001, 2019.
- [25] C. Langhammer, M. Schwind, B. Kasemo, and I. Zoric, “Localized surface plasmon resonances in aluminum nanodisks,” *Nano letters*, vol. 8, no. 5, pp. 1461–1471, 2008.
- [26] F.-P. Schmidt, H. Ditlbacher, U. Hohenester, A. Hohenau, F. Hofer, and J. R. Krenn, “Dark plasmonic breathing modes in silver nanodisks,” *Nano letters*, vol. 12, no. 11, pp. 5780–5783, 2012.
- [27] F. P. Schmidt, H. Ditlbacher, F. Hofer, J. R. Krenn, and U. Hohenester, “Morphing a plasmonic nanodisk into a nanotriangle,” *Nano Letters*, vol. 14, no. 8, pp. 4810–4815, 2014.
- [28] A. Campos, A. Arbouet, J. Martin, D. Gerard, J. Proust, J. Plain, and M. Kociak, “Plasmonic breathing and edge modes in aluminum nanotriangles,” *Acs Photonics*, vol. 4, no. 5, pp. 1257–1263, 2017.

- [29] G. M. Akselrod, C. Argyropoulos, T. B. Hoang, C. Ciraci, C. Fang, J. Huang, D. R. Smith, and M. H. Mikkelsen, “Probing the mechanisms of large purcell enhancement in plasmonic nanoantennas,” *Nature Photonics*, vol. 8, no. 11, pp. 835–840, 2014.
- [30] B. Gao, G. Arya, and A. R. Tao, “Self-orienting nanocubes for the assembly of plasmonic nanojunctions,” *Nature nanotechnology*, vol. 7, no. 7, pp. 433–437, 2012.
- [31] S. Zhang, K. Bao, N. J. Halas, H. Xu, and P. Nordlander, “Substrate-induced fano resonances of a plasmonic nanocube: a route to increased-sensitivity localized surface plasmon resonance sensors revealed,” *Nano letters*, vol. 11, no. 4, pp. 1657–1663, 2011.
- [32] M. A. Mahmoud and M. A. El-Sayed, “Different plasmon sensing behavior of silver and gold nanorods,” *The Journal of Physical Chemistry Letters*, vol. 4, no. 9, pp. 1541–1545, 2013.
- [33] M. Grzelczak, J. Pérez-Juste, P. Mulvaney, and L. M. Liz-Marzán, “Shape control in gold nanoparticle synthesis,” *Colloidal Synthesis of Plasmonic Nanometals*, pp. 197–220, 2020.
- [34] A. R. Tao, S. Habas, and P. Yang, “Shape control of colloidal metal nanocrystals,” *small*, vol. 4, no. 3, pp. 310–325, 2008.
- [35] M. Rycenga, C. M. Cobley, J. Zeng, W. Li, C. H. Moran, Q. Zhang, D. Qin, and Y. Xia, “Controlling the synthesis and assembly of silver nanostructures for plasmonic applications,” *Chemical reviews*, vol. 111, no. 6, pp. 3669–3712, 2011.
- [36] P. Nordlander, C. Oubre, E. Prodan, K. Li, and M. Stockman, “Plasmon hybridization in nanoparticle dimers,” *Nano letters*, vol. 4, no. 5, pp. 899–903, 2004.
- [37] E. Hao and G. C. Schatz, “Electromagnetic fields around silver nanoparticles and dimers,” *The Journal of chemical physics*, vol. 120, no. 1, pp. 357–366, 2004.
- [38] I. Romero, J. Aizpurua, G. W. Bryant, and F. J. G. De Abajo, “Plasmons in nearly touching metallic nanoparticles: singular response in the limit of touching dimers,” *Optics express*, vol. 14, no. 21, pp. 9988–9999, 2006.
- [39] C. Sönnichsen, B. M. Reinhard, J. Liphardt, and A. P. Alivisatos, “A molecular ruler based on plasmon coupling of single gold and silver nanoparticles,” *Nature biotechnology*, vol. 23, no. 6, pp. 741–745, 2005.
- [40] J. Zuloaga, E. Prodan, and P. Nordlander, “Quantum description of the plasmon resonances of a nanoparticle dimer,” *Nano letters*, vol. 9, no. 2, pp. 887–891, 2009.
- [41] P. A. D. Gonçalves, *Plasmonics and Light–Matter Interactions in Two-Dimensional Materials and in Metal Nanostructures: Classical and Quantum Considerations*. Springer Nature, 2020.
- [42] A. Kinkhabwala, Z. Yu, S. Fan, Y. Avlasevich, K. Müllen, and W. Moerner, “Large single-molecule fluorescence enhancements produced by a bowtie nanoantenna,” *Nature photonics*, vol. 3, no. 11, pp. 654–657, 2009.

- [43] C. Tabor, R. Murali, M. Mahmoud, and M. A. El-Sayed, "On the use of plasmonic nanoparticle pairs as a plasmon ruler: the dependence of the near-field dipole plasmon coupling on nanoparticle size and shape," *The Journal of Physical Chemistry A*, vol. 113, no. 10, pp. 1946–1953, 2009.
- [44] B. J. Roxworthy, K. D. Ko, A. Kumar, K. H. Fung, E. K. Chow, G. L. Liu, N. X. Fang, and K. C. Toussaint Jr, "Application of plasmonic bowtie nanoantenna arrays for optical trapping, stacking, and sorting," *Nano letters*, vol. 12, no. 2, pp. 796–801, 2012.
- [45] M. Hentschel, M. Saliba, R. Vogelgesang, H. Giessen, A. P. Alivisatos, and N. Liu, "Transition from isolated to collective modes in plasmonic oligomers," *Nano letters*, vol. 10, no. 7, pp. 2721–2726, 2010.
- [46] M. Hentschel, D. Dregely, R. Vogelgesang, H. Giessen, and N. Liu, "Plasmonic oligomers: the role of individual particles in collective behavior," *Acs Nano*, vol. 5, no. 3, pp. 2042–2050, 2011.
- [47] B. Gallinet and O. J. Martin, "Influence of electromagnetic interactions on the line shape of plasmonic fano resonances," *ACS nano*, vol. 5, no. 11, pp. 8999–9008, 2011.
- [48] M. Hentschel, M. Schäferling, T. Weiss, N. Liu, and H. Giessen, "Three-dimensional chiral plasmonic oligomers," *Nano letters*, vol. 12, no. 5, pp. 2542–2547, 2012.
- [49] H. Wang, D. W. Brandl, F. Le, P. Nordlander, and N. J. Halas, "Nanorice: a hybrid plasmonic nanostructure," *Nano letters*, vol. 6, no. 4, pp. 827–832, 2006.
- [50] C. Radloff and N. J. Halas, "Plasmonic properties of concentric nanoshells," *Nano letters*, vol. 4, no. 7, pp. 1323–1327, 2004.
- [51] S. Mukherjee, H. Sobhani, J. B. Lassiter, R. Bardhan, P. Nordlander, and N. J. Halas, "Fano shells: nanoparticles with built-in fano resonances," *Nano letters*, vol. 10, no. 7, pp. 2694–2701, 2010.
- [52] V. Kravets, F. Schedin, and A. Grigorenko, "Extremely narrow plasmon resonances based on diffraction coupling of localized plasmons in arrays of metallic nanoparticles," *Physical review letters*, vol. 101, no. 8, p. 087403, 2008.
- [53] G. Vecchi, V. Giannini, and J. G. Rivas, "Shaping the fluorescent emission by lattice resonances in plasmonic crystals of nanoantennas," *Physical review letters*, vol. 102, no. 14, p. 146807, 2009.
- [54] B. Auguie and W. L. Barnes, "Collective resonances in gold nanoparticle arrays," *Physical review letters*, vol. 101, no. 14, p. 143902, 2008.
- [55] F. G. De Abajo, "Colloquium: Light scattering by particle and hole arrays," *Reviews of Modern Physics*, vol. 79, no. 4, p. 1267, 2007.
- [56] V. G. Kravets, A. V. Kabashin, W. L. Barnes, and A. N. Grigorenko, "Plasmonic surface lattice resonances: a review of properties and applications," *Chemical reviews*, vol. 118, no. 12, pp. 5912–5951, 2018.
- [57] F. Wooten, *Optical properties of solids*. Academic Press, 1972.

- [58] C. Sheppard, "Approximate calculation of the reflection coefficient from a stratified medium," *Pure and Applied Optics: Journal of the European Optical Society Part A*, vol. 4, no. 5, p. 665, 1995.
- [59] S. J. Orfanidis, "Electromagnetic waves and antennas," 2002.
- [60] B. Osting, "Bragg structure and the first spectral gap," *Applied Mathematics Letters*, vol. 25, no. 11, pp. 1926–1930, 2012.
- [61] R. Paschotta, "Encyclopedia of laser physics and technology," (*No Title*), 2008.
- [62] Y. Fink, J. N. Winn, S. Fan, C. Chen, J. Michel, J. D. Joannopoulos, and E. L. Thomas, "A dielectric omnidirectional reflector," *Science*, vol. 282, no. 5394, pp. 1679–1682, 1998.
- [63] W. S. Chang, *Fundamentals of guided-wave optoelectronic devices*. Cambridge University Press, 2010.
- [64] G. T. Reed and A. P. Knights, *Silicon photonics: an introduction*. John Wiley & Sons, 2004.
- [65] R. Carminati, A. Cazé, D. Cao, F. Peragut, V. Krachmalnicoff, R. Pierrat, and Y. De Wilde, "Electromagnetic density of states in complex plasmonic systems," *Surface Science Reports*, vol. 70, no. 1, pp. 1–41, 2015.
- [66] J. M. Wylie and J. Sipe, "Quantum electrodynamics near an interface," *Physical Review A*, vol. 30, no. 3, p. 1185, 1984.
- [67] D. J. Griffiths and D. F. Schroeter, *Introduction to quantum mechanics*. Cambridge university press, 2018.
- [68] P. A. D. Gonçalves and P. A. D. Gonçalves, "Classical electrodynamics of solids," *Plasmonics and Light–Matter Interactions in Two-Dimensional Materials and in Metal Nanostructures: Classical and Quantum Considerations*, pp. 13–49, 2020.
- [69] G. W. Ford and W. H. Weber, "Electromagnetic interactions of molecules with metal surfaces," *Physics Reports*, vol. 113, no. 4, pp. 195–287, 1984.
- [70] K. F. MacDonald and N. I. Zheludev, "Active plasmonics: current status," *Laser & Photonics Reviews*, vol. 4, no. 4, pp. 562–567, 2010.
- [71] E. Purcell, "Measurement of magnetic resonance absorption by nuclear moments in a solid," *Phys. Rev.*, vol. 69, p. 681, 1946.
- [72] M. Pelton, "Modified spontaneous emission in nanophotonic structures," *Nature Photonics*, vol. 9, no. 7, pp. 427–435, 2015.
- [73] E. Yablonovitch, "Inhibited spontaneous emission in solid-state physics and electronics," *Physical review letters*, vol. 58, no. 20, p. 2059, 1987.
- [74] D. Bouchet and R. Carminati, "Quantum dipole emitters in structured environments: a scattering approach: tutorial," *JOSA A*, vol. 36, no. 2, pp. 186–195, 2019.

- [75] K. J. Russell, T.-L. Liu, S. Cui, and E. L. Hu, “Large spontaneous emission enhancement in plasmonic nanocavities,” *Nature Photonics*, vol. 6, no. 7, pp. 459–462, 2012.
- [76] A. F. Koenderink, “On the use of purcell factors for plasmon antennas,” *Optics letters*, vol. 35, no. 24, pp. 4208–4210, 2010.

# Chapter 4

## Computational and analytical methods

In this chapter, we introduce the computational tools used throughout this thesis. We begin by discussing the methods used to extract the optical response of studied structures, namely the Transfer Matrix Method (TMM), used in Chapter 6, the Finite Difference Time Domain (FDTD), our main tool to describe optical response in Chapters 5 and 7, and Finite Difference Eigenmode (FDE), employed in section 7.6, computational methods. Subsequently, we provide a brief overview of Runge-Kutta computational method, utilized for handling rate equations and numerical integrations within the simulation framework, used in section 6.2.

### 4.1 Transfer Matrix Method (TMM)

Transfer Matrix Method (TMM) stands out as a powerful tool for analyzing the propagation of light through a stratified optical medium, such as a multilayer stack with varying thicknesses  $d$  and optical constants  $n$  (as depicted in Figure 4.1) [1–4].

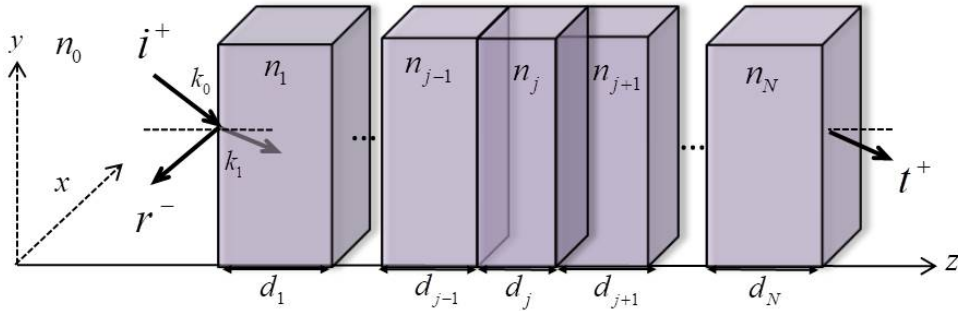


Figure 4.1: Schematic representation of a multilayer stack, consisting of  $N$  layers, with thicknesses  $d_j$  and complex refractive indices  $n_j$ . We assume an incident plane wave  $i^+$ , incoming from a semi-infinite medium  $n_0$  at an angle  $\theta_0$  (wavevector  $k_0$ ). The reflected wave to free-space  $r^-$  and transmitted wave through the multilayer stack  $t^+$  are also shown. The positive and negative signs, represent propagated wave direction to right and left of  $z$ -axis, respectively.

The fundamental concept of TMM lies in establishing a connection between the electric and magnetic fields at a specific position and their respective values at different positions through a  $2 \times 2$  matrix, known as the transfer matrix. This matrix is composed of two distinct components, the interface matrix, which relates the fields across a material

interface, and the propagation matrix, which characterizes the propagation of a plane wave across a uniform medium.

Once the transfer matrix is derived, it becomes feasible to determine the reflection and transmission coefficients of a multilayer stack. Additionally, the absorptivity of each absorptive layer within a stack can also be extracted [5, 6]. However, despite its effectiveness, TMM has some limitations, such as that it can only analyze the response of a given structure for a single wavelength at a time (as a frequency domain method). Nonetheless, this limitation can be improved by the rapid calculation of this method. Obtaining the response for a broad spectrum can be achieved by performing the calculation repeatedly for each individual wavelength. The most significant limitation of TMM is its assumption that all layers are isotropic and extend infinitely in the plane perpendicular to the direction of propagation (see Figure 4.1). Consequently, the layers that are simulated must have sufficient widths to prevent inaccuracies caused by this assumption. Furthermore, TMM, as utilized in this context, lacks the capability to integrate 2D or 3D geometric features, making it essential as a 1D method.

### 4.1.1 Interface Matrix

Considering the basic case of an interface between two adjacent materials with complex refractive indices  $n_j$  and  $n_{j+1}$ . In this general case, waves are incoming from both directions. A schematic, illustrating the relevant plane waves, under the simplified condition of normal incidence, is presented in Figure 4.2.

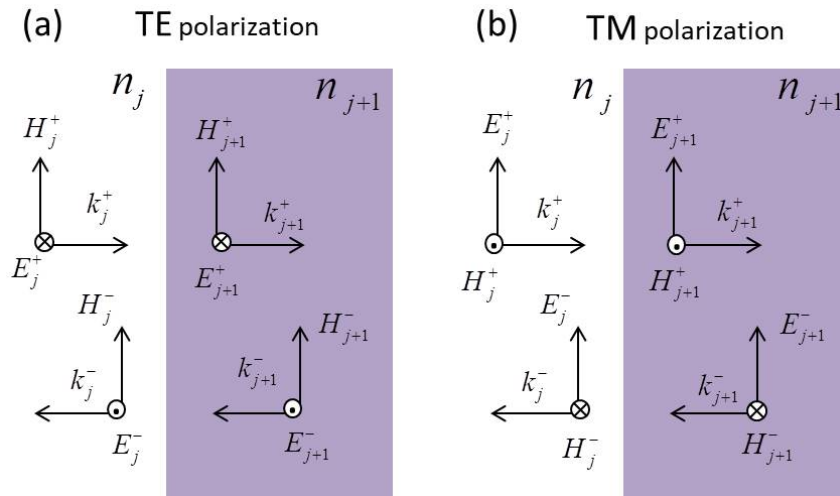


Figure 4.2: Schematic representation, for normal incidence, of TE- (a) and TM- (b) polarization of plane wave propagation through an interface between two adjacent materials with refractive indices  $n_j$  and  $n_{j+1}$ .

The outgoing waves on each side of the interface will result from the combination of the reflected amplitude of one incoming wave with the transmitted amplitude of the opposite incoming wave. By enforcing the boundary conditions for  $E$  and  $H$  directly at the interface, the electric field amplitudes on each side of the interface can be related to [1, 4]

$$\begin{pmatrix} E_{j+1}^+ \\ E_{j+1}^- \end{pmatrix} = I_{j,j+1} \begin{pmatrix} E_j^+ \\ E_j^- \end{pmatrix} \quad (4.1)$$

where  $I_{j,j+1}$  is the interface matrix for the transition of layered material  $j$  to its adjacent  $j + 1$ . This matrix depends on wave polarization, so  $I_{j,j+1}$  for TE polarization is

$$I_{j,j+1}^{TE} = \frac{1}{2} \begin{pmatrix} 1 + \frac{n_j \cos \theta_j}{n_{j+1} \cos \theta_{j+1}} & 1 - \frac{n_j \cos \theta_j}{n_{j+1} \cos \theta_{j+1}} \\ 1 - \frac{n_j \cos \theta_j}{n_{j+1} \cos \theta_{j+1}} & 1 + \frac{n_j \cos \theta_j}{n_{j+1} \cos \theta_{j+1}} \end{pmatrix} \quad (4.2)$$

where  $n_j$ ,  $n_{j+1}$  the complex refractive indices and  $j$ ,  $j+1$  the propagation angles at the respected layers. Transition matrix in case of TM polarization is

$$I_{j,j+1}^{TM} = \frac{1}{2} \begin{pmatrix} \frac{n_j}{n_{j+1}} + \frac{\cos \theta_j}{\cos \theta_{j+1}} & \frac{n_j}{n_{j+1}} - \frac{\cos \theta_j}{\cos \theta_{j+1}} \\ \frac{n_j}{n_{j+1}} - \frac{\cos \theta_j}{\cos \theta_{j+1}} & \frac{n_j}{n_{j+1}} + \frac{\cos \theta_j}{\cos \theta_{j+1}} \end{pmatrix} \quad (4.3)$$

Assuming angle-incidence, from a material layer with index  $n_0$  at an angle  $\theta_0$  (see Figure 4.1), and utilizing Snell's law, we can deduce that the angle at which propagation occurs within each layer, is determined by

$$\cos(\theta_j) = \sqrt{1 - \left(\frac{n_0}{n_j}\right)^2 \sin^2 \theta_0} \quad (4.4)$$

### 4.1.2 Propagation Matrix

In order to determine the propagation of light through a uniform medium, characterized by an index  $n_j$  and thickness  $d_j$ , we assume the presence of a wave traveling in the positive z-direction, with amplitude  $E_j^+$ , and another traveling in the negative z-direction, with an amplitude  $E_j^-$ . Following the propagation through this medium, the light is described by a phase factor  $\phi_j = 2\pi n_j d_j \cos \theta_j / \lambda$ . The wave amplitudes after propagating a layer  $E_{z+d_j}$ , with index  $n_j$  and thickness  $d_j$ , are related to those at the initial position  $E_z$  through the expression below

$$\begin{pmatrix} E_{z+d_j}^+ \\ E_{z+d_j}^- \end{pmatrix} = P_j \begin{pmatrix} E_z^+ \\ E_z^- \end{pmatrix} \quad (4.5)$$

where the propagation matrix  $P_j = \begin{pmatrix} e^{\phi_j} & 0 \\ 0 & e^{-\phi_j} \end{pmatrix}$  has no dependence to wave polarization.

### 4.1.3 Reflection, Transmission and Absorption coefficients

Transfer matrix  $M$  for a multilayer stack comprising  $N$  layers, as illustrated in Figure 4.1, can be obtained using the matrices, described in previous subsections, for the transition across individual layers  $I$  and the propagation of light through them  $P$ . Assuming light incoming from the semi-infinite material  $n_0$ , with initial amplitude  $E_i = 1$  and exits at the semi-infinite material with  $n_{N+1}$  (where no incoming light from the  $N+1$  layer is considered), the amplitudes of the incident (1), reflected ( $E_r$ ), and transmitted ( $E_t$ ) waves can be derived by

$$\begin{pmatrix} E_t \\ 0 \end{pmatrix} = M \begin{pmatrix} 1 \\ E_r \end{pmatrix} \quad (4.6)$$

where the final  $2 \times 2$  transfer matrix  $M$  is

$$M = I_{N,N+1} P_N I_{N-1,N} \dots I_{1,2} P_1 I_{0,1} \quad (4.7)$$

Using Equation 4.6, reflection (R) and transmission (T) coefficients of the multilayer stack can be defined as

$$R = \left| \frac{E_r}{E_i} \right|^2 = \left| -\frac{M_{21}}{M_{22}} \right|^2 \quad (4.8)$$

and

$$T = \left( \frac{n_{N+1} \cos \theta_{N+1}}{n_0 \cos \theta_0} \right) \left| \frac{E_t}{E_i} \right|^2 = \left( \frac{n_{N+1} \cos \theta_{N+1}}{n_0 \cos \theta_0} \right) \left| \frac{\det M}{M_{22}} \right|^2 \quad (4.9)$$

Assuming the existence of lossy layers in the multilayer structure, total absorption of the entire layered medium is

$$A = 1 - R - T \quad (4.10)$$

The absorption within a specific lossy layer can be obtained by

$$A_j = S_{j-1} - S_{j+1} \quad (4.11)$$

where  $S_{j-1}$ ,  $S_{j+1}$  are the radiative fluxes of electromagnetic energy through the previous and next layer (in respect to layer  $j$ ) and are defined by

$$S_j = \Re \left\{ \frac{n_j \cos \theta_j}{n_1 \cos \theta_1} \right\} (|E_j^+|^2 - |E_j^-|^2) - 2\Im \left\{ \frac{n_j \cos \theta_j}{n_1 \cos \theta_1} \right\} \Im \{ E_j^+ E_j^{-*} \} \quad (4.12)$$

where  $E_j^+$  and  $E_j^-$  correspond to the electric fields in layer  $j$  propagating in both light directions, as shown in Figure 4.1.

## 4.2 Finite Difference Time Domain(FDTD) Method

Investigating structures that involve reflections, interference, and scattering requires tools for simulating light propagation. Several methods can be utilized, including the Transfer Matrix Method (TMM), described in the previous section 4.1, Coupled Mode theory (used in a brief description of critical coupling mechanism in section B.1), beam propagation method, and eigenmode expansion method. Each of these methods presents distinct pros and cons in terms of accuracy, computational resources and suitability for selective applications. Among these techniques, the Finite-Difference Time-Domain (FDTD) method emerges as one of the most widely used and adaptable techniques in computational electrodynamics [7].

### 4.2.1 The Yee algorithm

FDTD method relies on an algorithm developed by K. S. Yee [8]. This algorithm discretizes both space and time, dividing space into Yee cells (as depicted in Figure 4.3), which represent arbitrary geometries. Time is discretized into small time-steps based on the time it takes for light to travel between cells. The electric and magnetic field components are arranged in Yee cells in a manner that satisfies Maxwell's curl equations and facilitates the use of second-order central differences for calculating space derivatives. The continuity of electric and magnetic fields is maintained across material interfaces parallel to any coordinate axis. Utilizing central difference operations, Gauss's laws are enforced,

resulting in a mesh that is divergence-free, when there is no existence of electric or magnetic charges. Yee formulation also enables the use of second-order central differences in solving the time derivatives of Maxwell's curl equations.

In FDTD method, subsequent time-stepping is employed, where  $H$  field computations are performed at each time-step using  $E$  field data from the previous time-step. This process continues until the simulation converges. Subsequent time-stepping is non-dissipative, ensuring that waves propagating across the Yee mesh do not decay due to artifacts, thereby enhancing the validity of this method. However, FDTD suffers from numerical dispersion, resulting in a frequency-dependent variance between numerically propagated waves and actual light waves. Ensuring algorithm stability necessitates to follow the Courant stability criterion, which relates spatial grid size and time-step.

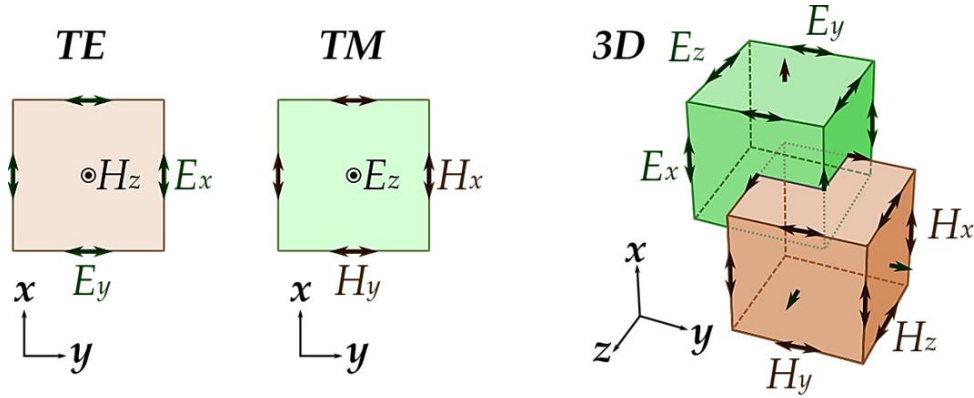


Figure 4.3: Schematic representations of a TE and TM 2D Yee cell (left) and a 3D box-shaped Yee cell (right), where  $E$  (or  $H$ ) field components are positioned on the edges and  $H$  (or  $E$ ) field components are on the faces.

Here, we explore how the optical behavior of dispersive materials is included in Maxwell equations and solved using the FDTD method. The curl Maxwell equations inside materials are the following

$$\nabla \times E = -\mu \frac{\partial H}{\partial t} \quad (4.13)$$

$$\nabla \times H = \frac{\partial \epsilon_0(E + \epsilon(\omega)E)}{\partial t} \quad (4.14)$$

Where the frequency-dependent dielectric function of material, which characterizes its dispersion, is  $\epsilon(\omega)$ . Material dispersion is considered by adopting a Drude-Lorentz model for  $\epsilon(\omega)$ , although other dispersive models (such as the Debye model, Plasma frequency model, etc.) can also be integrated [9, 10]. As extensively described in subsection 3.2.1, in the framework of Drude-Lorentz model,  $\epsilon(\omega)$  is expressed by Equation 3.32 [11]. Expressing the polarization  $P = \epsilon(\omega)E$  of the material as the sum of the Drude contribution, denoted as  $P_D$  and, each of the  $N$  Lorentz contributions, denoted as  $P_j$ , Equation 4.14 can be reformulated as

$$\nabla \times H = \epsilon_0 \epsilon_\infty \frac{\partial E}{\partial t} + \frac{\partial P_D}{\partial t} + \sum_{j=1}^N \frac{\partial P_j}{\partial t} \quad (4.15)$$

To incorporate material dispersion, FDTD employs time-domain differential equations for both Drude ( $P_D$ ) and each Lorentz ( $P_j$ ) polarization terms.

$$\frac{\partial^2 P_D}{\partial t^2} + \gamma_D \frac{\partial P_D}{\partial t} = \omega_P^2 \epsilon_0 E \quad (4.16)$$

$$\frac{\partial^2 P_j}{\partial t^2} + \Gamma_j \frac{\partial P_j}{\partial t} + \Omega_j^2 P_j = \Delta_j E \Omega_j^2 \epsilon_0 \quad (4.17)$$

To integrate Eqs. 4.16 and 4.17 into the FDTD algorithm, they need to be time-stepped, through the utilization of central differences (i.e.,  $\partial F/\partial x = (F(x + \Delta x/2) - F(x - \Delta x/2))/\Delta x$ ). Obtaining ADE for Drude polarization term of Equation 4.16, we can write [10]

$$P_{n+1}^D = c_{1,D} P_n^D + c_{2,D} P_{n-1}^D + c_{3,D} E_n \quad (4.18)$$

Similarly, the ADE for each Lorentz polarization term of Equation 4.17 becomes [10]

$$P_{n+1}^j = c_{1,L} P_n^j + c_{2,L} P_{n-1}^j + c_{3,L} E_n \quad (4.19)$$

Where  $c_{1,D} = (4\Delta t\gamma_D + 2)/(\Delta t\gamma_D + 2)$ ,  $c_{2,D} = (\Delta t\gamma_D - 2)/(\Delta t\gamma_D + 2)$  and  $c_{3,D} = (2\epsilon_0\Delta t\omega_P)/(\Delta t\gamma_D + 2)$  are the parameters used in Drude polarization term and  $c_{1,L} = (4 - 3\Delta t)/(\Delta t\Omega_j^2)$ ,  $c_{2,L} = (\Delta\Gamma_j - 2)/(\Delta\Gamma_j + 2)$  and  $c_{3,L} = (2\epsilon_0\Delta t\Delta\epsilon_j\Omega_j^2)/(\Delta\Gamma_j + 2)$  are those for each Lorentz polarization term.

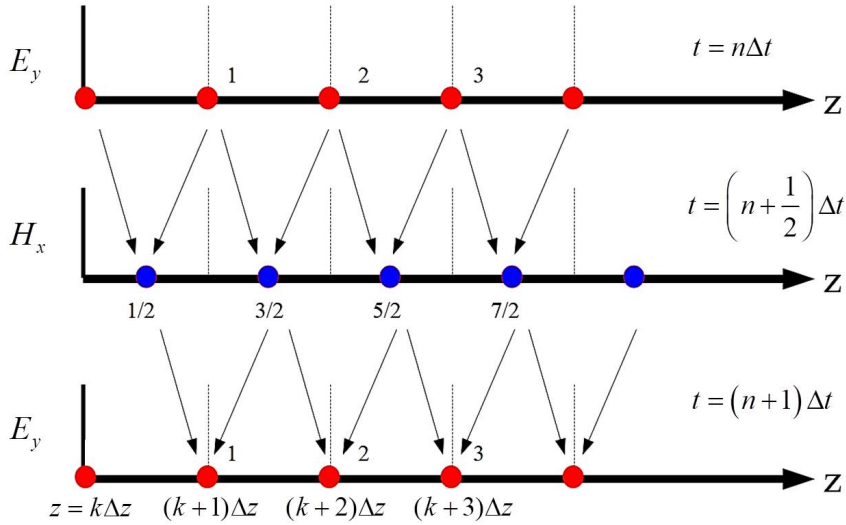


Figure 4.4: Schematic representation of a TE-polarized 1D Yee grid discretized in space ( $z$ ) and time ( $t$ ).

Considering a 1D Yee grid with TE-polarized propagating light, as illustrated in Figure 4.4, we can derive Maxwell's curl equations using the central differences as

$$(\nabla \times E)_y = -\mu \frac{\partial H_x}{\partial t} \quad (4.20)$$

$$(\nabla \times H)_x = \epsilon_0 \epsilon_\infty \frac{\partial E_y}{\partial t} + \frac{\partial P_D}{\partial t} + \sum_{j=1}^N \frac{\partial P_j}{\partial t} \quad (4.21)$$

Assuming an isotropic polarization for Drude and Lorentz terms, from Eqs. 4.20 and 4.21, we obtain both magnetic  $H_x$

$$H_x|_{k+1/2}^{n+1/2} = H_x|_{k+1/2}^{n-1/2} + \frac{\Delta t}{\mu \Delta x} (E_y|_{k+1}^n - E_y|_k^n) \quad (4.22)$$

and electric  $E_y$  field components

$$E_y|_k^{n+1} = E_y|_k^n - \frac{1}{\epsilon_0 \epsilon_\infty} (P_D|_k^{n+1} - P_D|_k^n) - \frac{1}{\epsilon_0 \epsilon_\infty} \sum_{j=1}^N (P_j|_k^{n+1} - P_j|_k^n) + \frac{\Delta t}{\epsilon_0 \epsilon_\infty \Delta z} (H_x|_{k+1/2}^{n+1/2} - H_x|_{k-1/2}^{n+1/2}) \quad (4.23)$$

Using the calculated quantities of  $P_D$  and  $P_j$  from Eqs. 4.18 and 4.19, respectively, E field can be derived and utilized to determine H field in the following time-step. The Yee algorithm proceeds with this subsequent time-stepping approach until the simulation satisfies convergence criteria and computation finishes. The respective equations for TM polarization, as well as for 2D and full 3D Yee grids (see Figure 4.3), can be similarly derived. To obtain frequency-dependent fields, a Fourier transformation is applied to the time-domain results. Throughout this thesis, FDTD simulations were conducted using the commercial FDTD solver Lumerical FDTD Solutions.

## 4.2.2 EM Sources in FDTD

Various electromagnetic sources can be utilized in FDTD simulations. In this thesis, two main sources were employed, such as a plane wave source and a dipole source (secondarily a mode source). Each of these sources is utilized for a different reason in injecting electromagnetic energy into the simulation area.

Specifically, plane wave source is utilized to introduce laterally-uniform electromagnetic energy from one side of the source region. In two-dimensional simulations, it injects energy along a line, while in three-dimensional simulations, it injects energy along a plane. On the other hand, a dipole source can be utilized to excite modes of cavities and resonators, or represent a point source, which emits a dipole radiation pattern (e.g. the spontaneous emission in LED devices). There are two types of dipole sources, the electric and magnetic dipoles. The electric dipole, used in this thesis, is equivalent to an oscillating point charge, whereas the magnetic dipole is equivalent to a current loop. Finally, the mode source can be utilized for injecting guided modes into the simulation area. By specifying the center location and span of mode source, guided modes for a selected structure can be computed. In three-dimensional simulations, these modes are computed across a plane, while in two-dimensional simulations, they are computed across a line. From a list of available modes, the desired mode can be selected for injection into the simulation area.

## 4.2.3 Boundary Conditions (BCs) in FDTD simulation

FDTD simulations offer the capability to calculate electric ( $E$ ) and magnetic ( $H$ ) fields at every point within the finite computational domain. In this simulation domain, it is

necessary to apply artificial boundaries, in order to adapt to the memory limitations of a computer. Under these boundaries, reflections and non-physical solutions appear in the simulation, necessitating special treatment, such as the utilization of Absorbing Boundary Conditions (ABCs) or Periodic Boundary Conditions (PBCs).

To simulate free-space, ABCs can be utilized surrounding the simulation region with an absorbing medium. ABCs employ lossy, impedance-matched medium, but they exhibit limitations for non-normal incident angles [9]. The use of Perfectly Matched Layers (PMLs) [12] can enhance the optical performance, by effectively splitting the field components in Maxwell's equations. Nonetheless, discretization in FDTD method may still result in spurious reflections. To face these difficulties, uni-axial mediums and complex frequency-shifted PMLs were developed [13, 14].

When examining a structure that displays periodicity along a specific axis, it is more efficient to simulate only a single unit cell and apply periodic boundary conditions (PBC) along that axis. This approach facilitates the repetition of the structure infinitely along the periodic axis, leading to significant reductions in computational resources. In non-periodic directions, absorbing boundary conditions (ABCs) can be employed, as mentioned previously.

#### 4.2.4 Benefits and limitations of FDTD Method

The main benefits of FDTD method stem directly from Yee algorithm [9, 15]. In contrast to frequency domain methods, FDTD enables obtaining device's response across a broad frequency spectrum in a single simulation run, as it addresses Maxwell's equations in the time domain. This is proved to be advantageous for broadband applications or unknown resonant frequencies. Following the Courant stability condition, FDTD exhibits exceptional stability. Furthermore, by employing the central-difference approach of the Yee algorithm, computer round-off errors are minimized. As the fields are numerically propagated across the simulation domain and Maxwell's curl equations are explicitly solved, this method avoids fake solutions. FDTD facilitates accurate modelling of dispersive and non-linear media, facilitating the investigation of various effects, related to linear or non-linear dielectric and magnetic structures. Additionally, FDTD can handle any geometry, provided that the grid discretization is fine enough to accurately represent small features.

However, the FDTD method has some limitations [9, 15]. As previously mentioned, the inherent numerical dispersion of the Yee formulation can be a restriction. This issue can be improved by employing a finer mesh grid, although this solution requires an increased number of computational resources. Simulating high-Q structures, where energy dissipation occurs slowly, FDTD demands lengthy computational times. Finally, approximating more complex geometries with dimensions smaller than the wavelength of interest, can be challenging with FDTD. In those cases, there is a need of finer mesh which will extend the computation time. Furthermore, these limitations can be confined through advanced meshing techniques, such as conformal meshing.

### 4.3 Finite Difference Eigenmode (FDE) Method

Eigenmode solvers are computational techniques essential for identifying the permissible optical modes in waveguides according to their geometry and frequency [7]. Among these methods, the Finite Difference Frequency Domain (FDFD) method is usually employed for solving the vector-wave equations derived from Maxwell's curl equations [16–18].

FDFD algorithms are especially well-suited for structures exhibiting high-index contrast and are utilized in full-vector Finite Difference Eigenmode (FDE) solvers [17]. FDE solvers calculate the spatial profile and frequency dependence of optical modes, by solving Maxwell's equations on the cross-section of a waveguide. Waveguide cross-section is discretized using a 2D Yee mesh [16], similar to the one used to explain FDTD solvers in section 4.2 (see Figure 4.3). FDE solvers can calculate waveguide mode field profiles, effective indices and losses.

FDFD method enables the efficient calculation of all field components through the solution of eigenvalue equations and the utilization of coefficient matrices. These matrices aid in memory storage and enhance computational efficiency. It is noteworthy that close to complex structures, where field variations are rapid, additional spatial discretization limitations may be needed, necessitating the use of smaller mesh sizes. Moreover, since FDE solvers operate in the frequency domain, they require computationally intensive calculations to derive wavelength-dependent outcomes, such as the dispersion relation for a specific mode. In Chapter 7 of this thesis, FDE simulations were conducted, utilizing the commercial FDE solver by Lumerical MODE Solutions.

## 4.4 Runge-Kutta calculation method

The three coupled rate equations (see Eqs. 2.14-2.16), mentioned in previous chapter, can describe the temporal optical response of graphene-based devices, analyzed in Chapter 6 of this thesis. These equations are commonly utilized alongside TMM, requiring numerous calculations to achieve a broadband result. Additionally, they are incorporated into self-consistent iterations, often requiring multiple calculations until they reach the convergence. Therefore, it is imperative to efficiently handle them. To address this, 4th order Runge-Kutta method is employed [19–21]. This method is an explicit iterative technique widely used for temporal discretization, as illustrated in Figure 4.5.

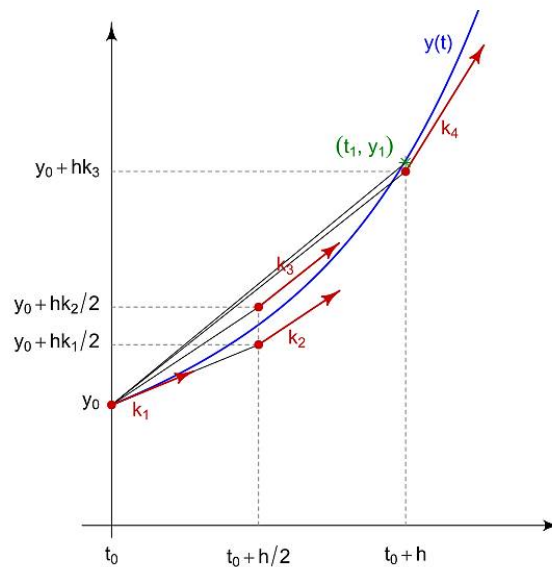


Figure 4.5: Schematic diagram of the time steps and derivatives of Runge-Kutta calculation method, that arise from the Equations 4.25.

For simplicity, we consider an initial differential equation as

$$f(t, y) = \frac{\partial y}{\partial t} \quad (4.24)$$

Where function  $f(t, y)$  and initial parameters  $t_0, y_0 = y(t_0)$  are known. With time-step  $\Delta t > 0$ ,  $y$  (for  $n$  integer) can be written as

$$y_{n+1} = y_n + \frac{\Delta t}{6}(k_1 + 2k_2 + 2k_3 + k_4) \quad (4.25)$$

$$t_{n+1} = t_n + \Delta t$$

Where the four coefficients  $k_1, k_2, k_3$  and  $k_4$ , shown in Figure 4.5, are

$$k_1 = f(t_n, y_n)$$

$$k_2 = f\left(t_n + \frac{\Delta t}{2}, y_n + \Delta t \frac{k_1}{2}\right) \quad (4.26)$$

$$k_3 = f\left(t_n + \frac{\Delta t}{2}, y_n + \Delta t \frac{k_2}{2}\right)$$

$$k_4 = f(t_n + \Delta t, y_n + \Delta t k_3)$$

In other words, the value  $y_{n+1}$  is determined by adding the previous value  $y_n$  to the weighted average of 4 increments. Each increment is the product of the time interval  $\Delta t$  and slope  $k$  (with additional weight on the middle point slopes). The 4th-order method, exhibiting  $O(t^4)$  order accumulation error, is allowed to provide accurate approximate solutions, without requiring excessively small discretization, in contrast to other numerical methods for ordinary differential equations (such as Euler's method).

## References

- [1] M. Born and E. Wolf, *Principles of optics: electromagnetic theory of propagation, interference and diffraction of light*. Elsevier, 2013.
- [2] T. G. Mackay and A. Lakhtakia, *The transfer-matrix method in electromagnetics and optics*. Springer Nature, 2022.
- [3] O. S. Heavens, *Optical properties of thin solid films*. Courier Corporation, 1991.
- [4] P. Yeh and M. Hendry, "Optical waves in layered media," *Physics Today*, vol. 43, no. 1, p. 77, 1990.
- [5] O. Deparis, "Poynting vector in transfer-matrix formalism for the calculation of light absorption profile in stratified isotropic optical media," *Optics letters*, vol. 36, no. 20, pp. 3960–3962, 2011.
- [6] D. V. Bellas, D. Toliopoulos, N. Kalfagiannis, A. Siozios, P. Nikolaou, P. C. Kelires, D. C. Koutsogeorgis, P. Patsalas, and E. Lidorikis, "Simulating the opto-thermal processes involved in laser induced self-assembly of surface and sub-surface plasmonic nano-structuring," *Thin Solid Films*, vol. 630, pp. 7–24, 2017.
- [7] L. Chrostowski and M. Hochberg, *Silicon photonics design: from devices to systems*. Cambridge University Press, 2015.

- [8] K. Yee, "Numerical solution of initial boundary value problems involving maxwell's equations in isotropic media," *IEEE Transactions on antennas and propagation*, vol. 14, no. 3, pp. 302–307, 1966.
- [9] A. Taflove, S. C. Hagness, and M. Picket-May, "Computational electromagnetics: the finite-difference time-domain method," *The Electrical Engineering Handbook*, vol. 3, no. 629-670, p. 15, 2005.
- [10] M. A. Alsunaidi and A. A. Al-Jabr, "A general ade-fdtd algorithm for the simulation of dispersive structures," *IEEE Photonics Technology Letters*, vol. 21, no. 12, pp. 817–819, 2009.
- [11] F. Wooten, *Optical properties of solids*. Citeseer, 1972.
- [12] J.-P. Berenger, "A perfectly matched layer for the absorption of electromagnetic waves," *Journal of computational physics*, vol. 114, no. 2, pp. 185–200, 1994.
- [13] S. D. Gedney, "An anisotropic perfectly matched layer-absorbing medium for the truncation of fdtd lattices," *IEEE transactions on Antennas and Propagation*, vol. 44, no. 12, pp. 1630–1639, 1996.
- [14] M. Kuzuoglu and R. Mittra, "Frequency dependence of the constitutive parameters of causal perfectly matched anisotropic absorbers," *IEEE Microwave and Guided wave letters*, vol. 6, no. 12, pp. 447–449, 1996.
- [15] W. Yu and R. Mittra, "A conformal finite difference time domain technique for modeling curved dielectric surfaces," *IEEE Microwave and Wireless Components Letters*, vol. 11, no. 1, pp. 25–27, 2001.
- [16] Z. Zhu and T. G. Brown, "Full-vectorial finite-difference analysis of microstructured optical fibers," *Optics express*, vol. 10, no. 17, pp. 853–864, 2002.
- [17] K. Chiang, "Review of numerical and approximate methods for the modal analysis of general optical dielectric waveguides," *Optical and Quantum Electronics*, vol. 26, pp. S113–S134, 1994.
- [18] C. Vassallo, "1993–1995 optical mode solvers," *Optical and Quantum Electronics*, vol. 29, no. 2, pp. 95–114, 1997.
- [19] K. Atkinson, *An introduction to numerical analysis*. John wiley & sons, 1991.
- [20] U. M. Ascher and L. R. Petzold, *Computer methods for ordinary differential equations and differential-algebraic equations*, vol. 61. Siam, 1998.
- [21] J. Stoer, "R. bulirsch introduction to numerical analysis springer-verlag," *Texts in Applied Mathematics*, vol. 12, p. 30, 2002.

## Chapter 5

# SERS of Graphene on Plasmonic Silicon Substrates

Integrating graphene with plasmonic nanostructures results in multi-functional hybrid systems with enhanced performance for numerous applications [1–5]. In this chapter, we take advantage of the remarkable mechanical properties of graphene to combine it with scalable three-dimensional (3D) plasmonic nanostructured silicon substrates, which enhance the interaction of graphene with electromagnetic radiation. Our FDTD simulations elucidate the advantages of 3D topography of the substrate. Arrays of silicon nanopillars, decorated with gold nanoparticles, are modeled with graphene, which conforms to the substrate nanotopography. Two-three orders of magnitude Raman intensity enhancement is obtained at 488, 514, 633, and 785 nm excitation wavelengths, similarly to the highest enhancements measured to date, concerning surface-enhanced Raman spectroscopy of graphene on plasmonic substrates [6–17]. Conformation of graphene to Au-decorated silicon nanopillars enables graphene to sample near fields from an increased number of nanoparticles. Due to synergistic effects with the nanopillars, different nanoparticles become more active for different wavelengths and locations on the pillars, providing broad-band enhancement. Nanostructured plasmonic silicon is a promising platform for integration with graphene and other 2D materials, for next-generation applications of large-area hybrid nanomaterials in the fields of sensing, photonics, optoelectronics and medical diagnostics.

*This chapter is based on:*

- Kanidi, M., Dagkli, A., Kelaidis, N., Palles, D., Aminalragia-Giamini, S., Marquez-Velasco, J., ... Kamitsos, E. I. (2019). *Surface-enhanced Raman spectroscopy of graphene integrated in plasmonic silicon platforms with three-dimensional nanotopography*. The Journal of Physical Chemistry C, 123(5), 3076-3087.

<https://doi.org/10.1021/acs.jpcc.8b10356>

## 5.1 Introduction

Most of graphene's photonic and optoelectronic applications [1–5] involve its interaction with electromagnetic fields, as extensively described in section 2.1. Therefore, enhancing this interaction is essential. Integrating SLG with plasmonic nanostructures results in experiencing enhanced electromagnetic near-fields, due to coupling with surface plasmon modes, described in section 3.1 [18]. Plasmonic nanostructures in combination with graphene or other two-dimensional materials have already demonstrated promising potential for the development of high-performance solar cells [19], photodetectors [5, 20], optical modulators [21], fuel cells [22], as well as chemical and biological sensors [23, 24].

A revealing process for the understanding and exploitation of the interaction of SLG with plasmonic substrates is Surface-Enhanced Raman Scattering (SERS), which fundamentally relies on light–graphene interaction, as described in subsection 2.1.5. Enhancing the Raman spectrum of graphene is important for understanding the behavior of graphene on a given substrate, as it allows for the identification of the number of layers, type of doping, strain, defects, temperature effects, chemical modification, disorder, and edges, among others [25–27]. The vital dependence of the properties of two-dimensional (2D) materials on the underlying substrate and the modulation of these properties by substrate engineering have been reviewed recently by Sun et al [28]. Integration of graphene with plasmonic metallic nanostructures has been shown to enhance the Raman signal of graphene by 2–3 orders of magnitude [6–17]. To this end, various kinds and geometries of metallic nanostructures have been employed, including nanodisks [12], nanodots [13], nanopyramids [11], polygons, dendrites, dense clusters [16], and irregular islands [7, 16], which resulted in measured enhancement factors of the Raman signal of graphene as high as  $10^3$ . However, most of these structures are limited to laboratory size areas, which lack scalability, constricting real-world applications [29–31]. Furthermore, they are mostly restricted to 2D topographies, usually lying on flat substrates, with which graphene behaves mainly as a rigid over- or under-layer. Therefore, the challenge remains for integration of graphene with large-scale plasmonic nanostructures, taking advantage of the mechanical stability of graphene in three-dimensional (3D) configurations.

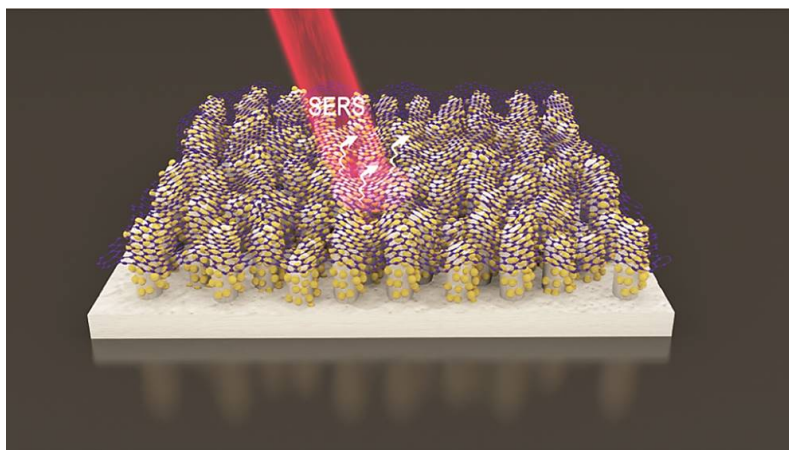


Figure 5.1: Schematic of the Raman signal of graphene, when it is on top of nanostructured silicon (3D) substrate decorated with gold nanoparticles [32].

In this chapter, we exploit the exceptional mechanical properties of graphene, by integrating it with scalable 3D plasmonic nanostructured silicon substrates, as schematically

illustrated in Figure 5.1. This combination enhances the interaction of graphene with electromagnetic radiation. The conformation of graphene to Au-decorated silicon nanopillars allows graphene to sample near fields from an increased number of nanoparticles. Through synergistic effects with the nanopillars, various nanoparticles become more active across different wavelengths and locations on the pillars, thus providing broad-band enhancement. Nanostructured plasmonic silicon emerges as a promising platform for integration with graphene and other 2D materials, enabling next-generation applications of large-area hybrid nanomaterials in the fields of sensing, photonics, optoelectronics, and medical diagnostics.

## 5.2 SERS measurements of SLG on Si substrates

Raman spectroscopy is a powerful tool for characterizing the structures of graphitic materials [33, 34], as extensively described in subsection 2.1.5. It has been used to investigate the behavior of electrons and phonons in graphene, as well as to monitor phenomena, as mentioned previously, such as doping [35–38], defects [39, 40], strain [41], disorder [42], chemical modifications [43], and edges [44]. The Raman bands of carbon materials are highly distinguishable and can accurately reveal subtle changes in crystal structure. For example, under 514 nm excitation, the characteristic Raman bands of graphene on silicon substrates include only the G band ( $1580\text{ cm}^{-1}$ ), the 2D band ( $2680\text{ cm}^{-1}$ ), and the 2D' band ( $3250\text{ cm}^{-1}$ ) [44]. However, Raman bands such as the T band ( $1087\text{ cm}^{-1}$ ), the D band ( $1350\text{ cm}^{-1}$ ), and the D' band ( $1620\text{ cm}^{-1}$ ) [45], which belong to the inner layer Raman active modes of  $sp^2$  carbon material, cannot be observed in intrinsic graphene (except at its edges). Most of these bands are related to defects in graphene, that may alter its electronic properties, and have great potential applications in electronic devices [46, 47]. SERS is widely used to detect interaction signals at the interface, due to its nanometer scale and high surface-selective sensitivity. It not only provides high surface sensitivity and signal enhancement but can also quench the fluorescence of the substrate to achieve high-quality Raman signal measurements.

In this study, large areas of femtosecond laser-structured arrays of silicon nanopillars, decorated with gold nanoparticles, are integrated with graphene, which conforms to the substrate nanotopography. Experimental Raman spectra of graphene are obtained at four different excitation wavelengths (488, 514, 633, and 785 nm), covering the entire visible range, on four different silicon substrates (flat pristine silicon, flat silicon with a 50 nm gold film, uncoated nanostructured silicon, and nanostructured silicon with gold nanoparticles). Figure 5.2 shows the measured Raman spectra of graphene on these four different silicon substrates and selected excitation wavelengths.

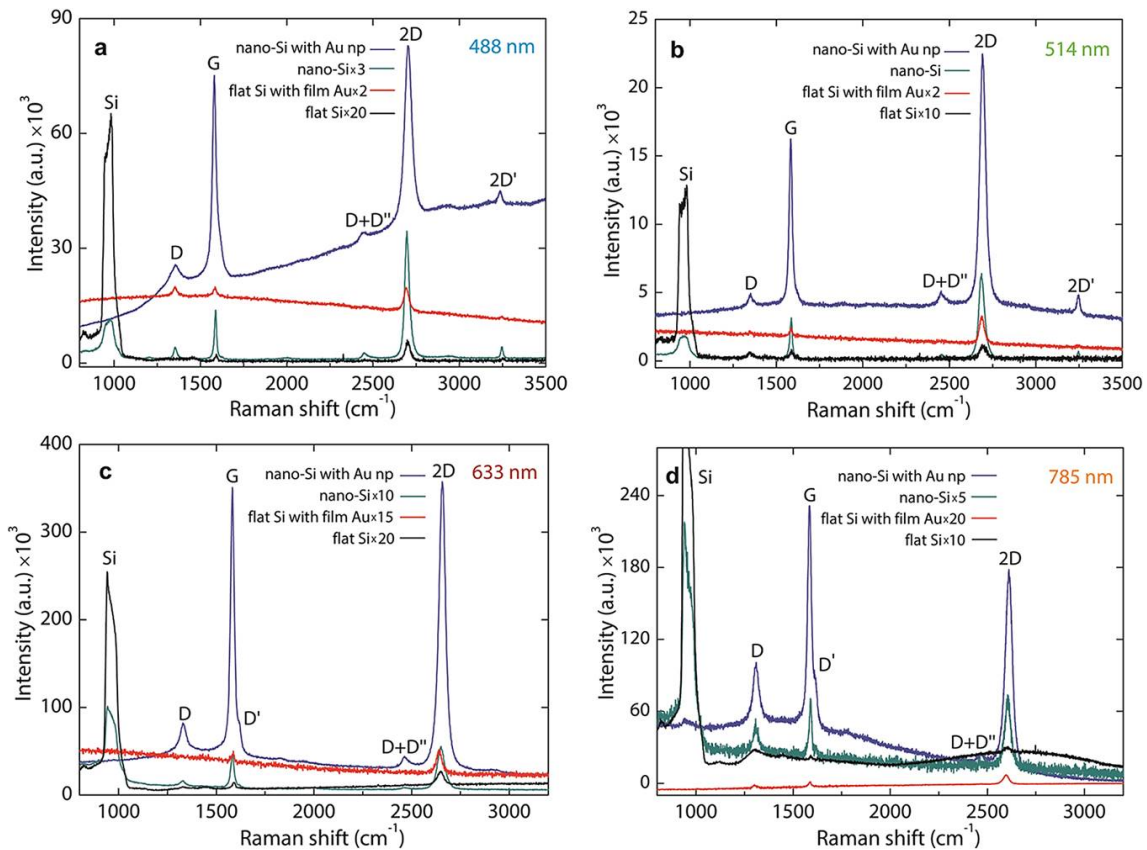


Figure 5.2: Experimental Raman spectra of graphene on flat pristine silicon, flat silicon with 50 nm gold film, uncoated nanostructured silicon, and nanostructured silicon with gold nanoparticles measured with (a) 488 nm, (b) 514 nm, (c) 633 nm, and (d) 785 nm excitation wavelengths. For clarity, Raman spectra have been magnified, when necessary, by the indicated magnification factors. Measurements performed by M. Kanidi [32].

Since the Raman spectra of graphene on plasmonic silicon substrate exhibit significant enhancement, the spectra on the other substrates are depicted magnified in Figure 5.2. This amplification enables the main spectral features to be visible. G and 2D peaks of graphene are clearly observed in the Raman spectra of all substrates, with notable enhancement on the plasmonic substrate (dark blue line). This enhancement in Raman scattering intensity for the plasmonic substrate enables the fine structure of graphene Raman spectrum to be discerned. Indeed, peaks that are typically challenging to detect in conventional Raman scattering of graphene on pristine silicon substrates, are now observable.

### 5.3 SERS on flat substrate

We complement the Raman measurements of section 5.2 with numerical simulations, to confirm the plasmonic nature of Raman enhancement and gain insight into the effect of the substrate topography. We use the FDTD method, described in section 4.2 [48, 49], following the procedure established in reference [13]. We assume that the absorption at a particular point in graphene is proportional to the locally enhanced tangential field intensity and that the Raman emission from that point is proportional to the corresponding Stokes-shifted enhanced intensity. Specifically, for an incident field  $|E_{\parallel}^0(r, \omega)|$  at point  $r$

on suspended graphene and modulated fields  $|E_{\parallel}(r, \omega)|$  and  $|E_{\parallel}(r, \omega_s)|$ , when graphene is on a substrate, we calculate the Raman signal enhancement as:

$$S(r, \omega) = \frac{|E_{\parallel}(r, \omega)|^2 |E_{\parallel}(r, \omega_s)|^2}{|E_{\parallel}^0(r, \omega)|^4} \quad (5.1)$$

Where  $\omega$  and  $\omega_s$  are the incident and the Stokes-shifted frequencies. In each calculation, only the electric field component parallel to the graphene basal plane is taken into account, as signified by the ( $\parallel$ ) subscript. For a flat substrate, is by symmetry the same for every point and thus yields the final result for enhancement, while for graphene on a corrugated substrate, integration has to be performed over the entire illuminated area. In our calculations, we only assume periodic cells and thus the integration is performed over the unit cell area.

We start with flat substrates, semi-infinite silicon and Au (50 nm)/Si, as shown in Figure 5.3. Taking the first substrate as the reference case, we plot the calculated G and 2D Raman enhancement factors,  $F = S_{Au/Si}/S_{Si}$ , along with the corresponding experimental points for G and 2D bands, for the four wavelengths of interest.

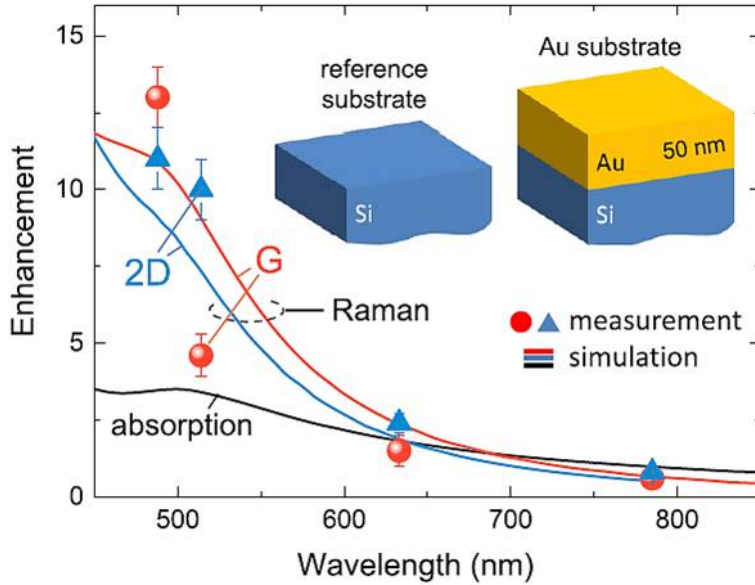


Figure 5.3: Measured and simulated Raman enhancement factors for graphene on Au (50 nm)/Si compared to graphene on silicon. The calculated graphene absorption enhancement is also plotted for reference. The solid red and blue lines denote simulation results, and the symbols denote the corresponding experimental data. Measurements performed by M. Kanidi [32].

An overall good agreement is found in regard to the spectral dependence, although there is some scattering in the data for the lower wavelengths. The reason for the large enhancement at low wavelengths is the very strong quenching in bare silicon case. In simple terms, for light reflected off a flat surface of a semi-infinite material with complex refractive index  $n$ , the reflected amplitude is  $r = (1 - n)/(1 + n)$  and the corresponding total complex field at the surface (where we assume that graphene would be) is  $E = 1 + r = 2/(1 + n)$ . Assuming graphene on that surface, its absorption is proportional to  $\sigma|E|^2$  (where  $\sigma$  is the in-plane graphene conductivity), the relative enhancement of

absorption, compared to graphene suspended in air, is  $4/|1+n|^2$ , and the relative Raman enhancement is  $16/|1+n|^4$ , where we assumed for simplicity zero Stokes shift. Here, we have to note that the above considerations are approximate, since the presence of graphene on the surface will slightly modify the field values. Graphene absorption enhancement, expressed as the ratio of absorption of graphene on gold to absorption of graphene on silicon, is also plotted in Figure 5.3. Using literature data for the refractive index of silicon [50] and gold [51] substrates and assuming for simplicity the latter to be semi-infinite instead of 50 nm, we obtain  $S_{Si} \cong 0.02$  and  $S_{Au} \cong 0.28$  at 500 nm incident wavelength ( $n_{Si} \cong 4.3+i0.07$ ,  $n_{Au} \cong 0.97+i1.87$ ), yielding  $S_{Si}/S_{Au} \cong 14$ , explaining the simulation results and measurements. At longer wavelengths, Au becomes more reflective and the actual field magnitude on the surface diminishes. For example, at 650 nm wavelength ( $n_{Si} \cong 3.85 + i0.0165$ ,  $n_{Au} \cong 0.156 + i3.6$ ) the Raman enhancement is estimated at  $S_{Si}/S_{Au} \cong 2.7$ , while at 800 nm wavelength ( $n_{Si} \cong 3.69 + i0.0065$ ,  $n_{Au} \cong 0.154 + i4.9$ ) we get a reduction  $S_{Si}/S_{Au} \cong 0.75$ . However, it is noteworthy that in all cases, there is a quenching compared to the Raman signal expected from graphene suspended in air. In light of this, we anticipate a significant increase in signal once we remove graphene away from the flat substrate, e.g., as in placing it on top of nanostructured silicon.

## 5.4 SERS on nanostructured Si substrate

For nanostructured silicon, we assume a simplified model consisting of a periodic square array of silicon pillars with period  $L=400$  nm, base radius  $\rho_0=150$  nm, and height  $z_t=500$  nm, as shown in Figure 5.4(a). The pillars follow the functional form  $z = z_t(1 - \rho^4/\rho_0^4)$ , where  $\rho = \sqrt{x^2 + y^2}$  is the radial position away from the pillar center.

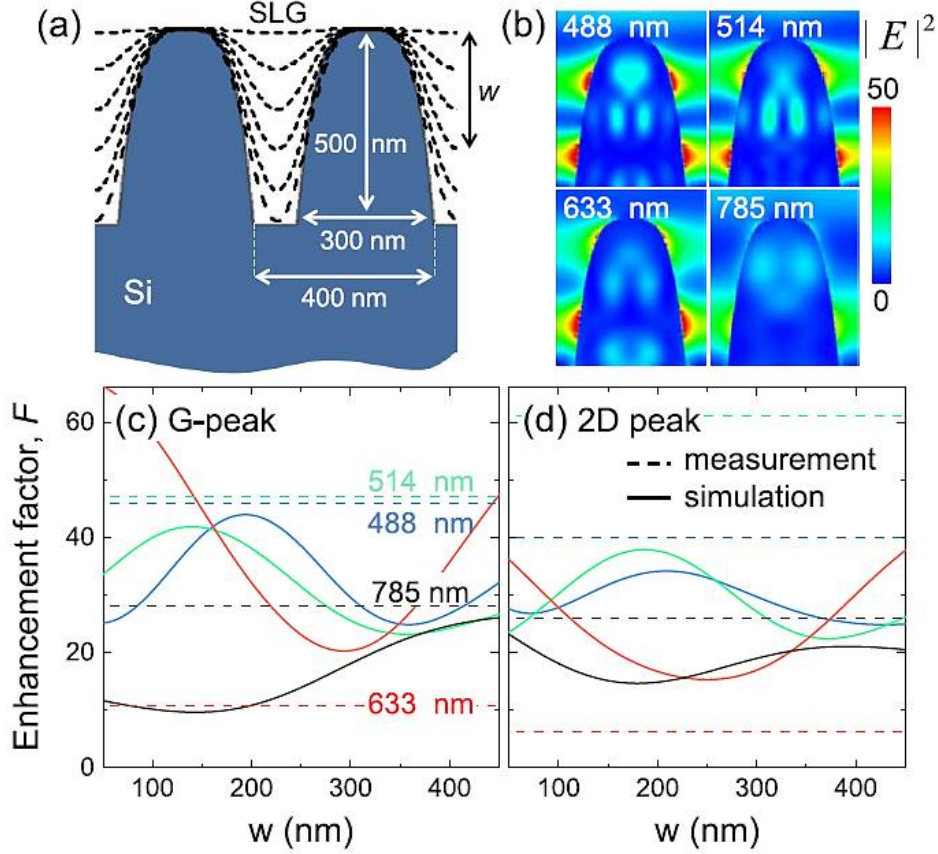


Figure 5.4: (a) Simulation model consists of a square array of silicon pillars. (b) Electric field intensity enhancement distribution (compared to the incident intensity) for the four wavelengths of interest. (c) and (d) Raman peak enhancement factors (with respect to graphene on flat silicon) as a function of the maximum graphene conformation depth,  $w$ , in-between the silicon pillars. The dashed lines indicate the experimental measurements. Measurements performed by M. Kanidi [32].

For the graphene conformation on top of nanostructured silicon, we assume a two-dimensional functional  $z = z f(x) f(y)$  with

$$f(x) = 1 - \alpha \left| \cos^d \left( \frac{\pi x}{L} \right) \right| \quad (5.2)$$

and similarly for  $y$ . Where  $\alpha = 1 - \sqrt{1 - w/z_t}$  and  $w$  is the maximum depth of the graphene sheet drop in-between the pillars (see Figure 5.4(a)). The exponent  $d$  determines the shape of graphene sheet on top of each pillar and is adjusted to better match the functional form of pillar itself at its top. In our calculations, we used  $d=4$  for the uncoated nanostructured silicon case and  $d=6$  for the Au-decorated nanostructured silicon. Different graphene conformations for various  $w$  values are shown in Figure 5.4(a) by dashed lines. Our goal is to calculate Raman enhancement as a function of  $w$  and gain insight into the effect of graphene conformation.

To avoid performing an enormous amount of calculations, we choose the simplified approach of performing the simulation without graphene and monitoring the modulated fields at every point in the structure. Then, in post-processing mode, we integrate the tangential product  $|E_{\parallel}(r, \omega)|^2 |E_{\parallel}(r, \omega_s)|^2$  over the presumed graphene sheet area. Here, we have to note that the graphene area is larger than  $L^2$ , due to conforming around the

silicon pillars. The parallel component is found by

$$E_{\parallel}(r) = E(r) \times n(r) \quad (5.3)$$

Where  $n(r)$  is graphene surface normal unit vector at position  $r(n) = (\frac{\partial z}{\partial x}, \frac{\partial z}{\partial y}, -1)$  and  $z = zf(x)f(y)$  is the two-dimensional functional, defining graphene conformation (see above).

The electric field intensity distribution  $|E(r, \omega)|^2/|E_0(r, \omega)|^2$  is shown on vertical cross section for the four selective incident wavelengths in Figure 5.4(b). The Fabry-Perot standing waves, which as expected vary for different wavelengths, give an indication of the importance of graphene conformation, particularly on the value of  $w$  parameter in our model. The Raman enhancement factors, with respect to graphene on flat silicon, are shown in Figs. 5.4(c-d) for the G and 2D bands, respectively, at the four wavelengths of interest. Strong fluctuations are observed as the graphene depth  $w$  increases. The variation in 2D is smaller than the one for G, which is, however, expected taking into account that  $\omega_s$  is more red-shifted in the former case. With dashed horizontal, lines denoting the experimental measurements, we note a good qualitative agreement for the three excitation wavelengths 488, 514, and 785 nm, but a rather large deviation for 633 nm. Theoretically, we do not expect such a small enhancement value at this particular wavelength and, thus, cannot explain this disagreement at this point. Aside from that and considering the large number of simplifications made in this theoretical study, regarding both the actual silicon nanostructure (random pillar heights, thicknesses, shapes, and separations) and graphene conformation on it, the agreement concerning the order of magnitude of the enhancement is more than satisfactory.

## 5.5 SERS on Au-decorated nanostructured Si substrate

Consequently, we simulate the Au-decorated nanostructured silicon substrate. A cross section of the model is shown in Figure 5.5(a), where 50 nm diameter gold spheres have been placed on the silicon pillars. Here, we ignore the presence of a native oxide silicon layer on the silicon pillars because its effect on the electromagnetic response of the substrate is negligible (see Appendix A.1). The graphene sheet conformation is now around the gold spheres as well. To keep our model simple, we assume the same functional form for graphene of Equation 5.2, but with its highest point to be through the nanoparticle center, i.e.  $z_t=525$  nm. This effectively assumes that graphene wraps around half of the nanoparticle.

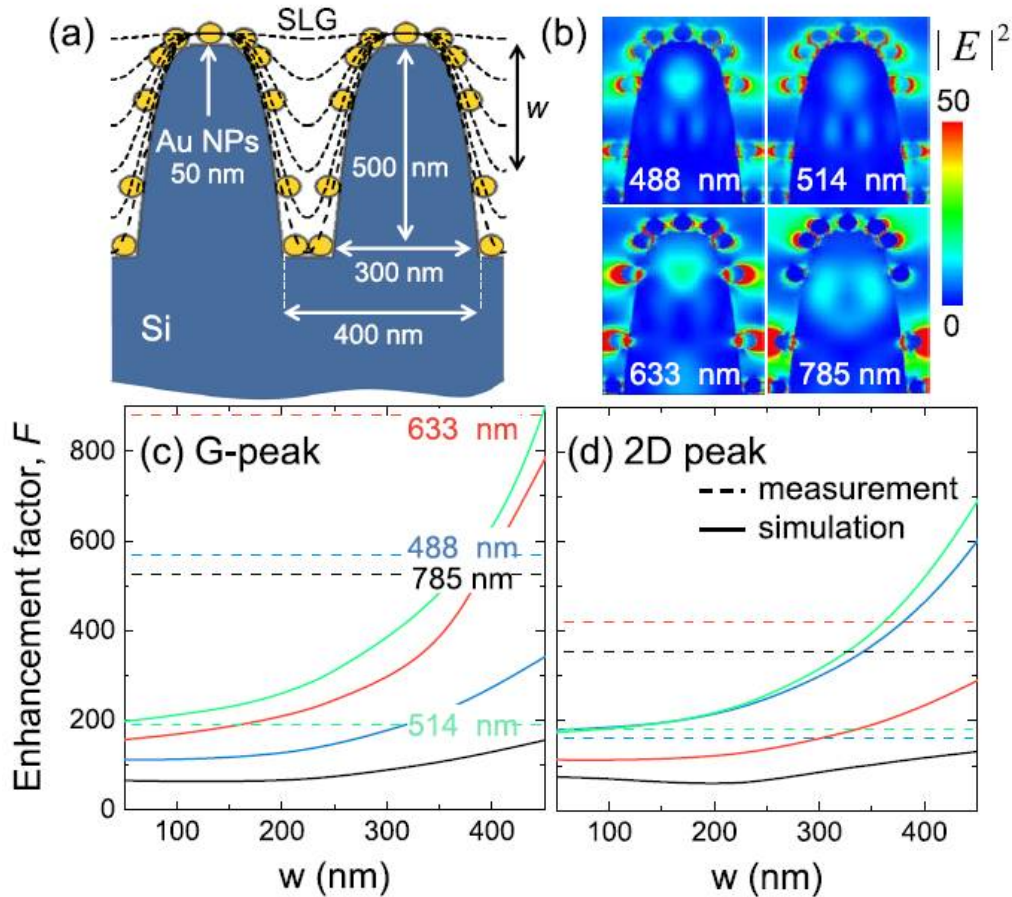


Figure 5.5: (a) Simulation model consists of a square array of silicon pillars decorated with gold nanoparticles. (b) Electric field intensity enhancement distribution (compared to the incident intensity) for the four wavelengths of interest. (c) G-peak and (d) 2D Raman peak enhancement factor (with respect to graphene on flat silicon) as a function of the maximum graphene conformation depth,  $w$ , in between the silicon pillars. The dashed lines indicate the experimental measurements. Measurements performed by M. Kanidi [32].

The Raman calculation follows the same process as before, utilizing the calculated field intensity distribution, whose profile for the four wavelengths is shown in Figure 5.5(b). Due to the Fabry–Pérot resonances, now different nanoparticles become more active for different wavelengths. Figs. 5.5(c) and (d) show the estimated Raman enhancement factors as a function of  $w$  with respect to graphene on flat silicon. The experimental results are denoted by the horizontal dashed lines. Rather than an oscillatory behavior, due to standing wave resonances, as in the case of uncoated nanostructured silicon, we note in simulation results a monotonic increase of Raman enhancement with increasing graphene conformation depth  $w$ . This is due to graphene sheet sampling more plasmonic nanoparticle near-fields and thus emitting a stronger SERS signal. Additionally, as shown in Figure 5.5(b), nanoparticles lying near the base of the silicon pillars create stronger electric near-fields, compared to nanoparticles lying near the top of the pillars. In our calculations, we ignore the quenching of plasmonic response of gold nanoparticles due to graphene absorption, as this is negligible for single-layer graphene (see Appendix A.2). There is, again, some scatter between experimental and simulation results, but this should be expected considering the added complexity of gold nanoparticle decorations (size, shape,

and distribution) combined with the complexity of nanostructured silicon substrate. Variations in gold nanoparticle's size, present in this study due to the spontaneous formation of nanoparticles, are expected to cause small changes in the distance of graphene from silicon nanopillars. However, the plasmonic response of nanoparticles heavily dominates Raman enhancement, as shown when comparing Figure 5.4 with Figure 5.5. Therefore, the effect of graphene's distance from silicon nanopillars is not noticeable. The actual Raman hot-spots on the graphene sheet, projected on a horizontal (xy) plane, are depicted in Figure 5.6 for  $\lambda=633$  nm and  $w=450$  nm.

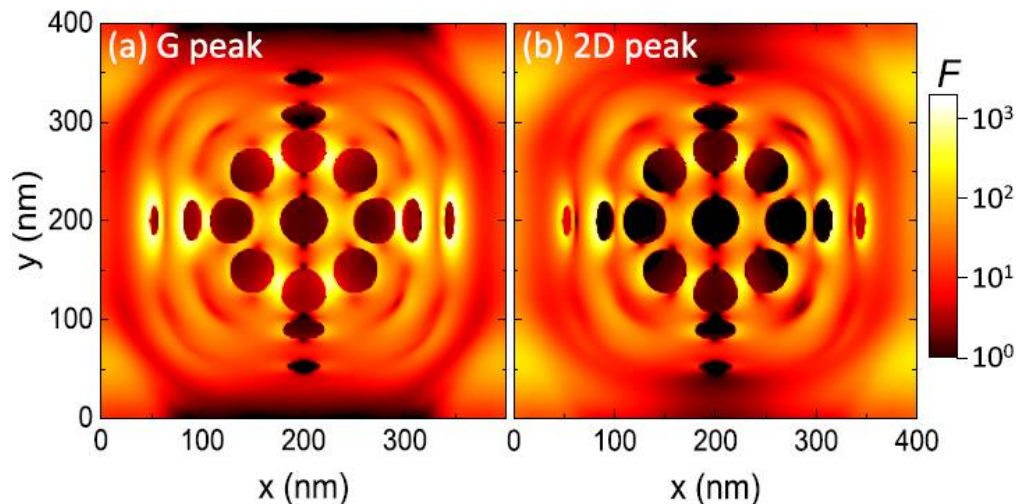


Figure 5.6: Distribution of Raman G (a) and 2D (b) peak enhancement factor of graphene on nanostructured silicon with gold nanoparticles (with respect to the flat silicon case) projected onto a horizontal plane for incident wavelength  $\lambda=633$  nm and graphene conformation depth  $w=450$  nm [32].

In Figure 5.6 the strong effect of plasmonic near-fields is evident. At Raman hot-spots, the local enhancement is calculated to reach values as high as  $\sim 2500$  and  $\sim 1600$  for the G and 2D peaks, respectively. Simulations of graphene on flat silicon decorated with gold nanoparticles (see Appendix A.3) show that SERS enhancement of graphene is an order of magnitude less than the enhancement on Au-decorated silicon pillars, which is caused by the destructive interference between incident waves and waves reflected off the flat silicon interface. Therefore, 3D topography, which disrupts the flat interface, is preferential for SERS on reflective surfaces.

## 5.6 Comparisons-Numerical verification

To summarize, a comparison of experimental Raman enhancement factors, measured by M.Kanidi from Theoretical and Physical Chemistry Institute of National Hellenic Research Foundation, with the results from our numerical simulations for selective excitation wavelengths is presented in this section. Table 1 shows the measured enhancement factors for G and 2D peaks of graphene for each substrate used in this work.

Table 1: Measured SLG Raman Intensity Enhancement Factors  $F_G$  and  $F_{2D}$ 

	Au film		nano-Si		nano-Si +NPs	
$\lambda$ (nm)	$F_G$	$F_{2D}$	$F_G$	$F_{2D}$	$F_G$	$F_{2D}$
488	$13 \pm 1$	$11 \pm 1$	$46 \pm 3$	$40 \pm 2$	$568 \pm 30$	$162 \pm 8$
514	$4.6 \pm 0.7$	$10 \pm 1$	$47 \pm 6$	$61 \pm 6$	$189 \pm 18$	$182 \pm 18$
633	$1.5 \pm 0.5$	$2.4 \pm 0.3$	$10.7 \pm 0.6$	$6.3 \pm 0.3$	$880 \pm 35$	$422 \pm 17$
785	$0.6 \pm 0.1$	$0.8 \pm 0.1$	$28 \pm 5$	$26 \pm 3$	$526 \pm 60$	$355 \pm 40$

The enhancement factors, presented in Table 1, are calculated with respect to graphene on flat silicon. As shown in the above table, the highest enhancement factors, between two and three orders of magnitude, are obtained using nanostructured silicon substrate with gold nanoparticles. In the following, we average the calculated results for all  $w$  values and plot them along with the experimental values in Figure 5.7.

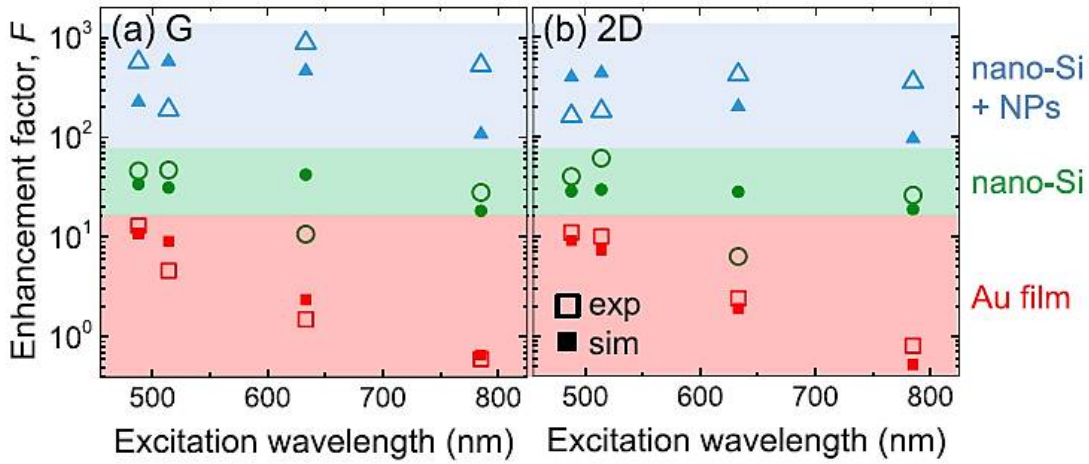


Figure 5.7: Summary comparison between the experimental (open symbols) and simulation (solid symbols) results for G (a) and 2D (b) peak Raman enhancement factors for graphene on flat Au (squares), uncoated nanostructured silicon (circles), and nanostructured silicon with gold nanoparticles (triangles), with respect to graphene on flat silicon [32].

The vertical axis (Raman enhancement factor  $F$ ) of Figure 5.7 is in logarithmic scale, so all three substrate cases are shown in the same graph. In terms of order of magnitude, a good overall agreement is found in all cases. We can confidently conclude that there is a clear plasmonic effect separating the decorated nanostructured silicon case from all the others. The scale of separation is about one order of magnitude. Also, as mentioned previously, the reference case is graphene on flat silicon. From our estimates in the beginning of the theoretical considerations, we expect a quenching of the order of 40 compared to graphene suspended in air. The actual numbers for quenching are 50, 35, and 30 for 500, 650, and 800 nm wavelengths, respectively. This puts the uncoated nanostructured silicon results on par with suspended graphene. This case is far from the highly quenching flat silicon surface and the Fabry-Perot resonances slightly modulate the actual final signal enhancement. The higher quenching for flat silicon at low wavelengths (see Figure 5.3) results in the higher enhancement values compared to the ones at longer wavelengths, as seen in Figure 5.7 (middle).

On the other hand, for decorated nanostructured silicon the Raman signal is clearly above the one from suspended graphene and definitely enhanced due to plasmonic fields. As a final comment, we note that while the scattering of measured and simulated data is expected given the large difference between simulated (periodic) and actual (random) substrate structures, the good overall agreement in terms of trends and order of magnitude is promising. For example, conducting measurements on periodic substrates, we could potentially use simulations to estimate the actual graphene conformation. Such periodic structures would also allow for controlling the period and width of silicon nanopillars, which in turn would affect the enhancement of graphene Raman signal. However, they are beyond the scope of this work, which focuses on the simplicity and scalability of laser processing.

Figure 5.7 shows that there is not a strong variation of the enhancement factor with excitation wavelength, even for the plasmonic nanostructured silicon substrate with gold nanoparticles. Indeed, this substrate provides significant enhancement over a broad range of excitation wavelengths, within the visible electromagnetic spectrum. The formation of aggregates of gold nanoparticles on the surface of this substrate leads to the broadening of plasmon resonance over the visible range. Additionally, the broadening of plasmon resonance is induced by the variation of dielectric environment, sampled by each nanoparticle on silicon nanopillars, as shown in Figure 5.5(a). Nanoparticles on pillars are no longer indistinguishable (like nanoparticles on a flat substrate), as the relative orientation of interface area between each nanoparticle and silicon (and graphene), varies according to its location on the nanopillar (Figs. 5.5(b) and 5.6). The broad range of excitation wavelengths for which significant enhancement is observed demonstrates that coated nanostructured silicon substrates are flexible for use with a wide range of Raman spectrometers, employing various laser sources for multiple applications [30].

## 5.7 Conclusions

The proposed 3D geometry has two advantages compared to 2D plasmonic geometries, achieving order of magnitude enhancement of the Raman signal of graphene. Firstly, due to its flexibility, graphene conforms to the 3D substrate, increasing its interface area with plasmonic nanoparticles and the sampling of enhanced near fields. Secondly, even for uncoated, bare silicon nanopillars, graphene adopts a semi-suspended topography between them, which results in enhanced electromagnetic interactions and Raman signal, similar to that of suspended graphene in air. Additionally, broadband enhancement of e-fields across the visible spectrum is achieved in contrast to most plasmonic substrates, which show narrow resonances. Our theoretical analysis reveals that the broadband enhancement is caused by the unique morphology of 3D substrates. This morphology leads both to the formation of aggregates of metallic nanoparticles on Si nanopillars, broadening the plasmon resonance, and to synergistic effects between the nanoparticles and the dielectric environment of nanopillars, which render different nanoparticles more active for different wavelengths and locations on the pillars. The maximum enhancement ( $\times 880$  for the G peak), obtained for  $\lambda=633$  nm excitation, is similar to the highest measured enhancements reported in the literature for SERS of graphene on plasmonic substrates. FDTD numerical simulations revealed local enhancement factors as high as  $\sim 2500$  and demonstrated a monotonic increase of enhancement with the degree of graphene conformation to the 3D topography of the substrate.

Optoelectronic devices will significantly benefit from hybrid nanostructured graphene-

silicon building blocks with high responsivity, due to the large surface area of the nanostructure, high response speeds, due to the reduced dimensions of the materials and spectrally broad photo-response. The broadband plasmonic enhancement of the proposed substrates is also beneficial for ultra-sensitive SERS-based sensors, operating with a variety of laser sources. The more convenient fabrication, scalability and improved electromagnetic enhancement of plasmonic silicon substrates, along with their successful integration with graphene, which may also be extended to most 2D materials and their heterojunctions, pave the way for future real-world applications of large-area 2D devices with complex functionalities in the fields of sensing, photonics and optoelectronics, among others.

## References

- [1] A. N. Grigorenko, M. Polini, and K. Novoselov, “Graphene plasmonics,” *Nature photonics*, vol. 6, no. 11, pp. 749–758, 2012.
- [2] F. Bonaccorso, Z. Sun, T. Hasan, and A. Ferrari, “Graphene photonics and optoelectronics,” *Nature photonics*, vol. 4, no. 9, pp. 611–622, 2010.
- [3] D. Jariwala, V. K. Sangwan, L. J. Lauhon, T. J. Marks, and M. C. Hersam, “Carbon nanomaterials for electronics, optoelectronics, photovoltaics, and sensing,” *Chemical Society Reviews*, vol. 42, no. 7, pp. 2824–2860, 2013.
- [4] X. Li, L. Tao, Z. Chen, H. Fang, X. Li, X. Wang, J.-B. Xu, and H. Zhu, “Graphene and related two-dimensional materials: Structure-property relationships for electronics and optoelectronics,” *Applied Physics Reviews*, vol. 4, no. 2, p. 021306, 2017.
- [5] X. Wang and X. Gan, “Graphene integrated photodetectors and opto-electronic devices—a review,” *Chinese Physics B*, vol. 26, no. 3, p. 034203, 2017.
- [6] Z. Osváth, A. Deák, K. Kertész, G. Molnár, G. Vértessy, D. Zámbo, C. Hwang, and L. P. Biró, “The structure and properties of graphene on gold nanoparticles,” *Nanoscale*, vol. 7, no. 12, pp. 5503–5509, 2015.
- [7] P. Wang, D. Zhang, L. Zhang, and Y. Fang, “The sers study of graphene deposited by gold nanoparticles with 785 nm excitation,” *Chemical Physics Letters*, vol. 556, pp. 146–150, 2013.
- [8] S. Zhang, X. Zhang, X. Liu, Z. Yin, H. Wang, H. Gao, and Y. Zhao, “Raman peak enhancement and shift of few-layer graphene induced by plasmonic coupling with silver nanoparticles,” *Applied Physics Letters*, vol. 104, no. 12, 2014.
- [9] A. Urich, A. Pospischil, M. M. Furchi, D. Dietze, K. Unterrainer, and T. Mueller, “Silver nanoisland enhanced raman interaction in graphene,” *Applied Physics Letters*, vol. 101, no. 15, 2012.
- [10] H. Zhou, C. Qiu, F. Yu, H. Yang, M. Chen, L. Hu, and L. Sun, “Thickness-dependent morphologies and surface-enhanced raman scattering of ag deposited on n-layer graphenes,” *The Journal of Physical Chemistry C*, vol. 115, no. 23, pp. 11348–11354, 2011.

- [11] P. Wang, W. Zhang, O. Liang, M. Pantoja, J. Katzer, T. Schroeder, and Y.-H. Xie, "Giant optical response from graphene-plasmonic system," *ACS nano*, vol. 6, no. 7, pp. 6244–6249, 2012.
- [12] S. Heeg, R. Fernandez-Garcia, A. Oikonomou, F. Schedin, R. Narula, S. A. Maier, A. Vijayaraghavan, and S. Reich, "Polarized plasmonic enhancement by au nanostructures probed through raman scattering of suspended graphene," *Nano letters*, vol. 13, no. 1, pp. 301–308, 2013.
- [13] F. Schedin, E. Lidorikis, A. Lombardo, V. G. Kravets, A. K. Geim, A. N. Grigorenko, K. S. Novoselov, and A. C. Ferrari, "Surface-enhanced raman spectroscopy of graphene," *ACS nano*, vol. 4, no. 10, pp. 5617–5626, 2010.
- [14] V. Kravets, F. Schedin, R. Jalil, L. Britnell, K. Novoselov, and A. Grigorenko, "Surface hydrogenation and optics of a graphene sheet transferred onto a plasmonic nanoarray," *The Journal of Physical Chemistry C*, vol. 116, no. 6, pp. 3882–3887, 2012.
- [15] C.-E. Cheng, C.-Y. Lin, H.-Y. Chang, C.-H. Huang, H.-Y. Lin, C.-H. Chen, C.-C. Hsu, C.-S. Chang, and F. S. S. Chien, "Surface-enhanced raman scattering of graphene with photo-assisted-synthesized gold nanoparticles," *Optics Express*, vol. 21, no. 5, pp. 6547–6554, 2013.
- [16] C. Qiu, H. Zhou, B. Cao, L. Sun, and T. Yu, "Raman spectroscopy of morphology-controlled deposition of au on graphene," *Carbon*, vol. 59, pp. 487–494, 2013.
- [17] K. Long, X. Luo, H. Nan, D. Du, W. Zhao, Z. Ni, and T. Qiu, "Surface-enhanced raman scattering from graphene covered gold nanocap arrays," *Journal of Applied Physics*, vol. 114, no. 18, 2013.
- [18] J. Mertens, A. L. Eiden, D. O. Sigle, F. Huang, A. Lombardo, Z. Sun, R. S. Sundaram, A. Colli, C. Tserkezis, J. Aizpurua, *et al.*, "Controlling subnanometer gaps in plasmonic dimers using graphene," *Nano letters*, vol. 13, no. 11, pp. 5033–5038, 2013.
- [19] X. Li, J. Zhu, and B. Wei, "Hybrid nanostructures of metal/two-dimensional nanomaterials for plasmon-enhanced applications," *Chemical Society Reviews*, vol. 45, no. 11, pp. 3145–3187, 2016.
- [20] Y. Li, Z. Li, C. Chi, H. Shan, L. Zheng, and Z. Fang, "Plasmonics of 2d nanomaterials: properties and applications," *Advanced science*, vol. 4, no. 8, p. 1600430, 2017.
- [21] H. Zhao, Q. Guo, F. Xia, and H. Wang, "Two-dimensional materials for nanophotonics application," *Nanophotonics*, vol. 4, no. 2, pp. 128–142, 2015.
- [22] C. Tan, X. Huang, and H. Zhang, "Synthesis and applications of graphene-based noble metal nanostructures," *Materials Today*, vol. 16, no. 1-2, pp. 29–36, 2013.
- [23] Y. Liu, X. Dong, and P. Chen, "Biological and chemical sensors based on graphene materials," *Chemical Society Reviews*, vol. 41, no. 6, pp. 2283–2307, 2012.

- [24] S. Sreejith, H. Joshi, and Y. Zhao, “Graphene-based materials in biosensing, bioimaging, and therapeutics,” *Graphene-based Materials in Health and Environment: New Paradigms*, pp. 35–61, 2016.
- [25] B. Tang, H. Guoxin, and H. Gao, “Raman spectroscopic characterization of graphene,” *Applied Spectroscopy Reviews*, vol. 45, no. 5, pp. 369–407, 2010.
- [26] A. C. Ferrari and D. M. Basko, “Raman spectroscopy as a versatile tool for studying the properties of graphene,” *Nature nanotechnology*, vol. 8, no. 4, pp. 235–246, 2013.
- [27] L. M. Malard, M. A. Pimenta, G. Dresselhaus, and M. S. Dresselhaus, “Raman spectroscopy in graphene,” *Physics reports*, vol. 473, no. 5-6, pp. 51–87, 2009.
- [28] Y. Sun, R. Wang, and K. Liu, “Substrate induced changes in atomically thin 2-dimensional semiconductors: Fundamentals, engineering, and applications,” *Applied Physics Reviews*, vol. 4, no. 1, 2017.
- [29] J. Yang, J. Li, Z. Du, Q. Gong, J. Teng, and M. Hong, “Laser hybrid micro/nano-structuring of si surfaces in air and its applications for sers detection,” *Scientific reports*, vol. 4, no. 1, p. 6657, 2014.
- [30] E. D. Diebold, N. H. Mack, S. K. Doorn, and E. Mazur, “Femtosecond laser-nanostructured substrates for surface-enhanced raman scattering,” *Langmuir*, vol. 25, no. 3, pp. 1790–1794, 2009.
- [31] V. Parmar, P. K. Kanaujia, R. K. Bommali, and G. V. Prakash, “Efficient surface enhanced raman scattering substrates from femtosecond laser based fabrication,” *Optical Materials*, vol. 72, pp. 86–90, 2017.
- [32] M. Kanidi, A. Dagkli, N. Kelaidis, D. Palles, S. Aminalragia-Giamini, J. Marquez-Velasco, A. Colli, A. Dimoulas, E. Lidorikis, M. Kandyla, *et al.*, “Surface-enhanced raman spectroscopy of graphene integrated in plasmonic silicon platforms with three-dimensional nanotopography,” *The Journal of Physical Chemistry C*, vol. 123, no. 5, pp. 3076–3087, 2019.
- [33] A. C. Ferrari and J. Robertson, “Raman spectroscopy in carbons: from nanotubes to diamond-preface,” 2004.
- [34] J. Park, A. Reina, R. Saito, J. Kong, G. Dresselhaus, and M. Dresselhaus, “G' band raman spectra of single, double and triple layer graphene,” *Carbon*, vol. 47, no. 5, pp. 1303–1310, 2009.
- [35] N. Jung, N. Kim, S. Jockusch, N. J. Turro, P. Kim, and L. Brus, “Charge transfer chemical doping of few layer graphenes: charge distribution and band gap formation,” *Nano letters*, vol. 9, no. 12, pp. 4133–4137, 2009.
- [36] A. Das, S. Pisana, B. Chakraborty, S. Piscanec, S. K. Saha, U. V. Waghmare, K. S. Novoselov, H. R. Krishnamurthy, A. K. Geim, A. C. Ferrari, *et al.*, “Monitoring dopants by raman scattering in an electrochemically top-gated graphene transistor,” *Nature nanotechnology*, vol. 3, no. 4, pp. 210–215, 2008.

- [37] Y. Shi, X. Dong, P. Chen, J. Wang, and L.-J. Li, "Effective doping of single-layer graphene from underlying sio 2 substrates," *Physical Review B*, vol. 79, no. 11, p. 115402, 2009.
- [38] C. Stampfer, F. Molitor, D. Graf, K. Ensslin, A. Jungen, C. Hierold, and L. Wirtz, "Raman imaging of doping domains in graphene on sio2," *Applied Physics Letters*, vol. 91, no. 24, 2007.
- [39] H. Liu, S. Ryu, Z. Chen, M. L. Steigerwald, C. Nuckolls, and L. E. Brus, "Photochemical reactivity of graphene," *Journal of the American Chemical Society*, vol. 131, no. 47, pp. 17099–17101, 2009.
- [40] A. Jorio, M. M. Lucchese, F. Stavale, E. H. M. Ferreira, M. V. Moutinho, R. B. Capaz, and C. A. Achete, "Raman study of ion-induced defects in n-layer graphene," *Journal of Physics: Condensed Matter*, vol. 22, no. 33, p. 334204, 2010.
- [41] T. Mohiuddin, A. Lombardo, R. Nair, A. Bonetti, G. Savini, R. Jalil, N. Bonini, D. Basko, C. Galiotis, N. Marzari, *et al.*, "Uniaxial strain in graphene by raman spectroscopy: G peak splitting, gröneisen parameters, and sample orientation," *Physical Review B*, vol. 79, no. 20, p. 205433, 2009.
- [42] M. Pimenta, G. Dresselhaus, M. S. Dresselhaus, L. Cancado, A. Jorio, and R. Saito, "Studying disorder in graphite-based systems by raman spectroscopy," *Physical chemistry chemical physics*, vol. 9, no. 11, pp. 1276–1290, 2007.
- [43] L. Jin, Q. Fu, R. Mu, D. Tan, and X. Bao, "Pb intercalation underneath a graphene layer on ru (0001) and its effect on graphene oxidation," *Physical Chemistry Chemical Physics*, vol. 13, no. 37, pp. 16655–16660, 2011.
- [44] A. C. Ferrari, J. C. Meyer, V. Scardaci, C. Casiraghi, M. Lazzeri, F. Mauri, S. Piscanec, D. Jiang, K. S. Novoselov, S. Roth, *et al.*, "Raman spectrum of graphene and graphene layers," *Physical review letters*, vol. 97, no. 18, p. 187401, 2006.
- [45] P. Tan, Y. Deng, Q. Zhao, and W. Cheng, "The intrinsic temperature effect of the raman spectra of graphite," *Applied physics letters*, vol. 74, no. 13, pp. 1818–1820, 1999.
- [46] F. Banhart, J. Kotakoski, and A. V. Krasheninnikov, "Structural defects in graphene," *ACS nano*, vol. 5, no. 1, pp. 26–41, 2011.
- [47] J. Bardarson, "J. tworzyd lo, pw brouwer, and cwj beenakker," *Phys. Rev. Lett.*, vol. 99, p. 106801, 2007.
- [48] S. Gedney, A. Taflove, and S. Hagness, "Computational electrodynamics: The finite-difference time domain method," *A. Taflove (Ed.)*, pp. 343–393, 2005.
- [49] E. Lidorikis, S. Egusa, and J. Joannopoulos, "Effective medium properties and photonic crystal superstructures of metallic nanoparticle arrays," *Journal of Applied Physics*, vol. 101, no. 5, 2007.
- [50] D. E. Aspnes and A. Studna, "Dielectric functions and optical parameters of si, ge, gap, gaas, gasb, inp, inas, and insb from 1.5 to 6.0 ev," *Physical review B*, vol. 27, no. 2, p. 985, 1983.

- [51] P. B. Johnson and R.-W. Christy, "Optical constants of the noble metals," *Physical review B*, vol. 6, no. 12, p. 4370, 1972.

## Chapter 6

# Graphene-based Optical Modulation and Pulse-Shaping

Efficient high-speed electro-optic modulation and ultrafast pulse-shaping in the near-IR spectrum are of great significance in a variety of applications, from optical communications to signal processing. Graphene stands out as a versatile absorbing 2D material for this purpose. Monolayer graphene is an effective and tunable absorber under both linear and non-linear optical intensities, having its melting point at more than 4000 K and broadband operation, ranging from visible to the terahertz (THz) frequency range [1–5].

In this chapter, we combine graphene with the resonance of an asymmetric single-port Bragg resonator designed at 1550 nm, which operates in the reflection mode and shows 100% absorption at RT [6]. This study affirms that 100% free-space signal modulation can be achieved, characterized by low insertion loss and gigahertz speed, regardless of the quality of graphene monolayer. Furthermore, with a minor adjustment, this device could be transformed into a sensitive acousto-absorption modulator, featuring an extinction ratio of 30 dB/Å, or an index sensor with a sensitivity of  $10^7\%$  per Refractive Index Unit (RIU). Under non-linear pulse excitation the same graphene-based optical nanodevice could operate as an ultrafast pulse-shaper. This Bragg nano-resonator is illuminated by a picosecond pulse, which manages to significantly increase non-equilibrium carrier density and graphene's electronic and lattice temperatures [7]. Under high incident power, intrinsic graphene absorptivity is modified via the elevated electronic temperature and mainly the existence of non-thermal photo-excited carriers in pumped SLG. This results in a change in cavity's optical reflectance, due to its deviation from critical coupling. In our modelling scheme, we explicitly study the formation of a hot electron gas in graphene, the phonon-mediated cooling, and the lattice temperatures. Manipulating graphene absorptivity through the appropriate combination of non-equilibrium carrier density and temperature, via incident power, and doping level, via applied gate voltage, electro-thermo-optical modulation is possible. Significantly, the deviation in graphene absorptivity (dependent on non-equilibrium carriers, temperature and doping) from its critical value allows us to modulate the input pulse's amplitude, duration, and shape, giving rise to single, double, or even triple peaks. Additionally, the modulated pulse can serve as a highly sensitive diagnostic tool for identifying micro-physical processes within graphene. Depending on the operational parameters, the graphene-loaded Bragg nano-resonator provides a unique capability to probe graphene carrier dynamics, eliminating the need for ultrafast spec-

trosopy. These innovative designs can be extended across the entire infrared spectrum by making the appropriate material selection and properly scaling the dimensions of layered materials.

*This chapter is based on our published work:*

- S. Doukas, A. Chatzilari, A. Dagkli, A. Papagiannopoulos and E. Lidorikis, *Deep and fast free-space electro-absorption modulation in a mobility-independent graphene-loaded Bragg resonator*, Appl. Phys. Lett. 113, 011102 (2018)

<https://doi.org/10.1063/1.5030699>

*And on our next publication in progress:*

- A. Dagkli, S. Doukas, A. Chatzilari, A. C. Ferrari, and E. Lidorikis, *Extreme pulse shaping from saturable absorption in a critically-coupled graphene-loaded photonic crystal cavity*, Under submission

## 6.1 Introduction

Graphene-based photonic components designed for signal modulation and ultrafast pulse-shaping within the near-infrared spectrum have found wide-ranging applications in optical signal processing, sensing, and communications [8–10]. These applications contain both free-space [11, 12] and integrated system [13] operations. In both cases the ideal wavelength is  $\lambda=1550$  nm [12]. Monolayer graphene holds significant promise as a 2D material for these purposes [9, 14], owing to its fast carrier relaxation times (on the order of picoseconds) [15], the broad spectral range of its electrically and thermally tunable conductivity [16, 17], and an especially high lattice melting point exceeding 4000 K [18].

Graphene-based NIR optical modulation has been successfully demonstrated in both waveguide-integrated [19–25] and free-space configurations [25–29]. Notably, in free-space applications, recent demonstrations have achieved an impressive modulation depth (MD) of up to 70% at a modulation frequency (MF) in the MHz range [27, 28]. Furthermore, the utilization of graphene for ultrafast pulse shaping in the near-IR regime has been established as well [30–32]. As mentioned in section 2.1, the intrinsic absorption of SLG is highly tunable across a wide spectrum, extending within the visible and mid-IR frequency range, via electrostatic gating, measuring approximately 2.3% [33, 34], when suspended in air, and  $2.3/n\%$ , when incorporated into a dielectric (with an index of  $n$ ) [35] at room temperature (RT). This absorption occurs for photon energies  $h\omega > 2E_{F,SLG}$  due to interband transitions, where  $E_{F,SLG}$  represents graphene Fermi level, determined by electrostatic doping. The absorption is notably reduced below this threshold, due to Pauli blocking [36, 37]. At lower frequencies, absorption resumes due to intraband transitions, leading to the appearance of graphene plasmonics [38–40]. Manipulation of graphene Fermi level  $E_{F,SLG}$  or its electronic temperature  $T_{e,SLG}$  and non-equilibrium carrier density, provide an avenue for tuning SLG absorptivity, promising significant opportunities for free-space and even integrated linear electro-optical or non-linear electro-thermo-optical modulation, respectively. However, given the overall limited absorption of graphene ( $<2.3\%$ ), it is essential to enhance the light-graphene interaction, typically achieved through the incorporation of a resonator structure, such as a nanocavity [26–29, 41–45] or plasmonics [23, 35, 46–51].

Numerical simulations by Doukas et al. [6] indicate that free-space modulators, which incorporate graphene within a Bragg-type resonator, have the potential to achieve Modulation Depths (MDs) exceeding 100%, while maintaining low Insertion Loss (IL) and ultrafast modulation frequencies (in the GHz range). These findings hold promise for free-space modulation in the NIR or mid-IR to THz regions. From [6] it is clear that a Bragg resonator device loaded with graphene and operating in reflection (R) mode could be dynamically tuned to achieve critical coupling (i.e., perfect absorption as described in Appendix B.1) regardless of graphene quality. This ensures consistently large MD (exceeding 100%), low IL of less than 1 dB, and a high modulation frequency exceeding 1 GHz. Moreover, a slight modification of this approach can transform it into an acousto-absorption modulator with a remarkable extinction ratio of around  $\sim 30$  dB/Å or an index sensor with a sensitivity of  $10^7\%$  per refractive index unit (RIU). In a similar context, our recent numerical simulations predict that the free-space graphene-based Bragg resonator used in [6] can be transformed to an ultrafast pulse-shaping device, that can electro-thermo-optically modulate the amplitude, duration, and shape of a high-power incident pulse. In our study, we demonstrate that this graphene-loaded Bragg resonator device, operating in reflection mode as well, can effectively shape a high power picosecond pulse, by control-

ling the existence of non-equilibrium carriers and electronic temperature of graphene, or graphene Fermi level. This control affects the deviation of graphene's absorptivity from its critical value, where total absorption reaches approximately 100% [52–54, 54, 55], and subsequently the reflected pulse. Furthermore, our recent results indicate that this scheme exhibits high sensitivity to slight alterations in graphene's e-e relaxation time. The remarkable sensitivity of our resonator motivates further research, aimed at identifying the micro-physical mechanisms within graphene and potentially paves the way for diagnosing intrinsic graphene processes without the need for ultrafast spectroscopy. These design principles and considerations, developed for 1550 nm, can be extended across the entire IR spectrum by appropriately selecting materials and scaling their dimensions.

## 6.2 Linear electro-absorption Modulation with Graphene

### 6.2.1 Device Layout

We consider an asymmetrical Bragg cavity, as illustrated in Figure 6.1(a), which comprises three periods of a Si/SiO<sub>2</sub> bilayer on each side, along with an Au back mirror. The thicknesses of the layers are  $d_{Si}=113.3$  nm and  $d_{SiO_2}=265.4$  nm, corresponding to quarter-wave layers at a wavelength of  $\lambda=1550$  nm, and the refractive indices are  $n_{Si}=3.42$  and  $n_{SiO_2}=1.46$ , respectively. The cavity consists of a SiO<sub>2</sub> double layer with an SLG layer in between. We define the permittivity of graphene using the Kubo formula (see Eqs. 2.7-2.9) at room temperature (RT) with an electron relaxation time  $\tau=200$  fs. We assume that electrostatic doping is applied by the bottom n-doped Si layer, considering all the other Si layers to be undoped, as depicted in Figure 6.1(a). The dielectric strength of SiO<sub>2</sub> is  $10^7$  V/cm [56] and the between-layer thickness  $d_{SiO_2}$  is 265.4 nm.

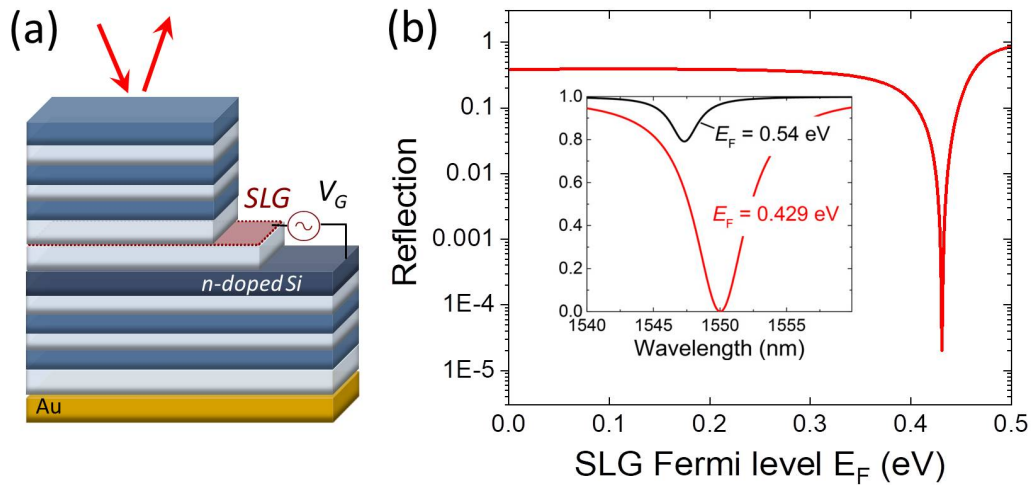


Figure 6.1: (a) Schematics of graphene-based single-port Bragg nanocavity device, with three Si/SiO<sub>2</sub> periods on either side of the cavity. (b) Reflection of the proposed device as a function of graphene electrostatic doping level  $E_F$  at 1550 nm. In the middle inset two selective doping levels, 0.54 eV and 0.429 eV are shown, respectively. Calculations shown in the inset were performed by A. Chatzilari [6].

We determine device's reflection (R) under normal incidence using Fresnel relations in conjunction with the Transfer Matrix Method (TMM), described in section 4.1. The analytical results at 1550 nm are presented in Figure 6.1(b) for different electrostatic doping levels. It is worth noting that in such a configuration, due to the absence of transmission (T), which is enforced by the Au back mirror, the critical coupling condition is satisfied (see Appendix B.1), signifying perfect absorption. We notice that at a specific critical doping level (i.e.  $E_{F,SLG}^c=0.429$  eV), the reflection at 1550 nm effectively approaches zero (see the inset of Figure 6.1). For any other doping level, the reflection becomes finite, typically approaching a value close to 1. This results in a modulation depth exceeding 100%. Our device behaves as a single-port resonator and the overall absorption can be derived by the general single-port coupled-mode theory as

$$A = \frac{4\gamma_a\gamma_d}{(\omega - \omega_0)^2 + (\gamma_a + \gamma_d)^2} \quad (6.1)$$

where  $\omega_0$  is the resonance frequency of the cavity,  $\gamma_a$  the total absorption rate of the system, and  $\gamma_d$  the decay rate of the cavity. In our device, absorption is contributed by several elements within the cavity, including graphene layer at the cavity center, the Au back mirror and n-Si gate beneath SLG. At resonant frequency (when  $\omega = \omega_0$ ), critical coupling is achieved, when the absorption rate matches the cavity's decay rate ( $\gamma_a = \gamma_d$ ). Consequently, for any given cavity, there is always a critical level of absorptivity, that ensures perfect absorption. Notably, any deviation from this condition results in a decrease in overall absorption. This implies that for a cavity with a small decay rate  $\gamma_d$ , indicating a high-Q factor, it is necessary to reduce the absorptivity of the cavity's elements  $\gamma_a$  to enhance the overall absorption. In this context, graphene emerges as a promising material, as its intrinsic absorptivity can be conveniently controlled and fine-tuned through electrostatic gating. We investigate the tunability of absorption in graphene with regard to achieving critical coupling in Figure 6.2.

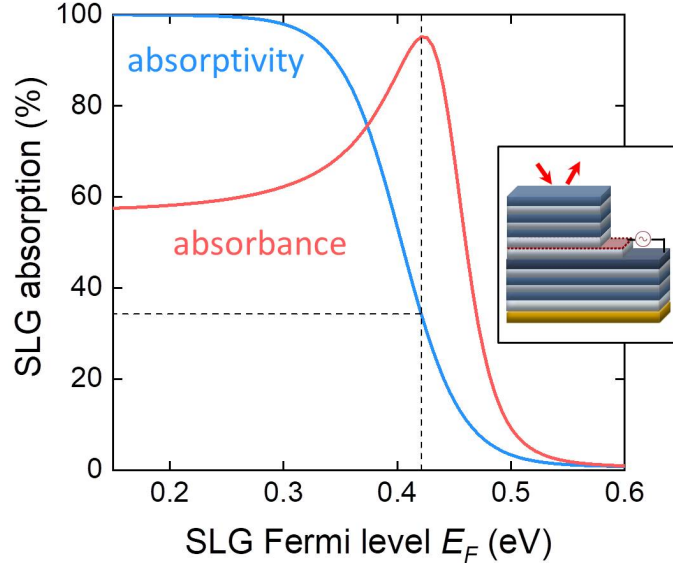


Figure 6.2: The absorption in graphene as a function of graphene doping  $E_F$  for Bragg nanocavity device with the Au mirror in contact with  $\text{SiO}_2$ . The light blue line is the normalized absorptivity of suspended graphene. The vertical dashed line shows the critical doping level for this device.

Here, we depict graphene absorption as a function of graphene doping. In Figure 6.2, we also plot the absorptivity of suspended graphene at  $\lambda=1550$  nm as a function of the Fermi level, given by  $A_{SLG} = 2\pi d_{SLG} \epsilon_2 \frac{\lambda}{n_{\text{SiO}_2}}$ , where  $d_{SLG}=0.335$  nm is the effective graphene thickness and  $\epsilon_2$  the imaginary part of the graphene's dielectric function. We notice that by doping graphene, the resonant wavelength shifts and a significant amount of the incident light is absorbed by it at a critical doping level shown in vertical dashed line (i.e. at  $E_F^c=0.429$  eV).

To limit the other constituent absorptions, such as Au and n-doped Si, we have considered the case in which the Au mirror is in direct contact with a  $\text{SiO}_2$  layer (as illustrated in the inset of Figure 6.2). This assumption is based on the following Equation 6.2 for the semi-infinite reflectance  $R_\infty$  for normal incidence at  $\lambda = 1550\text{nm}$ , with refractive index for Au  $n_{Au} = 0.51 + i10.7$ , calculated as

$$R_\infty = \frac{|n_{diel} - n_{Au}|^2}{(n_{diel} + n_{Au})^2} \quad (6.2)$$

The single-pass absorption under normal incidence could be  $A_{Au} = 1 - R_\infty$ . Consequently, the absorptivity at the  $\text{SiO}_2/\text{Au}$  interface is approximately 2.5%, which is about 2.2 times lower than 5.4%, if e.g. is substituted with a higher dielectric Si/Au interface. Furthermore, the low absorptivity of Au when in contact with  $\text{SiO}_2$ , implies high flexibility for fine-tuning with graphene. Additionally, when working in the reflection mode, high contrast is achieved in low index/Au case between critically coupled graphene and highly doped graphene. Consequently, from Equation 6.2 we can derive that an optimal configuration, for the dielectric in contact with Au mirror, is that with a low refractive index.

## 6.2.2 Modulation Depth and Frequencies

To assess the performance of the device, we define the modulation depth as

$$MD(\%) = 100 \frac{R_{max} - R_{min}}{R_{max}}, MD(dB) = 10 \log_{10} \frac{R_{max}}{R_{min}} \quad (6.3)$$

and the insertion loss as

$$IL(\%) = 100(1 - R_{max}), IL(dB) = -10 \log_{10}(R_{max}) \quad (6.4)$$

Where  $R_{max}$  represents the maximum reflectance at the highest graphene doping level (i.e. at  $E_{F,SLG} = 0.54$  eV for this device), while  $R_{min}$  corresponds to the minimum reflectance at critical coupling. The specific value of  $R_{min}$  varies depending on the device's structure and the quality of graphene. In Figure 6.3, we plot the modulation depth as a function of detuning  $\delta E_F = E_F - E_F^c$  from the critical coupling condition, i.e. the detuning of  $R_{min}$ .

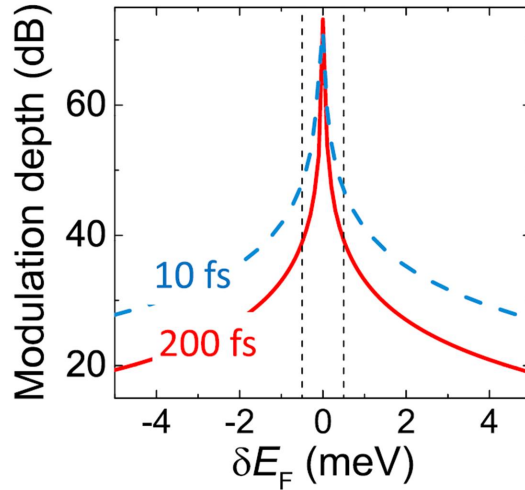


Figure 6.3: Modulation depth MD (dB), for relaxation times  $\tau=200$  fs (solid red) and  $\tau=10$  fs (dashed blue), as a function of detuning  $\delta E_F$  from  $R_{min}$ . Calculations performed by S. Doukas [6].

Significantly large values can be achieved by critically tuning the Fermi level of SLG. In the case of high-quality graphene (i.e.  $\tau=200$  fs), we determine that the modulation depth is  $6.5 \times 10^4$  (at critical doping level  $E_F^c = 0.429$  eV). We iterate the computation considering smaller electron relaxation time (corresponding to lower graphene mobility,  $\mu = e\tau v_F^2 / E_F$ ). For instance, the modulation depth is depicted for  $\tau=10$  fs. This is observed at the critical doping level  $E_F^c = 0.475$  eV. While the peak value remains the same in both cases, a broader response curve is evident for the smaller electron relaxation time, leading to an increased averaged modulation depth, as shown in Figure 6.3.

The optics-limited operating frequency, as described in reference [57], is calculated as

$$f_{opt} = \frac{c}{n_{SiO_2} 2LQ} \quad (6.5)$$

where  $c/n_{SiO_2}$  represents the speed of light in the dielectric,  $2L$  is the round-trip length of the cavity (comprising the middle two  $SiO_2$  layers), and  $Q$  denotes the cavity quality factor, defined as  $Q = \omega_0 / \delta\omega$ , where  $\omega_0$  represents the cavity mode frequency, and  $\delta\omega$

represents the Full Width at Half Maximum (FWHM) in  $\omega$  frequency range. In our case, involving 3 SiO<sub>2</sub>/Si bilayers, Doukas et al. [6] determined that Q is approximately 325, resulting in an optics-limited operating frequency of around 600 GHz. This frequency is in close agreement to the fundamental speed limits, imposed by photo-carrier generation and relaxation processes, which typically occur on the picosecond timescale, as discussed in reference [15].

On the other hand, the electronics-limited operating frequency is considerably lower, defined as

$$f_{el} = \frac{1}{2\pi R_{el}C} \quad (6.6)$$

where  $R_{el}$  represents the system's Ohmic resistance and  $C$  is the capacitance, given by  $C = \epsilon_0 \epsilon_{SiO_2} A / d_{SiO_2}$ . For a square area device of  $A = 50 \times 50 \text{ u}^2$  (in a typical optical beam area), Doukas et al. [6] also estimated the capacitance as approximately 0.33 pF, and for the  $\tau=200$  fs and  $\tau=10$  fs cases, the  $R_G$  values of approximately  $0.1 \text{ k}\Omega$  and  $1.8 \text{ k}\Omega$ , respectively, where  $R_G = \sigma^{-1} = (ne\mu)^{-1}$ , with  $n = E_F^2 / (\pi\hbar^2 v_F^2)$ , representing the charge density and  $\mu$ . The n-Si contribution,  $R_{Si}$ , is approximately 4 times larger than  $R_G$ , leading to  $R_{el}$  being approximately equal to  $R_G$ . This results in electronics-limited operating frequencies of approximately 5 GHz and 0.3 GHz for the  $\tau=200$  fs and  $\tau=10$  fs cases, respectively [6]. It is worth noting that higher-quality graphene can further increase the modulation frequencies.

### 6.2.3 Acousto-optic Modulation and Sensing

Until now, we have demonstrated that even the slightest deviation from critical coupling has a significant impact on the device's reflection performance. This observation could be exploited to design a highly sensitive acousto-optic modulator. Our approach involves introducing a separation distance  $x$ , between the Au mirror and the rest of the device, creating a secondary cavity, as depicted in the inset of Figure 6.4. For each  $x$  value, we tune the Fermi level of graphene to its corresponding critical coupling value  $E_F^c$ , and then plot the total absorption as a function of both mirror separation  $x$  and wavelength.

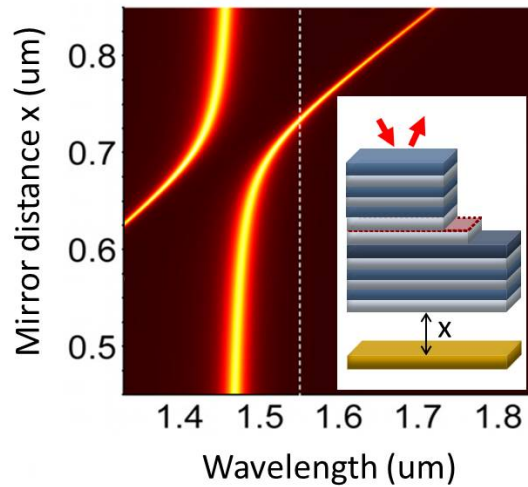


Figure 6.4: Overall absorption as a function of mirror separation and wavelength (color scale from 0 to 1). The inset schematics represents the acousto-optic modulation device configuration. Calculations performed by A. Chatzilari [6].

A strong anti-crossing behavior emerges, particularly around  $x = 700$  nm, attributed to interference effects between SiO<sub>2</sub> and mirror cavity, leading to an exceptionally sensitive response. Selecting  $x_0 = 735$  nm, where we observe perfect absorption at  $\lambda = 1550$  nm, we can calculate  $\langle MD \rangle$  as a function of mirror deflection  $\delta x = x - x_0$  (by 1 Å) and notice its significantly high values, that correspond to a sensitivity of approximately 30 dB/Å ( $R = 10^3 < R_0 >$ ). The only disadvantage could be the high overall reflection and consequently large insertion loss. Similarly, even a slight alteration in the refractive index within the mirror cavity will induce a measurable change in reflectance. Since the optical path length is  $n_x$ , a change in  $\delta n/n = \delta x/x$  will yield an equivalent change in  $\delta R/R$ . Based on the  $\langle MD \rangle$  calculations by Doukas et al. [6], we can estimate an index sensitivity on the order of 10<sup>7</sup>%/RIU (Refractive Index Unit). It is noteworthy that these high sensitivities remain independent of graphene mobility. The only need is to identify the appropriate  $E_F^c$  value to achieve critical coupling.

## 6.3 Non-linear Ultrafast Pulse-Shaping with Graphene

### 6.3.1 Non-linear Pulse Excitation - Non equilibrium carriers

Due to the conical band structure in SLG, interband photon absorption at energy  $E_{ph} = \hbar\omega$  results into non-equilibrium electron and hole populations at energies  $\epsilon_{ph} = \pm \hbar\omega/2$ . This process is quantified by the optical conductivity, which is described by the interband contribution of the Kubo formula [58, 59]. Rewriting Equation 2.9, we have

$$\sigma_{inter}(\omega, \Gamma, \mu, T_e) = \frac{-ie^2(\omega + 2i\Gamma)}{\pi\hbar^2} \int_0^\infty \frac{f_{FD}(\epsilon; \mu, T_e) - f_{FD}(-\epsilon; \mu, T_e)}{(\omega + 2i\Gamma)^2 - 4(\epsilon/\hbar)^2} d\epsilon \quad (6.7)$$

where  $\mu$  is the chemical potential,  $f_{FD}(\epsilon; \mu, T_e) = [e^{\frac{\epsilon - \mu}{k_B T_e}} - 1]^{-1}$  the Fermi-Dirac distribution function, and  $2\Gamma = \tau_{opt}^{-1}$ , where  $\tau_{opt}$  the effective dephasing time, due to both elastic and non-elastic electron-phonon and defect/impurity scattering [60]. The latter is related also to the charge mobility  $\mu_q$  and Fermi level  $E_F$  through the relation  $\tau_{opt} = \mu_q E_F / e v_F^2$  [38] with reported values ranging from 10 to 500 fs [60–62], where  $e$  is the elementary charge and  $v_F = 10^6$  m/s the Fermi velocity [63] in SLG.

The above Equation 6.7 implies a Lorentzian natural bandwidth of  $2\hbar\Gamma$  for this process, owing to the energy uncertainty offered by the scattering processes with phonons and impurities. This results in a minimal natural bandwidth  $\Delta E = 2\hbar\Gamma$  over which the excited non-equilibrium electrons and holes spread in the conduction and valence bands, respectively, even when excited by long pulses (i.e.,  $>$  ps duration) at quasi-cw single frequency conditions. In case of an excitation pulse of finite bandwidth (i.e, fs duration), we have to add the broadening, i.e.  $\Delta E = 2\hbar\Gamma + \hbar\Gamma_p$ , where  $2\Gamma_p = \tau_p^{-1}$  and  $\tau_p$  is the pulse duration. The broadening  $\Delta E$  affects several ultrafast [64, 65] and nonlinear processes in graphene (such as Kerr effect, high harmonic generation etc.), but most notably the saturable absorption [1, 66–68]. To take it into account, we assume the Lorentzian distribution:

$$L(\epsilon) = \hbar^2 \Gamma^2 / [(|\epsilon| - \hbar\omega/2)^2 + \hbar^2 \Gamma^2] \quad (6.8)$$

which has width  $2\hbar\Gamma$ , unit peak value, and integral  $\int_0^\infty L(\epsilon) d\epsilon = \pi\hbar\Gamma$ .

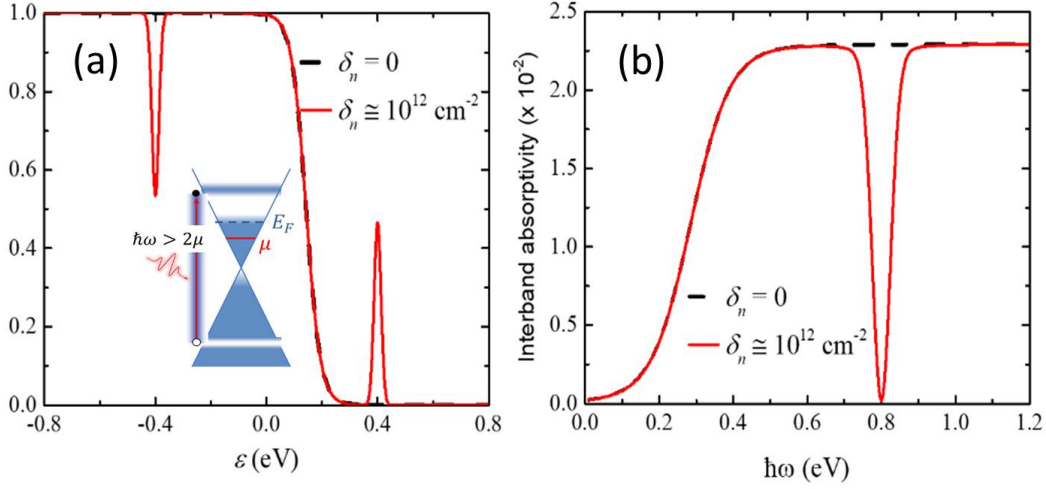


Figure 6.5: (a) Fermi-Dirac distribution as a function of energy  $\epsilon$  with (red line) and without (black dashed line) the existence of non-equilibrium carriers. We assumed that the non-equilibrium carrier density was  $\delta_n = 10^{12} \text{ cm}^{-2}$  (b) Interband SLG absorptivity in both cases as a function of photon energy  $\hbar\omega$  at  $\lambda=1550\text{nm}$ . Schematic inset of energy levels and carrier distribution in SLG, assuming photon energy  $\hbar\omega > 2\mu$ . The blue isolated area on top of the conduction band represents the non-equilibrium carrier distribution after photo-excitation. Calculations performed in collaboration with S. Doukas.

After photo-excitation, the non-equilibrium carriers  $n_{ne}$  undergo relaxation and through electron-electron scattering, Auger, and carrier multiplication processes [69], resulting in an equilibrium hot Fermi-Dirac distribution at some elevated electronic temperature  $T_e$  [70]. Assuming a quasi-cw excitation, this can be suitably described (see Equation 2.16) by the rate equation

$$\dot{n}_{ne} = \frac{\alpha I}{\hbar\omega} - \frac{n_{ne}}{\tau_{e-e}} \quad (6.9)$$

where  $\alpha$  is the instantaneous interband absorbance of SLG (see Equation 2.17),  $I$  the incoming light intensity, and  $\tau_{e-e}$  the electron-electron relaxation rate, typically measured around 20 fs [64, 69]. At the steady state, non-equilibrium carriers are obtained by

$$n_{ne} = \frac{\alpha I \tau_{e-e}}{\hbar\omega} \quad (6.10)$$

These carriers are spread over a Lorentzian distribution, such that

$$n_{ne} = \int_0^\infty v(\epsilon) g L(\epsilon) d\epsilon \quad (6.11)$$

where  $v(\epsilon) = 2|\epsilon|/(\pi\hbar^2 v_F^2)$  is the density of states at energy  $\epsilon$  and  $g$  is a normalization constant. Given that in general  $\hbar\omega/2 \gg 2\hbar\Gamma$  (e.g., for  $\lambda=1550 \text{ nm}$  the energy  $\hbar\omega/2=0.4 \text{ eV}$  while for  $\tau_{opt}=200 \text{ fs}$  it is  $2\hbar\Gamma=3.3 \text{ meV}$ ), we take  $v(\epsilon)$  out of the integral of Equation 6.11 and by use of Equation 6.10 we get

$$g = \frac{2}{\pi} \frac{n_{ne}}{v(\hbar\omega/2) \Delta E} = \frac{2\alpha I v_F^2}{\hbar\omega^2} \tau_{e-e} \tau_{opt} \quad (6.12)$$

where  $v(\hbar\omega/2) = |\epsilon|/(\pi\hbar^2v_F^2)$ . The corresponding non-equilibrium photo-excited carriers can be described through the modified Fermi-Dirac distribution of the following equation.

$$f_{FD}^* = f_{FD} + g[L(\epsilon) - L(-\epsilon)] \quad (6.13)$$

All electronic properties of graphene, i.e., absorbance, electrical conductance, thermal capacity, etc, in the presence of non-equilibrium carriers, can be calculated using the same procedure as in 2D Sommerfeld theory [71] by utilizing the modified F-D distribution of Equation 6.13.

To complete our methodology, we need the elevated equilibrium electronic temperature  $T_e$  and lattice temperature  $T_l$ , in a standard two-temperature model description [72] (mentioned in subsection 2.1.6). Specifically

$$\begin{aligned} c_e \dot{T}_e &= \alpha I - J_{e-ph}, \\ c_l \dot{T}_l &= J_{e-ph} - \Gamma_{SLG-sub}(T_l - T_{sub}) \end{aligned} \quad (6.14)$$

where  $c_e$  is the electronic heat capacity,  $c_l$  the lattice heat capacity,  $J_{e-ph}$  the electronic thermal cooling current into the phonon bath (for details see Appendix B.2),  $\Gamma_{SLG-sub}$  (in our case  $\Gamma_{SLG-SiO_2}=20 \text{ MWm}^{-2}\text{K}^{-1}$  [73]) the cooling rate of the SLG lattice into substrate, and  $T_{sub}$  the lattice temperature. In our case lattice temperature  $T_{SiO_2}$  is fixed at 300 K.

During high intensity non-linear excitation, saturable absorption manifests itself as a decrease in SLG absorptivity due to band filling [66, 67], as expressed by Equation 6.13. This is typically described as

$$\alpha(I) = \frac{\alpha_0}{1 + I/I_S} + \alpha_{ns} \quad (6.15)$$

where  $\alpha_0$  is the absorptivity at zero intensity (i.e., 2.3% for suspended undoped SLG),  $\alpha_{ns}$  the non-saturable part of the absorption (e.g., intraband free carrier absorption), which will be neglected in this study, and  $I_S$  the saturation intensity. Using Equation 6.10, we relate  $n_{ne}(I) = \alpha(I)I\tau_{e-e}/\hbar\omega$ . At  $I = I_S$  we have  $\alpha(I_S) = \alpha_0/2$  and  $n_{ne}(I_S) = \alpha_0 I_S \tau_{e-e}/2\hbar\omega$ . At the same time, however,  $n_{ne}(I_S)$  can be defined through Equation 6.11, i.e.,  $n_{ne}(I_S) = g_s \pi \hbar \Gamma v(\hbar\omega/2)$ , where  $g_s$  is the value needed to achieve half absorption. Combining the two relations for  $n_{ne}(I_S)$  we get:

$$I_S = \gamma n(\hbar\omega/2) \Delta E \alpha_0^{-1} \quad (6.16)$$

where  $\gamma = 4\pi g_s/\tau_{e-e}$  and  $n(\epsilon) = \epsilon^2/\pi\hbar^2v_F^2$  the number of total states up to energy  $\epsilon$ . Equation 6.16 can also be written as

$$I_S = n(\hbar\omega/2) \pi \hbar g_s \alpha_0^{-1} \tau_{e-e}^{-1} \tau_{opt}^{-1} \quad (6.17)$$

In Figure 6.6 we plot both the numerical (red line) and analytical (blue dashed line) solutions for SLG absorption as a function of incoming light intensity  $I$ , using our self-consistent model and Equation 6.15, respectively. We assume undoped SLG with  $E_{F,SLG}=0$ ,  $\Delta\hbar\omega=33 \text{ meV}$  and  $\tau_{e-e}=20 \text{ fs}$ . We also calculate the saturation intensity from Equation 6.17.

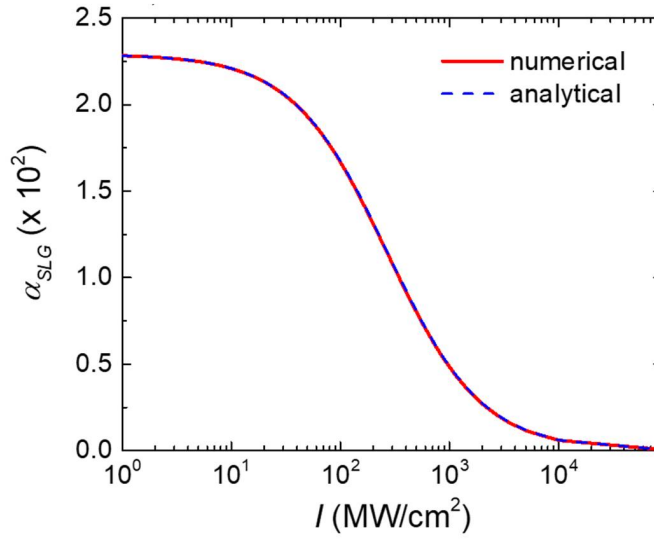


Figure 6.6: Numerical and analytical results, assuming  $E_{F,SLG}=0$ ,  $\Delta\hbar\omega=33$  meV and  $\tau_{e-e}=20$  fs, for SLG absorption as a function of incoming light intensity  $I$ . We calculate the saturation intensity  $I_s=270$  MW/cm<sup>2</sup>. Calculations performed in collaboration with S. Doukas.

From Figure 6.6, we observe the convergence of the two methods for calculating absorption in graphene in the steady-state case. In the next subsection, we will study cases of high-intensity non-linear incident pulses passing through the proposed nanodevice, described in detail in subsection 6.2.1.

### 6.3.2 Wavelength Detuning

Motivated by the shift in SLG absorbance, resulting from modifications in SLG absorptivity and the consequent variations in cavity reflectance, described in section 6.2 for linear photo-excitation, we explore the optical response of the same Bragg cavity combined with doped graphene under high-power non-linear pulse operation. Specifically, we examine graphene-light coupling, when doped SLG is integrated into the Bragg nanocavity system depicted in Figure 6.1(a), which is tuned in the critical coupling condition (see Appendix B.1) and exposed to a 2ps Gaussian pulse. Here, we will assume long (i.e., > ps) pulses and the quasi-cw approximation, to solve all self-consistent equations in time domain using a 4th-order Runge-Kutta integration scheme (see section 4.4).

The following diagrams, in Figure 6.7(a-b), show the rise in temperature  $T_{e,SLG}$ , the modification of SLG absorptivity and reflection, when a high peak power pulse penetrates the device at 1550 nm. We assume  $E_{F,SLG}=0.43$  eV,  $\tau_{e-e}=20$  fs and  $\tau_{opt}=200$  fs. We also plot in Figure 6.7(c-d) the same parameters for the detuned wavelength of 1548.5 nm. The dashed lines correspond to the respective magnitudes for no photo-excited carriers in graphene ( $n_{ne}=0$ ).

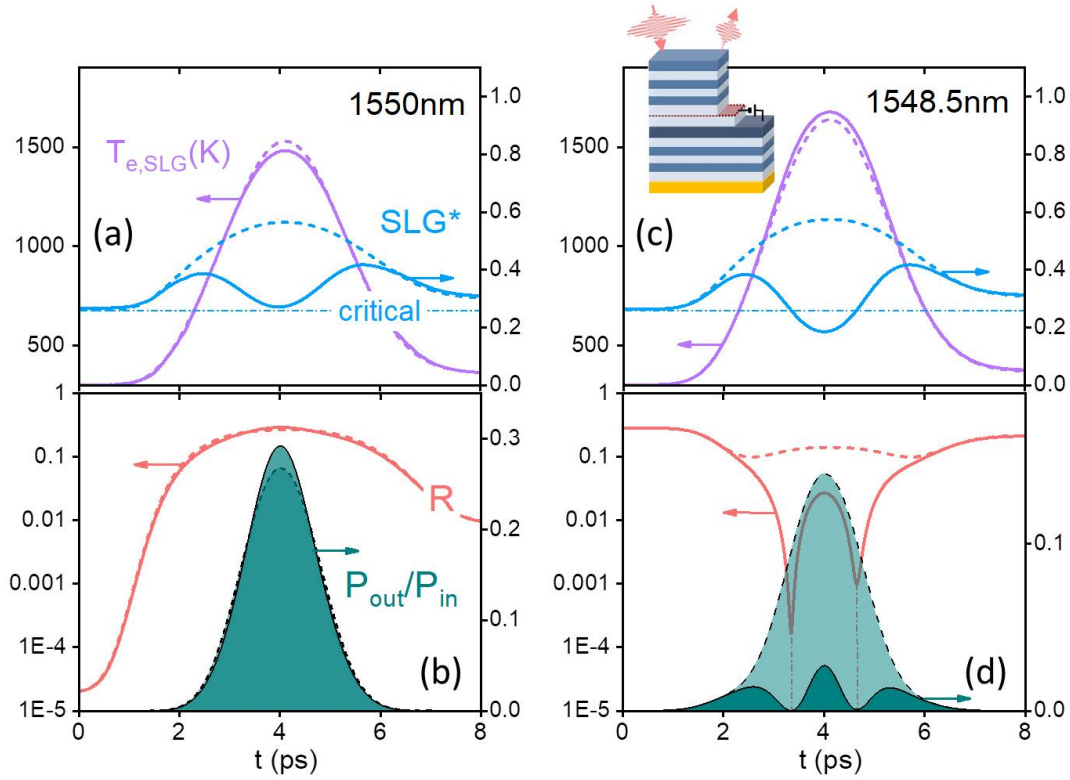


Figure 6.7: Temporal response of doped SLG ( $E_{F,SLG}=0.43$  eV,  $\tau_{e-e}=20$  fs,  $\tau_{opt}=200$  fs) combined with nanocavity, when illuminated by a 2 ps pulse with peak power  $\sim 2.6 \times 10^6$  W/cm<sup>2</sup>. Electronic temperature  $T_{e,SLG}$ , normalized SLG absorptivity (denoted by  $SLG^*$ ), reflection ( $R$ ), and power ratio ( $P_{out}/P_{in}$ ) for the SLG-cavity system at (a-b)  $\lambda=1550$  nm and (c-d)  $\lambda=1548.5$  nm in  $\sim$ ps timescale. The dashed lines correspond to the respective magnitudes for no photo-excited carriers in SLG ( $n_{ne}=0$ ).

Under high power pulse operation, with peak power  $\sim 2.6 \times 10^6$  W/cm<sup>2</sup>, the electronic temperature of graphene ( $T_{e,SLG}$ ) attains approximately 1500 K, as denoted by the light purple line in Figure 6.7(a,c), at both 1550 nm and the detuned wavelength of 1548.5 nm. This elevation in temperature results in a temporal change in SLG absorptivity, as illustrated by the light blue lines in the same diagrams. The deviation of absorptivity from the critical value of approximately 0.26 (horizontal dashed line in Figure 6.7(a,c)) is observed in both wavelength cases, with a more pronounced effect at 1548.5 nm, slightly offset from the resonant wavelength of the nanocavity. This significant deviation induces free-space reflection minima (depicted by the orange line) within specific time frames, as depicted in Figure 6.7(d). The short dashed vertical lines in Figure 6.7(d) mark snapshots, where graphene absorptivity equals its critical value, causing a reflection decline of approximately three orders of magnitude. This dynamic shapes a triple peak in the final reflected output pulse  $P_{out}(t)$ , determined by the product of  $R$  (reflectance) and  $P_{in}(t)$  (Gaussian input pulse), and normalized with the peak of  $P_{in}(t)$  (dark green areas). The variance in  $R_{minima}$  from reflection at RT is attributed to a slight change in the real part of graphene's dielectric index, impacting the cavity's decay rate. The ultimate reflected pulse exhibits an almost two orders of magnitude decline in amplitude compared to the incident pulse and manifests as a triple peak. This outcome underscores the versatility of our resonator for free-space pulse modulation, not only in amplitude (see section 6.1) and

time duration, but also in the formation of multiple peaks. It is noteworthy that ignoring the influence of photo-excited carriers (dashed lines in Figure 6.7) results in less variation in SLG absorptivity over time, affecting pulse amplitude modulation and, consequently, preventing pulse-shape operation.

### 6.3.3 The impact of SLG Fermi level for non-linear excitation

To assess the impact of graphene Fermi level on pulse shaping performance, we depict the power ratio  $P_{out}/P_{in}$  over time for three selected high peak powers and various graphene Fermi levels. The corresponding numerical results are illustrated in Figure 6.8.

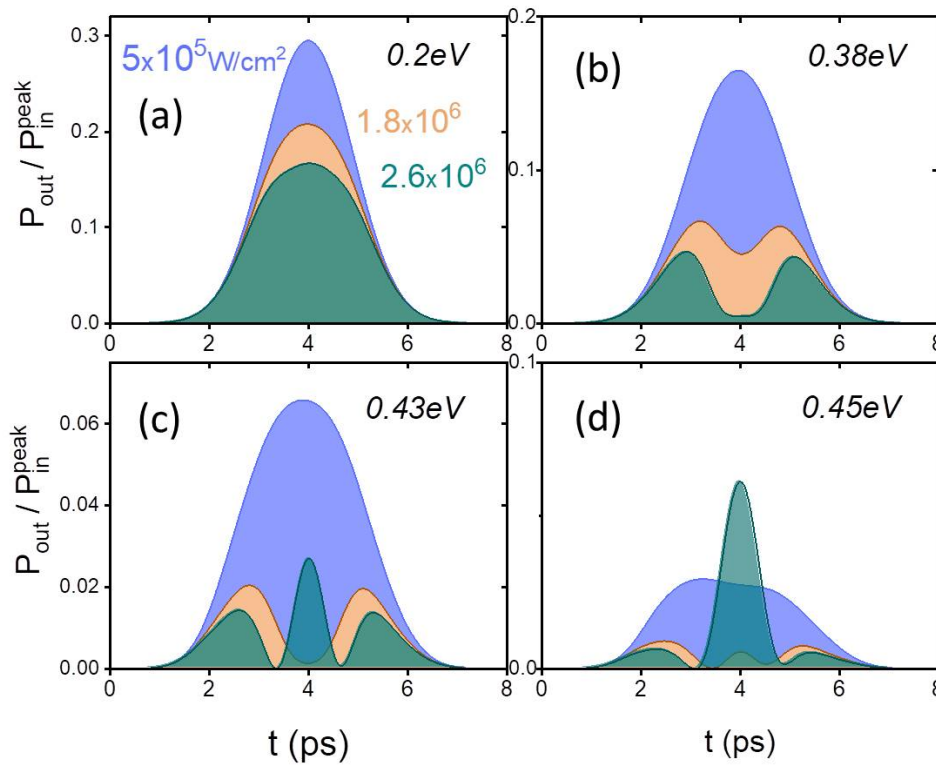


Figure 6.8: Temporal response of doped SLG combined with nanocavity, when illuminated by a 2ps pulse at  $\lambda=1548.5$  nm and peak power  $5 \times 10^5$ ,  $1.8 \times 10^6$  and  $2.6 \times 10^6$  W/cm<sup>2</sup>. (a-d)  $P_{out}/P_{in}$  ratio for four selective SLG Fermi levels  $E_{F,SLG}=0.2, 0.38, 0.43, 0.45$  eV.

Under an incident peak power of  $5 \times 10^5$  W/cm<sup>2</sup>, the elevated temperature of pumped graphene, with the concurrent existence of  $n_{ne}$  carriers, affects its absorptivity. This impact results in modulation of both the amplitude and time duration of the single-peak reflected pulse, as depicted by the purple areas. With a slight increase in peak power beyond  $10^6$  W/cm<sup>2</sup> and SLG Fermi level approaching  $E_{F,SLG}=0.43$  eV, the emergence of double peaks becomes evident (light orange areas). In the doping cases illustrated in Figure 6.8(c-d), the presence of double or even triple peaks (dark green areas) is observed. This observation underscores that through the appropriate selection of high power pulse and SLG Fermi level, we can effectively manipulate absorptivity to shape the output pulse. The ultimate

free-space  $P_{out}/P_{in}$  ratio is found to be incident peak power and doping dependent. To evaluate pulse-shaping performance over a broad range of peak  $P_{in}$  values and SLG Fermi levels, we present colormaps in  $\sim$ ps timescale in Figure 6.9.

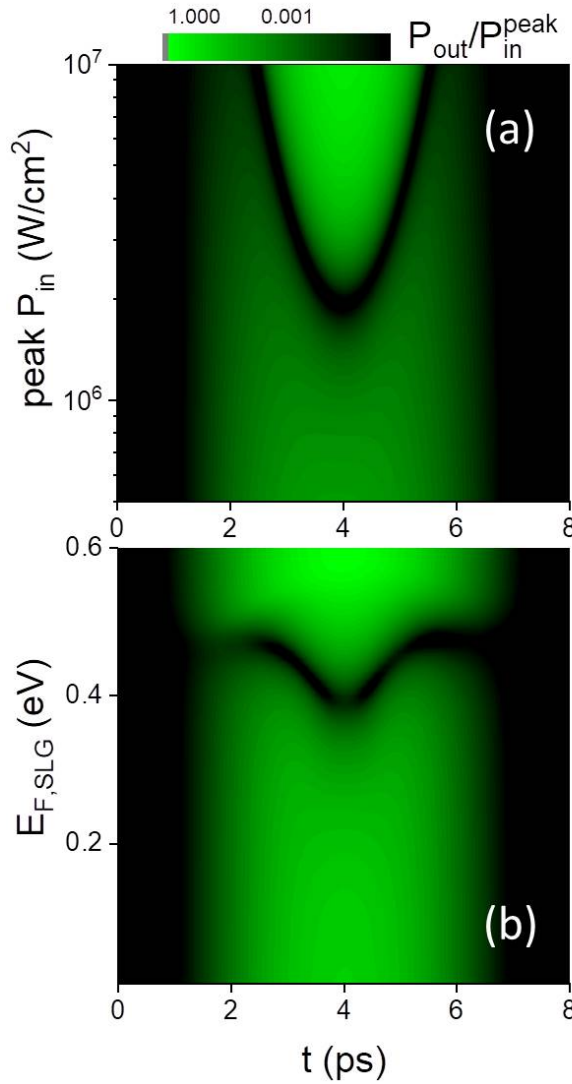


Figure 6.9: Temporal optical response under pulsed operation for (a) peak  $P_{in}$  range  $5 \times 10^5$ - $10^7$  W/cm<sup>2</sup> at 0.43 eV and (b) SLG Fermi level range of 0-0.6 eV for  $2.6 \times 10^6$  W/cm<sup>2</sup> in ps timescale.

At low peak powers of Figure 6.9(a), the limited  $T_{e,SLG}$  and the minimal impact of non-equilibrium carriers  $n_{ne}$  result in minor changes in SLG absorptivity, slightly affecting the reflected output pulse. However, at higher power levels, the presence of an elevated  $T_{e,SLG}$  and high non-equilibrium carrier distribution becomes crucial in modulating the cavity's optical response, affecting both amplitude and time duration of the output pulse. In this regime, the amplitude of free-space reflected pulse decreases, while its time duration broadens. An interesting peak power limit is  $10^6$  W/cm<sup>2</sup> for  $E_{F,SLG} = 0.43$  eV. Beyond this threshold, it leads to the formation of double and even triple peaks. In case of tuning SLG Fermi level (Figure 6.9 (b)), for a fixed peak power (i.e.,  $P_{in}(t) = 2.6 \times 10^6$  W/cm<sup>2</sup>), capable of generating a triple-peak performance, a notable change in the shape of the output pulse is observed between 0.38 eV and 0.45 eV, around the proposed Fermi level of 0.43

eV. This change is attributed to the sensitivity of SLG absorbance to doping changes, as described in section 6.1.

### 6.3.4 The effect of SLG e-e relaxation time and Sensitivity

So far, we have maintained electron-electron relaxation time ( $\tau_{e-e,SLG}$ ) at approximately 20 fs, as determined from the Heisenberg uncertainty principle for time and energy. This choice is made taking into account that the thermalization of the electron gas in graphene occurs on a sub-50 fs timescale [64, 69, 74–77]. To explore the impact of varying graphene e-e relaxation time within the range of 0.1-50 fs [64, 69], we plot in Figure 6.10 the output power ratio ( $P_{out}/P_{in}$ ) as a function of  $\tau_{e-e,SLG}$  on a  $\sim$ ps timescale. We model the same configuration under a selected incident power resulting in a triple output pulse (i.e.,  $2.6 \times 10^6$  W/cm<sup>2</sup>).

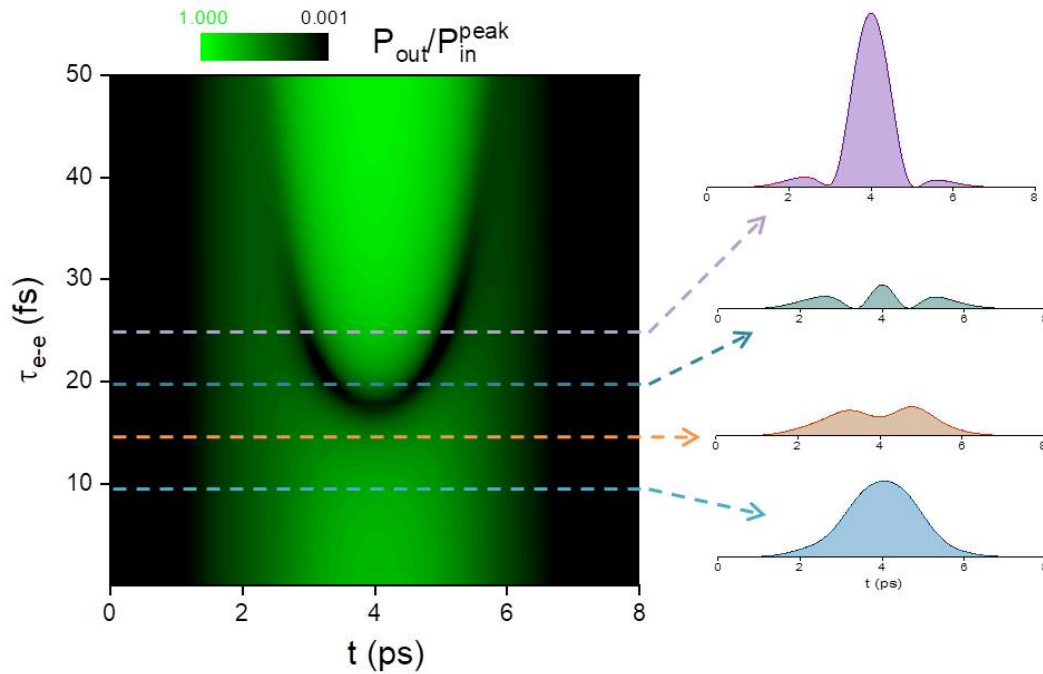


Figure 6.10: Temporal optical response under pulsed operation for peak  $P_{in}=2.6 \times 10^6$  W/cm<sup>2</sup>,  $\sim 0.43$  eV SLG Fermi level and SLG e-e relaxation time at the range of 0.1-50 fs.

Figure 6.10 confirms that even slight modifications in e-e scattering time within graphene result in a significant change of the cavity's optical response in terms of amplitude, time duration, and shape. The multi-color diagrams on the right inset of Figure 6.10, representing four different SLG e-e scattering times, can prove that as  $\tau_{e-e,SLG}$  is slightly increased, a single peak ( $\sim 10$  fs) transforms into a double ( $\sim 15$  fs) or even triple ( $\sim 20$  fs) peak configuration. For larger relaxation times (beyond  $\sim 25$  fs), a dominant center peak emerges, significantly increasing in amplitude and restoring the pulse shape to single peak performance. The remarkable sensitivity of the output pulse shape to a few  $\sim$ fs modification in  $\tau_{e-e,SLG}$ , suggests that the micro-physical processes within graphene play a significant

role in shaping nanocavity's optical response during pulse operation. This insight prompts the consideration of an inverse approach, wherein the output pulse shape could serve as a key diagnostic tool for understanding the internal graphene processes, without the need for ultrafast spectroscopy.

## 6.4 Conclusions

In summary, in this chapter we demonstrate efficient and high-speed graphene-based electro-absorption modulation and, primarily, ultrafast pulse-shaping with graphene under non-linear intensity light pulses. Utilizing a fine-tuned graphene-loaded Bragg resonator device, operating in the reflection mode, critical coupling can be achieved, regardless of graphene's quality. The key to this achievement lies in the ability to precisely tune the electrostatic doping of graphene, equating cavity's decay and absorption rates, without the need of altering the device's architecture. This approach consistently yields a significant modulation depth of over 100%, with minimal insertion loss and the capability for GHz modulation. Furthermore, this mechanism can be extended to various operational devices, including a highly sensitive acousto-absorption modulator, providing around 30 dB/Å, or an accurate index sensor with a sensitivity of approximately  $10^7\%/RIU$ . In this chapter, we assess the physical behavior and capabilities of the same graphene-based Bragg resonator under non-linear intensity light pulses, operating at 1550 nm. Taking into account all the relevant factors, we manage to reshape the incident high-power pulse and generate an output pulse with desired properties, including amplitude, duration, and shape. Through this graphene-based configuration, we notice light amplitude modulation and  $\sim$ ps pulse shaping, which can be attributed to the elevated SLG electronic temperature and the presence of non-equilibrium carriers in pumped graphene, affecting its absorptivity. Deviations from the critical value of SLG absorptivity play a pivotal role in modulating the pulse's amplitude and duration, potentially resulting in a single, double, or triple peak pulse in timescale. Furthermore, due to nanocavity's high sensitivity in graphene's e-e relaxation time changes, consequently resulting in output pulse shaping, the same device can serve as a highly sensitive diagnostic tool for identifying micro-physical processes in graphene. It is noteworthy that all our considerations and designs, specifically for  $\lambda=1550$  nm, can be easily extended across a broad spectrum. Our findings show that device's applicability can be extended from visible to THz, provided that the architecture and materials are appropriately selected, and SLG absorbance is not restrained by Pauli blocking at elevated temperatures.

## References

- [1] A. Marini, J. Cox, and F. G. De Abajo, "Theory of graphene saturable absorption," *Physical Review B*, vol. 95, no. 12, p. 125408, 2017.
- [2] Q. Bao and K. P. Loh, "Graphene photonics, plasmonics, and broadband optoelectronic devices," *ACS nano*, vol. 6, no. 5, pp. 3677–3694, 2012.
- [3] Z. Sun, T. Hasan, F. Torrisi, D. Popa, G. Privitera, F. Wang, F. Bonaccorso, D. M. Basko, and A. C. Ferrari, "Graphene mode-locked ultrafast laser," *ACS nano*, vol. 4, no. 2, pp. 803–810, 2010.

- [4] C. Ma, C. Wang, B. Gao, J. Adams, G. Wu, and H. Zhang, “Recent progress in ultra-fast lasers based on 2d materials as a saturable absorber,” *Applied Physics Reviews*, vol. 6, no. 4, 2019.
- [5] Z. Sun, A. Martinez, and F. Wang, “Optical modulators with 2d layered materials,” *Nature Photonics*, vol. 10, no. 4, pp. 227–238, 2016.
- [6] S. Doukas, A. Chatzilari, A. Dagkli, A. Papagiannopoulos, and E. Lidorikis, “Deep and fast free-space electro-absorption modulation in a mobility-independent graphene-loaded bragg resonator,” *Applied Physics Letters*, vol. 113, no. 1, 2018.
- [7] S. Doukas, P. Mensz, N. Myoung, A. Ferrari, I. Goykhman, and E. Lidorikis, “Thermionic graphene/silicon schottky infrared photodetectors,” *Physical Review B*, vol. 105, no. 11, p. 115417, 2022.
- [8] G. P. Agrawal, *Fiber-optic communication systems*. John Wiley & Sons, 2012.
- [9] F. Bonaccorso, Z. Sun, T. Hasan, and A. Ferrari, “Graphene photonics and optoelectronics,” *Nature photonics*, vol. 4, no. 9, pp. 611–622, 2010.
- [10] F. Koppens, T. Mueller, P. Avouris, A. Ferrari, M. Vitiello, and M. Polini, “Photodetectors based on graphene, other two-dimensional materials and hybrid systems,” *Nature nanotechnology*, vol. 9, no. 10, pp. 780–793, 2014.
- [11] A. K. Majumdar and J. C. Ricklin, *Free-space laser communications: principles and advances*, vol. 2. Springer Science & Business Media, 2010.
- [12] H. Kaushal and G. Kaddoum, “Optical communication in space: Challenges and mitigation techniques,” *IEEE communications surveys & tutorials*, vol. 19, no. 1, pp. 57–96, 2016.
- [13] G. T. Reed and A. P. Knights, *Silicon photonics: an introduction*. John Wiley & Sons, 2004.
- [14] F. Koppens, T. Mueller, and P. h. Avouris, “a c. ferrari, ms vitiello, and m. polini,” *Nat. Nanotechnol*, vol. 9, no. 10, pp. 780–93, 2014.
- [15] A. Urich, K. Unterrainer, and T. Mueller, “Intrinsic response time of graphene photodetectors,” *Nano letters*, vol. 11, no. 7, pp. 2804–2808, 2011.
- [16] A. C. Neto, F. Guinea, N. M. Peres, K. S. Novoselov, and A. K. Geim, “The electronic properties of graphene,” *Reviews of modern physics*, vol. 81, no. 1, p. 109, 2009.
- [17] A. C. Ferrari, F. Bonaccorso, V. Fal’Ko, K. S. Novoselov, S. Roche, P. Bøggild, S. Borini, F. H. Koppens, V. Palermo, N. Pugno, *et al.*, “Science and technology roadmap for graphene, related two-dimensional crystals, and hybrid systems,” *Nanoscale*, vol. 7, no. 11, pp. 4598–4810, 2015.
- [18] J. Los, K. Zakharchenko, M. Katsnelson, and A. Fasolino, “Melting temperature of graphene,” *Physical Review B*, vol. 91, no. 4, p. 045415, 2015.
- [19] M. Liu, X. Yin, E. Ulin-Avila, B. Geng, T. Zentgraf, L. Ju, F. Wang, and X. Zhang, “A graphene-based broadband optical modulator,” *Nature*, vol. 474, no. 7349, pp. 64–67, 2011.

- [20] C. T. Phare, Y.-H. Daniel Lee, J. Cardenas, and M. Lipson, “Graphene electro-optic modulator with 30 ghz bandwidth,” *Nature photonics*, vol. 9, no. 8, pp. 511–514, 2015.
- [21] N. Youngblood, Y. Anugrah, R. Ma, S. J. Koester, and M. Li, “Multifunctional graphene optical modulator and photodetector integrated on silicon waveguides,” *Nano letters*, vol. 14, no. 5, pp. 2741–2746, 2014.
- [22] M. Mohsin, D. Schall, M. Otto, A. Noculak, D. Neumaier, and H. Kurz, “Graphene based low insertion loss electro-absorption modulator on soi waveguide,” *Optics express*, vol. 22, no. 12, pp. 15292–15297, 2014.
- [23] D. Ansell, I. Radko, Z. Han, F. Rodriguez, S. Bozhevolnyi, and A. Grigorenko, “Hybrid graphene plasmonic waveguide modulators,” *Nature communications*, vol. 6, no. 1, p. 8846, 2015.
- [24] V. Soriano, M. Midrio, G. Contestabile, I. Asselberghs, J. Van Campenhout, C. Huyghebaert, I. Goykhman, A. Ott, A. Ferrari, and M. Romagnoli, “Graphene–silicon phase modulators with gigahertz bandwidth,” *Nature Photonics*, vol. 12, no. 1, pp. 40–44, 2018.
- [25] S. Yu, X. Wu, Y. Wang, X. Guo, and L. Tong, “2d materials for optical modulation: challenges and opportunities,” *Advanced Materials*, vol. 29, no. 14, p. 1606128, 2017.
- [26] C.-C. Lee, S. Suzuki, W. Xie, and T. Schibli, “Broadband graphene electro-optic modulators with sub-wavelength thickness,” *Optics express*, vol. 20, no. 5, pp. 5264–5269, 2012.
- [27] F. J. Rodriguez, D. E. Aznakayeva, O. P. Marshall, V. G. Kravets, and A. N. Grigorenko, “Solid-state electrolyte-gated graphene in optical modulators,” *Advanced Materials*, vol. 29, no. 19, p. 1606372, 2017.
- [28] T. Sun, J. Kim, J. M. Yuk, A. Zettl, F. Wang, and C. Chang-Hasnain, “Surface-normal electro-optic spatial light modulator using graphene integrated on a high-contrast grating resonator,” *Optics express*, vol. 24, no. 23, pp. 26035–26043, 2016.
- [29] A. Majumdar, J. Kim, J. Vuckovic, and F. Wang, “Electrical control of silicon photonic crystal cavity by graphene,” *Nano letters*, vol. 13, no. 2, pp. 515–518, 2013.
- [30] J. T. Kim, K. H. Chung, and C.-G. Choi, “Thermo-optic mode extinction modulator based on graphene plasmonic waveguide,” *Optics Express*, vol. 21, no. 13, pp. 15280–15286, 2013.
- [31] L. Yu, D. Dai, and S. He, “Graphene-based transparent flexible heat conductor for thermally tuning nanophotonic integrated devices,” *Applied Physics Letters*, vol. 105, no. 25, 2014.
- [32] S. Gan, C. Cheng, Y. Zhan, B. Huang, X. Gan, S. Li, S. Lin, X. Li, J. Zhao, H. Chen, *et al.*, “A highly efficient thermo-optic microring modulator assisted by graphene,” *Nanoscale*, vol. 7, no. 47, pp. 20249–20255, 2015.

- [33] R. R. Nair, P. Blake, A. N. Grigorenko, K. S. Novoselov, T. J. Booth, T. Stauber, N. M. Peres, and A. K. Geim, “Fine structure constant defines visual transparency of graphene,” *science*, vol. 320, no. 5881, pp. 1308–1308, 2008.
- [34] K. F. Mak, M. Y. Sfeir, Y. Wu, C. H. Lui, J. A. Misewich, and T. F. Heinz, “Measurement of the optical conductivity of graphene,” *Physical review letters*, vol. 101, no. 19, p. 196405, 2008.
- [35] T. Echtermeyer, S. Milana, U. Sassi, A. Eiden, M. Wu, E. Lidorikis, and A. Ferrari, “Surface plasmon polariton graphene photodetectors,” *Nano Letters*, vol. 16, no. 1, pp. 8–20, 2016.
- [36] F. Wang, Y. Zhang, C. Tian, C. Girit, A. Zettl, M. Crommie, and Y. R. Shen, “Gate-variable optical transitions in graphene,” *science*, vol. 320, no. 5873, pp. 206–209, 2008.
- [37] Z. Li, E. A. Henriksen, Z. Jiang, Z. Hao, M. C. Martin, P. Kim, H. L. Stormer, and D. N. Basov, “Dirac charge dynamics in graphene by infrared spectroscopy,” *Nature physics*, vol. 4, no. 7, pp. 532–535, 2008.
- [38] M. Jablan, H. Buljan, and M. Soljačić, “Plasmonics in graphene at infrared frequencies,” *Physical review B*, vol. 80, no. 24, p. 245435, 2009.
- [39] A. N. Grigorenko, M. Polini, and K. Novoselov, “Graphene plasmonics,” *Nature photonics*, vol. 6, no. 11, pp. 749–758, 2012.
- [40] F. J. Garcia de Abajo, “Graphene plasmonics: challenges and opportunities,” *Acs Photonics*, vol. 1, no. 3, pp. 135–152, 2014.
- [41] S. Thongrattanasiri, F. H. Koppens, and F. J. G. De Abajo, “Complete optical absorption in periodically patterned graphene,” *Physical review letters*, vol. 108, no. 4, p. 047401, 2012.
- [42] A. Ferreira, N. Peres, R. Ribeiro, and T. Stauber, “Graphene-based photodetector with two cavities,” *Physical Review B*, vol. 85, no. 11, p. 115438, 2012.
- [43] M. Furchi, A. Urich, A. Pospischil, G. Lilley, K. Unterrainer, H. Detz, P. Klang, A. M. Andrews, W. Schrenk, G. Strasser, *et al.*, “Microcavity-integrated graphene photodetector,” *Nano letters*, vol. 12, no. 6, pp. 2773–2777, 2012.
- [44] M. Engel, M. Steiner, A. Lombardo, A. C. Ferrari, H. v. Löhneysen, P. Avouris, and R. Krupke, “Light–matter interaction in a microcavity-controlled graphene transistor,” *Nature communications*, vol. 3, no. 1, p. 906, 2012.
- [45] W. Wang, A. Klots, Y. Yang, W. Li, I. I. Kravchenko, D. P. Briggs, K. I. Bolotin, and J. Valentine, “Enhanced absorption in two-dimensional materials via fano-resonant photonic crystals,” *Applied Physics Letters*, vol. 106, no. 18, 2015.
- [46] R. Yu, V. Pruneri, and F. J. García de Abajo, “Active modulation of visible light with graphene-loaded ultrathin metal plasmonic antennas,” *Scientific Reports*, vol. 6, no. 1, p. 32144, 2016.

- [47] T. Echtermeyer, L. Britnell, P. Jasnos, A. Lombardo, R. Gorbachev, A. Grigorenko, A. Geim, A. C. Ferrari, and K. Novoselov, “Strong plasmonic enhancement of photovoltage in graphene,” *Nature communications*, vol. 2, no. 1, p. 458, 2011.
- [48] V. Kravets, F. Schedin, R. Jalil, L. Britnell, K. Novoselov, and A. Grigorenko, “Surface hydrogenation and optics of a graphene sheet transferred onto a plasmonic nanoarray,” *The Journal of Physical Chemistry C*, vol. 116, no. 6, pp. 3882–3887, 2012.
- [49] B. D. Thackray, P. A. Thomas, G. H. Auton, F. J. Rodriguez, O. P. Marshall, V. G. Kravets, and A. N. Grigorenko, “Super-narrow, extremely high quality collective plasmon resonances at telecom wavelengths and their application in a hybrid graphene-plasmonic modulator,” *Nano letters*, vol. 15, no. 5, pp. 3519–3523, 2015.
- [50] F. Schedin, E. Lidorikis, A. Lombardo, V. G. Kravets, A. K. Geim, A. N. Grigorenko, K. S. Novoselov, and A. C. Ferrari, “Surface-enhanced raman spectroscopy of graphene,” *ACS nano*, vol. 4, no. 10, pp. 5617–5626, 2010.
- [51] F. Shi, Y. Chen, P. Han, and P. Tassin, “Broadband, spectrally flat, graphene-based terahertz modulators,” *Small*, vol. 11, no. 45, pp. 6044–6050, 2015.
- [52] A. Yariv, “Critical coupling and its control in optical waveguide-ring resonator systems,” *IEEE Photonics Technology Letters*, vol. 14, no. 4, pp. 483–485, 2002.
- [53] J. R. Tischler, M. S. Bradley, and V. Bulović, “Critically coupled resonators in vertical geometry using a planar mirror and a 5 nm thick absorbing film,” *Optics letters*, vol. 31, no. 13, pp. 2045–2047, 2006.
- [54] J. R. Piper, V. Liu, and S. Fan, “Total absorption by degenerate critical coupling,” *Applied Physics Letters*, vol. 104, no. 25, 2014.
- [55] Y. Liu, A. Chadha, D. Zhao, J. R. Piper, Y. Jia, Y. Shuai, L. Menon, H. Yang, Z. Ma, S. Fan, *et al.*, “Approaching total absorption at near infrared in a large area monolayer graphene by critical coupling,” *Applied Physics Letters*, vol. 105, no. 18, 2014.
- [56] S. Kasap and P. Capper, *Springer handbook of electronic and photonic materials*. Springer, 2017.
- [57] R. Yu, V. Pruneri, and F. J. García de Abajo, “Resonant visible light modulation with graphene,” *ACS Photonics*, vol. 2, no. 4, pp. 550–558, 2015.
- [58] G. W. Hanson, “Dyadic green’s functions and guided surface waves for a surface conductivity model of graphene,” *Journal of Applied Physics*, vol. 103, no. 6, 2008.
- [59] V. Osipov, V. Nesterenko, and Y. Shukrinov, “The international conference on theoretical physicsdubna-nano2008’,” in *Journal of Physics: Conference Series*, vol. 129, p. 011001, 2008.
- [60] M. Romagnoli, V. Soriano, M. Midrio, F. H. Koppens, C. Huyghebaert, D. Neumaier, P. Galli, W. Templ, A. D’Errico, and A. C. Ferrari, “Graphene-based integrated photonics for next-generation datacom and telecom,” *Nature Reviews Materials*, vol. 3, no. 10, pp. 392–414, 2018.

- [61] E. J. Dias, R. Yu, and F. J. Garcia de Abajo, “Thermal manipulation of plasmons in atomically thin films,” *Light: Science & Applications*, vol. 9, no. 1, p. 87, 2020.
- [62] S. Castilla, I. Vangelidis, V.-V. Pusapati, J. Goldstein, M. Autore, T. Slipchenko, K. Rajendran, S. Kim, K. Watanabe, T. Taniguchi, *et al.*, “Plasmonic antenna coupling to hyperbolic phonon-polaritons for sensitive and fast mid-infrared photodetection with graphene,” *Nature communications*, vol. 11, no. 1, p. 4872, 2020.
- [63] C. Hwang, D. A. Siegel, S.-K. Mo, W. Regan, A. Ismach, Y. Zhang, A. Zettl, and A. Lanzara, “Fermi velocity engineering in graphene by substrate modification,” *Scientific reports*, vol. 2, no. 1, p. 590, 2012.
- [64] D. Brida, A. Tomadin, C. Manzoni, Y. J. Kim, A. Lombardo, S. Milana, R. R. Nair, K. S. Novoselov, A. C. Ferrari, G. Cerullo, *et al.*, “Ultrafast collinear scattering and carrier multiplication in graphene,” *Nature communications*, vol. 4, no. 1, p. 1987, 2013.
- [65] E. Malic, T. Winzer, E. Bobkin, and A. Knorr, “Microscopic theory of absorption and ultrafast many-particle kinetics in graphene,” *Physical Review B*, vol. 84, no. 20, p. 205406, 2011.
- [66] Q. Bao, H. Zhang, Y. Wang, Z. Ni, Y. Yan, Z. X. Shen, K. P. Loh, and D. Y. Tang, “Atomic-layer graphene as a saturable absorber for ultrafast pulsed lasers,” *Advanced Functional Materials*, vol. 19, no. 19, pp. 3077–3083, 2009.
- [67] G. Xing, H. Guo, X. Zhang, T. C. Sum, and C. H. A. Huan, “The physics of ultrafast saturable absorption in graphene,” *Optics express*, vol. 18, no. 5, pp. 4564–4573, 2010.
- [68] G. Wang, A. A. Baker-Murray, and W. J. Blau, “Saturable absorption in 2d nanomaterials and related photonic devices,” *Laser & Photonics Reviews*, vol. 13, no. 7, p. 1800282, 2019.
- [69] A. Tomadin, D. Brida, G. Cerullo, A. C. Ferrari, and M. Polini, “Nonequilibrium dynamics of photoexcited electrons in graphene: Collinear scattering, auger processes, and the impact of screening,” *Physical Review B*, vol. 88, no. 3, p. 035430, 2013.
- [70] G. Soavi, G. Wang, H. Rostami, D. G. Purdie, D. De Fazio, T. Ma, B. Luo, J. Wang, A. K. Ott, D. Yoon, *et al.*, “Broadband, electrically tunable third-harmonic generation in graphene,” *Nature nanotechnology*, vol. 13, no. 7, pp. 583–588, 2018.
- [71] N. W. Ashcroft and N. Mermin, “Solid state physics (new york: Holt,” *Rinehart, and Winstoo*, 1976.
- [72] M. Massicotte, P. Schmidt, F. Vialla, K. Watanabe, T. Taniguchi, K.-J. Tielrooij, and F. H. Koppens, “Photo-thermionic effect in vertical graphene heterostructures,” *Nature communications*, vol. 7, no. 1, p. 12174, 2016.
- [73] Z. Xu and M. J. Buehler, “Heat dissipation at a graphene–substrate interface,” *Journal of Physics: Condensed Matter*, vol. 24, no. 47, p. 475305, 2012.

- [74] Z. Mics, K.-J. Tielrooij, K. Parvez, S. A. Jensen, I. Ivanov, X. Feng, K. Müllen, M. Bonn, and D. Turchinovich, “Thermodynamic picture of ultrafast charge transport in graphene,” *Nature communications*, vol. 6, no. 1, p. 7655, 2015.
- [75] M. Breusing, S. Kuehn, T. Winzer, E. Malić, F. Milde, N. Severin, J. Rabe, C. Ropers, A. Knorr, and T. Elsaesser, “Ultrafast nonequilibrium carrier dynamics in a single graphene layer,” *Physical Review B*, vol. 83, no. 15, p. 153410, 2011.
- [76] J. C. Johannsen, S. Ulstrup, F. Cilento, A. Crepaldi, M. Zacchigna, C. Cacho, I. E. Turcu, E. Springate, F. Fromm, C. Raidel, *et al.*, “Direct view of hot carrier dynamics in graphene,” *Physical Review Letters*, vol. 111, no. 2, p. 027403, 2013.
- [77] I. Gierz, J. C. Petersen, M. Mitrano, C. Cacho, I. E. Turcu, E. Springate, A. Stöhr, A. Köhler, U. Starke, and A. Cavalleri, “Snapshots of non-equilibrium dirac carrier distributions in graphene,” *Nature materials*, vol. 12, no. 12, pp. 1119–1124, 2013.

# Chapter 7

## TMD-based LED with Graphene

Layered Material (LMHs) or van der Waals Heterostructures (vdWHs), as described in section 2.4, offer the capability to produce electroluminescent (EL) devices that function from visible to NIR spectral range. Due to their direct bandgaps from visible to NIR and stable exciton particles at room temperature (RT) [1–10], LMHs, including monolayer TMDs, have the potential to be employed in the creation of 2D LEDs [11–20]. Such ultrafast and efficient nanoscale emitting semiconductors are an ideal choice for future directly modulated nanoscale light sources. Nonetheless, up to now these devices exhibit low EL quantum efficiency, approximately  $10^{-4}\%$  to 1%, and PL quantum efficiency from  $10^{-3}\%$  to 5%, respectively. On account of this, photonic cavity, plasmonic cavity and antenna-coupled TMD-based LEDs have demonstrated their potential and capabilities at high efficiency and speed (up to  $\sim$ GHz) for nanoscale light sources, outperforming nanolasers in speed. In this chapter, we FDTD model an 1L-TMD/hBN/SLG heterostructure, displaying enhanced LED emission at visible frequencies, when it is affected by a photonic cavity for free-space radiation, and/or exploiting antenna's plasmonic effects for both free-space and integrated photonics. Notably, we explore free-space 1L-WS<sub>2</sub>-based LED emission, when enhanced by a photonic cavity resonance and reveal an EL enhancement of  $\times 5.75$ , that reaches  $\times 16$  in the vertical direction (e.g., narrow NA=0.00125). Furthermore, we model an antenna-enhanced WSe<sub>2</sub>-LED positioned on top of a single-mode dielectric WG, exploiting plasmonic antenna near-field effects. Combining a geometry and material optimized plasmonic Bow-Tie antenna with a SiN waveguide, we manage to achieve an enhanced quantum efficiency of  $\sim 8$  dB and high-speed LED emission for integrated sources. The critical combination of plasmonic Purcell enhancement with light coupling into WG, enhances the amount and speed of waveguided light. Their ultrafast radiative lifetimes and high EL efficiency make these designs attractive for future high-speed directly modulated nano-emitters. All the considerations and designs studied here can also be extended for other TMD emission wavelengths.

*This chapter is based both on recently published work:*

- A. R. Cadore, B. L. T. Rosa, I. Paradisanos, S. Mignuzzi, D. De Fazio, E. M. Alexeev, A. Dagkli, J. E. Muench, G. Kakavelakis, S. M. Shinde, D. Yoon, S. Tongay, K. Watanabe, T. Taniguchi, E. Lidorikis, I. Goykhman, G. Soavi, and A. C. Ferrari, *Monolayer WS<sub>2</sub> electro- and photo-luminescence enhancement by TFSI treatment*, 2D Materials (2023)

<https://doi.org/10.48550/arXiv.2305.01791>

*And on our next publication in progress:*

- A. Dagkli and E. Lidorikis, *Plasmonic ultrafast integrated TMD-based LED with Graphene*

## 7.1 Introduction

The recent progress in developing atomically thin layers of van der Waals bonded solids has opened up new opportunities for the exploration of 2D physics and material applications. Among them, monolayers of TMDs provide an ideal platform for investigating light-matter interactions and many-body effects at the atomic scale [1, 21–23], as thoroughly described in section 2.4. In contrast to bulk semiconductors [22], due to their direct bandgaps, these monolayers offer reduced dielectric screening and spatial confinement of charge carriers [21], becoming promising candidates for new generation nanoscale LEDs. 1L-TMDs create a favorable environment for the generation of various excitonic complexes, that could be controlled by the modulation of carrier density [21–28].

LMHs which combine SLG, 1L-TMDs, and hBN, ranging from single-layer hBN to structures with hundreds of layers, hold great promise in the fields of electronics [29, 30], photonics [31] and optoelectronics [32, 33]. These LMHs, featuring direct bandgap 1L-TMDs, have the potential to be employed in the creation of LEDs [11–20], that offer high-speed modulation capabilities (up to GHz) [19, 27, 34] and the flexibility to tune the emission wavelength [19, 26, 27], spanning a wide range from visible to near-infrared wavelengths. However, so far, these devices demonstrate a low EL quantum efficiency, approximately  $10^{-4}\%$  [35, 36] to 1% [26, 27, 37–40], and PL quantum efficiency of  $10^{-3}\%$  [3, 41] to 5% [21–23], respectively. For this reason, photonic cavity [19, 42–44], plasmonic cavity [45, 46] and antenna-coupled [47–51] nanoscale light emitters have showcased their promising abilities and potential, displaying high efficiency and speed operation (in the GHz range), that are able to surpass nanolasers in terms of speed [46, 52–55].

Here, we FDTD model and explore photonic cavity enhanced 1L-WS<sub>2</sub>/hBN/SLG heterostructure for free-space light emission and Bow-Tie antenna-enhanced 1L-WSe<sub>2</sub>/hBN/SLG heterostructure for both free-space and integrated light emission.

## 7.2 TMD-based LED performance metrics

In this section, we will define important concepts and performance metrics related to 2D LEDs based on 1L-TMDs. Here, we consider an TMD/hBN/SLG based on a single tunnelling junction made of vertically stacked LMHs, as shown in Figure 7.1(a).

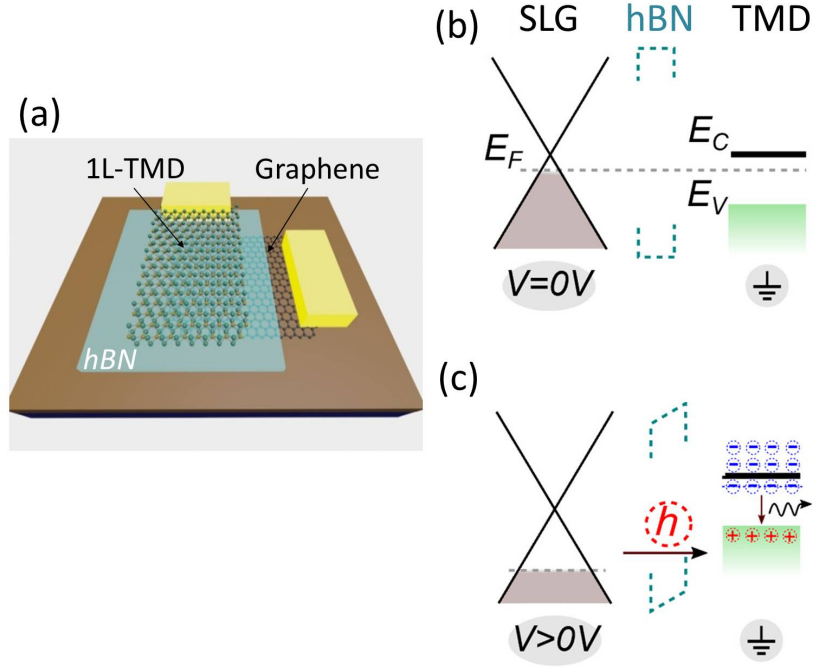


Figure 7.1: (a) Schematics of 1L-TMD/hBN/SLG LED. Band diagram for (b)  $V=0V$  and (c)  $V>0V$ . Tuning SLG's  $E_F$  (gray dotted line) across the 1L-TMD valence band edge,  $E_V$ , allows hole tunneling from SLG to 1L-TMD, resulting in light emission via electron-hole radiative recombination (e) from the n-type 1L-TMD. The blue circles represent electrons (e) accumulated on 1L-TMD due to the LMH, while the red circles are holes (h) injected into 1L-TMD through the hBN barrier.

The illustrations of Figure 7.1 show the cases of (b) zero-applied bias and (c) a finite positive bias applied to the SLG. Tuning graphene's Fermi level  $E_F$  across TMD conduction band edge  $E_C$ , allows hole tunneling from SLG, through hBN tunnelling barrier, to TMD (e.g. 1L-WS<sub>2</sub>), resulting in light emission via radiative recombination of the electrons with the holes residing in the n-doped TMD layer. The appearance of valence-band holes above the Fermi level is due to the natural n-doping of TMD.

## 7.2.1 LED quantum efficiency and light coupling into a WG

In LEDs based on 1L-TMDs, EL quantum efficiency depends on both the optical properties of the material [3, 9, 35–38, 56] and its doping level [26, 39–41, 57]. In this subsection we will describe the optical mechanisms and basic concepts in order to determine EL External Quantum Efficiency (EQE) of a TMD-based LED.

As mentioned in section 3.3, according to Fermi's Golden Rule, the radiative recombination rate of spontaneous emission  $\gamma_r$  for a typical LED is proportional to

$$\gamma_r \propto \frac{2\pi}{\hbar} |\langle i|M|j \rangle|^2 D(\omega) \quad (7.1)$$

Where  $D(\omega)$  is the density of states at  $\omega$  optical frequency and  $\langle i|M|j \rangle$  the transition probability (M matrix element) between initial  $i$  and final states  $j$  (also referred to as  $p_{ij}$ ).  $\gamma_r$  is proportional to  $D(\omega)$  and can be affected by dielectric or geometrical environment. The non-radiative recombination rate  $\gamma_{nr}$  (e.g., Auger recombination and polypionic recombination [47]) is absolutely affected by the selection of materials that are part

of emitting LMHs, when calibrating devices with identical 2D LED emitters. The Internal Quantum Efficiency (IQE) of LED  $\eta_{int}$ , which is the number of photons produced, due to e-h recombination in the active region [58], is obtained by the ratio of radiative recombination rate  $\gamma_r$  to the total recombination rate of LED (i.e. the sum of  $\gamma_r$  and  $\gamma_{nr}$  rates), as shown in the following expression

$$\eta_{int} = \frac{\gamma_r}{\gamma_r + \gamma_{nr}} \quad (7.2)$$

The above Equation 7.2 can also be written as a function of radiative ( $\tau_r = 1/\gamma_r$ ) and non-radiative ( $\tau_{nr} = 1/\gamma_{nr}$ ) recombination lifetimes

$$\eta_{int} = \frac{1}{1 + \frac{\tau_r}{\tau_{nr}}} = \frac{\tau}{\tau_r} \quad (7.3)$$

where  $\tau$  is the recombination lifetime of carriers in active region and it is also known as bulk recombination lifetime  $\tau^{-1} = (\tau_r + \tau_{nr})/\tau_{nr}\tau_r$ . The decrease of radiative lifetime  $\tau_r$  and the inversely proportional enhancement of  $\gamma_r$ , due to the presence of a cavity, or an antenna, is known as the Purcell effect [59]. The Purcell factor  $F$  expresses this  $\gamma_r$  change and can be derived from

$$F = \frac{3Q}{4\pi^2 n} \frac{\lambda^3}{V_{eff}} \quad (7.4)$$

It is defined for 3D structures of effective modal volume  $V_{eff} = \frac{\int \epsilon |E|^2 dV}{\max(\epsilon |E|^2)}$  and mode quality factor  $Q = \frac{\lambda}{\Delta\lambda}$ , with  $\Delta\lambda$  the narrow emission linewidth around  $\lambda$  [45]. When spontaneous emission happens, with the presence of a cavity or an antenna, radiative rate is enhanced by

$$\gamma_r = \frac{1}{\tau_r} = \frac{F\beta}{\tau^0} \quad (7.5)$$

where  $\beta$  is the fraction of spontaneous emission that is coupled into the fundamental cavity optical mode and  $\tau^0$  the bulk spontaneous emission lifetime for the calibration device. Supposing that we have small effective volume  $V_n = V_{eff}/(\lambda_0/2n)^3$ , the free spectral range of the mode will allow only one mode to overlap with the gain bandwidth, and thus  $\beta = 1$ . Assuming a constant current source, when spontaneous emission happens,  $\gamma_r$  is proportional to the density of states  $D(\omega)$  and, thus, to the total emitted optical power  $S_{tot}$ . For a given density of dipoles per unit volume, in case that each dipole represents radiation due to electron-hole recombination, a modification in  $\gamma_r$  can change  $S_{tot}$ , directly defined by FDTD simulations. The Purcell efficiency enhancement can be written as

$$\eta_{Purcell} = \frac{\gamma_r}{\gamma_r^0} = \frac{S_{tot}}{S_{tot}^0} \quad (7.6)$$

where (0) denotes the calibration device and  $S_{tot} = S_{free} + S_{lost} + S_{abs} (+S_{WG})$ .  $S_{free}$  is the useful free-space radiation power,  $S_{lost}$  is the power that is lost in the substrate,  $S_{abs}$  the absorbed power if absorbing materials are used, and  $S_{WG}$  the power that is coupled into dielectric WG, if studying waveguiding devices. Assuming that  $\gamma_{nr} = \gamma_{nr}^0$  (for an identical LMH), we can derive from Equation 7.2, for the calibration device, the unknown  $\gamma_{nr}$  as [60]

$$\gamma_{nr} = \gamma_r^0 (\eta_{int}^0)^{-1} - 1 \quad (7.7)$$

Substituting the derived  $\gamma_{nr}$  to Equation 7.2 for a proposed device, we determine

$$\eta_{int} = \frac{1}{1 + \frac{\gamma_r^0}{\gamma_r} (\eta_{int}^0 - 1)} \quad (7.8)$$

which can be also written, using Equation 7.6, as

$$\eta_{int}^{-1} = 1 + \eta_{Purcell}^{-1} (\eta_{int}^0 - 1) \quad (7.9)$$

The final EL quantum efficiency of LEDs ( $\eta$ ), which represents the ratio of emitted photons to injected electrons, while PL efficiency is the ratio of emitted photons to absorbed photons, is decomposed into three terms, which account the respective efficiencies of the carrier injection process ( $\eta_{inj}$ ), recombination process ( $\eta_{int}$ ), and photon emission process ( $\eta_{extr}$ ) of LED. This significant quantity can be written as

$$\eta = \eta_{inj} \eta_{int} \eta_{extr} \quad (7.10)$$

Where  $\eta_{inj}$  and  $\eta_{extr}$  are the injection and light extraction efficiencies, respectively.  $\eta_{extr}$  represents the light that goes out of the device and is the proportion of photons that escape from the device to the number of photons generated internally in the active region. In case of coupling light into a WG,  $\eta_{extr}$  corresponds to coupling efficiency ( $\eta_{coupling}$ ). These efficiencies can be directly obtained from FDTD calculations, as

$$\eta_{extr} = \frac{S_{free}}{S_{tot}}, \eta_{coupling} = \frac{S_{WG}}{S_{tot}} \quad (7.11)$$

The injection efficiency is merely affected by electrical circuit losses, assuming for simplicity that it is independent of the substrate and equal to 1. Namely, we suppose that all the electrons passing through the device are injected into the active region of LED. This approximation is not essentially sufficient, when we have to deal with a realistic experimental measurements. Combining 7.9 and 7.10, we can derive the final  $\eta$  for free space antenna-enhanced LED designs

$$\eta^{-1} = \eta_{extr}^{-1} (1 + \eta_{Purcell}^{-1} (\eta_{int}^0 - 1)) \quad (7.12)$$

For integrated WG designs  $\eta_{WG}$  can be respectively evaluated by

$$\eta_{WG}^{-1} = \eta_{coupling}^{-1} (1 + \eta_{Purcell}^{-1} (\eta_{int}^0 - 1)) \quad (7.13)$$

## 7.2.2 LED frequency response

In order to characterize the modulation frequency response of a cavity- or an antenna-enhanced nano-LED, the dynamic rate equations are studied [46]. In the most general case, nanoscale LEDs can be described by the standard laser rate equations, with the addition of Purcell enhancement [61], as

$$\begin{aligned} \frac{dN}{dt} &= J - GS - F\beta \frac{N}{\tau_{sp0}} - (1 - \beta) \frac{N}{\tau_{sp0}} - \frac{N}{\tau_{nr}} \\ \frac{dS}{dt} &= [\Gamma G - \frac{1}{\tau_{ph}}] S + \Gamma F \beta \frac{N}{\tau_{sp0}} \end{aligned} \quad (7.14)$$

Where  $N$  and  $S$  are the carrier and photon densities respectively,  $\tau_{ph} = 1/\gamma_{ph} = Q/\omega_0$  is the photon lifetime,  $\tau_{sp0}$  is the bulk spontaneous emission lifetime,  $J$  is the pump current,

$G$  the net stimulated emission gain (for lasers) and  $\Gamma \equiv \frac{\int_{\text{activerregion}} |E|^2 dV}{\int_{\text{entirecavity}} |E|^2 dV}$  the modal confinement factor (i.e. the fraction of photons within the active region interacting with gain material).

For a cavity-enhanced LED, we ignore stimulated emission contribution and non-radiative term. Since cavity's volume is small,  $\beta=1$  and the above expressions are modified to

$$\begin{aligned}\frac{dN}{dt} &= J - F \frac{N}{\tau_{sp0}} \\ \frac{dS}{dt} &= \Gamma F \frac{N}{\tau_{sp0}} - \frac{S}{\tau_{ph}}\end{aligned}\quad (7.15)$$

The modulation frequency response can then be found by taking the small-signal response, which is dominated by enhanced spontaneous emission rate  $\gamma_r = F\beta/\tau_{sp0}$  and photon decay rate  $\gamma_{ph}$ . If  $J = J_0 e^{i\omega t}$ ,  $N = N_0 e^{i\omega t}$  and  $S = S_0 e^{i\omega t}$ , this response will be the ratio of photon density change to current density change and can be written as

$$H(\omega) = \frac{\Delta S(\omega)}{\Delta J(\omega)} = \Gamma \tau_{ph} \frac{1}{(1 + \frac{i\omega}{\gamma_{ph}})(1 + \frac{i\omega}{\gamma_r})}\quad (7.16)$$

In order to estimate optical and electrical modulation frequency bandwidths of LED, we find the frequency at which  $|H(\omega)|$  and  $|H(\omega)|^2$  are half the DC response, respectively. For the optical 3-dB bandwidth we use the absolute value of the  $H(\omega)$  response, so

$$|H(\omega)| = \frac{1}{2} \Rightarrow \left|1 + \frac{i\omega}{\gamma_{ph}}\right| \left|1 + \frac{i\omega}{\gamma_r}\right| = 2 \Rightarrow \omega^4 \tau_{ph}^2 \tau_r^2 + \omega^2 (\tau_{ph}^2 + \tau_r^2) = 3\quad (7.17)$$

For the nano-LED, the resonance frequency is simplified to  $\omega^2 \simeq \frac{1}{\tau_{ph}\tau_r}$  and the bandwidth of Equation 7.17 is reduced to

$$f_{3dB}^{opt} = \frac{\sqrt{3}}{2\pi \sqrt{\tau_{ph}^2 + \tau_r^2}}\quad (7.18)$$

For electrical frequency bandwidth, we use the equality  $|H(\omega)|^2 = \frac{1}{2}$ . This yields a 3-dB modulation bandwidth of

$$f_{3dB}^{opt} = \frac{1}{2\pi \sqrt{\tau_{ph}^2 + \tau_r^2}}\quad (7.19)$$

### 7.3 Experimental TMD-based LED

Recent experimental study, performed by Cadore et al. [62], demonstrated that treating 1L-WS<sub>2</sub> based LEDs with the superacid bis-(trifluoromethane) sulfonimide (TFSI) significantly enhances the EL quantum efficiency by more than 10-fold at room temperature. In untreated devices, the predominant light emission comes from negatively charged excitons, whereas treated devices primarily involve radiative recombination of neutral excitons. This breakthrough opens the door to the development of tunable and highly efficient LMH-LEDs.

In this study, 2D LEDs were fabricated using 1L-WS<sub>2</sub> as the active material within a Metal-Insulator-Semiconductor (MIS) architecture. EL and gated-PL were evaluated both before and after subjecting the LEDs to TFSI treatment. The results revealed a remarkable enhancement in both EL efficiency ( $\eta$ ) and PL intensity following TFSI treatment. Specifically,  $\eta$  increased by more than 10-fold at RT, while PL intensity by a 5-fold increase. Before TFSI treatment, both excitons ( $X^-$  and  $X^0$ ) were detected in EL and PL. However, after treatment,  $X^0$  became the dominant exciton. This shift is attributed to the depletion of excess electrons and changes in the relaxation pathway induced by TFSI treatment. These findings hold significant implications for the development of more efficient LEDs and excitonic devices based on 1L-TMDs.

The selection of 1L-WS<sub>2</sub> as the active light-emitting layer was motivated by its direct bandgap [63–65] and larger PL emission compared to 1L-MoS<sub>2</sub> ( $\sim 60$  times stronger than 1L-MoS<sub>2</sub>) at RT [40]. Additionally,  $\eta$  can be up to  $\sim 50$  times larger than in case of 1L-MoS<sub>2</sub> [13, 14] at RT and previous studies [66–70] have shown that TFSI treatment can increase almost 10 times the PL intensity of 1L-WS<sub>2</sub>.

In Figure 7.2(a-b) the configuration of 1L-WS<sub>2</sub>/hBN/SLG tunnelling junction and the optical image of this device are shown. In this set-up, metallic electrodes provide contacts for voltage (V) application between SLG and 1L-WS<sub>2</sub>.

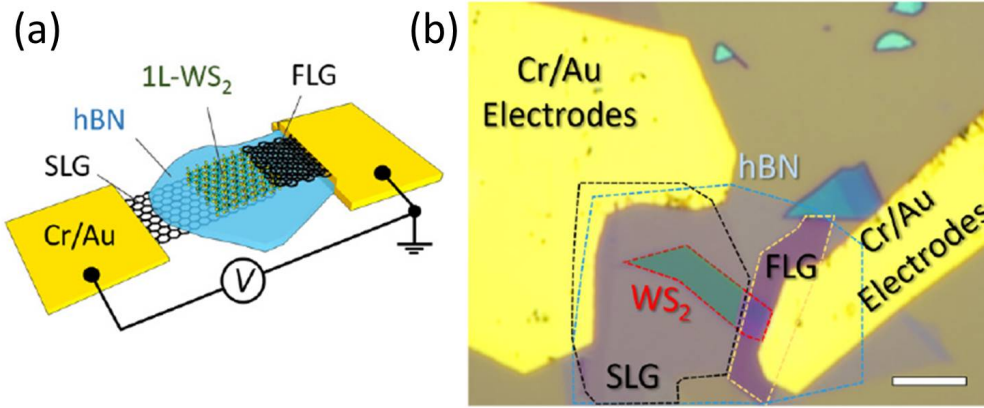


Figure 7.2: (a) Schematic of 1L-WS<sub>2</sub>-based LED. Cr/Au electrodes, SLG, FLG and hBN are indicated. (b) Optical image of this device produced by Cadore et al. [62]. The dashed lines delineate the footprint of SLG, FLG, hBN, and 1L-WS<sub>2</sub>. The active area is represented by the green-shaded region. The bottom SLG is contacted by Cr/Au, while FLG makes contact with the top 1L-WS<sub>2</sub>.

Cadore et al. [62] managed to estimate the EQE of LED illustrated in Figure 7.2(a). This efficiency was defined as the ratio of the number of emitted photons ( $N_{ph}$ ) and that of injected holes per second ( $N_h$ ) [71]

$$EQE = \frac{N_{ph}}{N_h} = \frac{\sum_{\lambda} N_{ph-counts}}{N_h} \times \frac{A_{eff}}{n_{sys}} \quad (7.20)$$

where  $\sum_{\lambda} N_{ph-counts}$  is the sum of photons collected by spectrometer over the measured spectral range  $A_{eff} = AA/A_{spot}$ , where  $A_{spot}$  is the microscope objective spot size  $A_{spot} \sim 2.2 \text{ um}^2$  ( $\lambda=618 \text{ nm}$  and  $NA=0.45$ ). The efficiency factor  $\eta_{sys} \sim 0.0051$  is defined by the ratio of the photons collected by the detector over the emitted photons (EL) at the sample position.

By utilizing Equation 7.20, an EQE of  $\sim 0.025\% \pm 0.021\%$  for pristine LEDs and  $\sim 0.195\% \pm 0.324\%$  for TFSI-treated LEDs is derived. This signifies an increase of  $8.7 \pm 1.5$ -fold, showcasing TFSI's capability to enhance EQE by nearly one order of magnitude. An EQE of approximately 0.2% surpasses previously reported values for 1L-WS<sub>2</sub>-based EL, such as  $\sim 0.1\%$  on a SiO<sub>2</sub>/SiN<sub>x</sub> microcavity [56],  $\sim 0.1\%$  for bulk organic emissive layers [72], and  $\sim 0.1\%$  for semiconducting (6,5) single-wall nanotubes [73]. The performance of WS<sub>2</sub>-LEDs can be further enhanced when situated within a photonic cavity [6, 19, 42–44, 46, 74–76].

## 7.4 TMD-based LED on typical SiO<sub>2</sub>/Si substrate

To evaluate the cavity enhanced EQE, we extract the performance metrics from experimental reference measurements on SiO<sub>2</sub>/Si substrate (i.e.  $EQE_{(ref)} \simeq 0.2\%$  for TFSI-treated LED at average  $\lambda=624$  nm) and project them on the simulation results of the cavity system. Figure 7.3(a) shows the position of experimental EL emission for pristine and TFSI-treated LEDs and (b) an illustration of the experimental reference device.

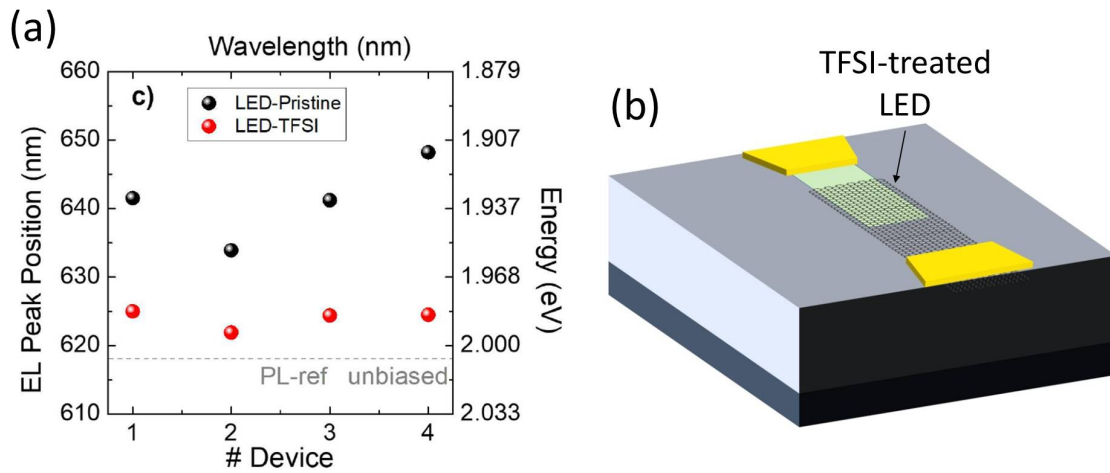


Figure 7.3: (a) Position of experimental EL emission for pristine (black circles) and TFSI-treated LEDs at similar tunneling current. These values are Lorentzian fits of EL spectra at similar current, following the centre of the main emission peak. (b) Schematic of the reference device consisting of a SLG/hBN (3 nm)/WS<sub>2</sub> tunneling junction LED on top of a typical SiO<sub>2</sub> (285 nm)/Si substrate. The absorbance of WS<sub>2</sub> is taken into account using its complex dielectric index derived by reference [77]. Experimental measurements performed by A. Cadore [62].

We initially estimate the reference internal quantum efficiency  $IQE_{(ref)}$  using Equation 7.10, where  $\eta_{(extr,ref)}$  and  $\eta_{(inj,ref)}$  are the extraction efficiency and injection efficiency on the reference SiO<sub>2</sub>/Si substrate, respectively. For simplicity, we assume that the latter is independent of the substrate and equal to 1. By 3D FDTD simulations [78] of a  $10 \times 10 \text{ um}^2$  reference system with a single transverse electric (TE) (i.e., parallel to the surface) point dipole emitter on the surface center at  $\lambda=624$  nm, we calculate  $\eta_{(extr,ref)} \simeq 14\%$ , i.e., a significant ( $\sim 86\%$ ) portion of the emitted light was absorbed and/or lost into the substrate. This yields for the TFSI-treated LED  $IQE_{ref} \simeq 1.43\%$ .

## 7.5 TMD-based LED inside a photonic cavity

As we mentioned before, the 1L-WS<sub>2</sub>-LED performance can be further improved if placed within a photonic cavity. Inside a cavity, the radiative density of states increases, leading to a proportional increase in radiative rate, due to the Purcell effect (see section 3.3). The photonic cavity, shown in the top inset of Figure 7.4, is asymmetric to enable maximal unidirectional emission. Nb<sub>2</sub>O<sub>5</sub>/SiO<sub>2</sub> bilayers are used for the Bragg mirrors, with N<sub>p</sub> the number of Nb<sub>2</sub>O<sub>5</sub>/SiO<sub>2</sub> periods on top, a SiO<sub>2</sub> cavity in the middle and an Ag back mirror. At λ=624 nm the refractive indices are  $n_{Nb_2O_5} = 2.325$  [79],  $n_{SiO_2} = 1.457$  [80],  $n_{Ag} = 0.0581 + i4.212$  [81],  $n_{SLG} = 2.787 + i1.443$  [82, 83],  $n_{hBN} = 2.12$  [84],  $n_{WS_2} = 5.38 + i0.382$  [77]. The layer thicknesses are  $d_{Nb_2O_5}=67$  nm,  $d_{SiO_2}=107$  nm and  $d_{cav}=191$  nm, while the 1L-WS<sub>2</sub>/h-BN(3 nm)/SLG LED heterostructure is placed in the middle of the SiO<sub>2</sub> cavity layer.

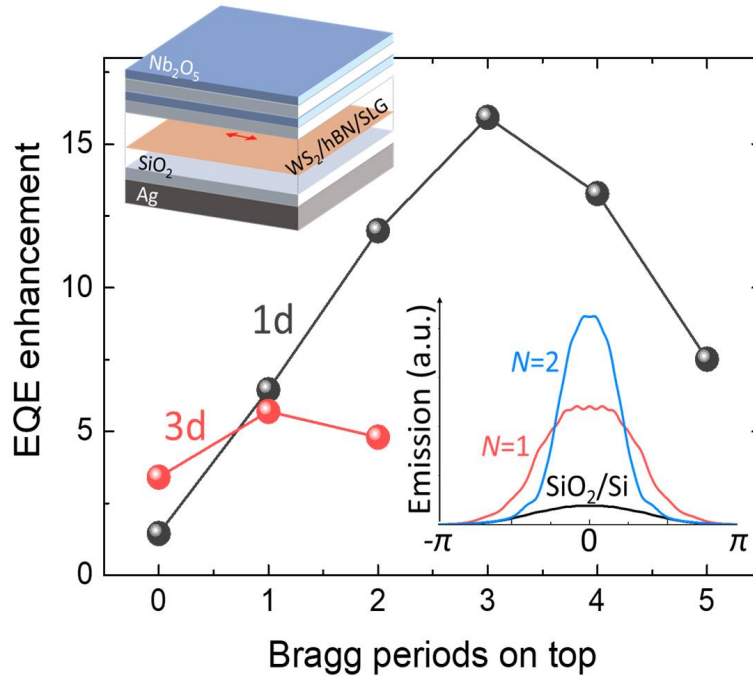


Figure 7.4: TFSI-treated 1L-WS<sub>2</sub>-LED enhanced EQE (3D calculation) in a cavity as a function of the number N<sub>p</sub> of Bragg periods on top (see top inset). Also plotted is the emissivity enhancement for vertical emission (1D calculation). The angular far-field intensity distribution for 3 device cases (3D calculations) is shown in the lower inset. All calculations are performed assuming electroluminescence wavelength λ = 624 nm [62].

FDTD simulations predict the cavity enhanced EQE as a function of N<sub>p</sub>, shown in Figure 7.4. For N<sub>p</sub>=1 the EQE gets a ×5.75 enhancement, reaching ~1.15%, attributed to a Purcell enhancement of ×1.15 and a ×5 increase in extraction efficiency. Cavity effects also enhance the directionality of light, as shown in the bottom inset of Figure 7.4 for the SiO<sub>2</sub>/Si reference structure as well as for the N<sub>p</sub>=1 and N<sub>p</sub>=2 cavity structures. To quantify the enhancement in the vertical direction (e.g., were we to use a narrow numerical aperture, e.g., NA=0.0125 [85]), we also plot the normal emission enhancement through 1D calculations in Figure 7.4. These are in alignment with the angular plots of the full 3D systems (lower inset of Figure 7.4) and predict an optimal cavity with N<sub>p</sub>=3 and relative

normal emissivity enhancement of  $\times 16$ . Further enhancement mechanisms can also be considered, such as plasmonic cavities and/or antenna-coupling [47–50, 53, 86], as well as dielectric domes on top of the device to further boost extraction.

## 7.6 Antenna-enhanced ultrafast TMD-based LED

Plasmonic nano-antennas, locally enhance e-fields within their antenna gap, in contrast to the flat planar resonant cavities studied in the previous section. This leads to a significant increase in the rate of light emission and a simultaneous reduction in their spontaneous emission time. As a result, they are particularly valuable for plasmonically enhanced highly efficient [47–49] and ultrafast [52, 87] (up to GHz) TMD-based LED applications.

In this section, we study 1L-WSe<sub>2</sub>/hBN/SLG LED [11, 85, 88] under plasmonic Bow-Tie antenna for free-space and, especially, for integrated photonics. Namely, we model WSe<sub>2</sub>-based LED, under Bow-Tie antenna, when on top of a typical free-space SiO<sub>2</sub>/Si substrate and/or planarized SiN/SiO<sub>2</sub> WG devices for integrated light emission [2]. We use practical considerations to calibrate devices, as described in sections 7.2 and 7.4, assuming  $\sim 1\%$  EQE, when on top of a typical SiO<sub>2</sub>/Si substrate [15, 17, 18]. We geometrically optimize and tune plasmonic resonance at  $\sim 750$  nm (the absorption resonance WSe<sub>2</sub>) and combine  $\eta_{coupling}$  into WG (or  $\eta_{extr}$  for free-space radiation) with the improved Purcell enhancement, exploiting Bow-Tie antenna's near-field effects [87]. We demonstrate that a critical combination of  $\eta_{Purcell}$  and  $\eta_{coupling}$  (or  $\eta_{extr}$ ) can boost by over one order of magnitude the final  $\eta_{WG}$  enhancement (or  $\eta$ ). Higher  $\eta_{WG}$  can be achieved using low-loss antenna materials, such as Ag, and a one-sided omnidirectional Bragg grating, totally reflecting light into a single-mode WG. Remarkably, we find that the plasmonic resonance, due to antenna's near-fields, enhances radiative emission rate, producing one order of magnitude higher  $\eta_{WG}$ , compared to no antenna cases. Our numerical work predicts that, for an optimized device with low antenna losses (aL) (i.e., high  $\eta_{coupling}$ ) and high  $\eta_{Purcell}$ ,  $\eta_{WG}$  can reach about  $\sim 16\%$  (-8 dB), by the appropriate material selection, dielectric environment and scaling of Bow-Tie dimensions. Furthermore, radiative lifetime reduces to a few  $\sim$ fs, increasing LED's speed, which is merely limited by photon lifetime.

### 7.6.1 Antenna-enhanced TMD-based LED for free-space emission

By coupling nanoscale LED to an external plasmonic antenna, its spontaneous emission rate can be dramatically increased alluding to the exciting possibility of an antenna-enhanced LED, that can be directly modulated faster than a laser. In this study, 1L-WSe<sub>2</sub>-based LED is modelled using the 3D FDTD method, described in [78], in conjunction with a Bow-Tie nano-antenna, when placed on a dielectric substrate. As described in section 7.4, facing the unknown  $\gamma_{nr}$  parameter, we need to initially assume a calibration device, in order to determine the EQE (see  $\eta$  in Eqs. 7.12-7.13) of LED devices. Experimental measurements for a WSe<sub>2</sub>/hBN/SLG LED, lying on top of a standard SiO<sub>2</sub> (285 nm)/Si substrate (see Figure 7.3(b)), have revealed that  $EQE_{(ref)}$  reaches up to  $\sim 1\%$  at 750 nm (within the emission spectrum of WSe<sub>2</sub>). Taking this into account and directly defining by 3D FDTD calculation  $\eta_{(extr,ref)} \simeq 12.5\%$ , we estimate  $IQE_{(ref)} \simeq 8\%$  of this device (see Equation 7.10), in order to calibrate selected plasmonic antenna layouts.

Subsequently, LED configurations with a gold Bow-Tie nano-antenna on a SiO<sub>2</sub>(3 um)/Si substrate for free-space radiation (see Figure 7.5(a)) were examined, wherein the calculation of plasmonic Purcell enhancement factor, metal and substrate losses, as well as

the internal and external quantum efficiencies of LED, were obtained. Dipole's orientation is assumed to be along antenna's length (TE polarization) and the refractive indices at  $\lambda=750$  nm are  $n_{Au} = 0.1388 + i4.491$  [81],  $n_{SiO_2} = 1.454$  [80] and  $n_{Si} = 3.67$  [89].

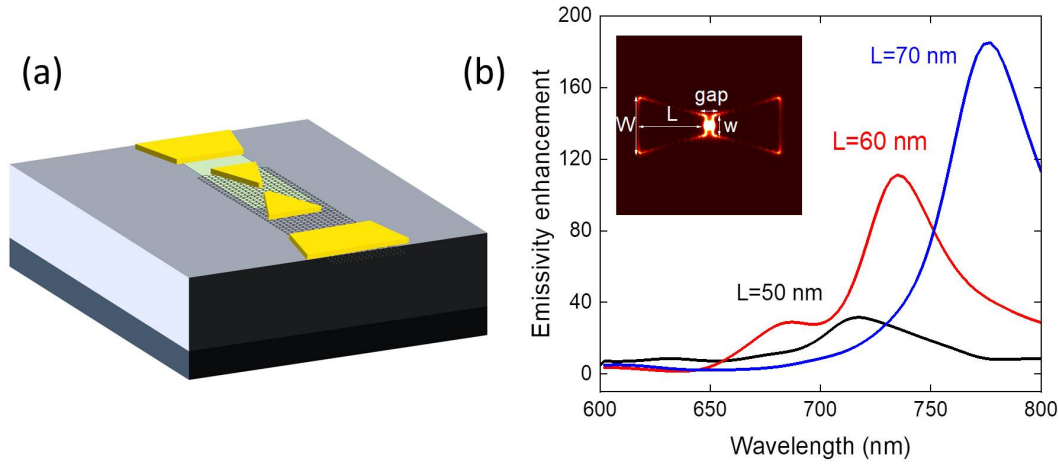


Figure 7.5: (a) Schematic of Bow-Tie antenna-enhanced  $WSe_2/hBN/SLG$  LED on top of  $SiO_2$  (3  $\mu m$ )/Si substrate. (b) Emissivity enhancement ( $S_{free}^{with}/S_{free}^{w/out}$ ) as a function of wavelength for three different antenna's length (L) cases. Inset: Electric-field intensity distribution under geometrically optimized TE-polarized Bow-Tie antenna at  $\lambda=750$  nm. The geometrical parameters of antenna's length, width, small width and gap length are also shown in figure.

As mentioned, Bow-Tie nano-antenna generates enhanced plasmonic fields in close proximity, particularly within its gap, as depicted in the inset of Figure 7.5(b) (white color), thereby enhancing LED performance. This results in a highly increased LED's emissivity enhancement compared to no antenna case ( $S_{free}^{with}/S_{free}^{w/out}$ ), which red-shifts when antenna's length L gets bigger (see Figure 7.5(b)). By appropriately selecting nano-antenna's geometry, material losses can be limited, resulting in an improved Purcell efficiency enhancement (see subsection 7.2.1) and, thus, increased free-space light emission. Furthermore, by carefully choosing the geometrical parameters of nano-antenna, it is possible to achieve the desired spectral shift of plasmonic resonance within the emission range of any TMD emitter. Thus, cases of different L and gap lengths were studied in order to propose an optimized geometry.

In Figure 7.6, we plot  $\eta_{Purcell}$  as a function of wavelength for selective L and gaps. We use a fixed antenna's width  $W=60$  nm, small width  $w=20$  nm and thickness  $t=20$  nm.

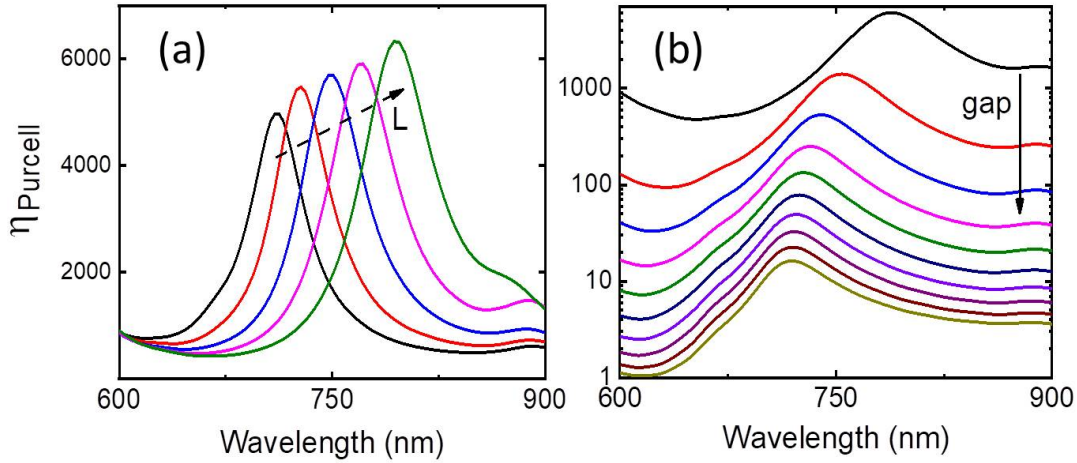


Figure 7.6: Bow-Tie antenna-enhanced  $\text{WSe}_2/\text{hBN}/\text{SLG}$  LED for free-space: Purcell efficiency enhancement as a function of wavelength for variable Bow-Tie antenna's lengths  $L$  (a) and gaps (b). In both (a-b) we use fixed  $W=60$  nm,  $w=20$  nm and  $t=20$  nm.

It is noteworthy that, by increasing antenna's length  $L$  (i.e.  $L=60-80$  nm), Purcell enhancement red-shifts, surpassing three orders of magnitude compared to the same set-up without the antenna (Figure 7.6(a)). Similarly, decreasing gap length (i.e.  $\text{gap}=100-10$  nm) leads to a significant exponential enhancement in Purcell efficiency, accompanied by a slight red-shift (Figure 7.6(b)). Our geometric optimization points towards an arrangement with a narrow gap (approximately 10 nm) and a length  $L$  of around 70 nm, adjusted to demonstrate plasmonic resonance near 750 nm. This optimized design for free-space radiation yielded a Purcell enhancement of  $\sim 6 \times 10^3$  and a final enhanced EQE of  $\sim 5.5\%$ , approximately five times higher than that of the configuration without the antenna.

## 7.6.2 Antenna-enhanced TMD-based LED for integrated photonics

In this work, optical analysis was also conducted on integrated  $\text{WSe}_2$ -based LED configurations, when combined with a Bow-Tie plasmonic nano-antenna [2, 11, 85, 88]. To enhance coupling of a plasmonically enhanced LED with a dielectric waveguide, it is crucial to first of all study the same WG device without the antenna, in order to determine coupling efficiency  $\eta_{\text{coupling}}$  (see Equation 7.11). Figure 7.7(a) shows a schematic of  $\text{WSe}_2$ -based LED on top of a planarized SiN WG lying on  $\text{SiO}_2(3 \text{ um})/\text{Si}$  substrate. The refractive index of SiN at 750 nm is  $n_{\text{SiN}}=2.028$  [90]. Multi-mode WG thickness and width are fixed at  $h_{\text{WG}}=400$  nm and  $w_{\text{WG}}=1.1$  um, respectively.

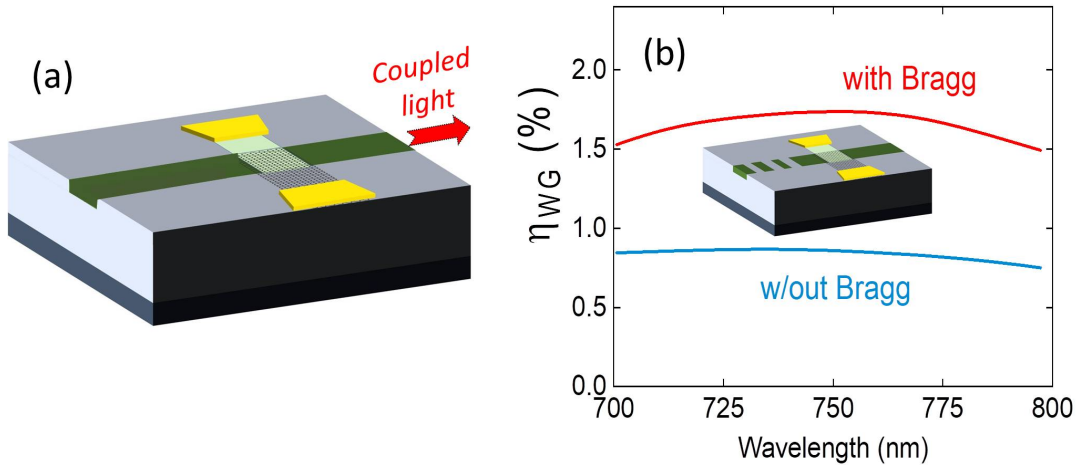


Figure 7.7: (a) Schematic of 1L-WSe<sub>2</sub>/hBN/SLG LED on top of a planarized SiN WG lying on SiO<sub>2</sub>(3 μm)/Si substrate. (b) WG efficiency ( $\eta_{WG}$ ) as a function of wavelength without (light blue line) and with (red line) a lateral planarized DBR mirror (optimized to omnidirectionally reflect light). Schematic of a similar 1L-WSe<sub>2</sub>-based LED device with a back Bragg grating is shown in the middle inset.

Our exploration into SiN waveguides commences by analyzing their properties, when not taking into account the plasmonic influence of the nano-antenna. Our primary objective is to achieve optimal light coupling within the waveguide. In Figure 7.7(b), we conduct EQE calculations for a multi-mode WG device, both with and without the presence of a horizontal dielectric back grating (illustrated in the middle inset of Figure 7.7(b)), showcasing horizontal interference phenomena. The planarized SiN/SiO<sub>2</sub> back grating we use is fine-tuned to reflect nearly 100% of incident polygonal light. The period of back grating is fixed at  $p=260$  nm ( $N_p=20$  periods) and the duty cycle is 0.5 ( $d(\text{SiN})=130$  nm), respectively. It is noteworthy that the light emitted by the WSe<sub>2</sub>-based LED primarily dissipates into the substrate and disperses into free space, permitting only a limited fraction of light to couple into the waveguide. As shown in Figure 7.7(b), without the lateral Bragg reflector coupled light reaches less than  $\sim 1\%$ , while by using the omni-directional Bragg, all the enhanced light was directed in one side, thereby providing a two-fold increase in performance. This results in an improvement in the optical efficiency of LED within the waveguide of  $\eta_{WG} \simeq 2\%$ .

Figure 7.8(a) shows e-field intensity distribution (xz cross section) in the multi-mode SiN WG. Here, we observe the presence of a hybridized mode within the waveguide, characterized by a dark antinode region in the center of waveguide's cross-section. In our pursuit of achieving the optimal light coupling for the fundamental mode within the waveguide, we conducted geometric optimization of the planarized SiN waveguide, as depicted in Figure 7.8(c-d).

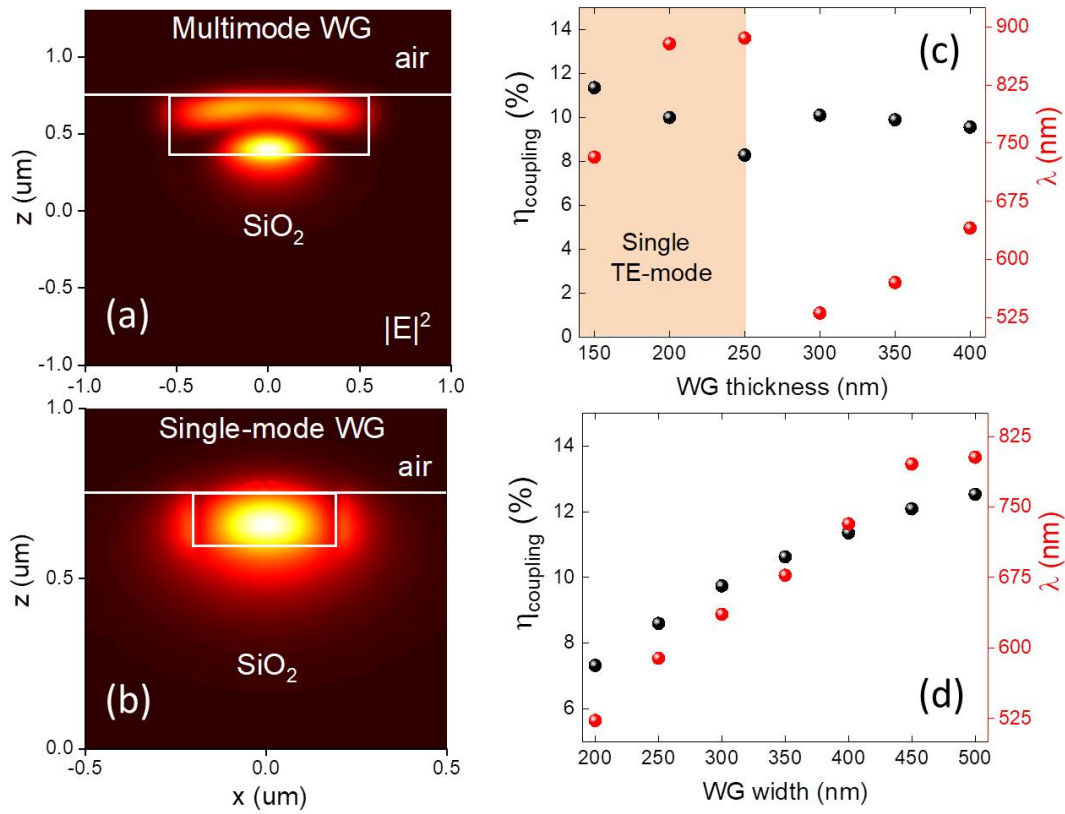


Figure 7.8: E-field intensity spatial distribution (xz cross section) in case of (a) a typical easy to fabricate multi-mode (1.1  $\mu\text{m}$  x 400 nm) and (b) an optimal single-mode (400 nm x 150 nm) SiN WG under WSe<sub>2</sub>-based LED.  $\eta_{coupling}$  (black circles) and resonant wavelength  $\lambda$  (red circles) as a function of WG thickness (c) and width (d).

In Figure 7.8(c), it is evident that coupling efficiency  $\eta_{coupling}$  exhibits a range of variation between  $\sim 8\text{-}12\%$  for WG thicknesses ranging from 150 nm to 400 nm (fixed WG width at 400 nm). Additionally, our observation reveals that with an increase in WG thickness, the resonant wavelength undergoes a shift towards longer wavelengths. Beyond a threshold thickness of approximately 250 nm, a secondary mode emerges, consequently causing the resonance to shift towards shorter wavelengths. Maintaining a constant WG height at 150 nm, we observe, once more, a wavelength shift towards longer wavelengths with an increase in WG width, as illustrated in Figure 7.8(d). The single-mode waveguide with the best coupling efficiency at 750 nm was found to have small dimensions (400 nm x 150 nm), as this allowed for a more enhanced overlap with the fundamental WG mode. Figure 7.8(b) shows e-field intensity spatial distribution for this optimal single-mode WG case. In this case, light coupling achieves an approximate value of  $\sim 12\%$  at 750 nm, with the fundamental mode exclusively propagating within the waveguide.

Up to this point, our aim was to enhance the coupled light within the single-mode waveguide. Moving forward, our focus has shifted towards enhancing the radiation of WSe<sub>2</sub>-based LED, by leveraging Purcell enhancement and employing the suitable nano-antenna. Gold Bow-Tie nano-antenna is designed and placed on top of the planarized SiN waveguide integrated with the dielectric omnidirectional Bragg grating mentioned above on a SiO<sub>2</sub>(3  $\mu\text{m}$ )/Si substrate, as depicted in the schematic representation of Figure 7.9.

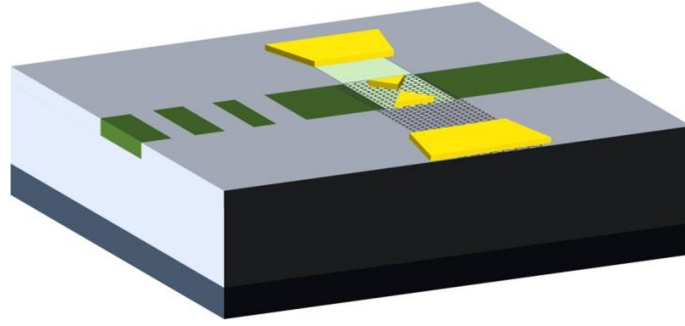


Figure 7.9: Schematic of WSe<sub>2</sub>-based LED on a planarized single-mode (400 nm x 150 nm) SiN waveguide and a one-sided omnidirectional SiN/SiO<sub>2</sub> Bragg grating, with the addition of a metallic Bow-Tie nano-antenna positioned on top.

As described in Section 7.6.1 for free-space radiation, by carefully selecting nano-antenna's geometry, we are able to enhance by orders of magnitude the Purcell enhancement. Utilizing the LED configuration of Figure 7.9, we also manage to enhance the percentage of light entering SiN WG, thereby increasing the coupling of the fundamental mode. Furthermore, with the use of the polygonal dielectric reflector, shown in the schematic, designed to exhibit omnidirectional performance, all the enhanced light propagates in one direction, providing performance improvement of a factor of  $\times 2$ . As a result, the optical efficiency of LED within the waveguide is enhanced. The enhanced performance of this integrated plasmonic LED configuration is depicted in Figure 7.10.

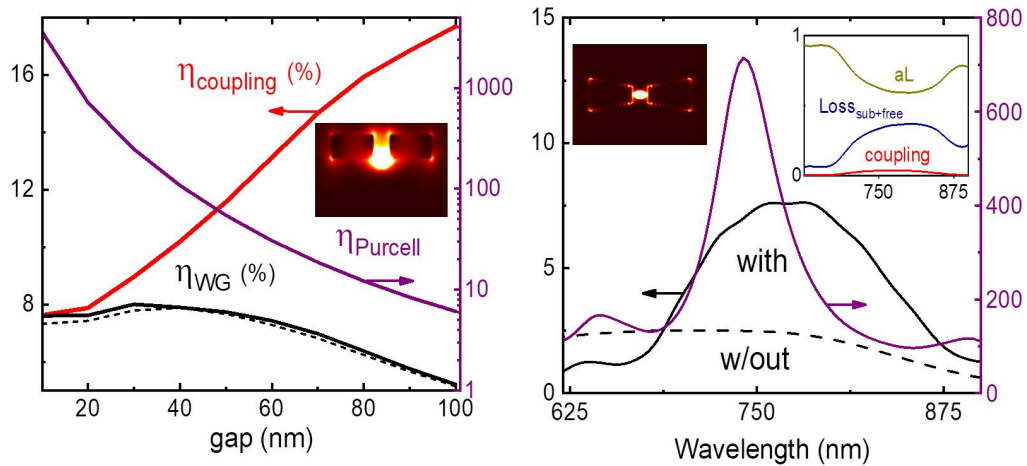


Figure 7.10: (a)  $\eta_{\text{coupling}}$  (red),  $\eta_{\text{Purcell}}$  (purple) and final  $\eta_{\text{WG}}$  (black continuous line) efficiencies for variable Bow-Tie antenna gaps at different resonant wavelengths (see Appendix C.1). The black dashed line represents  $\eta_{\text{WG}}$  at 750 nm. (b) Final  $\eta_{\text{WG}}$  and  $\eta_{\text{Purcell}}$  enhancement as a function of wavelength with the existence of the optimal Bow-Tie antenna of gap=20 nm. Right inset: Coupling efficiency, antenna (aL) and substrate+free losses for the same antenna geometry. Left inset: E-field intensity distribution at the bottom of the optimal antenna at 750 nm. Fixed antenna's length  $L=50$  nm, width  $W=40$  nm, small width  $w=20$  nm and thickness  $t=20$  nm.

Figure 7.10(a) depicts  $\eta_{\text{Purcell}}$  enhancement,  $\eta_{\text{coupling}}$  percentage of light within the

waveguide and the final  $\eta_{WG}$  efficiency as functions of antenna's gap length. As the gap size decreases, an increase in Purcell enhancement is observed, as expected from our previous free-space study and Appendix C.1, accompanied by an inversely proportional reduction in coupling within the waveguide. Following Equation 7.13 for  $\eta_{(ref)} \simeq 1\%$  at 750 nm, we are led to the final  $\eta_{WG}$  (black dashed line). In Appendix C.2, alternative values of  $\eta_{(ref)}$  are used to derive the final  $\eta_{WG}$  enhancement. The final  $\eta_{WG}$  for the optimal antenna geometry with the respective Purcell enhancement, due to antenna's near-fields, as a function of wavelength are both shown in Figure 7.10(b). The performance of this integrated LED configuration increases by a factor of  $\times 3$  ( $\sim 7\%$ ), compared to the same set-up without the antenna (dashed line). While  $\eta_{Purcell}$  enhancement reaches nearly  $\sim 700$ , the relatively low  $\eta_{coupling}$  efficiency results in an even low enhancement of  $\eta_{WG}$  compared to the case without the antenna. Therefore, we depict coupling efficiency and losses, i.e., antenna material losses (aL) as well as the sum of substrate and free-space losses ( $Loss_{sub+free}$ ), in the right inset of Figure 7.10(b). It is evident that both the losses attributed to antenna material (approximately 63% for gold) and  $Loss_{sub+free}$  ( $\sim 30\%$ ) are notably high at 750 nm. This high level of losses contributes to a considerable low coupling efficiency ( $\sim 7\%$ ) that affects  $\eta_{WG}$ .

As mentioned above, antenna losses significantly affects the ability to couple light into the waveguide. One effective approach to mitigate absorption losses within the antenna is by employing a low-loss material (see Appendix C.3). Using an Ag Bow-Tie antenna, for instance, losses are mitigated due to the interband transitions being shifted towards higher energies. The implementation of Ag metallic antenna effectively addresses high losses and results in improved coupling efficiency for higher wavelengths, as illustrated in Figure 7.11.

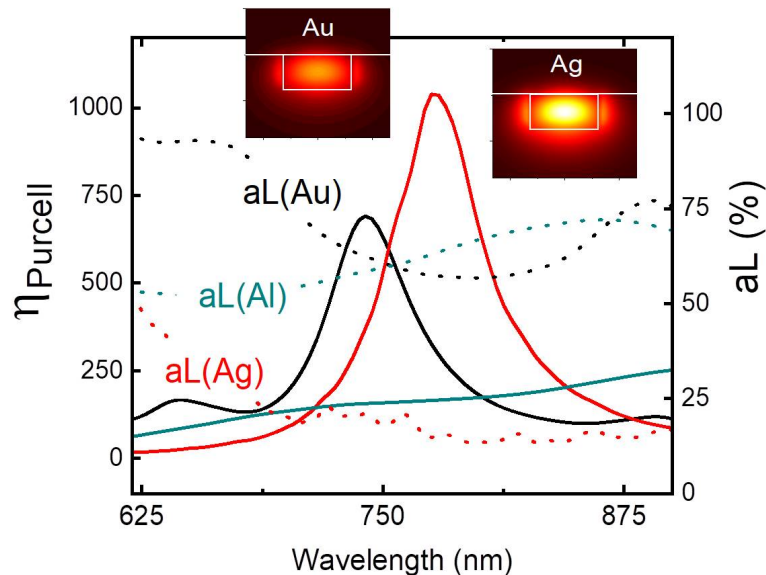


Figure 7.11:  $\eta_{Purcell}$  enhancement (continuous lines) and antenna losses (aL) (dotted lines) for Au (black), Al (dark green) and Ag (red) Bow-Tie antenna material cases. The top insets correspond to e-field intensity distributions on the WG cross-section in case of Au and Ag Bow-Tie antenna, respectively.

From Figure 7.11, the metal that exhibits the lowest losses ( $aL(Ag) \simeq 15\%$  at 750 nm)

and appears to be the most suitable for light scattering and LED efficiency enhancement is Ag. Geometric parameters are customized for each material. For instance, Ag antenna's dimensions are set as follows:  $L=70$  nm,  $gap=20$  nm,  $W=40$  nm,  $w=20$  nm and  $t=20$  nm.

Figure 7.12(a) shows the final efficiency of the waveguided light for the three different metallic antennas and without the plasmonic enhancement (dashed line).

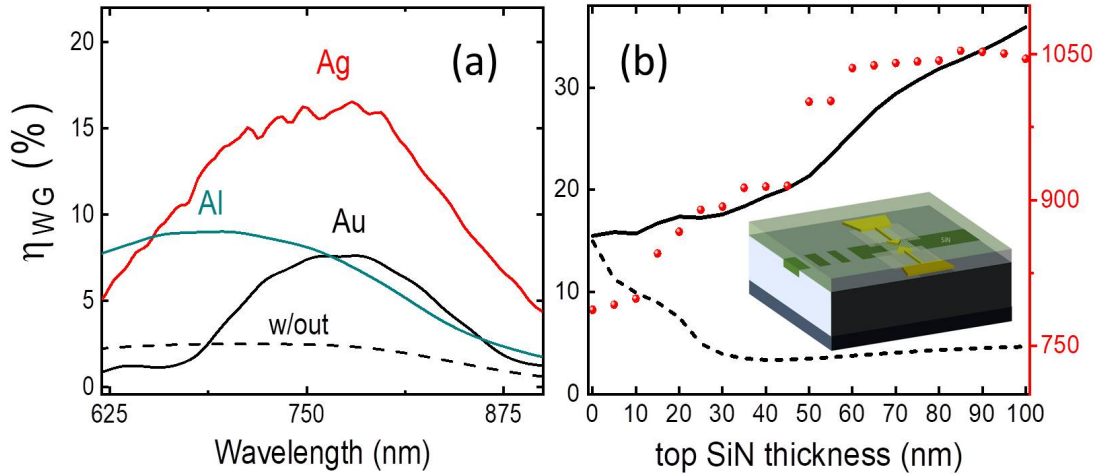


Figure 7.12: (a)  $\eta_{WG}$  efficiency for Au (black), Al (green) and Ag (red) Bow-Tie antenna cases as a function of wavelength. (b) Maximum red-shifted  $\eta_{WG}$  in case of Ag antenna immersed in SiN ( $\leq 100$  nm). The black dashed line represents  $\eta_{WG}$  at 750 nm. Inset: Schematic of Bow-Tie antenna-enhanced WSe<sub>2</sub>-based LED on the planarized SiN waveguide of Figure 7.9, when embedded in SiN with thickness  $\leq 100$  nm.

In case of Ag,  $\eta_{WG}$  efficiency increases by up to 8 times ( $\sim 16\%$ ,  $-8$  dB) at 750 nm, compared to the simple case without the antenna. Furthermore, when Ag antenna is immersed in SiN with a thickness of  $\leq 100$  nm (see the middle inset of Figure 7.12(b)), further enhancement of  $\eta_{WG}$  is achieved for the fundamental WG mode (up to  $\sim 35\%$ ) (see Figure 7.12(b)), along with a concurrent red-shift of the plasmonic resonance, due to the increase in the effective index of the arrangement.

## 7.7 Conclusions

In summary, this chapter provides a comprehensive exploration of nanoscale LEDs based on TMDs, driven by their potential for achieving high efficiency and speed, both for free-space and WG device applications. Notably, our research reveals an enhancement of  $\times 5.75$  in free-space WS<sub>2</sub>-LED emission, when affected by a photonic cavity, that reaches  $\times 16$  in the vertical direction (e.g., narrow NA=0.00125). Simultaneously, when a WSe<sub>2</sub>-LED is positioned on top of a single-mode dielectric SiN WG, antenna-coupling effects contribute to enhancing integrated LED emission. Utilizing a geometrically and material optimized plasmonic Bow-Tie antenna on top of nano-LED is a versatile tool in achieving higher efficiency ( $\sim 8$  dB) and faster LED emission (up to  $\sim$ GHz) for integrated sources. A critical combination of the plasmonic Purcell enhancement, due to the existence of metallic

nano-antenna, with the convenient light coupling into WG, brings a significant enhancement in the amount and speed of waveguided light. The key to this is to geometrically tune plasmonic resonance and coupling overlap at the desired wavelength range. The co-occurrence of high EL efficiency and ultrafast operation make these designs attractive for future high-speed directly modulated nano-emitters.

## References

- [1] K. F. Mak and J. Shan, “Photonics and optoelectronics of 2d semiconductor transition metal dichalcogenides,” *Nature Photonics*, vol. 10, no. 4, pp. 216–226, 2016.
- [2] T. Ren and K. P. Loh, “On-chip integrated photonic circuits based on two-dimensional materials and hexagonal boron nitride as the optical confinement layer,” *Journal of Applied Physics*, vol. 125, no. 23, 2019.
- [3] J. S. Ross, P. Klement, A. M. Jones, N. J. Ghimire, J. Yan, D. Mandrus, T. Taniguchi, K. Watanabe, K. Kitamura, W. Yao, *et al.*, “Electrically tunable excitonic light-emitting diodes based on monolayer wse<sub>2</sub> p–n junctions,” *Nature nanotechnology*, vol. 9, no. 4, pp. 268–272, 2014.
- [4] R. Cheng, D. Li, H. Zhou, C. Wang, A. Yin, S. Jiang, Y. Liu, Y. Chen, Y. Huang, and X. Duan, “Electroluminescence and photocurrent generation from atomically sharp wse<sub>2</sub>/mos<sub>2</sub> heterojunction p–n diodes,” *Nano letters*, vol. 14, no. 10, pp. 5590–5597, 2014.
- [5] L. Britnell, R. M. Ribeiro, A. Eckmann, R. Jalil, B. D. Belle, A. Mishchenko, Y.-J. Kim, R. V. Gorbachev, T. Georgiou, S. V. Morozov, *et al.*, “Strong light-matter interactions in heterostructures of atomically thin films,” *Science*, vol. 340, no. 6138, pp. 1311–1314, 2013.
- [6] M. Brotons-Gisbert, J. P. Martínez-Pastor, G. C. Ballesteros, B. D. Gerardot, and J. F. Sánchez-Royo, “Engineering light emission of two-dimensional materials in both the weak and strong coupling regimes,” *Nanophotonics*, vol. 7, no. 1, pp. 253–267, 2018.
- [7] Y. Ye, Z. J. Wong, X. Lu, X. Ni, H. Zhu, X. Chen, Y. Wang, and X. Zhang, “Monolayer excitonic laser,” *Nature Photonics*, vol. 9, no. 11, pp. 733–737, 2015.
- [8] L. Dobusch, S. Schuler, V. Perebeinos, and T. Mueller, “Thermal light emission from monolayer mos<sub>2</sub>,” *Advanced Materials*, vol. 29, no. 31, p. 1701304, 2017.
- [9] B. W. Baugher, H. O. Churchill, Y. Yang, and P. Jarillo-Herrero, “Optoelectronic devices based on electrically tunable p–n diodes in a monolayer dichalcogenide,” *Nature nanotechnology*, vol. 9, no. 4, pp. 262–267, 2014.
- [10] C.-H. Lee, G.-H. Lee, A. M. Van Der Zande, W. Chen, Y. Li, M. Han, X. Cui, G. Arefe, C. Nuckolls, T. F. Heinz, *et al.*, “Atomically thin p–n junctions with van der waals heterointerfaces,” *Nature nanotechnology*, vol. 9, no. 9, pp. 676–681, 2014.
- [11] X. Li, L. Tao, Z. Chen, H. Fang, X. Li, X. Wang, J.-B. Xu, and H. Zhu, “Graphene and related two-dimensional materials: Structure-property relationships for electronics and optoelectronics,” *Applied Physics Reviews*, vol. 4, no. 2, 2017.

- [12] W. Choi, N. Choudhary, G. H. Han, J. Park, D. Akinwande, and Y. H. Lee, “Recent development of two-dimensional transition metal dichalcogenides and their applications,” *Materials Today*, vol. 20, no. 3, pp. 116–130, 2017.
- [13] Z. Wang, Q. Jingjing, X. Wang, Z. Zhang, Y. Chen, X. Huang, and W. Huang, “Two-dimensional light-emitting materials: preparation, properties and applications,” *Chemical Society Reviews*, vol. 47, no. 16, pp. 6128–6174, 2018.
- [14] W. Zheng, Y. Jiang, X. Hu, H. Li, Z. Zeng, X. Wang, and A. Pan, “Light emission properties of 2d transition metal dichalcogenides: fundamentals and applications,” *Advanced Optical Materials*, vol. 6, no. 21, p. 1800420, 2018.
- [15] C. Palacios-Berraquero and C. Palacios-Berraquero, “Atomically-thin quantum light emitting diodes,” *Quantum confined excitons in 2-dimensional materials*, pp. 71–89, 2018.
- [16] S. Jo, N. Ubrig, H. Berger, A. B. Kuzmenko, and A. F. Morpurgo, “Mono-and bilayer wse2 light-emitting transistors,” *Nano letters*, vol. 14, no. 4, pp. 2019–2025, 2014.
- [17] F. Withers, O. Del Pozo-Zamudio, A. Mishchenko, A. Rooney, A. Gholinia, K. Watanabe, T. Taniguchi, S. J. Haigh, A. Geim, A. Tartakovskii, *et al.*, “Light-emitting diodes by band-structure engineering in van der waals heterostructures,” *Nature materials*, vol. 14, no. 3, pp. 301–306, 2015.
- [18] F. Withers, O. Del Pozo-Zamudio, S. Schwarz, S. Dufferwiel, P. Walker, T. Godde, A. Rooney, A. Gholinia, C. Woods, P. Blake, *et al.*, “Wse2 light-emitting tunneling transistors with enhanced brightness at room temperature,” *Nano letters*, vol. 15, no. 12, pp. 8223–8228, 2015.
- [19] C.-H. Liu, G. Clark, T. Fryett, S. Wu, J. Zheng, F. Hatami, X. Xu, and A. Majumdar, “Nanocavity integrated van der waals heterostructure light-emitting tunneling diode,” *Nano letters*, vol. 17, no. 1, pp. 200–205, 2017.
- [20] R. J. P. Román, Y. Auad, L. Grasso, F. Alvarez, I. D. Barcelos, and L. F. Zagonel, “Tunneling-current-induced local excitonic luminescence in p-doped wse 2 monolayers,” *Nanoscale*, vol. 12, no. 25, pp. 13460–13470, 2020.
- [21] C. Schneider, M. M. Glazov, T. Korn, S. Höfling, and B. Urbaszek, “Two-dimensional semiconductors in the regime of strong light-matter coupling,” *Nature communications*, vol. 9, no. 1, p. 2695, 2018.
- [22] G. Wang, A. Chernikov, M. M. Glazov, T. F. Heinz, X. Marie, T. Amand, and B. Urbaszek, “Colloquium: Excitons in atomically thin transition metal dichalcogenides,” *Reviews of Modern Physics*, vol. 90, no. 2, p. 021001, 2018.
- [23] T. Mueller and E. Malic, “Exciton physics and device application of two-dimensional transition metal dichalcogenide semiconductors,” *npj 2D Materials and Applications*, vol. 2, no. 1, p. 29, 2018.
- [24] M. M. Glazov, “Optical properties of charged excitons in two-dimensional semiconductors,” *The Journal of Chemical Physics*, vol. 153, no. 3, 2020.

- [25] M. Barbone, A. R.-P. Montblanch, D. M. Kara, C. Palacios-Berraquero, A. R. Cadore, D. De Fazio, B. Pingault, E. Mostaani, H. Li, B. Chen, *et al.*, “Charge-tuneable biexciton complexes in monolayer wse<sub>2</sub>,” *Nature communications*, vol. 9, no. 1, p. 3721, 2018.
- [26] J. Wang, F. Lin, I. Verzhbitskiy, K. Watanabe, T. Taniguchi, J. Martin, and G. Eda, “Polarity tunable trionic electroluminescence in monolayer wse<sub>2</sub>,” *Nano Letters*, vol. 19, no. 10, pp. 7470–7475, 2019.
- [27] M. Paur, A. J. Molina-Mendoza, R. Bratschitsch, K. Watanabe, T. Taniguchi, and T. Mueller, “Electroluminescence from multi-particle exciton complexes in transition metal dichalcogenide semiconductors,” *Nature Communications*, vol. 10, no. 1, p. 1709, 2019.
- [28] D.-H. Lien, S. Z. Uddin, M. Yeh, M. Amani, H. Kim, J. W. Ager III, E. Yablonovitch, and A. Javey, “Electrical suppression of all nonradiative recombination pathways in monolayer semiconductors,” *Science*, vol. 364, no. 6439, pp. 468–471, 2019.
- [29] A. C. Ferrari, F. Bonaccorso, V. Fal’Ko, K. S. Novoselov, S. Roche, P. Bøggild, S. Borini, F. H. Koppens, V. Palermo, N. Pugno, *et al.*, “Science and technology roadmap for graphene, related two-dimensional crystals, and hybrid systems,” *Nanoscale*, vol. 7, no. 11, pp. 4598–4810, 2015.
- [30] S. Manzeli, D. Ovchinnikov, D. Pasquier, O. Yazyev, and A. Kis, “Ising pairing in superconducting nbse<sub>2</sub> atomic layers,” *Nat. Rev. Mater*, vol. 2, p. 17033, 2017.
- [31] F. Bonaccorso, Z. Sun, T. Hasan, and A. Ferrari, “Graphene photonics and optoelectronics,” *Nature photonics*, vol. 4, no. 9, pp. 611–622, 2010.
- [32] F. Koppens, T. Mueller, P. Avouris, A. Ferrari, M. Vitiello, and M. Polini, “Photodetectors based on graphene, other two-dimensional materials and hybrid systems,” *Nature nanotechnology*, vol. 9, no. 10, pp. 780–793, 2014.
- [33] M. Romagnoli, V. Sorianello, M. Midrio, F. H. Koppens, C. Huyghebaert, D. Neumaier, P. Galli, W. Templ, A. D’Errico, and A. C. Ferrari, “Graphene-based integrated photonics for next-generation datacom and telecom,” *Nature Reviews Materials*, vol. 3, no. 10, pp. 392–414, 2018.
- [34] D. Kwak, M. Paur, K. Watanabe, T. Taniguchi, and T. Mueller, “High-speed electroluminescence modulation in monolayer ws<sub>2</sub>,” *Advanced Materials Technologies*, vol. 7, no. 5, p. 2100915, 2022.
- [35] D. Andrzejewski, H. Myja, M. Heuken, A. Grundmann, H. Kalisch, A. Vescan, T. Kümmell, and G. Bacher, “Scalable large-area p–i–n light-emitting diodes based on ws<sub>2</sub> monolayers grown via mocvd,” *ACS Photonics*, vol. 6, no. 8, pp. 1832–1839, 2019.
- [36] D. Andrzejewski, E. Hopmann, M. John, T. Kümmell, and G. Bacher, “Ws<sub>2</sub> monolayer-based light-emitting devices in a vertical p–n architecture,” *Nanoscale*, vol. 11, no. 17, pp. 8372–8379, 2019.

- [37] R. Sundaram, M. Engel, A. Lombardo, R. Krupke, A. Ferrari, P. Avouris, and M. Steiner, “Electroluminescence in single layer mos<sub>2</sub>,” *Nano letters*, vol. 13, no. 4, pp. 1416–1421, 2013.
- [38] Y. Sheng, T. Chen, Y. Lu, R.-J. Chang, S. Sinha, and J. H. Warner, “High-performance ws<sub>2</sub> monolayer light-emitting tunneling devices using 2d materials grown by chemical vapor deposition,” *ACS nano*, vol. 13, no. 4, pp. 4530–4537, 2019.
- [39] S. Wang, J. Wang, W. Zhao, F. Giustiniano, L. Chu, I. Verzhbitskiy, J. Zhou Yong, and G. Eda, “Efficient carrier-to-exciton conversion in field emission tunnel diodes based on mis-type van der waals heterostack,” *Nano letters*, vol. 17, no. 8, pp. 5156–5162, 2017.
- [40] L. Yuan and L. Huang, “Exciton dynamics and annihilation in ws<sub>2</sub> 2d semiconductors,” *Nanoscale*, vol. 7, no. 16, pp. 7402–7408, 2015.
- [41] H. Wang, C. Zhang, and F. Rana, “Ultrafast dynamics of defect-assisted electron–hole recombination in monolayer mos<sub>2</sub>,” *Nano letters*, vol. 15, no. 1, pp. 339–345, 2015.
- [42] S. Dufferwiel, S. Schwarz, F. Withers, A. Trichet, F. Li, M. Sich, O. Del Pozo-Zamudio, C. Clark, A. Nalitov, D. Solnyshkov, *et al.*, “Exciton–polaritons in van der waals heterostructures embedded in tunable microcavities,” *Nature communications*, vol. 6, no. 1, p. 8579, 2015.
- [43] X. Gan, Y. Gao, K. Fai Mak, X. Yao, R.-J. Shiue, A. Van Der Zande, M. E. Trusheim, F. Hatami, T. F. Heinz, J. Hone, *et al.*, “Controlling the spontaneous emission rate of monolayer mos<sub>2</sub> in a photonic crystal nanocavity,” *Applied physics letters*, vol. 103, no. 18, 2013.
- [44] C. Javerzac-Galy, A. Kumar, R. D. Schilling, N. Piro, S. Khorasani, M. Barbone, I. Goykhman, J. B. Khurgin, A. C. Ferrari, and T. J. Kippenberg, “Excitonic emission of monolayer semiconductors near-field coupled to high-q microresonators,” *Nano Letters*, vol. 18, no. 5, pp. 3138–3146, 2018.
- [45] R. G. Baets, D. G. Delbeke, R. Bockstaele, and P. Bienstman, “Resonant-cavity light-emitting diodes: a review,” *Light-Emitting Diodes: Research, Manufacturing, and Applications VII*, vol. 4996, pp. 74–86, 2003.
- [46] E. K. Lau, A. Lakhani, R. S. Tucker, and M. C. Wu, “Enhanced modulation bandwidth of nanocavity light emitting devices,” *Optics Express*, vol. 17, no. 10, pp. 7790–7799, 2009.
- [47] L. Ma, P. Yu, W. Wang, H.-C. Kuo, A. O. Govorov, S. Sun, and Z. Wang, “Nanoantenna-enhanced light-emitting diodes: Fundamental and recent progress,” *Laser & Photonics Reviews*, vol. 15, no. 5, p. 2000367, 2021.
- [48] H. Chen, J. Yang, E. Rusak, J. Straubel, R. Guo, Y. W. Myint, J. Pei, M. Decker, I. Staude, C. Rockstuhl, *et al.*, “Manipulation of photoluminescence of two-dimensional mos<sub>2</sub> by gold nanoantennas,” *Scientific reports*, vol. 6, no. 1, p. 22296, 2016.

- [49] A. Kinkhabwala, Z. Yu, S. Fan, Y. Avlasevich, K. Müllen, and W. Moerner, “Large single-molecule fluorescence enhancements produced by a bowtie nanoantenna,” *Nature photonics*, vol. 3, no. 11, pp. 654–657, 2009.
- [50] L. Sortino, P. Zotev, S. Mignuzzi, J. Cambiasso, D. Schmidt, A. Genco, M. Aßmann, M. Bayer, S. Maier, R. Sapienza, *et al.*, “Enhanced light-matter interaction in an atomically thin semiconductor coupled with dielectric nano-antennas,” *Nature communications*, vol. 10, no. 1, p. 5119, 2019.
- [51] M. S. Eggleston, K. Messer, L. Zhang, E. Yablonovitch, and M. C. Wu, “Optical antenna enhanced spontaneous emission,” *Proceedings of the National Academy of Sciences*, vol. 112, no. 6, pp. 1704–1709, 2015.
- [52] X. Li and Q. Gu, “High-speed on-chip light sources at the nanoscale,” *Advances in Physics: X*, vol. 4, no. 1, p. 1658541, 2019.
- [53] M. S. Eggleston, S. B. Desai, K. Messer, S. A. Fortuna, S. Madhupathy, J. Xiao, X. Zhang, E. Yablonovitch, A. Javey, and M. C. Wu, “Ultrafast spontaneous emission from a slot-antenna coupled wse2 monolayer,” *ACS Photonics*, vol. 5, no. 7, pp. 2701–2705, 2018.
- [54] G. Walter, C. Wu, H. Then, M. Feng, and N. Holonyak, “Tilted-charge high speed (7 ghz) light emitting diode,” *Applied Physics Letters*, vol. 94, no. 23, 2009.
- [55] S. A. Fortuna, A. Taghizadeh, E. Yablonovitch, and M. C. Wu, “Toward 100 ghz direct modulation rate of antenna coupled nanoled,” in *2016 IEEE Photonics Conference (IPC)*, pp. 216–217, IEEE, 2016.
- [56] J. Gu, B. Chakraborty, M. Khatoniar, and V. M. Menon, “A room-temperature polariton light-emitting diode based on monolayer ws<sub>2</sub>,” *Nature nanotechnology*, vol. 14, no. 11, pp. 1024–1028, 2019.
- [57] Y. Zhang, T. Oka, R. Suzuki, J. Ye, and Y. Iwasa, “Electrically switchable chiral light-emitting transistor,” *Science*, vol. 344, no. 6185, pp. 725–728, 2014.
- [58] E. F. Schubert, *Light-Emitting Diodes (2006)*. E. Fred Schubert, 2006.
- [59] E. Purcell, “Purcell\_1946\_spontaneousemission. pdf,” *Phys. Rev. B*, vol. 69, p. 681, 1946.
- [60] M. Pelton, “Modified spontaneous emission in nanophotonic structures,” *Nature Photonics*, vol. 9, no. 7, pp. 427–435, 2015.
- [61] T. Baba, “Photonic crystals and microdisk cavities based on gainasp-inp system,” *IEEE journal of selected topics in quantum electronics*, vol. 3, no. 3, pp. 808–830, 1997.
- [62] A. Cadore, B. L. T. Rosa, I. Paradisanos, S. Mignuzzi, D. De Fazio, E. Alexeev, A. Dagkli, J. Muench, G. Kakavelakis, S. M. Schinde, *et al.*, “Monolayer ws<sub>2</sub> electro-and photo-luminescence enhancement by tfsi treatment,” *2D Materials*, 2024.

- [63] A. Berkdemir, H. R. Gutiérrez, A. R. Botello-Méndez, N. Perea-López, A. L. Elías, C.-I. Chia, B. Wang, V. H. Crespi, F. López-Urías, J.-C. Charlier, *et al.*, “Identification of individual and few layers of ws<sub>2</sub> using raman spectroscopy,” *Scientific reports*, vol. 3, no. 1, p. 1755, 2013.
- [64] A. Molina-Sanchez and L. Wirtz, “Phonons in single-layer and few-layer mos<sub>2</sub> and ws<sub>2</sub>,” *Physical Review B*, vol. 84, no. 15, p. 155413, 2011.
- [65] W. Zhao, Z. Ghorannevis, K. K. Amara, J. R. Pang, M. Toh, X. Zhang, C. Kloc, P. H. Tan, and G. Eda, “Lattice dynamics in mono- and few-layer sheets of ws<sub>2</sub> and wse<sub>2</sub>,” *Nanoscale*, vol. 5, no. 20, pp. 9677–9683, 2013.
- [66] A. O. A. Tanoh, J. Alexander-Webber, J. Xiao, G. Delport, C. A. Williams, H. Bretscher, N. Gauriot, J. Allardice, R. Pandya, Y. Fan, *et al.*, “Enhancing photoluminescence and mobilities in ws<sub>2</sub> monolayers with oleic acid ligands,” *Nano letters*, vol. 19, no. 9, pp. 6299–6307, 2019.
- [67] M. Amani, D.-H. Lien, D. Kiriya, J. Xiao, A. Azcatl, J. Noh, S. R. Madhupathy, R. Addou, S. Kc, M. Dubey, *et al.*, “Near-unity photoluminescence quantum yield in mos<sub>2</sub>,” *Science*, vol. 350, no. 6264, pp. 1065–1068, 2015.
- [68] M. R. Molas, K. Gołasa, Ł. Bala, K. Nogajewski, M. Bartos, M. Potemski, and A. Babiński, “Tuning carrier concentration in a superacid treated mos<sub>2</sub> monolayer,” *Scientific Reports*, vol. 9, no. 1, p. 1989, 2019.
- [69] A. Alharbi, P. Zahl, and D. Shahrjerdi, “Material and device properties of superacid-treated monolayer molybdenum disulfide,” *Applied Physics Letters*, vol. 110, no. 3, 2017.
- [70] F. Cadiz, S. Tricard, M. Gay, D. Lagarde, G. Wang, C. Robert, P. Renucci, B. Urbaszek, and X. Marie, “Well separated trion and neutral excitons on superacid treated mos<sub>2</sub> monolayers,” *Applied Physics Letters*, vol. 108, no. 25, 2016.
- [71] E. F. Schubert, *Light-Emitting Diodes (2018)*. E. Fred Schubert, 2018.
- [72] C. R. Gubbin, S. A. Maier, and S. Kéna-Cohen, “Low-voltage polariton electroluminescence from an ultrastrongly coupled organic light-emitting diode,” *Applied Physics Letters*, vol. 104, no. 23, 2014.
- [73] A. Graf, M. Held, Y. Zakharko, L. Tropic, M. C. Gather, and J. Zaumseil, “Electrical pumping and tuning of exciton-polaritons in carbon nanotube microcavities,” *Nature materials*, vol. 16, no. 9, pp. 911–917, 2017.
- [74] T. Galfsky, Z. Sun, C. R. Conside, C.-T. Chou, W.-C. Ko, Y.-H. Lee, E. E. Narimanov, and V. M. Menon, “Broadband enhancement of spontaneous emission in two-dimensional semiconductors using photonic hypercrystals,” *Nano letters*, vol. 16, no. 8, pp. 4940–4945, 2016.
- [75] Y. J. Noori, Y. Cao, J. Roberts, C. Woodhead, R. Bernardo-Gavito, P. Tovee, and R. J. Young, “Photonic crystals for enhanced light extraction from 2d materials,” *Acs Photonics*, vol. 3, no. 12, pp. 2515–2520, 2016.

- [76] S. Wu, S. Buckley, A. M. Jones, J. S. Ross, N. J. Ghimire, J. Yan, D. G. Mandrus, W. Yao, F. Hatami, J. Vučković, *et al.*, “Control of two-dimensional excitonic light emission via photonic crystal,” *2D Materials*, vol. 1, no. 1, p. 011001, 2014.
- [77] C. Hsu, R. Frisenda, R. Schmidt, A. Arora, S. M. De Vasconcellos, R. Bratschitsch, H. S. van der Zant, and A. Castellanos-Gomez, “Thickness-dependent refractive index of 1l, 2l, and 3l mos<sub>2</sub>, mose<sub>2</sub>, ws<sub>2</sub>, and wse<sub>2</sub>,” *Advanced optical materials*, vol. 7, no. 13, p. 1900239, 2019.
- [78] A. Taflove, “Computati: The finite-difference time-domain method,” *Artech House*, 1995.
- [79] B. Horcholle, C. Labbé, X. Portier, P. Marie, C. Frilay, W. Yuan, W. Jadwisienczak, D. Ingram, C. Grygiel, and J. Cardin, “Growth and study of tb<sub>3</sub>+ doped nb<sub>2</sub>o<sub>5</sub> thin films by radiofrequency magnetron sputtering: Photoluminescence properties,” *Applied Surface Science*, vol. 597, p. 153711, 2022.
- [80] I. H. Malitson, “Interspecimen comparison of the refractive index of fused silica,” *Josa*, vol. 55, no. 10, pp. 1205–1209, 1965.
- [81] P. B. Johnson and R.-W. Christy, “Optical constants of the noble metals,” *Physical review B*, vol. 6, no. 12, p. 4370, 1972.
- [82] V. Kravets, A. Grigorenko, R. Nair, P. Blake, S. Anissimova, K. Novoselov, and A. Geim, “Spectroscopic ellipsometry of graphene and an exciton-shifted van hove peak in absorption,” *Physical Review B*, vol. 81, no. 15, p. 155413, 2010.
- [83] T. Echtermeyer, S. Milana, U. Sassi, A. Eiden, M. Wu, E. Lidorikis, and A. Ferrari, “Surface plasmon polariton graphene photodetectors,” *Nano Letters*, vol. 16, no. 1, pp. 8–20, 2016.
- [84] S.-Y. Lee, T.-Y. Jeong, S. Jung, and K.-J. Yee, “Refractive index dispersion of hexagonal boron nitride in the visible and near-infrared,” *physica status solidi (b)*, vol. 256, no. 6, p. 1800417, 2019.
- [85] O. Del Pozo-Zamudio, A. Genco, S. Schwarz, F. Withers, P. Walker, T. Godde, R. Schofield, A. Rooney, E. Prestat, K. Watanabe, *et al.*, “Electrically pumped wse<sub>2</sub>-based light-emitting van der waals heterostructures embedded in monolithic dielectric microcavities,” *2D Materials*, vol. 7, no. 3, p. 031006, 2020.
- [86] O. Bitton and G. Haran, “Plasmonic cavities and individual quantum emitters in the strong coupling limit,” *Accounts of chemical research*, vol. 55, no. 12, pp. 1659–1668, 2022.
- [87] P. Ma, Y. Salamin, B. Baeuerle, A. Josten, W. Heni, A. Emboras, and J. Leuthold, “Plasmonically enhanced graphene photodetector featuring 100 gbit/s data reception, high responsivity, and compact size,” *ACS Photonics*, vol. 6, no. 1, pp. 154–161, 2018.
- [88] Y. Zhu, X. Sun, Y. Tang, L. Fu, and Y. Lu, “Two-dimensional materials for light emitting applications: Achievement, challenge and future perspectives,” *Nano Research*, vol. 14, pp. 1912–1936, 2021.

- [89] D. E. Aspnes and A. Studna, “Dielectric functions and optical parameters of si, ge, gap, gaas, gasb, inp, inas, and insb from 1.5 to 6.0 ev,” *Physical review B*, vol. 27, no. 2, p. 985, 1983.
- [90] K. Luke, Y. Okawachi, M. R. Lamont, A. L. Gaeta, and M. Lipson, “Broadband mid-infrared frequency comb generation in a si<sub>3</sub>n<sub>4</sub> microresonator,” *Optics letters*, vol. 40, no. 21, pp. 4823–4826, 2015.

# Chapter 8

## Conclusions and Outlook

### 8.1 Summary

Chapter 1 introduces the necessity for high-speed and efficient optoelectronic devices. It discusses the limitations of current bulk materials used in optoelectronics (i.e., GaN, GaAs and their alloys with In, Al, P, etc.), emphasizing the need for alternative solutions. SLG and other 2D materials, such as TMDs, are proposed as potential candidates for efficient photonic and optoelectronic platforms. In this chapter the primary objectives of thesis are briefly described. These objectives are to investigate the enhanced graphene-light interaction, as well as exploring the applications of graphene and 2D TMDs in optoelectronic devices, including nanoscale optical modulators, sensors and nanoscale LEDs, operating from visible to NIR frequency range.

In Chapter 2, a thorough theoretical review of graphene's, TMD's and vdWH's optoelectronic properties is presented. Furthermore, the concepts outlined in this chapter serve as the basis for investigating graphene and TMD-based optoelectronic devices studied throughout the thesis.

Chapter 3 introduces the fundamental principles of light-matter interactions explored in this thesis. It offers a comprehensive review of the plasmonic response of metals, photonics and dipole emission.

Chapter 4 briefly discusses the computational tools and analytical methods that are used for numerical analysis throughout this thesis.

Chapter 5 delves into the interaction between graphene and light, specifically when integrating graphene with 3D plasmonic nanostructured silicon substrates. Our computational findings, supported by experimental measurements [1], demonstrate that the alignment of SLG with metallic nanoparticle-decorated silicon nanopillars enables graphene to sample near-fields from an increased number of nanoparticles. Furthermore, the synergistic effects between the nanoparticles and silicon nanopillars lead to a non-local broadband SERS enhancement, reaching up to three orders of magnitude, compared to graphene on flat silicon.

Chapter 6 discusses two diverse applications of graphene. In the first one, graphene is used for IR optical modulation (Doukas et al.[2]), while, in the latter, graphene is introduced as an effective material for ultrafast pulse-shaping. In this chapter, graphene is integrated with an asymmetric Fabry-Perot nanocavity to be utilized in both free-space IR electro-optic modulation and ultrafast pulse-shaping. Regarding optical modulation, our research demonstrates that high-performance and fast modulation can be achieved regardless of graphene quality. Additionally, this device can be transformed into a highly

sensitive acousto-absorption modulator. In terms of pulse-shaping with graphene, our exploration reveals that SLG, acting as a tunable saturable absorber, can serve as a versatile tool for modulating the amplitude, time duration, and even shape of pulses, leading to the generation of multiple peaks. Moreover, this pulse-shaper can be used as a sensitive diagnostic tool for identifying intrinsic graphene processes.

Chapter 7 presents a comprehensive investigation of nanoscale LEDs based on 1L-TMDs, driven by their potential for achieving high efficiency and speed. Our focus encompasses both free-space and integrated photonic devices, highlighting their versatile applicability. Within this study, we investigate a TMD/hBN/graphene emitting heterostructure, using monolayer WS<sub>2</sub> and/or WSe<sub>2</sub>, respectively. Our investigation reveals an interesting enhancement in LED emission, when affected by a photonic cavity [3], influencing its directionality (bigger enhancement in the vertical direction) for free-space applications. Moreover, when situated atop a dielectric SiN waveguide and beneath a Bow-Tie plasmonic antenna, antenna-coupling effects come into play, significantly enhancing the efficiency and speed of integrated LED emission.

## 8.2 Outlook and future perspectives

As mentioned, the increasing potential of 2D materials, such as graphene and TMDs, along with their heterostructures, for applications in photonics and optoelectronics, has garnered increasing attention [4–10]. The optoelectronic devices, based on these 2D materials, have been successfully demonstrated, spanning optical modulators [11], photodetectors [12, 13], sensors, nanoscale LEDs [14] and more. The recent research focused on these devices stems from their potential to offer enhanced efficiency, high speed, wavelength tunability and mechanical flexibility. Notably, SLG and TMDs, due to their unique properties [15–21], hold significant promise across various optoelectronic applications. In addition, combining these materials within LMHs is promising for the development of multi-functional, high-performance optoelectronic devices.

Despite notable advancements in the development of 2D material-based optoelectronic devices, several challenges remain for their widespread commercialization and practical application. One major challenge is the need for scalable, high-quality, and cost-effective synthesis methods. Furthermore, leveraging the unique properties of graphene and other 2D materials, and achieving high-performance optoelectronic devices is essential for commercial success. Consequently, realistic modeling tools, that accurately represent 2D material's optical, electrical and thermal properties are essential for designing and optimizing new device concepts and architectures. In this thesis, we employ both computational and analytical approaches that incorporate the opto-thermo-electrical properties of 2D materials, enabling the study of these materials within a complete device framework. These methods are applicable to both continuous-wave (CW) and pulsed operation, covering a wide range of operational parameters. This provides comprehensive tools for designing and optimizing configurations based on graphene and other 2D materials. We accurately capture the interaction between the electrical, optical, and thermal properties of 2D materials upon photo-excitation, offering valuable insights into the underlying physics and facilitating realistic design optimization.

The reliability of our methods is demonstrated in Chapters 5, 6, and 7, where they have been validated against experimental results from the literature. We model and study optoelectronic devices based on graphene and 2D TMDs, demonstrating that with the appropriate design and optimization, these devices can achieve performances comparable, or even

higher, to state-of-the-art configurations. As an example, the effective use of graphene, when it is conformed on 3D plasmonic substrates, offers a broadband three-order of magnitude SERS enhancement, that can be compared with efficient device configurations and exploited for applications of large-area hybrid nanomaterials [22–24] in the fields of sensing, medical diagnostics etc. Furthermore, under linear CW incident light, graphene can be used as an effectively tunable absorbing material for optical modulation via applied voltage at NIR. The graphene-based gate-tunable configuration proposed in this thesis is demonstrated to feature a MD of  $\sim 30$  dB and low IL at GHz frequencies, outperforming previous reports [25–35]. Furthermore, the temporal response of the same scheme under non-linear high power incident pulses, can support novel ultrafast pulse-shaping operation [36–38]. Manipulating graphene absorptivity via incident power and/or doping, we manage to modulate the amplitude, duration and shape, giving rise to multiple secondary peaks at picosecond timescale. This scheme could be convenient in signal processing and is a promising component for optical communication systems. Due to ultrafast carrier dynamics and slow cooling processes of graphene, this sensitive device could be easily also used as an innovative probe into graphene fs-scale dynamics by simply measuring the response under intense ps-pulses. Additionally, using experimentally evaluated emitting LMHs, we develop and propose an easy and versatile post-analysis method for the calculation of EL quantum efficiency. Following this method, we effectively obtain an enhanced EL EQE in both photonic cavity and antenna-enhanced LED configurations at visible frequencies. When the proposed WS<sub>2</sub>-based LED is affected by an optimized photonic cavity, reveals a free-space EL enhancement of  $\times 5.75$ , that reaches  $\times 16$  in the vertical direction (e.g., narrow NA). This EL enhancement is comparable to recent findings [39–46] and our simple post-analysis method shows great promise and can be utilized in novel and practical arrangements. Furthermore, FDTD modeling a Bow-Tie antenna-enhanced WSe<sub>2</sub>-LED on top of a SiN WG, we manage to achieve an enhanced EL quantum efficiency of  $\sim 8$  dB and high-speed ( $\sim$ GHz) single-mode LED emission, that can compete with widely used conventional organic LEDs (OLEDs). Our proposed schemes hold promise for applications in flexible LEDs and directly modulated LEDs for integrated photonics. Due to the recent investigation of emitting LMHs, their implementation in nanoscale LEDs remains quite unexplored, presenting several challenges, such as higher EL and PL quantum yields [47–51] and single-photon emission for integrated quantum LEDs (QLEDs) [52–55]. Thus, our study could be also extended in these fields.

It is noteworthy that the methodologies developed in this thesis effectively capture the interaction of 2D materials' properties across a broad range of excitation spectra and various device configurations. The final conclusions obtained here extend beyond the proposed devices, offering applicability to desired alternative configurations, consisting of various combinations of 2D materials, that are not limited to a specific frequency range. Our research, providing a framework for designing and optimizing realistic optical devices, facilitates the relation between fundamental physics and practical device engineering.

## References

- [1] M. Kanidi, A. Dagkli, N. Kelaidis, D. Palles, S. Aminalragia-Giamini, J. Marquez-Velasco, A. Colli, A. Dimoulas, E. Lidorikis, M. Kandyla, *et al.*, “Surface-enhanced raman spectroscopy of graphene integrated in plasmonic silicon platforms with three-

- dimensional nanotopography,” *The Journal of Physical Chemistry C*, vol. 123, no. 5, pp. 3076–3087, 2019.
- [2] S. Doukas, A. Chatzilari, A. Dagkli, A. Papagiannopoulos, and E. Lidorikis, “Deep and fast free-space electro-absorption modulation in a mobility-independent graphene-loaded bragg resonator,” *Applied Physics Letters*, vol. 113, no. 1, 2018.
- [3] A. Cadore, B. L. T. Rosa, I. Paradisanos, S. Mignuzzi, D. De Fazio, E. Alexeev, A. Dagkli, J. Muench, G. Kakavelakis, S. M. Schinde, *et al.*, “Monolayer ws<sub>2</sub> electro-and photo-luminescence enhancement by tfsi treatment,” *2D Materials*, 2024.
- [4] F. Bonaccorso, Z. Sun, T. Hasan, and A. Ferrari, “Graphene photonics and optoelectronics,” *Nature photonics*, vol. 4, no. 9, pp. 611–622, 2010.
- [5] Q. Bao and K. P. Loh, “Graphene photonics, plasmonics, and broadband optoelectronic devices,” *ACS nano*, vol. 6, no. 5, pp. 3677–3694, 2012.
- [6] X. Duan, C. Wang, A. Pan, R. Yu, and X. Duan, “Two-dimensional transition metal dichalcogenides as atomically thin semiconductors: opportunities and challenges,” *Chemical Society Reviews*, vol. 44, no. 24, pp. 8859–8876, 2015.
- [7] A. Bablich, S. Kataria, and M. C. Lemme, “Graphene and two-dimensional materials for optoelectronic applications,” *Electronics*, vol. 5, no. 1, p. 13, 2016.
- [8] Q. Wang, J. Lai, and D. Sun, “Review of photo response in semiconductor transition metal dichalcogenides based photosensitive devices,” *Optical Materials Express*, vol. 6, no. 7, pp. 2313–2327, 2016.
- [9] F. Xia, H. Wang, D. Xiao, M. Dubey, and A. Ramasubramaniam, “Two-dimensional material nanophotonics,” *Nature Photonics*, vol. 8, no. 12, pp. 899–907, 2014.
- [10] K. F. Mak and J. Shan, “Photonics and optoelectronics of 2d semiconductor transition metal dichalcogenides,” *Nature Photonics*, vol. 10, no. 4, pp. 216–226, 2016.
- [11] Z. Sun, A. Martinez, and F. Wang, “Optical modulators with 2d layered materials,” *Nature Photonics*, vol. 10, no. 4, pp. 227–238, 2016.
- [12] F. Koppens, T. Mueller, P. Avouris, A. Ferrari, M. Vitiello, and M. Polini, “Photodetectors based on graphene, other two-dimensional materials and hybrid systems,” *Nature nanotechnology*, vol. 9, no. 10, pp. 780–793, 2014.
- [13] Z. Lou, Z. Liang, and G. Shen, “Photodetectors based on two dimensional materials,” *Journal of Semiconductors*, vol. 37, no. 9, p. 091001, 2016.
- [14] F. Withers, O. Del Pozo-Zamudio, A. Mishchenko, A. Rooney, A. Gholinia, K. Watanabe, T. Taniguchi, S. J. Haigh, A. Geim, A. Tartakovskii, *et al.*, “Light-emitting diodes by band-structure engineering in van der waals heterostructures,” *Nature materials*, vol. 14, no. 3, pp. 301–306, 2015.
- [15] R. R. Nair, P. Blake, A. N. Grigorenko, K. S. Novoselov, T. J. Booth, T. Stauber, N. M. Peres, and A. K. Geim, “Fine structure constant defines visual transparency of graphene,” *science*, vol. 320, no. 5881, pp. 1308–1308, 2008.

- [16] N. M. Gabor, J. C. Song, Q. Ma, N. L. Nair, T. Taychatanapat, K. Watanabe, T. Taniguchi, L. S. Levitov, and P. Jarillo-Herrero, “Hot carrier–assisted intrinsic photoresponse in graphene,” *Science*, vol. 334, no. 6056, pp. 648–652, 2011.
- [17] T. Mueller, F. Xia, and P. Avouris, “Graphene photodetectors for high-speed optical communications,” *Nature photonics*, vol. 4, no. 5, pp. 297–301, 2010.
- [18] X. Gan, R.-J. Shiue, Y. Gao, I. Meric, T. F. Heinz, K. Shepard, J. Hone, S. Assefa, and D. Englund, “Chip-integrated ultrafast graphene photodetector with high responsivity,” *Nature photonics*, vol. 7, no. 11, pp. 883–887, 2013.
- [19] K. F. Mak, C. Lee, J. Hone, J. Shan, and T. F. Heinz, “Atomically thin mos 2: a new direct-gap semiconductor,” *Physical review letters*, vol. 105, no. 13, p. 136805, 2010.
- [20] Y. Li, A. Chernikov, X. Zhang, A. Rigosi, H. M. Hill, A. M. Van Der Zande, D. A. Chenet, E.-M. Shih, J. Hone, and T. F. Heinz, “Measurement of the optical dielectric function of monolayer transition-metal dichalcogenides: Mos 2, mo s e 2, ws 2, and ws e 2,” *Physical Review B*, vol. 90, no. 20, p. 205422, 2014.
- [21] L. Britnell, R. M. Ribeiro, A. Eckmann, R. Jalil, B. D. Belle, A. Mishchenko, Y.-J. Kim, R. V. Gorbachev, T. Georgiou, S. V. Morozov, *et al.*, “Strong light-matter interactions in heterostructures of atomically thin films,” *Science*, vol. 340, no. 6138, pp. 1311–1314, 2013.
- [22] J. Yang, J. Li, Z. Du, Q. Gong, J. Teng, and M. Hong, “Laser hybrid micro/nano-structuring of si surfaces in air and its applications for sers detection,” *Scientific reports*, vol. 4, no. 1, p. 6657, 2014.
- [23] E. D. Diebold, N. H. Mack, S. K. Doorn, and E. Mazur, “Femtosecond laser-nanostructured substrates for surface-enhanced raman scattering,” *Langmuir*, vol. 25, no. 3, pp. 1790–1794, 2009.
- [24] V. Parmar, P. K. Kanaujia, R. K. Bommali, and G. V. Prakash, “Efficient surface enhanced raman scattering substrates from femtosecond laser based fabrication,” *Optical Materials*, vol. 72, pp. 86–90, 2017.
- [25] M. Liu, X. Yin, E. Ulin-Avila, B. Geng, T. Zentgraf, L. Ju, F. Wang, and X. Zhang, “A graphene-based broadband optical modulator,” *Nature*, vol. 474, no. 7349, pp. 64–67, 2011.
- [26] C. T. Phare, Y.-H. Daniel Lee, J. Cardenas, and M. Lipson, “Graphene electro-optic modulator with 30 ghz bandwidth,” *Nature photonics*, vol. 9, no. 8, pp. 511–514, 2015.
- [27] N. Youngblood, Y. Anugrah, R. Ma, S. J. Koester, and M. Li, “Multifunctional graphene optical modulator and photodetector integrated on silicon waveguides,” *Nano letters*, vol. 14, no. 5, pp. 2741–2746, 2014.
- [28] M. Mohsin, D. Schall, M. Otto, A. Nocolak, D. Neumaier, and H. Kurz, “Graphene based low insertion loss electro-absorption modulator on soi waveguide,” *Optics express*, vol. 22, no. 12, pp. 15292–15297, 2014.

- [29] D. Ansell, I. Radko, Z. Han, F. Rodriguez, S. Bozhevolnyi, and A. Grigorenko, “Hybrid graphene plasmonic waveguide modulators,” *Nature communications*, vol. 6, no. 1, p. 8846, 2015.
- [30] V. Soriano, M. Midrio, G. Contestabile, I. Asselberghs, J. Van Campenhout, C. Huyghebaert, I. Goykhman, A. Ott, A. Ferrari, and M. Romagnoli, “Graphene–silicon phase modulators with gigahertz bandwidth,” *Nature Photonics*, vol. 12, no. 1, pp. 40–44, 2018.
- [31] S. Yu, X. Wu, Y. Wang, X. Guo, and L. Tong, “2d materials for optical modulation: challenges and opportunities,” *Advanced Materials*, vol. 29, no. 14, p. 1606128, 2017.
- [32] C.-C. Lee, S. Suzuki, W. Xie, and T. Schibli, “Broadband graphene electro-optic modulators with sub-wavelength thickness,” *Optics express*, vol. 20, no. 5, pp. 5264–5269, 2012.
- [33] F. J. Rodriguez, D. E. Aznakayeva, O. P. Marshall, V. G. Kravets, and A. N. Grigorenko, “Solid-state electrolyte-gated graphene in optical modulators,” *Advanced Materials*, vol. 29, no. 19, p. 1606372, 2017.
- [34] T. Sun, J. Kim, J. M. Yuk, A. Zettl, F. Wang, and C. Chang-Hasnain, “Surface-normal electro-optic spatial light modulator using graphene integrated on a high-contrast grating resonator,” *Optics express*, vol. 24, no. 23, pp. 26035–26043, 2016.
- [35] A. Majumdar, J. Kim, J. Vuckovic, and F. Wang, “Electrical control of silicon photonic crystal cavity by graphene,” *Nano letters*, vol. 13, no. 2, pp. 515–518, 2013.
- [36] J. T. Kim, K. H. Chung, and C.-G. Choi, “Thermo-optic mode extinction modulator based on graphene plasmonic waveguide,” *Optics Express*, vol. 21, no. 13, pp. 15280–15286, 2013.
- [37] L. Yu, D. Dai, and S. He, “Graphene-based transparent flexible heat conductor for thermally tuning nanophotonic integrated devices,” *Applied Physics Letters*, vol. 105, no. 25, 2014.
- [38] S. Gan, C. Cheng, Y. Zhan, B. Huang, X. Gan, S. Li, S. Lin, X. Li, J. Zhao, H. Chen, *et al.*, “A highly efficient thermo-optic microring modulator assisted by graphene,” *Nanoscale*, vol. 7, no. 47, pp. 20249–20255, 2015.
- [39] D. Andrzejewski, H. Myja, M. Heuken, A. Grundmann, H. Kalisch, A. Vescan, T. Kümmell, and G. Bacher, “Scalable large-area p–i–n light-emitting diodes based on ws<sub>2</sub> monolayers grown via mocvd,” *ACS Photonics*, vol. 6, no. 8, pp. 1832–1839, 2019.
- [40] D. Andrzejewski, E. Hopmann, M. John, T. Kümmell, and G. Bacher, “Ws<sub>2</sub> monolayer-based light-emitting devices in a vertical p–n architecture,” *Nanoscale*, vol. 11, no. 17, pp. 8372–8379, 2019.
- [41] J. Wang, F. Lin, I. Verzhbitskiy, K. Watanabe, T. Taniguchi, J. Martin, and G. Eda, “Polarity tunable trionic electroluminescence in monolayer wse<sub>2</sub>,” *Nano Letters*, vol. 19, no. 10, pp. 7470–7475, 2019.

- [42] M. Paur, A. J. Molina-Mendoza, R. Bratschitsch, K. Watanabe, T. Taniguchi, and T. Mueller, “Electroluminescence from multi-particle exciton complexes in transition metal dichalcogenide semiconductors,” *Nature Communications*, vol. 10, no. 1, p. 1709, 2019.
- [43] R. Sundaram, M. Engel, A. Lombardo, R. Krupke, A. Ferrari, P. Avouris, and M. Steiner, “Electroluminescence in single layer mos<sub>2</sub>,” *Nano letters*, vol. 13, no. 4, pp. 1416–1421, 2013.
- [44] Y. Sheng, T. Chen, Y. Lu, R.-J. Chang, S. Sinha, and J. H. Warner, “High-performance ws<sub>2</sub> monolayer light-emitting tunneling devices using 2d materials grown by chemical vapor deposition,” *ACS nano*, vol. 13, no. 4, pp. 4530–4537, 2019.
- [45] S. Wang, J. Wang, W. Zhao, F. Giustiniano, L. Chu, I. Verzhbitskiy, J. Zhou Yong, and G. Eda, “Efficient carrier-to-exciton conversion in field emission tunnel diodes based on mis-type van der waals heterostack,” *Nano letters*, vol. 17, no. 8, pp. 5156–5162, 2017.
- [46] L. Yuan and L. Huang, “Exciton dynamics and annihilation in ws<sub>2</sub> 2d semiconductors,” *Nanoscale*, vol. 7, no. 16, pp. 7402–7408, 2015.
- [47] J. S. Ross, P. Klement, A. M. Jones, N. J. Ghimire, J. Yan, D. Mandrus, T. Taniguchi, K. Watanabe, K. Kitamura, W. Yao, *et al.*, “Electrically tunable excitonic light-emitting diodes based on monolayer wse<sub>2</sub> p–n junctions,” *Nature nanotechnology*, vol. 9, no. 4, pp. 268–272, 2014.
- [48] H. Wang, C. Zhang, and F. Rana, “Ultrafast dynamics of defect-assisted electron–hole recombination in monolayer mos<sub>2</sub>,” *Nano letters*, vol. 15, no. 1, pp. 339–345, 2015.
- [49] C. Schneider, M. M. Glazov, T. Korn, S. Höfling, and B. Urbaszek, “Two-dimensional semiconductors in the regime of strong light-matter coupling,” *Nature communications*, vol. 9, no. 1, p. 2695, 2018.
- [50] G. Wang, A. Chernikov, M. M. Glazov, T. F. Heinz, X. Marie, T. Amand, and B. Urbaszek, “Colloquium: Excitons in atomically thin transition metal dichalcogenides,” *Reviews of Modern Physics*, vol. 90, no. 2, p. 021001, 2018.
- [51] T. Mueller and E. Malic, “Exciton physics and device application of two-dimensional transition metal dichalcogenide semiconductors,” *npj 2D Materials and Applications*, vol. 2, no. 1, p. 29, 2018.
- [52] C. Palacios-Berraquero and C. Palacios-Berraquero, “Atomically-thin quantum light emitting diodes,” *Quantum confined excitons in 2-dimensional materials*, pp. 71–89, 2018.
- [53] Z. Yuan, B. E. Kardynal, R. M. Stevenson, A. J. Shields, C. J. Lobo, K. Cooper, N. S. Beattie, D. A. Ritchie, and M. Pepper, “Electrically driven single-photon source,” *science*, vol. 295, no. 5552, pp. 102–105, 2002.

- [54] G. Clark, J. R. Schaibley, J. Ross, T. Taniguchi, K. Watanabe, J. R. Hendrickson, S. Mou, W. Yao, and X. Xu, “Single defect light-emitting diode in a van der waals heterostructure,” *Nano letters*, vol. 16, no. 6, pp. 3944–3948, 2016.
- [55] A. Politi, J. C. Matthews, and J. L. O’Brien, “Shor’s quantum factoring algorithm on a photonic chip,” *Science*, vol. 325, no. 5945, pp. 1221–1221, 2009.

# Appendix A

## SERS of Graphene on Plasmonic Silicon Substrates

### A.1 The role of SiO<sub>2</sub> layer

To estimate the effect of the native oxide layer on the electromagnetic response, we plot in Figure A.1 the FDTD simulated [1–6] absorption enhancement of a 50 nm Au nanoparticle on top of a flat Si substrate with and without a 2 nm native oxide layer in between. A small increase (about 6%) in enhancement is indeed found, when the oxide layer is taken into account, but it is small enough to be insignificant in relation to the main conclusions of our work. It is noteworthy that this effect cancels out with the SLG quenching shown below.

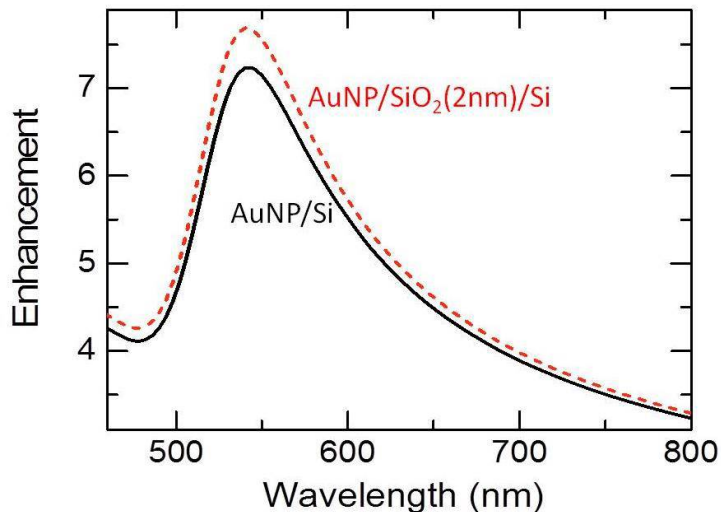


Figure A.1: Absorption enhancement of an Au nanoparticle on top of a flat Si substrate, with and without a 2 nm native silicon oxide in between them.

If we replace silicon with silicon oxide in the nanostructured substrate, we will have weaker scattering and weaker vertical interference, which should in general cause a lower SERS enhancement. On the other hand, interference effects could also result into increased phenomena. For completeness, and to demonstrate the richness of responses expected by interference, in Figure A.2 we plot the absorption enhancement in the AuNP/SiO<sub>2</sub>/Si system (Si flat substrate) as a function of SiO<sub>2</sub> thickness.

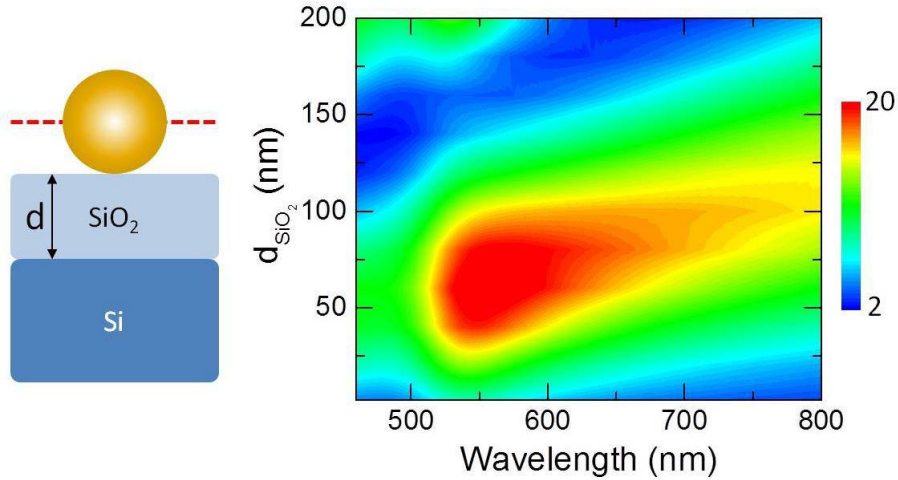


Figure A.2: Absorption enhancement for the AuNP/SiO<sub>2</sub>/Si system as a function of oxide thickness.

We find very strong resonances alternating with quenching, characteristic of the Fabry-Perot nature of the system. In any case, however, given that this is experimentally out of reach (for the nanostructured substrate case), such a study is beyond the scope of this thesis.

## A.2 Quenching effect of graphene on the optical properties of Au nanoparticles

Graphene absorbs 2.3% of light when suspended in air, which is a small amount overall, but massive considering it is only one atom thick, as described in section 2.1. As a result, we expect little quenching of the localized surface plasmon resonance (LSPR) response in Au nanoparticles, when only a single graphene layer is involved, while strong quenching should be expected in the case of many graphene layers surrounding the nanoparticles. To show the level of quenching expected by SLG in our study, in Figure A.3 we plot the integrated field intensity enhancement, equivalent to the absorption enhancement, defined as  $(S|E_0|^2)^{-1} \int |E|^2 dS$  on a plane bisecting the nanoparticle, where  $|E_0|^2$  is the incident intensity and  $S$  the area) in the cases (a) with and (b) without a SLG being on the bisecting plane.

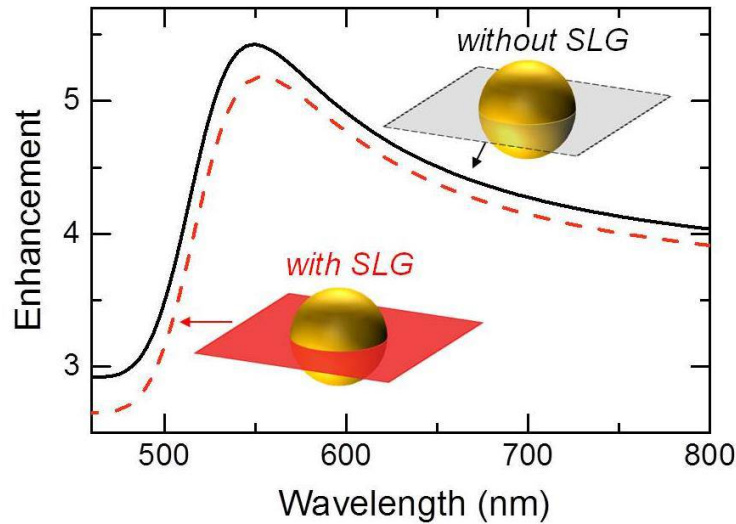


Figure A.3: Field intensity enhancement by Au nanoparticles, suspended in air, integrated over a bisecting plane through the nanoparticle center. For the red dashed line, a SLG is actually present on the integrating plane quenching by about 4% the LSPR. Nanoparticles have diameter 50 nm at a square lattice arrangement on a plane with 80 nm periodicity.

For simplicity, the Au nanoparticles are suspended in air. We observe indeed a small quenching of the order 4%, justifying our assumption of negligible influence of graphene on the LSPR properties of the Au nanoparticles.

### A.3 SERS of graphene on flat silicon with Au nanoparticles

Figure A.4 shows a schematic of Au nanoparticles on silicon nanopillars (left) and on a flat silicon substrate (right). A larger cross section between graphene and Au nanoparticles is assumed in the flat silicon case, and it is of interest to calculate if this can result in larger SERS enhancements.

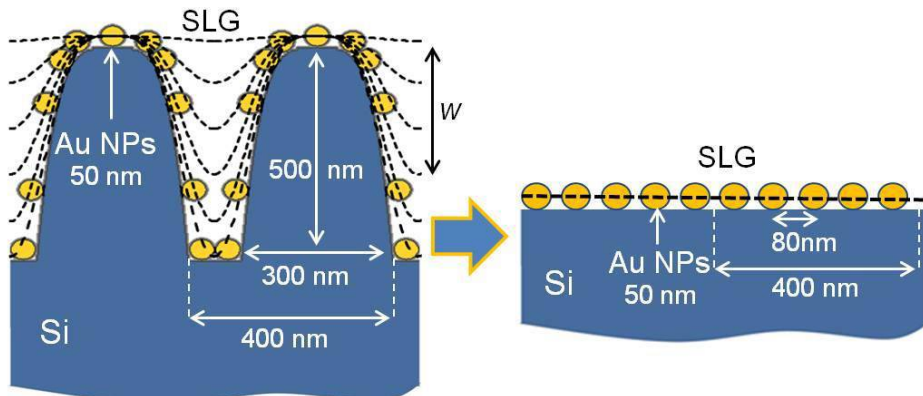


Figure A.4: A schematic of the experimental system (left) and Au nanoparticles on a flat silicon substrate (right).

In Figure A.5 we plot the SERS enhancement of graphene on Au nanoparticles on a flat silicon substrate. The reference device, as always, is graphene on bare Si. We find

up to two orders of magnitude increase, which is still, however, an order of magnitude smaller than what we get with Au nanoparticles on the silicon nanopillars.

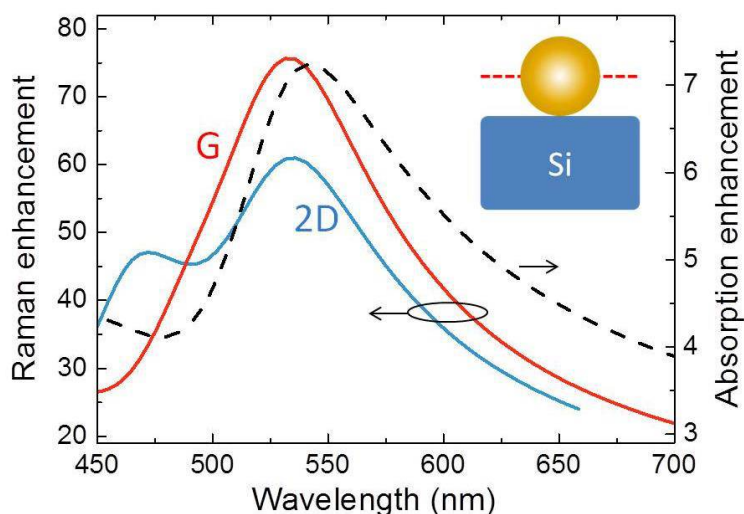


Figure A.5: SERS and absorption enhancement of graphene on Au nanoparticles on a flat Si substrate.

The reason is that when the Au nanoparticles are deposited on a flat silicon substrate, there is some destructive interferences between incident waves and waves reflected off the flat silicon interface. In essence, the effective field intensity at the interface is  $\sim |1 + r|^2 \simeq 0.2$ , where  $r = (1 - n)/(1 + n)$ , with  $n=3.45$  the Si index of refraction. Thus, the effective light field exciting the LSPR is smaller when the nanoparticles are on the flat silicon interface. This is generally true for any highly reflective surface. Given that SERS scales approximately with the fourth power of the field, this explains the one order of magnitude decrease compared to Au nanoparticles on nanostructured Si, where this destructive interference has been destroyed by disrupting the flat interface. This effect is also clearly seen in Figure A.2, where the enhancement increases significantly as we move graphene away from Si. So even though there is a larger cross section between nanoparticles and graphene in the flat silicon case, the LSPR itself is strongly quenched and thus a smaller signal is received compared to Au nanoparticles on the nanostructured Si case.

## References

- [1] A. Taflove, S. C. Hagness, and M. Picket-May, "Computational electromagnetics: the finite-difference time-domain method," *The Electrical Engineering Handbook*, vol. 3, no. 629-670, p. 15, 2005.
- [2] F. Schedin, E. Lidorikis, A. Lombardo, V. G. Kravets, A. K. Geim, A. N. Grigorenko, K. S. Novoselov, and A. C. Ferrari, "Surface-enhanced raman spectroscopy of graphene," *ACS nano*, vol. 4, no. 10, pp. 5617–5626, 2010.
- [3] F. Wooten, *Optical properties of solids*. Citeseer, 1972.
- [4] P. B. Johnson and R.-W. Christy, "Optical constants of the noble metals," *Physical review B*, vol. 6, no. 12, p. 4370, 1972.

- [5] E. Lidorikis, S. Egusa, and J. Joannopoulos, "Effective medium properties and photonic crystal superstructures of metallic nanoparticle arrays," *Journal of Applied Physics*, vol. 101, no. 5, 2007.
- [6] D. E. Aspnes and A. Studna, "Dielectric functions and optical parameters of si, ge, gap, gaas, gasb, inp, inas, and insb from 1.5 to 6.0 ev," *Physical review B*, vol. 27, no. 2, p. 985, 1983.

# Appendix B

## Graphene-based Optical Modulation and Pulse-shaping

### B.1 Critical Coupling

Graphene's absorption of approximately 2.3% in the visible to near-infrared (NIR) range is remarkable, considering the atomic-thickness of its structure. However, in practical applications, this absorption rate needs improvement, especially considering that placing graphene on a substrate or embedding it in a dielectric further reduces its absorption. For instance, when graphene is placed between a dielectric with index  $n_1$  and a substrate with index  $n_2$  in the thin film limit [1], its absorption from visible to NIR range becomes

$$A_{SLG} \sim 0.023 \frac{4n_1}{(n_1 + n_2)^2} \quad (\text{B.1})$$

In the visible to NIR spectral range, extensive research has been conducted to enhance single-layer graphene (SLG) absorption. This research has led to the development of graphene-based perfect absorbers [2–4]. To attain this goal, studies have explored various techniques, such as utilizing localized surface plasmon resonances on metals [1, 5] (see subsection 3.1.3), Fabry-Perot cavity resonances [6–8] (see subsection 3.2.2), and guided mode resonances [9–13] (see subsection 3.2.3).

In this thesis, specifically in chapter 6, critical coupling mechanism is employed to enhance graphene's absorption [2, 9, 14]. This mechanism relies on a resonant effect, where perfect absorption within a cavity is achievable under specific conditions. Considering a lossy resonant cavity with stored energy  $|a|^2$  in a single resonance at  $\omega_0$ , interacting with input and output (reflected) waves of amplitudes  $u$  and  $y_r$  respectively, as illustrated in the top insets of Figure B.1. The configuration of middle top inset can be analyzed using coupled mode theory [14] as follows:

$$\frac{da}{dt} = (-i\omega_0 - \gamma_d - \gamma_a)a + u\sqrt{2\gamma_d}, y_r = a\sqrt{2\gamma_d} - u \quad (\text{B.2})$$

where  $\gamma_d$  represents the mode leakage rate, and  $\gamma_a$  denotes the resonator absorption rate. It is important to note that this configuration constitutes a single-port system, meaning that light is incoming from only one side, while the transmission through the cavity is inhibited by a metallic back-mirror. This back-mirror is essential for achieving perfect absorption because in a double-port system see Figure B.1 (a)), the maximum attainable absorption, assuming illumination from only one side of the cavity, is limited to 50% [9, 14].

The single-port system can be implemented in two different configurations, one featuring only the totally reflecting back-mirror (see Figure B.1 (b)), and the other incorporating a partially transmitting mirror positioned in front of the resonant cavity (see Figure B.1 (c)). The former setup can be created by placing a dielectric spacer between the resonator and a metallic back-mirror, while the latter can be constructed using dielectric Bragg cavities situated between the resonator and the metallic back-mirror. It is noteworthy that the third configuration is particularly well-suited for materials with weak absorption characteristics, such as SLG in the VIS–NIR regime. In configurations (b-c), the reflection is described by [9, 14]

$$R = \left| \frac{y_r}{u} \right|^2 = \frac{(\omega_0 - \omega)^2 + (\gamma_a - \gamma_d)^2}{(\omega_0 - \omega)^2 + (\gamma_a + \gamma_d)^2} \quad (\text{B.3})$$

and the absorption [9, 14]

$$A \equiv 1 - R = \frac{4\gamma_a\gamma_d}{(\omega_0 - \omega)^2 + (\gamma_a + \gamma_d)^2} \quad (\text{B.4})$$

From Equation B.4, it is evident that at resonance ( $\omega = \omega_0$ ), when cavity decay rate  $\gamma_d$  equals the absorption rate  $\gamma_a$ , perfect absorption (e.g.,  $A = 100\%$ ) occurs.

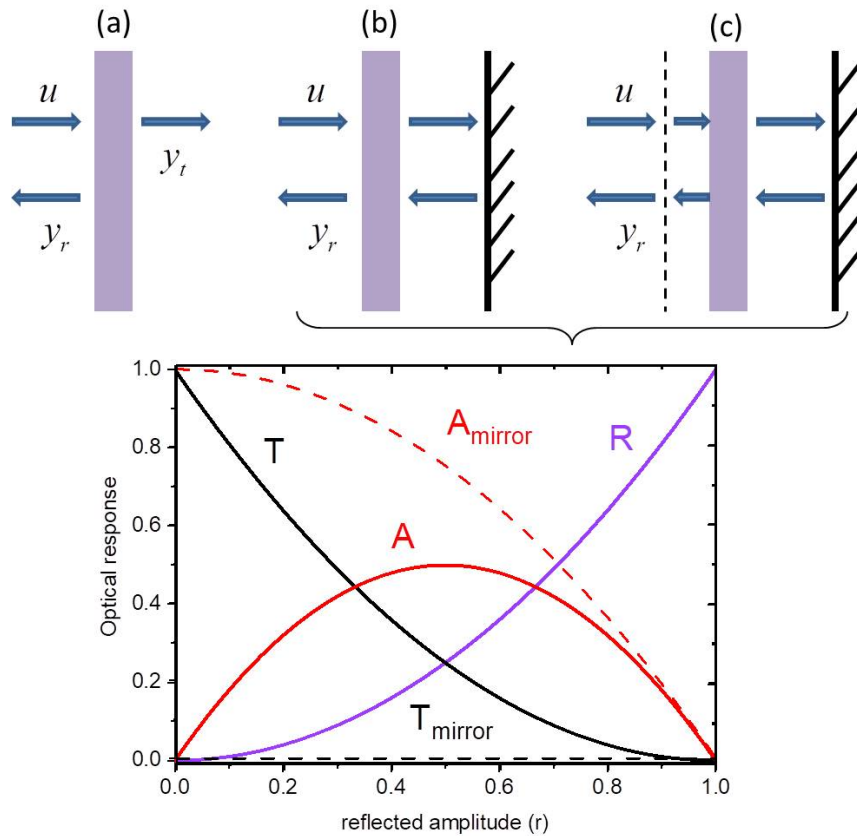


Figure B.1: Schematics of a double-port device (a), a resonant optical cavity with a totally reflecting back mirror (b) and a resonant cavity with a back mirror along with a partial transmitting mirror in front of the cavity (c). (b-c) single-port cases used to utilize critical coupling mechanisms.

The above mechanism is particularly useful for graphene-based devices, due to SLG's

absorption tunability, for example using electrostatic gating, providing the opportunity to follow critical coupling conditions. In this thesis critical coupling was exploited to enhance light absorption in graphene-based optical modulation devices, studied in Chapter 6.

## B.2 Electronic thermal cooling current

To calculate e-ph cooling current  $J_{e-ph}$ , we assume electron-phonon scattering [15], with optical [16–19] and acoustic phonons, via disorder-assisted super-collisions [20–24]. It is noteworthy that there is an ongoing debate about whether  $J_{e-ph}$  is primarily influenced by optical phonon scattering  $J_{op}$  or disorder-assisted super-collisions  $J_{sc}$  [21, 23–25]. Here, for simplicity, we assume that  $J_{op}$  and  $J_{sc}$  have approximately the same contribution in  $J_{e-ph}$ .

$$J_{e-ph} \equiv J_{op} + J_{sc} \quad (\text{B.5})$$

We ignore the normal (momentum-conserving) acoustic phonon scattering because of SLG's small Fermi surface [22, 26]. Instead, we focus on the thermal current resulting from optical phonon scattering [25, 27, 28].

$$J_{op} = \sum_i \left\{ \frac{9\hbar^2 \Omega_{i,SLG}^3 (\gamma'_0)^2}{\pi (\hbar v_{F,SLG})^4 \rho_{SLG}} \times \left[ N\left(\frac{\Omega_{i,SLG}}{k_B T_{e,SLG}}\right) - N\left(\frac{\Omega_{i,SLG}}{k_B T_{l,SLG}}\right) \right] F(\mu_{SLG}, T_{e,SLG}) \right\} \quad (\text{B.6})$$

Where

$$F(\mu_{SLG}, T_{e,SLG}) = \int_{-\infty}^{\infty} |x(1-x)| \{f[\Omega_i(x-1)] - f(\Omega_i x)\} dx \quad (\text{B.7})$$

We consider two optical phonon branches [19, 29, 30], with  $\Omega_K=161$  meV, corresponding to Raman D peak at K point of the Brillouin zone, and  $\Omega_\Gamma=196$  meV, corresponding to Raman G peak at  $\Gamma$  point of the Brillouin zone. We define  $\rho_{SLG} = 7.6 \times 10^{-7} \text{ Kg/m}^2$  as the SLG mass density [26, 31–34],  $\gamma'_0$  is the derivative of the nearest-neighbor coupling amplitude,  $N(x) = (e^x - 1)^{-1}$  the Bose distribution [28], and  $f$  the Fermi-Dirac distribution.

Another pathway for cooling SLG carriers is through disorder-mediated (momentum non-conserving) emission of acoustic phonons, known as super-collisions. Super-collisions involve three-body collisions between carriers, phonons, and impurities [20–24]. This cooling mechanism is represented by assuming disordered short-range scatterers with a fixed mean-free path  $l$  of 100 nm throughout this study. The resulting thermal current, attributed to disorder-assisted super-collisions, is given by

$$J_{sc} = \gamma_{sc}(T_{e,SLG}^3 - T_{l,SLG}^3) \quad (\text{B.8})$$

where

$$\gamma_{sc} = \frac{9.62 D_{SLG}^2 k_B^3}{2 \rho_{SLG} s_{SLG}^2 \hbar k_{F,SLG} l} \frac{4(n_{e,SLG} + n_{h,SLG} + 2\delta n_{e,SLG})}{\pi (\hbar v_{F,SLG})^4} \quad (\text{B.9})$$

Where  $n_e$  ( $n_h$ ) electron (hole) concentration and  $\delta n_e$  the non-equilibrium photo-excited carrier density. The  $k_{F,SLG}l$  disorder parameter is the product of graphene Fermi wavevector  $k_{F,SLG}$  and mean free path for short-range scatterers  $l$ , which is proportional to the concentration of impurities.

## References

- [1] T. Echtermeyer, S. Milana, U. Sassi, A. Eiden, M. Wu, E. Lidorikis, and A. Ferrari, “Surface plasmon polariton graphene photodetectors,” *Nano Letters*, vol. 16, no. 1, pp. 8–20, 2016.
- [2] C. Guo, J. Zhang, W. Xu, K. Liu, X. Yuan, S. Qin, and Z. Zhu, “Graphene-based perfect absorption structures in the visible to terahertz band and their optoelectronics applications,” *Nanomaterials*, vol. 8, no. 12, p. 1033, 2018.
- [3] A. Nematpour, M. L. Grilli, L. Lancellotti, and N. Lisi, “Towards perfect absorption of single layer cvd graphene in an optical resonant cavity: Challenges and experimental achievements,” *Materials*, vol. 15, no. 1, p. 352, 2022.
- [4] S. K. Patel, J. Surve, J. Parmar, and T. K. Nguyen, “Review on graphene-based absorbers for infrared to ultraviolet frequencies,” *Journal of Advanced Engineering and Computation*, vol. 5, no. 4, pp. 214–238, 2021.
- [5] S. Song, Q. Chen, L. Jin, and F. Sun, “Great light absorption enhancement in a graphene photodetector integrated with a metamaterial perfect absorber,” *Nanoscale*, vol. 5, no. 20, pp. 9615–9619, 2013.
- [6] A. Ferreira, N. Peres, R. Ribeiro, and T. Stauber, “Graphene-based photodetector with two cavities,” *Physical Review B*, vol. 85, no. 11, p. 115438, 2012.
- [7] M. Furchi, A. Urich, A. Pospischil, G. Lilley, K. Unterrainer, H. Detz, P. Klang, A. M. Andrews, W. Schrenk, G. Strasser, *et al.*, “Microcavity-integrated graphene photodetector,” *Nano letters*, vol. 12, no. 6, pp. 2773–2777, 2012.
- [8] A. Nematpour, N. Lisi, L. Lancellotti, R. Chierchia, and M. L. Grilli, “Experimental mid-infrared absorption (84%) of single-layer graphene in a reflective asymmetric fabry–perot filter: Implications for photodetectors,” *ACS Applied Nano Materials*, vol. 4, no. 2, pp. 1495–1502, 2021.
- [9] J. R. Piper and S. Fan, “Total absorption in a graphene monolayer in the optical regime by critical coupling with a photonic crystal guided resonance,” *Acs Photonics*, vol. 1, no. 4, pp. 347–353, 2014.
- [10] M. Grande, M. Vincenti, T. Stomeo, G. Bianco, D. De Ceglia, N. Aközbeek, V. Petruzzelli, G. Bruno, M. De Vittorio, M. Scalora, *et al.*, “Graphene-based perfect optical absorbers harnessing guided mode resonances,” *Optics express*, vol. 23, no. 16, pp. 21032–21042, 2015.
- [11] Y. Fan, C. Guo, Z. Zhu, W. Xu, F. Wu, X. Yuan, and S. Qin, “Monolayer-graphene-based perfect absorption structures in the near infrared,” *Optics express*, vol. 25, no. 12, pp. 13079–13086, 2017.

- [12] Y. Long, L. Shen, H. Xu, H. Deng, and Y. Li, “Achieving ultranarrow graphene perfect absorbers by exciting guided-mode resonance of one-dimensional photonic crystals,” *Scientific reports*, vol. 6, no. 1, p. 32312, 2016.
- [13] C.-C. Guo, Z.-H. Zhu, X.-D. Yuan, W.-M. Ye, K. Liu, J.-F. Zhang, W. Xu, and S.-Q. Qin, “Experimental demonstration of total absorption over 99% in the near infrared for monolayer-graphene-based subwavelength structures,” *Advanced Optical Materials*, vol. 4, no. 12, pp. 1955–1960, 2016.
- [14] H. A. Haus, “Waves and fields in optoelectronics,” (*No Title*), 1984.
- [15] S. Doukas, P. Mensz, N. Myoung, A. Ferrari, I. Goykhman, and E. Lidorikis, “Thermionic graphene/silicon schottky infrared photodetectors,” *Physical Review B*, vol. 105, no. 11, p. 115417, 2022.
- [16] A. Tomadin, D. Brida, G. Cerullo, A. C. Ferrari, and M. Polini, “Nonequilibrium dynamics of photoexcited electrons in graphene: Collinear scattering, auger processes, and the impact of screening,” *Physical Review B*, vol. 88, no. 3, p. 035430, 2013.
- [17] D. Brida, A. Tomadin, C. Manzoni, Y. J. Kim, A. Lombardo, S. Milana, R. R. Nair, K. S. Novoselov, A. C. Ferrari, G. Cerullo, *et al.*, “Ultrafast collinear scattering and carrier multiplication in graphene,” *Nature communications*, vol. 4, no. 1, p. 1987, 2013.
- [18] M. Lazzeri, S. Piscanec, F. Mauri, A. Ferrari, and J. Robertson, “Electron transport and hot phonons in carbon nanotubes,” *Physical review letters*, vol. 95, no. 23, p. 236802, 2005.
- [19] S. Piscanec, M. Lazzeri, F. Mauri, A. Ferrari, and J. Robertson, “Kohn anomalies and electron-phonon interactions in graphite,” *Physical review letters*, vol. 93, no. 18, p. 185503, 2004.
- [20] J. F. Rodriguez-Nieva, M. S. Dresselhaus, and J. C. Song, “Enhanced thermionic-dominated photoresponse in graphene schottky junctions,” *Nano Letters*, vol. 16, no. 10, pp. 6036–6041, 2016.
- [21] M. W. Graham, S.-F. Shi, D. C. Ralph, J. Park, and P. L. McEuen, “Photocurrent measurements of supercollision cooling in graphene,” *Nature Physics*, vol. 9, no. 2, pp. 103–108, 2013.
- [22] J. C. Song and L. S. Levitov, “Energy flows in graphene: hot carrier dynamics and cooling,” *Journal of Physics: Condensed Matter*, vol. 27, no. 16, p. 164201, 2015.
- [23] J. C. Song, M. Y. Reizer, and L. S. Levitov, “Disorder-assisted electron-phonon scattering and cooling pathways in graphene,” *Physical review letters*, vol. 109, no. 10, p. 106602, 2012.
- [24] A. Betz, S. H. Jhang, E. Pallecchi, R. Ferreira, G. Fève, J.-M. Berroir, and B. Plaçais, “Supercollision cooling in undoped graphene,” *Nature Physics*, vol. 9, no. 2, pp. 109–112, 2013.

- [25] E. A. Pogna, X. Jia, A. Principi, A. Block, L. Banszerus, J. Zhang, X. Liu, T. Sohler, S. Forti, K. Soundarapandian, *et al.*, “Hot-carrier cooling in high-quality graphene is intrinsically limited by optical phonons,” *ACS nano*, vol. 15, no. 7, pp. 11285–11295, 2021.
- [26] D. K. Efetov and P. Kim, “Controlling electron-phonon interactions in graphene at ultrahigh carrier densities,” *Physical review letters*, vol. 105, no. 25, p. 256805, 2010.
- [27] R. Bistritzer and A. H. MacDonald, “Electronic cooling in graphene,” *Physical Review Letters*, vol. 102, no. 20, p. 206410, 2009.
- [28] J. Viljas and T. Heikkilä, “Electron-phonon heat transfer in monolayer and bilayer graphene,” *Physical Review B*, vol. 81, no. 24, p. 245404, 2010.
- [29] A. C. Ferrari, J. C. Meyer, V. Scardaci, C. Casiraghi, M. Lazzeri, F. Mauri, S. Piscanec, D. Jiang, K. S. Novoselov, S. Roth, *et al.*, “Raman spectrum of graphene and graphene layers,” *Physical review letters*, vol. 97, no. 18, p. 187401, 2006.
- [30] A. C. Ferrari, “Raman spectroscopy of graphene and graphite: Disorder, electron-phonon coupling, doping and nonadiabatic effects,” *Solid state communications*, vol. 143, no. 1-2, pp. 47–57, 2007.
- [31] T. Low, V. Perebeinos, R. Kim, M. Freitag, and P. Avouris, “Cooling of photoexcited carriers in graphene by internal and substrate phonons,” *Physical Review B*, vol. 86, no. 4, p. 045413, 2012.
- [32] E. Hwang and S. D. Sarma, “Acoustic phonon scattering limited carrier mobility in two-dimensional extrinsic graphene,” *Physical Review B*, vol. 77, no. 11, p. 115449, 2008.
- [33] J. Chen, C. Jang, S. Xiao, M. Ishigami, and M. Fuhrer, “Intrinsic and extrinsic performance limits of graphene devices on sio<sub>2</sub> nat,” *Nanotechnol*, vol. 3, pp. 206–209, 2008.
- [34] K. I. Bolotin, K. J. Sikes, J. Hone, H. Stormer, and P. Kim, “Temperature-dependent transport in suspended graphene,” *Physical review letters*, vol. 101, no. 9, p. 096802, 2008.

# Appendix C

## TMD-based LEDs with Graphene

### C.1 Bow-Tie antenna on WG: Geometrical optimization

Here, we geometrically optimize a gold Bow-Tie antenna positioned on top of 1L-WSe<sub>2</sub>/hBN/SLG LED waveguide design, depicted in Figure C.1(a). As in free-space emission (see section 7.6.1), antenna dimensions, including width (W), length (L) and gap length (gap) are scaled for a buried single-mode SiN WG, with a one-sided totally reflecting back grating. Figure C.1(b-d) shows the Purcell efficiency enhancement for variable W, L and gap lengths as a function of wavelength.

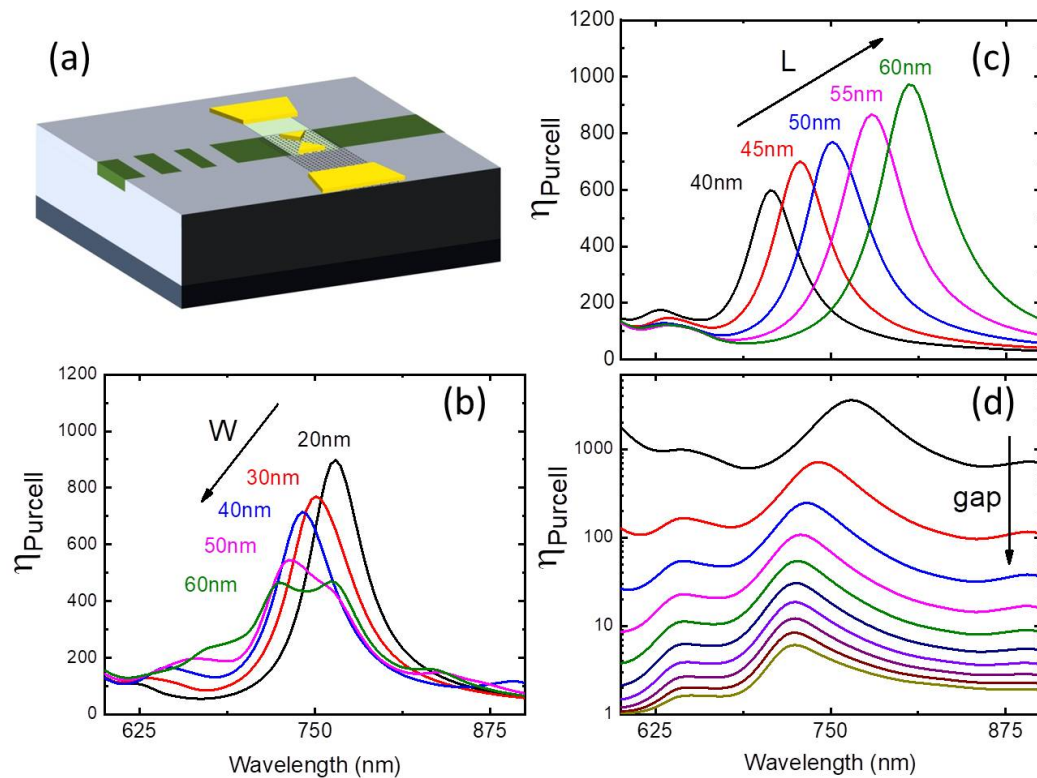


Figure C.1: Antenna-enhanced integrated LED: Purcell efficiency as a function of wavelength for variable Bow-Tie antenna (b) widths (W), (c) lengths L and (d) gaps.

Choosing the appropriate antenna dimensions for high  $\eta_{Purcell}$  and limiting material absorption (at 750 nm), we can plasmonically enhance the final WG efficiency  $\eta_{WG}$ .

## C.2 Reference LED device's EL efficiency

Different values of  $\eta_0 \equiv \eta_{(ref)}$  are employed to calculate the final  $\eta_{WG}$  enhancement in the optimal Au Bow-Tie antenna case, described in the main text.

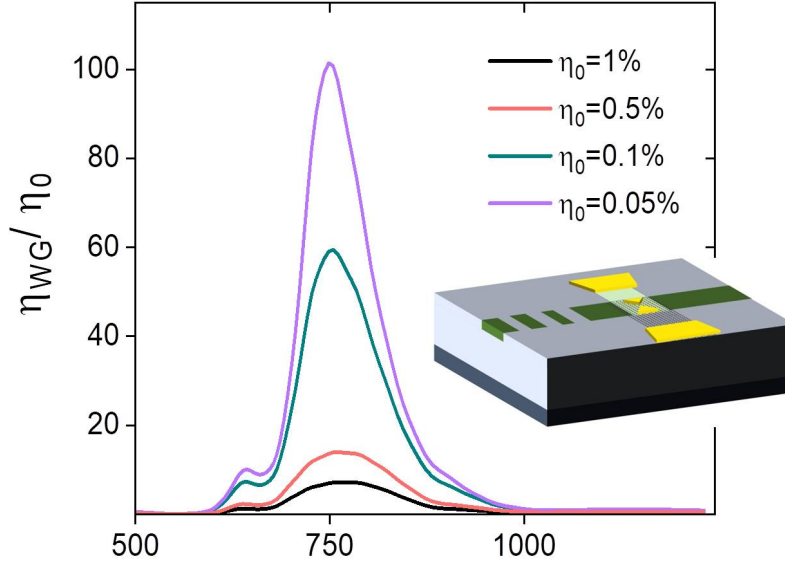


Figure C.2: Antenna-enhanced integrated LED: WG efficiency enhancement  $\eta_{WG}/\eta_0$  as a function of wavelength for  $\eta_0 \leq 1\%$ .

Assuming low reference efficiencies  $\eta_0 \leq 1\%$ , we observe significant enhancements in final  $\eta_{WG}$ , compared to  $\eta_0$ , that can reach up to order of magnitude, as shown in Figure C.2. The above results show the versatility of our post-analysis method for variable  $\eta_0$  and could prove valuable when experimental measurements exhibit low EL efficiency for the under study TMD emitters.

## C.3 Bow-Tie antenna: Material Parameters

In our FDTD method [1] (see section 4.2 of the main text), Maxwell's equations including polarizability terms are time-integrated on a computational grid, as outlined in [2]. At a point in a dispersive material, each relevant polarizability term contributes to an absorption  $A_j = 1/2\Re(J_j^*E)$ , where the polarization current is  $J_j = \vartheta P_j/\vartheta t$ . Upon Fourier transforming the time series of  $E$  and  $J_j$ , we obtain the spectral absorption at every point in every dispersive material. The polarization equations imply a Drude-Lorentz model [3] for the dielectric function (see Equation 3.32), where the first term is the Drude free-electron contribution and the second contains Lorentz oscillators corresponding to inter-band transitions. To accurately reproduce the dielectric functions of Au, Ag, Al we fit the

experimental data derived by [4] and represented as colored squares in Figure C.3. For Au antenna,  $\epsilon_1 = -20.148$ ,  $\epsilon_2 = 1.2470$ ,  $\epsilon_2/\epsilon_1 = 0.0619$  and  $\alpha = 7.5245e+5 \text{ cm}^{-1}$ , for Ag,  $\epsilon_1 = -26.986$ ,  $\epsilon_2 = 0.32380$ ,  $\epsilon_2/\epsilon_1 = 0.0119$  and  $\alpha = 8.7042e+5 \text{ cm}^{-1}$ , and for Al,  $\epsilon_1 = -65.255$ ,  $\epsilon_2 = 39.848$ ,  $\epsilon_2/\epsilon_1 = 0.6107$  and  $\alpha = 1.4104e+5 \text{ cm}^{-1}$ .

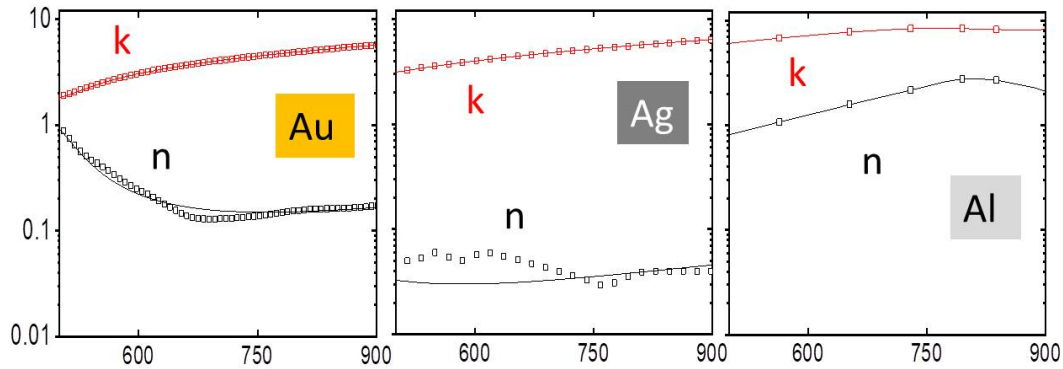


Figure C.3: Experimental (squares) and Drude-Lorentz fits (lines) for the refractive indices of (a) Au, (b) Ag and (c) Al antenna used in our LED configurations.

Despite the higher absorption coefficient  $\alpha$  in case of Ag, the ratio between the imaginary and real parts of the dielectric function ( $\epsilon_2/\epsilon_1$ ) at 750 nm is lower, resulting in a correspondingly lower antenna loss (aL).

## References

- [1] A. Taflove, S. C. Hagness, and M. Picket-May, "Computational electromagnetics: the finite-difference time-domain method," *The Electrical Engineering Handbook*, vol. 3, no. 629-670, p. 15, 2005.
- [2] F. Schedin, E. Lidorikis, A. Lombardo, V. G. Kravets, A. K. Geim, A. N. Grigorenko, K. S. Novoselov, and A. C. Ferrari, "Surface-enhanced raman spectroscopy of graphene," *ACS nano*, vol. 4, no. 10, pp. 5617–5626, 2010.
- [3] F. Wooten, *Optical properties of solids*. Citeseer, 1972.
- [4] P. B. Johnson and R.-W. Christy, "Optical constants of the noble metals," *Physical review B*, vol. 6, no. 12, p. 4370, 1972.

# Curriculum Vitae

## Personal information

First name/Surname **Alva Dagkli (Ph.D. candidate)**  
e-mail [a.dagkli@uoi.gr](mailto:a.dagkli@uoi.gr),  
[alvadagli@gmail.com](mailto:alvadagli@gmail.com)  
Date of birth [https://www.researchgate.net/profile/Alva\\_Dagkli](https://www.researchgate.net/profile/Alva_Dagkli)  
15/10/1988

## Research activities

Dates 2020 – 2021  
Position **Research assistant - Ph.D. candidate**  
Working Project Graphene Flagship EU project (**Core 3**), WP: Photonics and Optoelectronics  
Department of Materials Science and Engineering, University of Ioannina, Greece

Dates 2018 –2020  
Position **Research assistant - Ph.D. candidate**  
Working Project Graphene Flagship EU project (**Core 2**), WP: Photonics and Optoelectronics  
Department of Materials Science and Engineering, University of Ioannina, Greece

Dates 2014 – 2018  
Position **Research assistant - M.Sc. student, Ph.D. candidate**  
Working Project Graphene Flagship EU project (**Core 1**), WP: Photonics and Optoelectronics  
Department of Materials Science and Engineering, University of Ioannina, Greece

## Education

Dates 2016-2024  
Title **Ph.D. Department of Materials Science and Engineering, University of Ioannina, Greece**  
Thesis title: “Enhanced light-matter interactions and optoelectronic devices based on graphene and other 2D materials”  
Supervisor: Prof. Eleftherios Lidorikis

Dates 2012-2016  
Title **M.Sc. Physics department, University of Ioannina, Greece**  
Thesis title: “Theoretical study and design of nanostructures for optimizing their optical performance in graphene-based light harvesting and detection applications.”  
Supervisor: Prof. Constantine Kosmidis

Dates 2006-2012  
Title **B.Sc. Physics department, University of Ioannina, Greece**  
Thesis title: “Theoretical study and simulation of the magnetic bottle spectrometer.”  
Supervisor: Emmanouil Benis, Associate Professor

## Research Interests

- Computational electrodynamics
- Nanophotonics, plasmonics and enhanced light emission
- Graphene and TMD based optoelectronic device modeling
- Enhanced graphene-based photodetection, optical modulation and sensing
- Enhanced TMD-based nanoscale LEDs for free-space emission and integrated photonics

## Scientific Publications

- Title Monolayer WS<sub>2</sub> electro- and photo-luminescence enhancement by TFSI treatment  
Authors A. R. Cadore, B. L. T. Rosa, I. Paradisanos, S. Mignuzzi, D. De Fazio, E. M. Alexeev, **A. Dagkli**, J. E. Muench, G. Kakavelakis, S. M. Shinde, D. Yoon, S. Tongay, K. Watanabe, T. Taniguchi, E. Lidorikis, I. Goykhman, G. Soavi, and A. C. Ferrari  
Reference 2D Materials (2024)
- Title Surface-enhanced Raman spectroscopy of graphene integrated in plasmonic silicon platforms with three-dimensional nanotopography  
Authors Kanidi, M., **Dagkli, A.**, Kelaidis, N., Palles, D., Aministragia-Giamini, S., Marquez-Velasco, J., ... Kamitsos, E. I.  
Reference The Journal of Physical Chemistry C, 123(5), 3076-3087(2019)
- Title Deep and fast free-space electro-absorption modulation in a mobility-independent graphene-loaded Bragg resonator  
Authors S. Doukas, A. Chatzilari, **A. Dagkli**, A. Papagiannopoulos and E. Lidorikis  
Reference Appl. Phys. Lett. 113, 011102 (2018)

## Conferences and Meetings

- Type Poster presentation  
Title of presentation *Electro-optic free-space ultrafast pulse-shaping in a graphene-loaded Bragg resonator*  
Authors **A. Dagkli**, A. Chatzilari, S. Doukas, E. Lidorikis  
Symposium XXXVI Panhellenic Conference on Solid State Physics and Materials Science  
Date and Location 26-28 September **2022**, Heraklion, Greece
- Type Poster presentation  
Title of presentation *Light emitting diodes based on layered material heterostructures on cavities*  
Authors **A. Dagkli**, D. De Fazio, I. Goykhman, A.C. Ferrari, E. Lidorikis  
Symposium XXXIV Panhellenic Conference on Solid State Physics and Materials Science  
Date and Location 11-14 September **2019**, Patras, Greece
- Type Poster presentation  
Title of presentation *Surface-enhanced Raman spectroscopy of graphene integrated in plasmonic silicon platforms with a three dimensional nanotopography*  
Authors **A. Dagkli**, E. Lidorikis, M. Kanidi, M. Kandyla, A. Colli, N. Kelaidis, D. Palles, S.A. Giamini, J. Marquez, A. Dimoulas, E.I. Kamitsos  
Symposium 15th International Conference on Nanoscience Nanotechnologies (NN18)  
Date and Location 3-6 July **2018**, Thessaloniki, Greece
- Type Poster presentation  
Title of presentation *Deep and fast free-space electro-absorption modulation in a mobility-independent graphene-loaded Bragg resonator*

Authors	<b>A. Dagkli</b> , S. Doukas, A. Chatzilari, A. Papagiannopoulos, E. Lidorikis
Symposium	Graphene Week 2018
Date and Location	10-14 September <b>2018</b> , San Sebastian, Spain
Type	Oral presentation
Title of presentation	<i>LEDs based on 2D material heterostructures</i>
Authors	<b>A. Dagkli</b> and E. Lidorikis
Symposium	Graphene Flagship Meeting (Core I (8.2.3) and Core II (8.3.4))
Date and Location	18-20 December <b>2017</b> , Aachen, Germany
Type	Poster presentation
Title of presentation	<i>Modeling of surface enhanced Raman spectroscopy in monolayer graphene on top of plasmonic substrates</i>
Authors	<b>A. Dagkli</b> , E. Lidorikis, M. Kanidi, M. Kandyla, N. Kelaidis, D. Palles, S.A. Giamini, J. Marquez, A. Dimoulas, E.I. Kamitsos
Symposium	Graphene Week 2017
Date and Location	25-29 September <b>2017</b> , Athens, Greece
Type	Poster presentation
Title of presentation	<i>Modeling of enhanced absorption caused by plasmonic near-fields</i>
Authors	<b>Alkmini Dagkli</b> , Evangelou Sofia, E. Lidorikis
Symposium	Graphene Week 2015
Date and Location	22-26 June <b>2015</b> , Manchester, England

### Other education and training

Dates	2017 – 2023 <b>Teaching Assistant</b> , Electronic and magnetic materials laboratory (7 <sup>th</sup> semester) Department of Materials Science and Engineering, University of Ioannina, Greece
Dates	2013 – 2021 <b>Teaching Assistant</b> , Fortran and C++ Programming at the Computers Laboratory (1 <sup>st</sup> and 2 <sup>nd</sup> semester) Department of Materials Science and Engineering, University of Ioannina, Greece
English	First Certificate in English, University of Cambridge (Europe level B2) Certificate of Proficiency in English, University of Michigan (Europe level C2)
mother language	Greek
Computer skills	<ul style="list-style-type: none"> <li>❖ Use of Linux environment, Microsoft Windows and Microsoft Office package (Word, Excel, Power Point).</li> <li>❖ Coding: Fortran, C, C++, Matlab, Python</li> <li>❖ Data analysis: OriginLab.</li> <li>❖ Commercial software: Lumerical Solution (FDTD, FDE) commercial package</li> <li>❖ Misc: Latex typesetting</li> </ul>